UNIVERSIDAD MICHOACANA DE
SAN NICOLÁS DE HIDALGO

FACULTAD DE INGENIERÍA ELÉCTRICA
DIVISIÓN DE ESTUDIOS DE POSGRADO

Assessment of the Impact of Wind Power Generation on the Steady-State Operation of Power Systems

by
Uriel Fernando Sandoval Pérez

A thesis submitted in fulfilment of the requirements

for the degree of

Master of Science in Electrical Engineering

Advisor
Dr. Claudio Rubén Fuerte Esquivel

MORELIA, MICHOACÁN June 2015

ASSESSMENT OF THE IMPACT OF WIND POWER GENERATION ON THE STEADY-STATE OPERATION OF POWER SYSTEMS

Los Miembros del Jurado de Examen de Grado aprueban
la **Tesis de Maestría en Ciencias en Ingeniería Eléctrica** de ***Uriel Fernando Sandoval Pérez***

Dr. J. Jesús Rico Melgoza
Presidente del Jurado

Dr. Claudio Rubén Fuerte Esquivel
Director de Tesis

Dra. Elisa Espinosa Juárez
Vocal

Dr. Antonio Ramos Paz
Vocal

M.C. Jesús González Flores
Revisor Externo

Dr. Félix Calderón Solorio
Jefe de la División de Estudios de Posgrado de la Facultad de Ingeniería Eléctrica. UMSNH.
(Por reconocimiento de firmas)

UNIVERSIDAD MICHOACANA DE SAN NICOLÁS DE HIDALGO
Junio 2015

Abstract

Over the years, the use of wind energy conversion systems has become the most rapidly growing renewable energy source utilized in electricity generation all over the world. Even though wind energy is beneficial from the environmental standpoint, it makes the already complex task of achieving system controllability even more demanding. Consequently, the quantification of the effects that the large-scale integration of wind generation will cause on the network is a very important matter that requires special attention when planning and operating an electrical power system.

Based on the information mentioned above, the objective of this thesis is to provide an all-encompassing mathematical modeling framework as well as advanced analytical and numerical methods for the assessment of grid-connected wind energy conversion systems considering of the main design and operating characteristics of these resources and the electrical power grid.

On the one hand, the conventional power flow problem is expanded to incorporate three steady-state models of the most common wind generator technologies. The variable-speed wind generators' ability to provide load-frequency control support is well represented based on the distributed *slack bus* concept. Within this distributed *slack bus* concept the active power imbalance is modulated by all the generators in the system. In this context, a unified framework of study is formulated to directly assess how conventional and wind generators simultaneously provide the primary frequency regulation. Moreover, the steady-state voltage stability is also assessed in this work. In this direction, two approaches are considered: the traditional continuation power flow and a new power flow-based technique which directly eliminates the singularity of the Jacobian matrix by defining a new *type of bus*. Both the frequency regulation and the voltage collapse phenomena were studied by considering each device's operative limits as complementarity constraints. The resultant set of complementarity constraints is included in the power flow mathematical formulation by using the Fischer-Burmeister merit function.

On the other hand, a power flow method which considers those uncertainties that arise from the wind generation behavior is described and implemented. This method, which is based on a point estimation technique, is tested against thousands of Monte Carlo simulations. Furthermore, in this context of wind generation uncertainties, an enhanced security-constrained optimal power flow is also formulated to economically and securely dispatch active power generation by taking into account that wind generation varies within a forecasted interval.

Resumen

Con el paso del tiempo, el uso de sistemas de conversión de energía eólica para generar electricidad se ha vuelto la fuente de energía renovable con el mayor crecimiento alrededor del mundo. Aún cuando la energía eólica es benéfica desde el punto de vista ambiental, ésta hace todavía más complejo el control de los sistemas de potencia. Consecuentemente, la cuantificación de los efectos que la integración a larga escala de generación eólica va a causar en la red es un asunto muy importante que requiere especial atención para la planificación y operación de un sistema eléctrico de potencia.

Basándose en lo anterior, el objetivo de esta tesis es de proveer un esquema que abarque ampliamente el modelado matemático así como los métodos analíticos y numéricos para la evaluación de sistemas de generación eólicos interconectados a la red. Lo anterior considerando las principales características de diseño y operación de estas fuentes de energía y de la red eléctrica de potencia.

Por un lado, el problema de flujos convencionales es expandido para incorporar tres modelos de estado estable de las tecnologías más comunes de generadores eólicos. La habilidad de proveer soporte al control de demanda-frecuencia de generadores eólicos de velocidad variable es bien representada basándose en el concepto de *nodo slack* distribuido. Este concepto de *nodo slack* distribuido se refiere la modulación del desbalance de potencia activa por parte de todos los generadores en el sistema. En este contexto, es formulado un esquema unificado de estudio para evaluar directamente de que forma tanto los generadores convencionales como los eólicos proveen simultáneamente regulación primaria de frecuencia. Además, la estabilidad de voltaje en estado estable también es evaluada en este trabajo. En esta dirección, dos enfoques son considerados: el estudio tradicional de flujos continuos y una nueva técnica basada en flujos de potencia la cual elimina directamente la singularidad de la matriz Jacobiana utilizando un nuevo *tipo de nodo*. Tanto los estudios de regulación de frecuencia como los del fenómeno de estabilidad de voltaje fueron realizados considerando límites operativos de cada dispositivo utilizando restricciones de complementariedad. El conjunto resultante de restricciones de complementariedad es incluido en la formulación matemática del estudio de flujos de potencia utilizando la función de mérito de Fischer-Burmeister.

Por otro lado, es descrito e implementado un método de flujos de potencia el cual considera aquellas incertidumbres relacionadas con el comportamiento de la generación eólica. Este método, el cual está basado en una técnica de estimación de puntos, es probado contra miles de simulaciones Monte Carlo. De igual forma, en este contexto de incertidumbres de generación eólica, se formuló un estudio de flujos óptimos basado en restricciones de seguridad el cual despacha tanto seguramente como económicamente la generación de potencia activa considerando que la generación eólica varía en un intervalo cerrado previamente pronosticado.

Palabras clave: Flujos de potencia, estabilidad, voltaje, eólica, alteatorio.

Acknowledgements

Thanks. . .

Contents

List of Figures

List of Tables

List of Acronyms and Symbols

Acronyms

5PEM	Five Point Estimation Method.
AVR	Automatic Voltage Regulator.
CDF	Cumulative distribution function.
CPF	Continuation Power Flow.
DFIG	Doubly-Fed Induction Generator.
FSWG	Fixed-Speed Wind Generator.
GSC	Grid-side converter.
LIB	Limit-induced bifurcation.
MCP	Mixed complementarity problem.
MPPT	Maximum Power Point Tracking.
MSC	Machine-side converter.
NLP	Nonlinear programming.
NR	Newton-Raphson.
OPF	Optimal power flow.
PDF	Probability distribution function.
pu	Per unit.
PVC	Point of Voltage Collapse.
SC-OPF	Security-constrained optimal power flow.
SNB	Saddle-node bifurcation.
SSWG	Semi-Variable Speed Wind Generator.

STATCOM	Static Synchronous Compensator.
SVC	Static VAr Compensator.
VSC	Voltage Source Converter.

Indices

$k, m \in \mathcal{B}$	k-th or m-th bus.

Matrices

$\mathbf{g}(\mathbf{y}) \in \mathbb{R}^{n_y}$	Vector of nonlinear equations.
$\mathbf{g_y}(\mathbf{y}) \in \mathbb{R}^{n_y \times n_y}$	Jacobian matrix of $\mathbf{g}(\mathbf{y})$.
$\bar{\mathbf{i}} \in \mathbb{C}^{n_b}$	Vector of complex nodal currents.
$\bar{\boldsymbol{v}} \in \mathbb{C}^{n_b \times n_b}$	Vector of complex nodal voltages.
$\bar{\mathbf{Y}} \in \mathbb{C}^{n_b \times n_b}$	Matrix of nodal admittance.
$\boldsymbol{\theta} \in \mathbb{R}^{n_b}$	Vector of bus voltage angles.
$\boldsymbol{v} \in \mathbb{R}^{n_b}$	Vector of bus voltage magnitudes.
$\boldsymbol{x} \in \mathbb{R}^{n_x}$	Vector of additional state variables.
$\boldsymbol{z} \in \mathbb{R}^{n_x}$	Vector of complementarity variables.
$\boldsymbol{\Delta p} \in \mathbb{R}^{n_b}$	Vector of active power nodal mismatches.
$\boldsymbol{\Delta q} \in \mathbb{R}^{n_b}$	Vector of reactive power nodal mismatches.
$\mathbf{h} \in \mathbb{R}^{n_x}$	Vector of additional equations.
$\boldsymbol{\Phi} \in \mathbb{R}^{n_z}$	Vector of complementarity constraints.

Sets

$\mathcal{B}$	Set of AC buses.
$\mathcal{C}$	Set of contingency cases.
$\mathcal{G}$	Set of conventional generators.
$\mathcal{L}$	Set of transmission devices.
$\mathcal{S}$	Set of wind scenarios.
$\mathcal{W}$	Set of wind generators.

Variables

$\bar{s}$	Complex power value.
$\Delta p, \Delta q$	Active and reactive power mismatches, respectively.
ω_m	Mechanical angular speed.
n_b	Number of network buses.
n_w	Number of wind-farms.
n_x	Number of additional state variables.
n_y	Total number of algebraic state variables.
p, q	Active and reactive power values, respectively.
p_W	Mechanical power extracted from the wind.
v_{ref}	Voltage set point or reference value.

Chapter 1

Introduction

1.1 Motivation of Thesis

Electrical generation based in wind energy is a well-established conversion process in the modern electrical power systems. Attempts to convert wind energy to electric energy began early in the 20th century. Until the late 1980s, however, the wide-spread use of wind power generation was constrained because of its high initial investment cost. Over the last couple of decades, regulatory incentives such as subsidies, higher fuel prices, and stronger environmental initiatives, as well as significant advances in the design, construction and operation of wind generators, have played a major role in closing the cost gap. One example of such wind power development is the increase of maximum nameplate capacity of single wind turbines from around 50 kW in the 1980s to nearly 5 MW found in current commercially available models [Ackermann, 2012].

A result of this rapid technological development is the fast increase in the number of wind power facilities around the world. According to Global the Wind Energy Council (GWEC) statistics, global wind increased by 35.28 GW in 2013, bringing the total wind energy capacity up to 318 GW [GWEC, 2014]. In terms of global wind power capacity, China is leading with 28.7%, followed by the US and Germany with 19.2% and 10.8%, respectively [GWEC, 2014]. In addition to with wind power, solar, geothermal, wave, and tidal energy are being explored as alternative green power sources; however wind remains one of the most promising because of its low relative cost and resource potential.

Fig. 1.1 shows the the levelized cost of electricity (LCOE) for different plant types entering service in 2020 [EIA, 2015]. The LCOE represents the per-megawatthour cost (in real dollars) of building and operating a generating plant over an assumed financial life and duty cycle. Key inputs to calculating LCOE include capital costs, fuel costs, fixed and variable operations and maintenance costs, financing costs, and an assumed

utilization rate for each plant type. By combining all these costs and by considering a 30-year cost recovery period, the wind-onshore energy shows to be a competitive technology against other fuel-based energies.

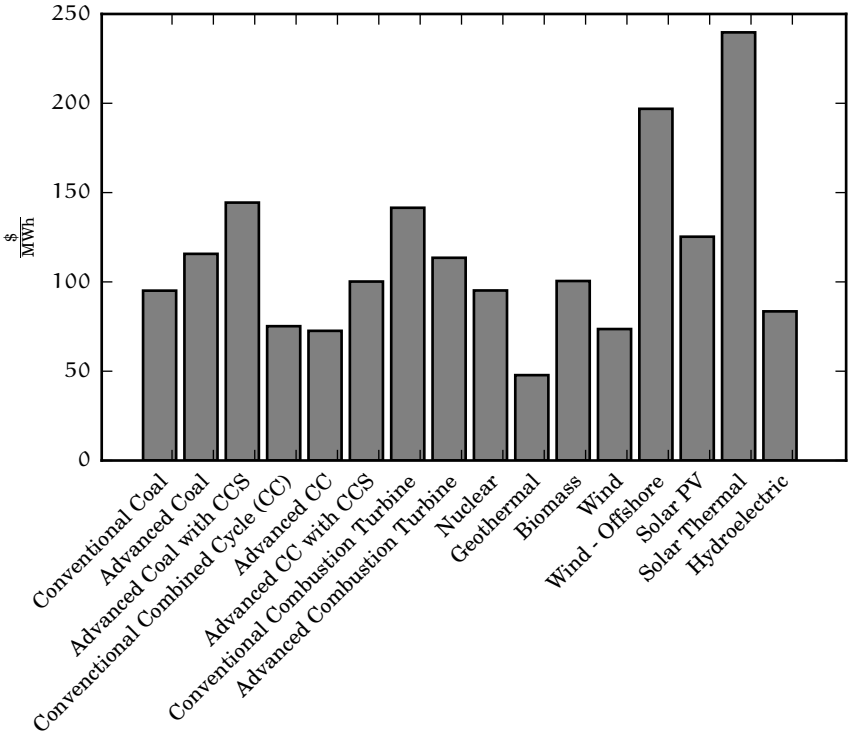

FIGURE 1.1: Average levelized energy costs (2013) for plants entering service in 2020.

Fundamentally, power systems have been designed and operated around the concept of generation delivery from large synchronous machines [Sauer, 1998; Anderson and Fouad, 2003; Machowski et al., 2011]. These machines have high levels of reliability and complex control systems that allow the system to maintain high levels of operational security. With the introduction of highly rated wind power facilities, the departure from the traditional hydrothermal generation is presenting several technical and economical challenges. This thesis focuses on issues associated with wind power as seen not only from the system-wide perspective but also from the wind farm facility operation. In this direction, the following section frames the work presented in this thesis in the context of the described issues above.

1.2 Technical Issues in the Integration of Wind Energy in Electric Power Systems

Some issues related to the planning and operation of power networks with embedded wind generators under consideration are described below.

Steady-State Analysis With the passage of time, new kinds of wind generators are appearing in the market, with more power electronics than ever before, new control functionality, new types of rotating machines, lack of gearboxes, etc. This has provided the motivation for electrical engineers to develop mathematical representations of the new equipment and the electrical networks to which they are connected to. The use of correct mathematical models will ensure its real applicability and therefore the possible solution of existing wind integration problems [Lubosny, 2010]. A suitable power flow algorithm considering steady-state models of wind generators may become a useful tool for the planning and operation of power networks. This power flow simulation can be addressed by means of a distributed slack approach which considers the frequency deviation as an unknown variable. This approach is more convenient not only because it considers the interaction of wind energy in the power flow problem but also because the integration and coordination of this energy in the primary regulation control can be analyzed. Furthermore, power flow solutions are required to gather good initial conditions for dynamic simulation studies. From the outset of this research, the effort is directed towards addressing the steady-state, positive-sequence modeling and analysis of the various kinds of wind power generators.

Voltage Stability As wind penetration levels increase, synchronous generation an its accompanying automatic voltage regulators (AVR) will be displaced. This will have significant impact on the voltage stability of the system, particularly if the new wind generation is not controlled appropriately. As the nature of the power system changes, it will become increasingly critical for wind generation to provide the necessary support and control of reactive power for ensuring the secure system operation. Overall, wind generation can be a valuable resource for the power system if it is controlled appropriately, specifically if wind can support the reactive power flows in the system. It is within this context where this work directs its efforts to asses the impact of wind generation on voltage stability phenomena.

Stochastic Analysis The essential characteristic of wind energy exploitation is its intrinsic dependence on weather conditions. Consequently, the facilities devoted to producing electricity from the force of the wind constitute a new source of uncertainty in the power system operation and planning [Restrepo Hernandez, 2011]. These wind farms cannot be scheduled or dispatched at the will of the wind producer, thus impacting basic aspects of the daily operation of today's power systems, as seen below.

System Security and Reliability The inherent randomness of wind power availability makes it necessary to have reserves that absorb unpredictable wind power fluctuations. In this thesis, a tool for estimating and describing the stochastic behavior of the wind is revised and implemented.

Real-time Economic Dispatch In real-time operation, by looking seconds to hours ahead, the main challenge presented by wind power is its variability, which translates into the need to ramp traditional hydrothermal generation up or down in order to balance such variability. Frequent ramping actions have economical adverse effects such as mechanical wear and tear as well as increased inefficiency in the use of conventional hydrothermal generation. Furthermore, in certain thermal-dominated systems, wind power may exceed the ramping capabilities of the conventional generation units, which compromises the capability to serve the demand. In this dissertation an enhanced security-constrained optimal power flow (SC-OPF) is presented, which strives to devise the best economic dispatch actions to create an economically and operationally secure power system under wind power variation.

1.3 State of the Art

For clarity and exactness, the state-of-the-art revision will be divided into the following topics stated below.

1.3.1 Steady-State Models of Wind Generators for Power Flow Studies

Research in this area of power systems is not new by any means. The earlier publications may be traced back to around 2000. [Feijoo and Cidras, 2000] presented a model of a fixed-speed wind generator with the active power obtained from the power curve while the reactive power was estimated by using an approximated quadratic function dependent on the active power and the voltage magnitude measured at the wind generator's terminals; this model is referred to as the *PQ model*.

Nevertheless, the work presented in [Slootweg et al., 2001] is an initialization method for dynamic analysis and it is important to highlight that the several detailed models of wind generation were addressed there. As an *initialization method* the author refers to the techniques employed to determine the first dynamic state variables of a dynamic study. In this context, in [Slootweg et al., 2001] a set of sequential algorithms are reported, with one algorithm per wind generator model, which for given active and reactive powers as well as terminal voltage magnitude and angle, a set of internal wind generator variables can be computed. This approach has the merit of presenting a detailed mathematical formulation of each wind generation model. In the same research area of initialization methods, [Ruiz-Vega et al., 2002] presented a model to compute the steady-state operating point of induction motors by using a power flow program. The described methodology is quite similar to the one presented in [Feijoo and Cidras, 2000].

A couple of years later in [Divya and Rao, 2006] a model is introduced where the active and reactive power outputs are expressed in terms of the generator's variables and parameters using no approximations. In the same work, a double-fed induction generator (DFIG) model for power flow studies is presented, where the total rotor current magnitude is checked at each iteration. If a limit violation in the total rotor current magnitude is detected, the wind generator model then gives priority to the reactive power over the active power generation in order to support the bus voltage magnitude at the connecting bus. From the conventional power flow viewpoint, this model is treated as a *PQ bus* with a fixed unity power factor.

An alternative modeling approach for fixed-speed wind generators is to determine an equivalent variable impedance expressed in terms of the slip as well as the rotor and stator winding parameters [Feijoo, 2009]. This impedance is included in the system's admittance matrix, and the network nodal voltages are computed through the power flow analysis. With these calculated voltages, the value of the slip is separately computed to match the air-gap power with the mechanical wind power. This modeling technique is referred to as the *RX model*.

Concerning the steady-state models of DFIG, more recently [Padron and Lorenzo, 2010] reported two different initialization techniques for a third-order dynamic model of a DFIG wind generator. One of these initialization methods takes the voltage magnitude and angle at the DFIG's terminals together with the active power generation and then solves for the internal DFIG's state variables from a set of steady-state equations representing the steady-state operation of the DFIG. This set of equations has no approximations, and as a result, the rotor's voltage and current as well as the machine's slip are obtained. Another method considers as input data the wind speed as well as the reactive power generation of the DFIG; with both parameters the same steady-state equations of the DFIG are solved. This work contributes a detailed steady-state representation of the DFIG with no approximations.

Note that in all of these works the state variables of wind generators are not taken into account in the power flow formulation, which means that these variables are solved in a sequential form in which a subproblem is formulated and solved separately at the end of each power flow iteration. This sequential iterative approach is rather attractive, because it is straightforward in its implementation of the wind generator models in existing Newton-Raphson programs; however, caution has to be exercised because the approach will yield no quadratic convergence, and in some extreme cases the solution will diverge [Smed et al., 1991; Fuerte-Esquivel and Acha, 1997].

A fundamentally different approach for modeling wind generators (and other nonconventional devices), within the framework of the power flow problem, is to combine the state variables of the corresponding devices and the network voltages' magnitudes and angles in a single frame of reference for a unified iterative solution.

The number of iterations required to obtain the solution in this unified framework is fewer than those required by the sequential one because all the state variables are simultaneously adjusted. Moreover, this unified approach arrives at the solution with local quadratic convergence regardless of network size if proper initial conditions are selected, and the set of nonlinear equations is smooth [Ortega and Rheinboldt, 1970]. The use of unified solutions in the solution of power flows with wind generation devices was first suggested in [Fuerte-Esquivel et al., 2001].

By considering the latter unified technique, [Aree and Acha, 2011] presented a power flow-based initialization method for dynamic studies with induction machines which considers the machine's slip within the power flow problem: it is solved along with the system's voltage magnitudes and angles. In the same direction, [Castro et al., 2011, 2012] presented the most common wind generation steady-state models suitable for power flow studies. The principle contribution of those works is the steady-state models of both the fixed- and semi-variable speed wind generators. Both works, however, have an area of opportunity: the DFIG and the full-scale converter-based wind generators are basically modeled as conventional generators (*PV or PQ buses*), which do not reflect the real interaction of such generators with the rest of the network.

In more recent years, [Li, 2013] proposed a method to calculate steady-state equilibrium points of DFIG under maximum power point tracking (MPPT) operation. While this steady-state model is well-established and solved in a unified fashion, it uses a sequential algorithm in case the DFIG reaches its rating output, and a regulation of the active power through a pitch-angle control is needed.

Finally, steady-state models of the permanent magnet synchronous generator (PMSG) are mainly focused on representations under the dq reference as shown in [Slootweg et al., 2001] or by considering equivalent PQ models as described in [Castro et al., 2011, 2012], respectively.

1.3.2 Constrained Power Flows

Since its introduction in [Tinney and Hart, 1967], the Newton-Raphson method has been satisfactorily used for the solution of the power flow problem. In this context, it is well-known that the overall efficiency of the method not only depends on the initial given conditions but also on its ability to efficiently adjust the control variable values when one of their limits is violated during the iterative solution process [Stott, 1974]. Some of these adjustments are related to the set-point limits of control devices: generator q_G limits, on-load transformer taps, current limits of reactive power sources and firing angles of power electronics-based controllers.

Traditionally these adjustments are heuristically performed by one of the following schemes: error feedback mechanisms as shown in [Stott, 1974], application of the

adjustments at the end of the second iteration [Tinney and Hart, 1967], or limits' revision until the power flow has converged *sufficiently* as introduced in [Chang and Brandwajn, 1988]. In this research area, in [Mamandur and Berg, 1982] an alternative formulation of the power flow problem is presented, which computes the reactive generated power q_G of the *PV buses* as a state variable within the Newton-Raphson method. If the constraint $q_{G,i}^{min} \leqslant q_{G,i} \leqslant q_{G,i}^{max}, \forall i \in \mathcal{G}$ is not satisfied at the second iteration, the i-th generator is fixed; its reference voltage $v_{ref,i}$ is now considered as a state variable. This methodology is rather interesting because, as opposed to the conventional formulation, the reactive power output q_G is automatically computed.

Now the method based on the convergence error has been shown to be effective because the adjustments are performed in a more algorithmic way as opposed to the first two empirical procedures mentioned above. Nevertheless, this method can encounter problems in situations where a bus continues switching between the *PV* and the *PQ* type in alternative iterations which cycles indefinitely the Newton-Raphson convergence [Chang and Brandwajn, 1988]. Satisfactory results have been reported when simulating power systems with embedded HVDC and FACTS controllers as reported in [Canizares and Alvarado, 1993; Fuerte-Esquivel and Acha, 1997].

In recent years, the complementarity approach has been envisioned as an attractive technique for including the network apparatus limits within the power flow problem. This approach is advantageous because the concept of complementarity is synonymous with the notion of system equilibrium [Ferris and Pang, 1997]; therefore, its usage is the more direct way to state an equilibrium between the control law of each network device and its associated limits. This approach has been used in some power system applications which require handling mutually exclusive constraints, including the following: optimal power flow by considering reactive power and load tap-changing transformers' limits [Rosehart et al., 2005; Roman and Rosehart, 2006], respectively, dynamic modeling of DFIG wind generators [Díaz et al., 2012], steady-state analysis of droop-regulated microgrids which takes into account both active and reactive power limits [Díaz and Gonzalez-Moran, 2012], modeling of the diode bridge rectifier behavior [Rico-Melgoza et al., 2012], power flow studies under input data uncertainties which consider reactive power limits [Vaccaro et al., 2013; Pirnia et al., 2013], and scenario-based optimal power flows which take into account reactive power limits [Tinoco De Rubira, 2015]. More recently [Sundaresh and Nagendra Rao, 2014] have incorporated the *PV bus* reactive power limits in the Newton-Raphson power flow problem by means of complementarity constraints and the Fischer-Burmeister merit function [Fischer, 1992]. While the proposed scheme is rather attractive, the authors use a scalar parameter α to *penalize* a couple of therms in the Fischer-Burmeister merit function; the authors do not mathematically explain the purpose of this parameter or the calculation of its value.

To the best of the author's knowledge, currently there is no work or software that models different operative limits from the *PV buses'* reactive power limits, such as FACTS or wind generators, in a unified framework solution by using complementarity constraints.

1.3.3 Analysis of the Voltage Collapse Phenomena Considering Wind Generation

The steady-state voltage stability subject has been addressed by means of the continuation power flow (CPF). The CPF is a technique that strives to solve a consecutive series of power flow solutions by varying a system's parameter, typically the loading factor. Since its introduction in [Ajjarapu and Christy, 1992], the technique has been used to obtain the maximum loading condition at which a power system continues operating under steady acceptable voltage levels.

Despite the importance of obtaining the maximum loading condition of power systems under high wind penetration. The low number of reports in this research area is rather surprising. For instance, [Cutsem and Vournas, 2007] introduced a model of the induction machine suitable for CPF studies. [Ullah and Thiringer, 2007] addressed a brief analysis about the improvements of using variable-speed wind turbines in the steady-state voltage stability. The authors modeled three types of wind turbines: *system A* is the fixed-speed wind generator and is modeled as an induction machine, and *systems B and C* stand for the full power converter and DFIG wind generators, respectively. Both are modeled as negative loads through a negative conductance and a positive susceptance. The modeling stage is highly idealized and does include the existent voltage droops inside the wind generator. [Milano, 2008] presented different remedial actions for voltage problems originated by high wind penetration. Three different schemes are proposed: voltage control through ULTCs, voltage control through local voltage regulation by wind generators, and voltage control through SVCs. In the comparison of these three schemes, the voltage control by either wind generators or SVCs yielded the best performance in terms of the maximum loading condition. The wind generation model is based on the DFIG steady-state representation with no simplifications. In [Hedayati et al., 2008], a method for the placement of distributed generation units, wind generation in particular, in distribution networks is presented. The method is based on a CPF analysis and the determination of most sensitive buses to the voltage collapse.

On the other hand, in [Ghiocel and Chow, 2014; Ghiocel et al., 2014] a new method for computing the voltage stability margins by using a new type of bus is reported. This simulation alters the Jacobian matrix such that it is nonsingular at the critical voltage point. Because minor changes to traditional power flow solvers are required, this method is rather attractive.

This thesis advances with an enhanced continuation power flow program which includes models of both fixed-speed and variable-speed wind generators. The reactive power limits of wind generation schemes are also included. On the other hand, the fixed-speed wind generator described in [Castro et al., 2011] is implemented with the possibility of including FACTS controller devices such as SVCs or STATCOMs to mitigate its reactive power consumption.

1.3.4 Point Estimation Techniques for Stochastic Power Flow Studies

In power system analysis, the use of techniques that can account for uncertainty is required to control and minimize risks associated with the design and operation of electrical networks. By using deterministic power flow routines, one must run them many times so as to encompass all, or at least the majority of, possible system states. In this context, the Monte Carlo simulation randomly generates values for uncertain input variables, and these values are then taken into account to solve a deterministic power flow. The main drawback of the Monte Carlo method is the great number of simulations required to attain convergence. The same deterministic routines, however, can be used to solve the problem in each simulation.

To reduce this computational burden, approximate methods can provide and approximate the description of the statistical properties of output random variables without many simulations. Within these techniques, point estimate methods stand out [Morales and Perez-Ruiz, 2007].

According to [Morales and Perez-Ruiz, 2007], the number of works using point estimate methods is very scarce. In [Borkowska, 1974], a study of the electrical network as a DC equivalent model is reported. The author considered the bus load as independent random variables. This is believed to be the first paper that involves the propagation of the uncertainties in the input data to the results of the power flow problem. [Meliopoulos et al., 1990] used a linearization involving a deterministic power flow solution at the anticipated expected value of the probabilistic solution. They then linearized the problem around the expected values, anticipating coupling effects between active and reactive powers. Linearization of the power flow problem input about expected values yielded acceptable mean values and standard deviations as long as the variations for input values were small.

[Schellenberg et al., 2005] presented an extension of the optimal power flow method by using cumulants to combine probabilistic distribution functions with a deterministic computation method. More recently, [Su, 2005; Morales and Perez-Ruiz, 2007] applied Hong's point estimation method [Hong, 1998] to the probabilistic power flow problem. Neither of the two techniques can be used to calculate stochastic power flows with high penetration of wind power because the wind generation is a mixture of discrete

and continuous distributions [Outcalt, 2009]; both techniques assume that the power distribution is continuous. [Villanueva et al., 2011] introduced a procedure for calculating the power flow probability density function (PDF) in an electrical power network. The PDF is obtained by utilizing quadratic approximations and a mixture of continuous and discrete functions, which are very similar to those used in [Outcalt, 2009].

The method implemented in this thesis has been introduced in [Outcalt, 2009] and aims to represent the probabilistic distribution function of the wind generation in a single set of five points.

1.3.5 Security-Constrained Optimal Power Flow

The objective of the economic dispatch of an electric power system is to determine a generation schedule that minimizes the system operating cost and does not violate any of the system operating constraints such as maximum line power flows, bus voltage magnitudes, etc. Within this context, it has been recognized that the conventional economic dispatch may be unsafe: it may not be possible to keep the system in a normal state after a major disturbance. In order to avoid these *insecure* operating points, the first *preventive* security-constrained optimal power flow (SC-OPF) was proposed in [Alsac and Stott, 1974], which is an optimization problem that minimizes the operating cost by considering that the system must be robust enough to face a predefined set of N-1 contingencies. This approach is rather conservative, because it does not involve the system's corrective capabilities which can occur after the disturbance has occurred.

In [Monticelli et al., 1987], the approach to the SC-OPF was reformulated by taking into account the system's rescheduling capabilities. The described optimization problem proposed that system equilibrium point could be *shifted* to other equilibrium points with the support of corrective actions, mainly the rescheduling of active power generation. While this classical formulation is indeed very useful, it no longer covers in a fully satisfactory way the need encountered in today's operation and operational planning environments. Because of the increasing penetration of renewable and other uncontrollable generation sources, the set of contingencies should now also incorporate (possibly large) variations in power injections in addition to equipment failures.

Within this context, now the operators must anticipate second stage decisions to deal with these *injection pattern contingencies* which span complex continuous spaces and are highly dependent on system conditions and on real-time information gathered about exogenous variables such as weather forecasts and market prices [Capitanescu et al., 2011]. In order to improve the conventional SC-OPF, two approaches to address the multi-stage decision making problem under uncertainty have been proposed in the optimal control and stochastic programming literature.

- The stochastic security criterion proposed in [Bouffard et al., 2005] uses an objective function which trades the cost of preventive actions for the expected cost of corrective actions. This formulation relies on the probabilities of disturbances' occurrence for which sufficiently accurate values may not be available. Another drawback of this formulation is that in order to build tractable approximations is one must discretize a set of uncertain scenarios, in this case wind scenarios.

- The second approach for managing this uncertainty problem is to avoid the use of probabilistic concepts and to substitute them with concepts from robust control theory. This approach has its focus on ascertaining the security of the system by looking at parameters and contingencies that could lead the operation into a *worst-case* equilibrium point. The aim of this worst-case approach is to determine whether, for the assumed range of the uncertain parameters, it is necessary to take such strategic decisions to ensure system controllability over the course of the forecasted scenario. This approach has been proposed in [Capitanescu et al., 2011].

The development of a robust worst-case SC-OPF will be carried out by taking into account the latter approach.

1.4 Objectives

The main objective of the present work is to describe and implement a set of models and methodologies which allows the assessment of the integration of wind power into electrical networks, all from a steady-state operation viewpoint.

In order to achieve this main objective, a set of goals is described below.

- To mathematically model the most common wind generation schemes and their associated control devices, e.g. voltage or frequency support controllers.

- To obtain a proper and adequate representation of a power system network within a distributed slack concept.

- To introduce operative limits of all modeled devices within the formulation of the power flow problem by using complementarity constraints.

- To simulate and analyze the periodic state of a power system including wind generators and the contribution of the latter in the voltage stability and the frequency regulation phenomena.

- To formulate a steady-state model of the permanent magnet synchronous generator suitable for power flow and voltage stability studies. In the same direction, an existent steady-state model of the double-feed induction generator is improved by taking into account its voltage and frequency support capabilities.
- To prove the effectiveness and feasibility of a *point estimation* method that aims to rapidly and properly analyze the stochastic behavior of wind generation.
- To formulate an optimization problem suitable for economically and securely dispatch the active power generation in a power system highly penetrated by wind power.

1.5 Methodology

The employed methodology to assess the steady-state operation of a power system was based on formulating and solving the power flow problem in a broader sense. In this context, the models were represented through the necessary equations that describe their behavior, which were solved along with the conventional *power mismatch equations* in a unified way. The resultant set of nonlinear equations are solved by the Newton-Raphson method.

With this general framework, the development of routines to simulate and analyze voltage stability and frequency regulation problems was very straightforward. The voltage stability phenomena is studied through the continuation power flow approach, while the frequency regulation is analyzed through the primary regulation response and its implementation in a distributed slack concept.

Finally, in order to develop an enhanced economic dispatch software, the variability of wind generation was taken into account by coding a robust security-constrained optimal power flow by means of a mathematical programming language.

1.6 Thesis Outline

The remainder of this thesis is organized as follows.

Chapter 2 presents the steady-state models of various wind power generators. Models of FACTS controllers and induction machines are also presented.

Chapter 3 The required nonlinear equations to accurately represent each of the prior devices in a power flow study are presented in this chapter. A set of cases studies to analyze the performance of the complementarity approach against other limits-handling schemes is also reported. Finally, the integration of wind power and its

joint operation with traditional hydrothermal generation is assessed at the end of the chapter.

Chapter 4 addresses the impact of wind generation in the maximum loading condition and the voltage stability phenomena in a power system. As well as in the previous chapter, the New England test system is used for the simulations.

Chapter 5 describes the five-point estimation method for the purpose of obtaining and studying the stochastic behavior of the wind generation. The resultant methodology is compared against thousands Monte Carlo simulations.

Chapter 6 illustrates the applicability of an optimization problem for dispatching conventional generation such that the power system is able to support a N-1 contingency, even considering that wind generation varies.

Chapter 7 gives the general conclusions of the thesis and provides suggestions for future research.

Chapter 2

Steady-State Modeling of a Power System with Embedded Wind Generation

2.1 Introduction

In this chapter models of load, induction machine, FACTS controllers, synchronous and wind generators embedded in the power system are presented.

The most relevant parts of each device as well as device operative limits are considered.

2.2 Steady-State Modeling of Power System Devices

Generally speaking, an electric power system is composed of the following:

- A transmission network which interconnects the system buses to transmit the energy from the generation facilities to consumers.
- The connected equipment such as generators, transformers, loads, and mechanically or electronically controlled devices.

The specific steady-state models of these components are reported in the following sections in order to formulate an adequate framework to assess equilibrium points in power systems. Common power system notation is used.

2.2.1 Synchronous Generator

[Okamura et al., 1975] presented the model of a synchronous generator (SG) by considering its regulation control. In this model, generated active power p_G is adjusted according to the primary frequency control which main objective is to keep frequency deviations within acceptable limits after the occurrence of large active power imbalances. This frequency regulation is mathematically represented by a linear response:

$$p_G = p_{G,0} - \left(\frac{1}{R}\right)\Delta f \tag{2.1a}$$

$$p_G^{min} \leqslant p_G \leqslant p_G^{max}, \tag{2.1b}$$

where R stands for the machine speed droop, $p_{G,0}$ is the base case active power generation, and Δf is the system frequency deviation in pu

Regarding the existing relationship between the reactive power and voltage magnitude control, the proposed approach differs from the widely used *PV generator* concept. The formulation includes a quasi-steady-state equivalent of the automatic voltage regulator (AVR) [Calvaer and Van Geert, 1984] that more accurately represents the voltage regulation behavior [Calvaer and Van Geert, 1984][Van Cutsem, 1991]. By using this model, the reactive power is computed as follows [Van Cutsem, 1991]:

$$q_G = q_{G,0} + \frac{v_k\,(v_{ref} - v_k)}{x_{mq}} \tag{2.2a}$$

$$q_G^{min} \leqslant q_G \leqslant q_G^{max}, \tag{2.2b}$$

where v_{ref} is the specified voltage at bus k, $q_{G,0}$ is the base case reactive power, and x_{mq} stands for a hypothetical reactance that represents the sensitivity of terminal voltage magnitude v_k to changes in the reactive current i_{q_G}(which is proportional to the reactive power). The value of this x_{mq} reactance is calculated using [Calvaer and Van Geert, 1984]:

$$x_{mq} = \frac{\partial v_k}{\partial i_{q_G}} = \frac{x_d \cos\delta_s}{k_A \cos\delta_s} + \frac{(x_d - x_q)\, i_q x_d k_A \cos\delta_s}{e_q\,(k_A + \cos\delta_s)^2}, \tag{2.3}$$

where x_d and x_q are the synchronous reactances of direct and quadrature axes, respectively, δ_s is the internal machine angle, e_q is the voltage behind x_q, i_q is the

quadrature axis current, and k_A is the AVR open-loop gain. This reactance is calculated only once at the beginning of the iterative solution process.

The synchronous generator is capable to provide active or reactive support while operating within its active and reactive limits. These limits are constrained by Eqs. (2.1b) and (2.2b).

2.2.1.1 Reference Generator

The concept of *slack generator* does not exist in the context of distributed power flows. In fact, this generator is now referred as the *reference generator* which holds the voltage angle at a fixed value:

$$\delta_k = \delta_{\text{ref}}\,, \tag{2.4}$$

where δ_{ref} is the voltage angle of the reference generator, and δ_k is the voltage angle of the bus at which this reference generator is connected.

2.2.2 Transmission, Transformer and Phase Shifter

A standard π transmission line model is used to represent lines, transformers, and phase shifters [Zimmerman et al., 2011]. This model has a series impedance $\bar{z}_s = r_s + jx_s = \bar{y}_s^{-1}$ and a total shunt susceptance $b^{sh} = 2b_k^{sh} = 2b_m^{sh}$. The transformer, with a tap ratio that has a magnitude τ and a phase shift angle θ, is located at the sending end of the branch, as shown in Fig. 2.1.

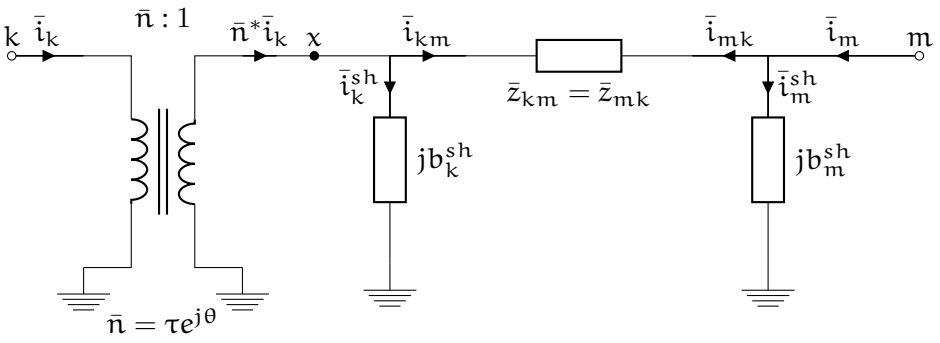

FIGURE 2.1: π standard model for lines and transformers.

From the equivalent circuit shown in Fig. 2.1, the complex power injected at each bus is

$$\bar{s}_k = \bar{v}_k \bar{i}_k^* \tag{2.5}$$

$$\bar{s}_m = \bar{v}_m \bar{i}_m^* \,. \tag{2.6}$$

From Kirchhoff's current law, the injected current $\bar{i}_k$ is written as

$$\bar{n}^* i_k = \bar{i}_{km} + \bar{i}_k^{sh} \,, \tag{2.7}$$

which can be expressed in terms of nodal voltages as

$$\begin{aligned} \bar{n}^* \bar{i}_k &= \bar{y}_s \left(\bar{v}_x - \bar{v}_m\right) + j b_k^{sh} \bar{v}_x \\ &= \frac{\bar{v}_k}{\bar{n}} \left(\bar{y}_s + j b_k^{sh}\right) - \bar{v}_m \bar{y}_s \end{aligned} \tag{2.8}$$

$$\bar{i}_k = \frac{\bar{v}_k}{\tau^2} \left(\bar{y}_s + j b_k^{sh}\right) - \frac{\bar{v}_m}{\bar{n}^*} \bar{y}_s \,, \tag{2.9}$$

Applying the same procedure of analysis to bus m yields

$$\bar{i}_m = \bar{v}_m \left(\bar{y}_s + j b_m^{sh}\right) - \frac{\bar{v}_k}{\bar{n}} \bar{y}_s \,. \tag{2.10}$$

By representing Eqs. (2.9) and (2.10) in a matrix form the later current equations are written as

$$\begin{bmatrix} \bar{i}_k \\ \bar{i}_m \end{bmatrix} = \begin{bmatrix} \frac{1}{\tau^2}\left(\bar{y}_s + j b_k^{sh}\right) & -\frac{1}{\bar{n}^*} \bar{y}_s \\ -\frac{1}{\bar{n}} \bar{y}_s & \bar{y}_s + j b_m^{sh} \end{bmatrix} \begin{bmatrix} \bar{v}_k \\ \bar{v}_m \end{bmatrix} \tag{2.11}$$

$$= \begin{bmatrix} \bar{Y}_{kk} & \bar{Y}_{km} \\ \bar{Y}_{mk} & \bar{Y}_{mm} \end{bmatrix} \begin{bmatrix} \bar{v}_k \\ \bar{v}_m \end{bmatrix} \,. \tag{2.12}$$

From the above representation, the net power flow injected at k and m is calculated as follows:

$$p_k = v_k^2 G_{kk} + v_k v_m \left(G_{km} \cos \delta_{km} + B_{km} \sin \delta_{km}\right) \tag{2.13}$$

$$q_k = -v_k^2 B_{kk} + v_k v_m \left(G_{km} \sin \delta_{km} - B_{km} \cos \delta_{km}\right) \tag{2.14}$$

$$p_m = v_m^2 G_{mm} + v_m v_k \left(G_{mk} \cos \delta_{mk} + B_{mk} \sin \delta_{mk}\right) \tag{2.15}$$

$$q_m = -v_m^2 B_{mm} + v_m v_k \left(G_{mk} \sin \delta_{mk} - B_{mk} \cos \delta_{mk}\right) , \tag{2.16}$$

where

$$\delta_{km} = \delta_k - \delta_m = -\delta_{mk} \tag{2.17}$$

$$\bar{Y}_{km} = G_{km} + jB_{km} . \tag{2.18}$$

$$\tag{2.19}$$

2.2.3 Load

Most of the loads in power systems are voltage and frequency dependent, and their demanded power varies according to changes in these variables [Okamura et al., 1975]. The static representation of their demanded active and reactive powers is described below:

$$p_L = p_{L,0} \left(1 + k_{pf} \Delta f\right) \left[k_{pp} + k_{pc} \left(\frac{v_k}{v_{k_0}}\right) + k_{pz} \left(\frac{v_k}{v_{k_0}}\right)^2\right] \tag{2.20a}$$

$$q_L = q_{L,0} \left(1 + k_{qf} \Delta f\right) \left[k_{qp} + k_{qc} \left(\frac{v_k}{v_{k_0}}\right) + k_{qz} \left(\frac{v_k}{v_{k_0}}\right)^2\right] , \tag{2.20b}$$

where $p_{L,0}$ and $q_{L,0}$ are the specified base active and reactive powers drawn by the load, respectively, v_{k_0} is the nominal operating voltage of the bus where the load is connected, k_{pf} and k_{qf} are the coefficients of the frequency characteristic, whereas k_{pp}, k_{qq}, k_{pc}, k_{qc}, k_{pz} and k_{qz} are the coefficients of the voltage characteristic of the load.

2.2.4 Induction Machine

The steady-state model for the induction machine is based on a squirrel-cage asynchronous machine [Machowski et al., 2011]. The mathematical model suitable for steady-state analysis is derived from the equivalent electrical circuit shown in Fig. 2.2. The subscripts s, m and r represent stator, magnetization branch and rotor variables.

The model can be simplified using an equivalent admittance:

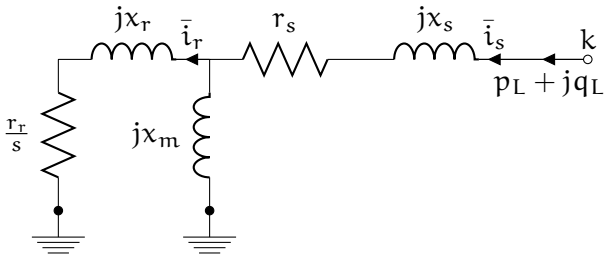

FIGURE 2.2: Electrical circuit of the induction machine model.

$$\begin{aligned}\bar{y}_{eq} &= \left[r_s + jx_s + \frac{jx_m\left(jx_r + \frac{r_r}{s}\right)}{j\left(x_m + x_r\right) + \frac{r_r}{s}} \right]^{-1} , \\ &= g_{eq} + jb_{eq}\end{aligned} \tag{2.21}$$

whereas the active and reactive power injections are

$$\begin{aligned}\bar{s}_L &= \bar{v}_k \bar{i}_s^* = \bar{v}_k \bar{v}_k^* \bar{y}_{eq}^* \\ &= v_k^2 \bar{y}_{eq}^*\end{aligned} \tag{2.22}$$

$$p_L = v_k^2 g_{eq} \tag{2.23}$$

$$q_L = v_k^2 \left(-b_{eq}\right) . \tag{2.24}$$

An additional equation is needed to calculate the mechanical angular speed (ω_m). This equation finds an internal equilibrium point in the induction machine given the conversion process of electrical power into mechanical power [Castro et al., 2011]:

$$p_c + p_m = 0 , \tag{2.25}$$

where p_c is the power converted from electrical to mechanical form (vice versa if the induction machine is working as a generator) [Machowski et al., 2011]. Furthermore, p_m is the mechanical power extracted (or injected) from(to) the machine [Milano, 2010]:

$$p_c = i_r^2 r_r \frac{1-s}{s} \tag{2.26}$$

$$p_m = p_{m,0}\left[a\left(\frac{\omega_m}{\omega_{m,0}}\right)^2 + b\frac{\omega_m}{\omega_{m,0}} + c \right] , \tag{2.27}$$

where $\omega_{m,0}$ stands for the specified angular speed, $p_{m,0}$ is the initial mechanical power, and the rotor current i_r is calculated using:

$$i_r = i_s z_{mr} = v_k y_{eq} z_{mr} \,. \tag{2.28}$$

In addition the impedance $\bar{z}_{mr}$ is a current divider given by

$$\begin{aligned} \bar{z}_{mr} &= \frac{jx_m}{j\,(x_m + x_r) + \frac{r_r}{s}} \\ &= r_{mr} + jx_{mr} \,. \end{aligned} \tag{2.29}$$

Induction Machine's Slip The stator winding produces a magnetic field that rotates at synchronous speed ω_s^*, if the rotor is rotating at a speed ω_m^* slightly different to ω_s^*, an emf will be induced in the rotor at a frequency proportional to the difference between these two speeds, referred to as the slip frequency f_{slip}. The slip speed is defined as the difference between these two speeds [Vittal and Ayyanar, 2012]:

$$\omega_{slip}^* = \omega_s^* - \omega_m^* \tag{2.30}$$

$$= \omega_b^* + \Delta\omega_s^* - \omega_m^* \,, \tag{2.31}$$

where the superscript * means that values are in real units, $\omega_b^* = 2\pi f_n$ is the synchronous base speed, f_n is the nominal system's frequency, and $\Delta\omega_s^*$ is the speed deviation from the base speed. In a per-unit system, the per-unit slip or simply slip is normalized to the base synchronous speed [Machowski et al., 2011]:

$$s = \frac{\omega_b^* + \Delta\omega_s^* - \omega_m^*}{\omega_b^*} \tag{2.32}$$

$$= 1 + \Delta f - \omega_m \,. \tag{2.33}$$

Therefore, in a distributed slack basis and by considering that the system's frequency deviation Δf is in per-unit, the induction machine's slip will be computed by means of Eq. (2.33) hereinafter. The same equation applies for either fixed-peed or doubly-fed wind generators, which will be presented later.

2.2.5 FACTS Devices

The reactive power consumption of induction machine-based wind generators makes necessary including voltage or power factor control devices inside a wind farm facility necessary. In this context, two FACTS devices are commonly used: the static VAR compensator (SVC) and the static synchronous compensator (STATCOM) [Anaya-Lara

et al., 2011]. This section briefly describes the implemented SVC and STATCOM steady-state models to assess the penetration of wind generation in a comprehensive way.

2.2.5.1 Regulation Slope

In many applications, the static compensators are not used as perfect terminal voltage regulators, but rather the terminal voltage is allowed to vary in proportion with the compensating current. There are several reasons for this [Hingorani and Gyugyi, 2000]:

1. The linear operating range of a compensator with given maximum capacitive and inductive ratings can be extended if a regulation *droop* is allowed. Regulation *droop* means that the terminal voltage is allowed to be smaller than its nominal no-load value at full capacitive compensation and, conversely, it is allowed to be higher than the nominal value at full inductive compensation.
2. Perfect regulation (zero droop or slope) could result in a poorly defined operating point, and a tendency of oscillation, if the system impedance exhibited a *flat* region (low impedance) in the operating steady-state frequency.
3. A regulation *droop* or slope tends to enforce automatic load sharing between static compensators as well as other voltage regulating devices normally employed to control voltage magnitudes.

Having these reasons in mind, the implemented models of static compensators (either SVC or STATCOM) consider a voltage droop using a fictional reactance x_{sl} as recommended in [Taylor et al., 1994].

2.2.5.2 Static VAR Compensator

An integrated model of the static VAR compensator (SVC) with its step-down transformer was implemented based on models reported in [Canizares and Faur, 1999; Fuerte-Esquivel et al., 2000].

As shown in Fig. 2.3(a) this controller is connected to bus c through a step-down transformer with reactance x_t. The controller is composed of a fixed capacitor x_c in parallel with a thyristor-controlled reactor (TCR) x_l.

By assuming that the controller voltage is sinusoidal and by performing a Fourier analysis on the inductor current waveform, the SVC at fundamental frequency can be readily demonstrated to be equivalent to the variable reactance x_e[Canizares and Faur, 1999; Fuerte-Esquivel et al., 2000]:

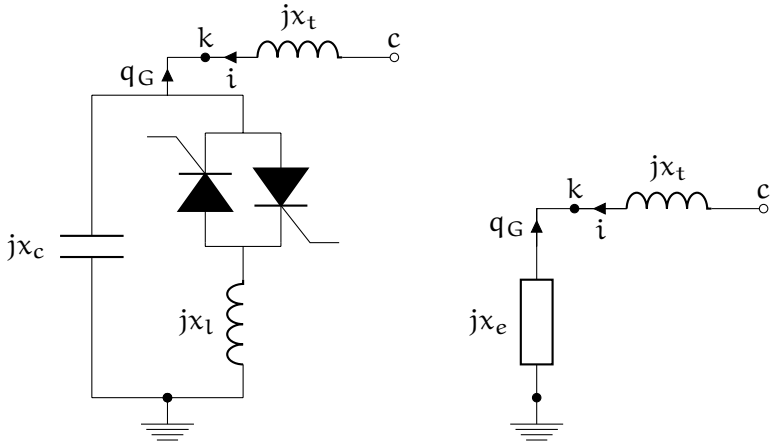

(a) SVC steady-state circuit. (b) SVC equivalent circuit.

FIGURE 2.3: Static VAR compensator representation.

$$x_e = x_c \frac{\frac{\pi}{\tau}}{\sin(2\alpha) - 2\alpha + \pi\left(2 - \frac{1}{\tau}\right)}, \tag{2.34}$$

where $\tau = \frac{x_c}{x_l}$.

On the other hand, considering the reasons stated in Section 2.2.5.1, the control law of the SVC is represented by the following voltage-current characteristic:

$$v_c = v_{ref} - x_{sl} i \tag{2.35}$$

$$= v_{ref} - x_{sl} b_e v_k\,, \tag{2.36}$$

where $b_e = -\frac{1}{x_e}$, and the values for the slope x_{sl} are in the range of 2% to 5% with respect to the SVC base. The limits of the controller are given by the firing angle limits: $\alpha^{min} \leqslant \alpha \leqslant \alpha^{max}$.This steady-state control law is depicted in Fig. 2.4: the controller is able to regulate the terminal voltage at node c within firing angle limits. If a limit is reached, the firing angle is fixed, and the SVC behaves as fixed admittance. Lastly, the step-down transformer is modeled as another transmission device.

2.2.5.3 Static Synchronous Compensator

The implementation of the static synchronous compensator (STATCOM) model is based on [Cañizares et al., 2003].

From Fig. 2.5, the STATCOM controller is connected at bus k using a step-down transformer with an impedance $\bar{z}_t = r_t + jx_t$. The converter bus voltage magnitude is

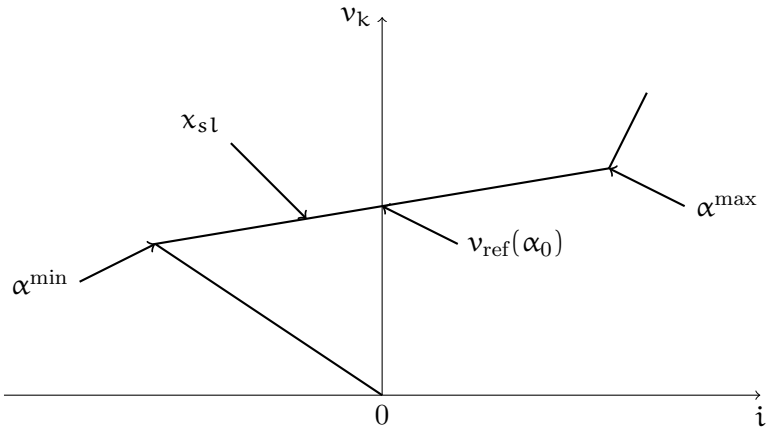

FIGURE 2.4: Typical steady-state V-I characteristic of the SVC.

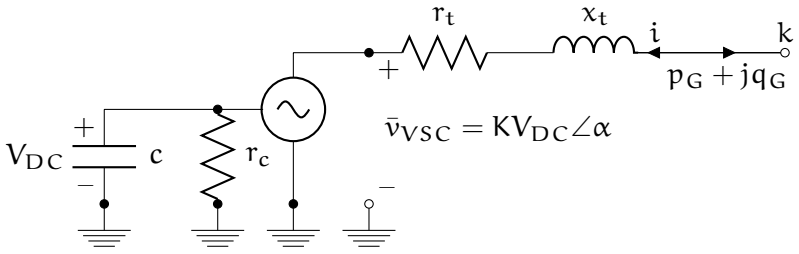

FIGURE 2.5: STATCOM steady-state circuit representation.

proportional with the DC capacitor voltage:

$$v_{VSC} = KV_{DC}\,, \tag{2.37}$$

where V_{DC} is the average DC voltage on the DC capacitor, and v_{VSC} is the RMS value converter output voltage. The K factor comes from the magnitude of the fundamental frequency component of the Fourier series representation of the voltage source converter (VSC) output voltage. This factor is constant and equal to 0.9 for the 12-pulse phase-controlled VSC. On the other hand, the DC-side voltage V_{DC} must be maintained at a prescribed reference:

$$V_{DC} = V_{DC,ref}\,. \tag{2.38}$$

Now, the fundamental equation that links the DC-side with the AC-side voltage is the following active power balance:

$$p_G + p_{DC} + p_{loss} = 0 \tag{2.39a}$$

$$p_G + g_c V_{DC}^2 + r_t i^2 = 0\,, \tag{2.39b}$$

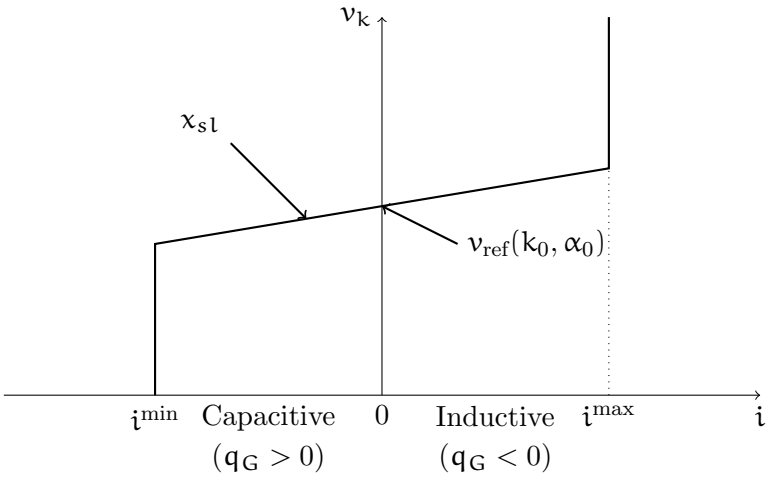

FIGURE 2.6: Typical steady-state V-I characteristic of the STATCOM.

which basically represents the balance between the controller's AC power p_G and DC power p_{DC}. The conductance g_C is used to model the *switching inertia* of the converter because of the electronic switches and their associates' snubber circuits.

Furthermore, another two equations are added to consider the active and reactive power flow from high-voltage bus (bus k) to the VSC:

$$p_G = -v_k^2 g_t + KV_{DC} v_k g_t \cos(\delta_k - \alpha) + KV_{DC} v_k b_t \sin(\delta_k - \alpha) \tag{2.40}$$

$$q_G = +v_k^2 b_t - KV_{DC} v_k b_t \cos(\delta_k - \alpha) + KV_{DC} v_k g_t \sin(\delta_k - \alpha)\ , \tag{2.41}$$

where α is the firing angle of the VSC, and $\bar{y}_t = \frac{1}{\bar{z}_t} = g_t + jb_t$.

Turning to the steady-state STATCOM control law, this one is very similar to the one used in the VSC:

$$v_k = v_{ref} \pm x_{sl} i\,. \tag{2.42}$$

This control law will be valid within the operational limits of the controller, which are basically defined by the current limits in the electronic switches: $i^{min} \leqslant i \leqslant i^{max}$. With these considerations, the V-I characteristic shown in Fig. 2.6 is fully represented; in the case that any current limit is reached, the STATCOM will behave as a constant current source.

2.2.6 Wind Generators

This section presents steady-state models of the most common wind generators. Four types of wind power conversion systems are presented:

Type 1 Fixed-speed wind generator with squirrel-cage induction machine.

Type 2 Wind generator with wound-rotor induction generator and limited speed variation through an external resistor.

Type 3 Doubly-fed induction generators with variable speed.

Type 4 Permanent magnet synchronous generator using a full-scale converter.

A brief description of each technology is provided in the following sections.

2.2.6.1 Aerodynamic Model of the Wind Turbine

The mechanical power extracted from the wind by a wind turbine is a function of the wind speed, blade pitch angle, and shaft speed. The algebraic equation shown below characterizes this power [Vittal and Ayyanar, 2012]:

$$p_W = \frac{1}{2}\rho v_W^3 A c_p(\lambda)\,, \tag{2.43}$$

where p_W is the mechanical power extracted from the wind (w), ρ is the air density (kg/m^3), A is the swept area of the rotor blades (m^2), v_W is the wind speed (m/s), and $c_p(\lambda)$ is the function of performance coefficient given by [Ackermann, 2012]

$$c_p(\lambda) = c_1\left(\frac{c_2}{\gamma} - c_3\beta - c_4\beta^{c_5} - c_6\right)e^{-\frac{c_7}{\gamma}} \tag{2.44a}$$

$$\gamma = \left(\frac{1}{\lambda + c_8\beta} - \frac{c_9}{\beta^3+1}\right)^{-1} \tag{2.44b}$$

$$\lambda = \frac{r n_{gb}\omega_s\omega_m}{v_W} \tag{2.44c}$$

where β is the pitch angle of the rotor blades (deg.), λ is the tip speed ratio, n_{gb} is the gearbox ratio, ω_b is the angular synchronous base speed (rad/s), ω_m is the mechanical angular speed (pu), r is the radius swept by the rotor blades (m), and the constants $c_1 \ldots c_9$ are parameters of design of the wind turbine.

If a maximum power point tracking (MPPT) control is available, p_W can be expressed in terms of an optimal *design constant* k_{opt}:

$$p_W = k_{opt}\omega_m^3 \,. \tag{2.45}$$

This equation is widely reported [Fox, 2007; Pardalos et al., 2014] and used [Padron and Lorenzo, 2010; Li, 2013] because of its simplicity and easy implementation. Drawbacks of Eq. (2.45) is that it does not consider wind speed as an input parameter, and the wind turbine operation cannot be represented when it is not tracking MPPs. Therefore, a mathematical formulation of the MPPT control is presented below, which considers wind speed as an input variable and also the possibility of deloading operation.

Maximum Power Point Tracking (MPPT) Control The control of a variable-speed wind turbine below the rated wind speed is achieved by controlling the mechanical angular speed. The main goal is to maximize the mechanical power extracted at different wind speeds, which can be achieved by adjusting the turbine speed in such a way that the optimal tip speed ratio λ_{opt} is maintained [Vittal and Ayyanar, 2012].

The value of $c_p(\lambda)$ is maximum when $\beta = 0$, since at this position the incidence angle of the blade is fully upwind. Hence, this optimal value can be found by setting $\beta = 0$ and by applying the first-order optimality conditions to $c_p(\lambda)$:

$$\frac{\partial c_p(\lambda)}{\partial \lambda} = -\frac{c_1}{\lambda^3}\left(c_2\lambda + c_7\left(c_2\left(c_9\lambda - 1\right) + c_6\lambda\right)\right) e^{\frac{c_7}{\lambda}\left(c_9\lambda - 1\right)} = 0 \,, \tag{2.46}$$

and by solving Eq. (2.46) for λ

$$\lambda_{opt} = \frac{c_2 c_7}{c_2 c_7 c_9 + c_2 + c_6 c_7} \,. \tag{2.47}$$

By employing Eqs. (2.44c) and (2.47) and by solving for ω_m

$$\omega_{m,opt} = \frac{v_W c_2 c_7}{r n_{gb} w_s \left(c_2 c_7 c_9 + c_2 + c_6 c_7\right)} \,. \tag{2.48}$$

Thus, for a given wind speed, the wind turbine has a mechanical angular speed $\omega_m = \omega_{m,opt}$ at which the maximum power point (MPP) is achieved. To obtain the maximum available power from the wind at different wind speeds, ω_m must be adjusted to ensure its operation at all MPPs.

Blade angle control Wind turbines are designed to produce as much electric energy as possible at all different wind speeds below rated wind. At wind speeds above rated wind, however, the mechanical power extracted from the wind must be limited in order to prevent overloads in the mechanical construction of the wind turbine and generator [Pardalos et al., 2014].

In passive-stall-controlled wind turbines, the rotor presents a fixed blade angle. The geometry of the rotor blade profile is aerodynamically designed to ensure that it creates turbulence on the side of the rotor blade when the wind speed becomes too high. By using this passive method, the power extracted from the wind is reduced for high wind speeds. There is another type of control called active-stall, where the reduction of the mechanical power is achieved by rotating the blades into a stall position.

In pitch-controlled wind turbines, the mechanical power extracted from the wind is reduced by rotating the blades into the feathered position (the blade is moved against the incoming wind). It supposes that the blade pitch angle is increased, and the angle of attack is decreased. This control principle is mostly used in variable speed wind turbines. This blade pitch angle control allows

- The prevention of overloads in the wind turbine with high wind.
- An active control of the power production, and thus, a reduction of the power production when regulation power is required by the system operator.
- A deloaded operation to maintain spinning reserve, which will permit a release of power when a power imbalance perturbation occurs [Castro et al., 2012].

Both control schemes are depicted in Figure 2.7.

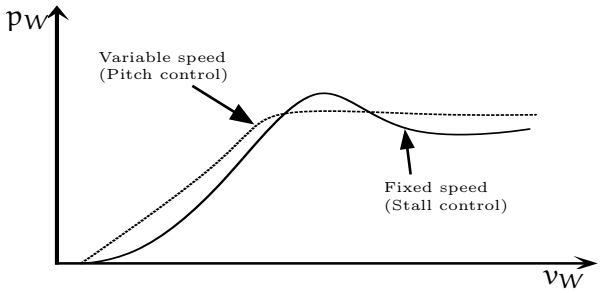

FIGURE 2.7: Typical power-out curves for a stall-controlled and pitch-controlled turbine.

2.2.6.2 Fixed Speed Wind Generator

The schematic of a fixed-peed wind fenerator (FSWG) is shown in Fig. 2.8. In this type of machine, the induction generator is directly interconnected to the electrical grid.

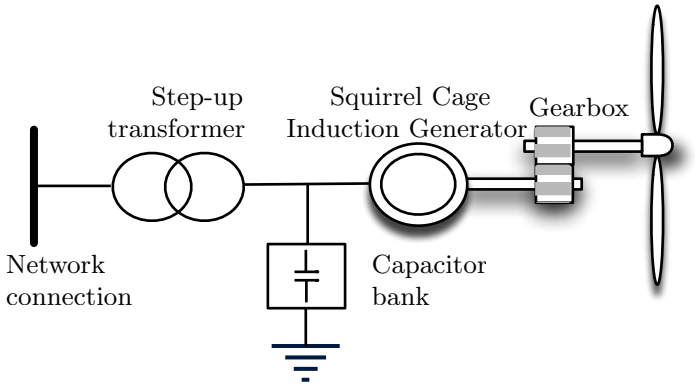

FIGURE 2.8: Schematic representation of Type 1 wind turbine generator.

The gearbox and the number of pole pairs of the induction generator determine the fixed speed of the wind turbine. At high wind speeds the wind turbine rotor limits the power extracted by using a passive-stall control scheme. This wind generator consumes reactive power, so that a capacitor bank, SVC or STATCOM is added to improve the power factor [Ackermann, 2012; Vittal et al., 2010; Vittal and Ayyanar, 2012].

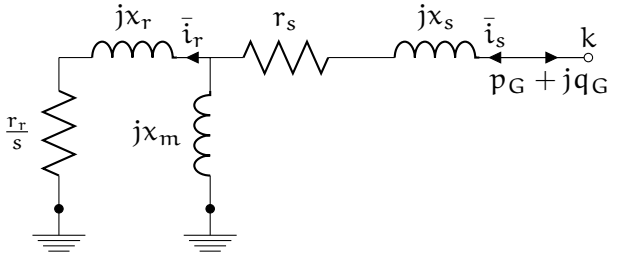

FIGURE 2.9: Electrical circuit of the induction machine model.

The steady-state representation of the FSWG is derived from the equivalent circuit of an induction machine (Fig. 2.9). The subscripts s, m and r represent stator, magnetization branch and rotor variables, respectively.

By considering a machine connected at bus k, a terminal equivalent admittance is used to simplify the model:

$$\bar{y}_{eq} = \left[r_s + jx_s + \frac{jx_m\left(jx_r + \frac{r_r}{s}\right)}{j\left(x_m + x_r\right) + \frac{r_r}{s}} \right]^{-1} \tag{2.49}$$

$$= g_{eq} + jb_{eq}\,, \tag{2.50}$$

where the machine's slip s is computed by using Eq. (2.33).

Therefore, generated active p_G, reactive q_G and electromechanical converted p_c powers are expressed as follows:

$$p_G = -{v_k}^2 g_{eq} \tag{2.51}$$

$$q_G = -{v_k}^2 (-b_{eq}) \tag{2.52}$$

$$\begin{aligned} p_c &= {i_r}^2 r_r \frac{1-s}{s} \\ &= (v_k y_{eq} z_{mr})^2 r_r \frac{1-s}{s}\,, \end{aligned} \tag{2.53}$$

where the impedance $\bar{z}_{mr}$ is a current divider given by

$$\bar{z}_{mr} = \frac{jx_m}{j(x_m + x_r) + \frac{r_r}{s}}\,. \tag{2.54}$$

Moreover, one additional equation is deployed to link the conversion process from mechanical to electrical power:

$$p_c + p_W = 0\,, \tag{2.55}$$

where p_W is computed by using Eq. (2.43).

Active generation limits are inherently imposed in Eq. (2.43) by the stall design of the wind turbine blades [Lubosny, 2010].

2.2.6.3 Semi-Variable Speed Wind Generator

The semi-variable speed wind generator (SSWG) incorporates a wound-rotor induction machine with a variable rotor resistor by means of a power electronic converter. The stator winding is directly connected to the grid, whereas the rotor winding is connected in series to the external resistor (Fig. 2.10).

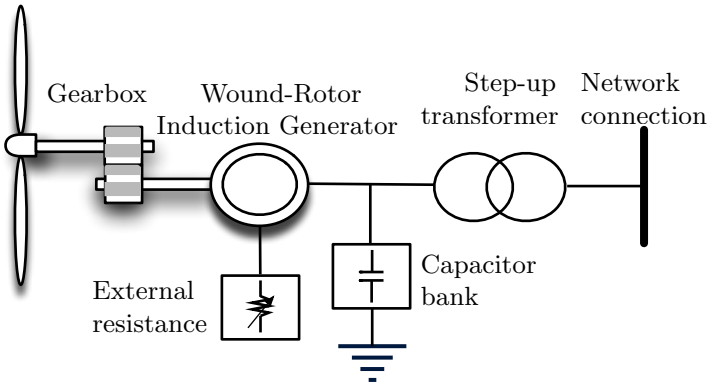

FIGURE 2.10: Schematic representation of Type 2 wind turbine generator.

Variable-speed operation can be achieved by controlling the variable resistance and thus, the generator slip. This slip power, however, is dissipated in the external resistor as losses. As shown in Fig. 2.11, the connection of an extra resistor ($r_{ext} = 4r_r$) to the rotor does not have a considerable influence over the produced power versus wind speed characteristics. A little difference is visible only near the rated power. The same generation behavior has been reported in [Lubosny, 2010].

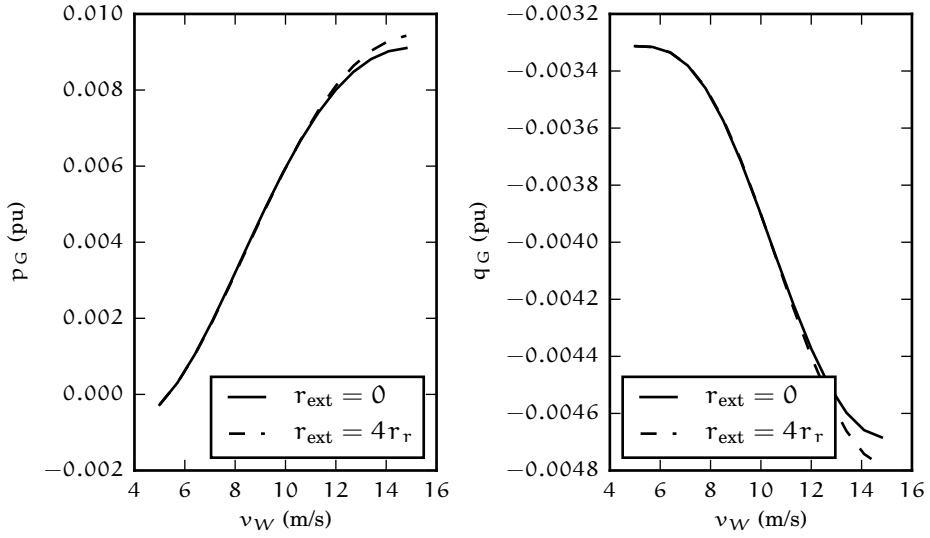

FIGURE 2.11: SSWG power versus wind speed characteristics.

The main effect of the inclusion of r_{ext} occurs under dynamic operating states. The performance of the wind generator with dynamic slip allows the generator to vary its RPM by up to 10% during violent gusts of wind, in addition to minimizing the load on the shaft and other mechanical parts of the turbine.

Hence, for steady-state analysis, the external resistance could be an extra parameter r_{ext}, whereas the new rotor resistance is

$$r_r = r_{int} + r_{ext}\,, \tag{2.56}$$

where r_{int} stands for the internal rotor resistance.

With this modification, the semi-variable wind generator can be modeled as the previous FSWG model.

2.2.6.4 Doubly-Fed Induction Generator Wind Generator

The doubly-fed induction generator (DFIG) wind generator uses a wound-rotor induction machine. The stator of this wound rotor induction machine is directly connected to the

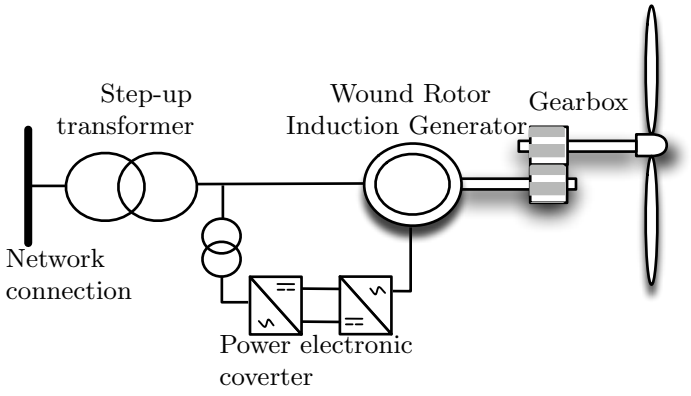

FIGURE 2.12: Schematic representation of DFIG wind turbine.

grid, and the rotor winding is also connected to the grid but by using slip rings to a machine-side converter, as shown in Fig. 2.12. The net output power from the machine in this design is the sum power from the machine's stator and that from the rotor into the grid. Power is injected from the rotor through the converter into the grid when the machine operates at supersynchronous speed. When the machine operates at subsynchronous speeds active power is absorbed from the grid [Vittal and Ayyanar, 2012].

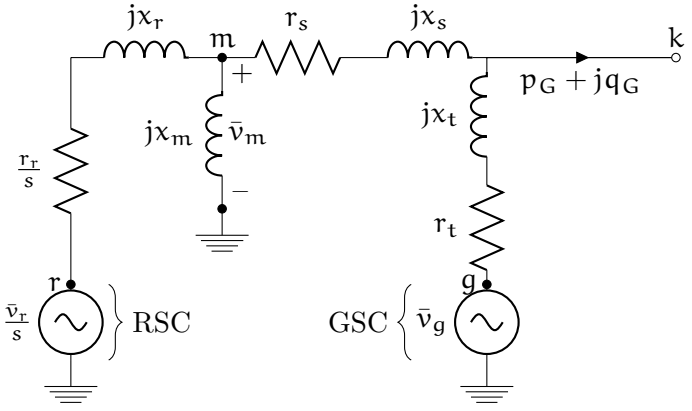

FIGURE 2.13: Equivalent circuit of the DFIG.

The steady-state model is developed from the electrical circuit of a wound-rotor induction machine which is shown in Fig. 2.13 [Vittal and Ayyanar, 2012]. The rotor's terminal is connected to a back-to-back converter in series with a step-up transformer. The modeling of the back-to-back converter is based on [Acha et al., 2004; Li, 2013]. For modeling purposes, the back-to-back converter is divided into a rotor-side converter (RSC) and a grid-side converter (GSC).

RSC control The RSC has the capability of adjusting the rotor currents to obtain the desired active and reactive power outputs on the stator side. The active power set point is obtained by including a MPPT scheme as discussed in Section 2.2.6.1. The reactive

power set point is dependent on the control mode of the DFIG. The two commonly used control modes are [Vittal and Ayyanar, 2012]

- Power factor control
- Voltage control

The stator and rotor reactive powers are controlled in the power factor control mode to maintain a constant power factor at the point of interconnection. The reactive power is controlled in the voltage control mode to maintain the voltage magnitude at a specified value. Various approaches have been proposed to implement terminal voltage control [Cartwright et al., 2004; Kayikci and Milanovic, 2007; Konopinski et al., 2009] and have shown that enhanced voltage control improves voltage performance in the system. With this consideration, two specific control objectives are considered for modeling:

1. Maximum power extraction by controlling the mechanical power such that the rotor speed always tracks MPPs. In other words, control the mechanical power to be equal to the wind power obtained when $\omega_m = \omega_{m,opt}$. This control law is modeled as the following shaft power equilibrium [Li, 2013]:

$$p_W + p_{mr}(1-s) = 0 \tag{2.57}$$

   with

$$p_{mr} = \Re\left(\bar{v}_m \left(\frac{\bar{v}_m - \frac{\bar{v}_r}{s}}{\frac{r_r}{s} + jx_r}\right)^*\right). \tag{2.58}$$

2. Control of either the terminal or a remote bus voltage magnitude. This remote bus could be the high-side voltage of the step-down transformer. Thereby, the RSC must adjust the reactive currents injected to meet the following:

$$v_c = v_{ref} - x_{sl} q_G\,, \tag{2.59}$$

   where v_{ref} stands for the specified voltage of the remote bus c, x_{sl} is the voltage droop, and q_G is the generated reactive power.

GSC control The main role of the grid-side converter is to provide a path for the active power exchange in the positive or negative direction between the rotor-side converter and the grid. It does so by regulating the DC-link voltage. In the subsynchronous mode when the RSC absorbs power from the DC-link, the GSC draws power from the grid and supplies it to the DC-link. In addition, in the supersynchronous mode, the GSC reverses power direction and injects the power from

the RSC into the grid. In steady-state, the DC current drawn by the GSC equals the DC current injected by the RSC. On the other hand, the reactive power of GSC can be controlled independently of the active power exchanged. Because of the DC link between the two converters, the reactive power processed by the GSC is also independent of the reactive power processed by the RSC. This work considers a constant voltage at the DC power link; therefore, by considering a unity power factor operation, the GSC is modeled with two power balance equations:

$$p_{gk} + p_{rot} = 0 \tag{2.60}$$

$$q_{gk} = 0 \tag{2.61}$$

with

$$p_{gk} + jq_{gk} = \bar{v}_g \left(\frac{\bar{v}_g - \bar{v}_k}{r_t + jx_t} \right)^* \tag{2.62}$$

$$p_{rot} = \Re \left(\bar{v}_r \left(\frac{\frac{\bar{v}_r}{s} - \bar{v}_m}{\frac{r_r}{s} + jx_r} \right)^* \right) . \tag{2.63}$$

Power Equilibrium at the Magnetization Branch From the electrical circuit shown in Fig. 2.13, the power balance in the magnetization branch is determined by

$$p_{mk} + p_{mr} = 0 \tag{2.64}$$

$$q_{mk} + q_{mm} + q_{mr} = 0 \tag{2.65}$$

with

$$p_{mk} + jq_{mk} = \bar{v}_m \left(\frac{\bar{v}_m - \bar{v}_k}{r_s + jx_s} \right)^* \tag{2.66}$$

$$p_{mr} + jq_{mr} = \bar{v}_m \left(\frac{\bar{v}_m - \frac{\bar{v}_r}{s}}{\frac{r_r}{s} + jx_r} \right)^* \tag{2.67}$$

$$q_{mm} = -\frac{v_m^2}{x_m} . \tag{2.68}$$

Finally, the active and reactive powers generated by the DFIG are the sum of the powers injected to the grid by the stator and the rotor (by using the back-to-back converter):

$$p_G = -\left(p_{km} + p_{kg}\right) \tag{2.69}$$

$$q_G = -\left(q_{km} + q_{kg}\right) \tag{2.70}$$

$$0 \leqslant p_G \leqslant p_G^{max} \tag{2.71}$$

$$q_G^{min} \leqslant q_G \leqslant q_G^{max} \tag{2.72}$$

with

$$p_{km} + jq_{km} = \bar{v}_k \left(\frac{\bar{v}_k - \bar{v}_m}{r_s + jx_s}\right)^* \tag{2.73}$$

$$p_{kg} + jq_{kg} = \bar{v}_k \left(\frac{\bar{v}_k - \bar{v}_g}{r_t + jx_t}\right)^* . \tag{2.74}$$

Operative limits are basically imposed by the DFIG's active and reactive power ratings (Eqs. (2.71) and (2.72)).

2.2.6.5 Permanent Magnet Synchronous Generator Wind Generator

Unlike DFIG, permanent magnet synchronous generator (PMSG) wind generator supplies all its generated active power through a full-scale converter. Such wind generators have the advantage of being able to fully control the speed range from 0 to 100% of the synchronous speed, support reactive power compensation and have a smooth grid connection [Pardalos et al., 2014].

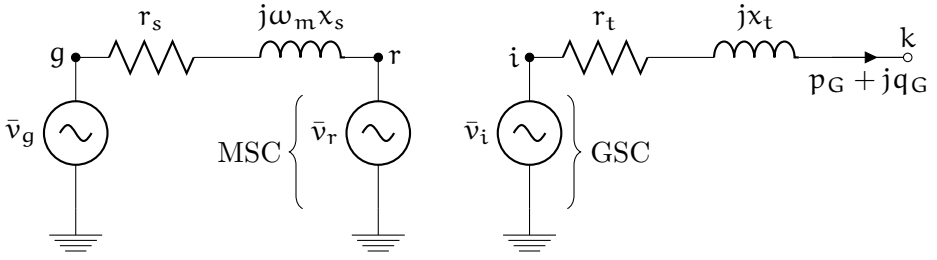

FIGURE 2.14: Equivalent circuit of the PMSG-based wind generator.

For steady-state analysis purpose consider the equivalent electrical circuit shown in Fig. 2.14. The PMSG is represented as a constant voltage source $\bar{v}_g$ in series with the stator's resistance r_s and the synchronous reactance x_s. Furthermore, it is connected to the grid through a back-to-back controller which consists of two converters: machine-side converter (MSC) and grid-side converter (GSC). Both converters are connected through a lossless DC link where voltage V_{DC} is considered constant. A step-up transformer with $r_t + jx_t$ impedance is used to connect the GSC to the grid. Considering that the induced emf E_g is related to the flux linkage produced by the permanent magnets and

the rotor shaft speed, voltage $\bar{v}_g$ is

$$\bar{v}_g = E_g \angle \delta_g = \omega_m \psi_{pm} \angle 0\,, \tag{2.75}$$

where ψ_{pm} is the constant permanent magnet's field flux. Since PMSG is electrically decoupled from the grid, setting an internal angular reference is necessary. In this case the rotor angle is considered fixed to zero, i.e. $\delta_g = 0$.

The transference process of power from the rotor shaft to the grid is described below.

MSC control The MSC is controlled to obtain the maximum active power at any particular wind speed so as to maximize energy capture [Machowski et al., 2011]. Traditionally this optimal operation is achieved by using the *load angle control technique* [Fox, 2007] which adjusts the MSC voltage angle to extract the maximum power. In this case, the wind turbine is considered to be rotating at the optimal mechanical speed $\omega_m = \omega_{m,opt}$; hence, the power delivered to the MSC is maximum, and its voltage must be adjusted to receive and transfer it. Understanding that the machine side is operated under the constant power factor pf, the MSC has to agree with the following equations:

$$p_W = p_{gr} \tag{2.76}$$

$$q_{rg} = \alpha\,(p_{rg}) \tag{2.77}$$

with

$$p_{rg} + jq_{rg} = \bar{v}_r \left(\frac{\bar{v}_r - \bar{v}_g}{r_s + jx_s} \right)^* \tag{2.78}$$

$$p_{gr} = \Re \left(\bar{v}_g \left(\frac{\bar{v}_g - \bar{v}_r}{r_s + jx_s} \right)^* \right) \tag{2.79}$$

$$\alpha = \tan\left[\cos^{-1}(pf)\right]\,. \tag{2.80}$$

GSC control Once the active power is flowing through the DC-link, the GSC has to transfer all this power and maintain a constant voltage on the DC link capacitor. It also controls the voltage magnitude at the transformer's high-voltage side (bus k) or at a remote bus (bus c). For steady-state analysis the GSC is modeled as two equations:

$$p_{rg} + p_{ik} = 0 \tag{2.81}$$

$$v_c = v_{ref} - x_{sl} q_G \tag{2.82}$$

$$\tag{2.83}$$

with

$$p_{ik} = \Re\left(\bar{v}_i \left(\frac{\bar{v}_i - \bar{v}_k}{r_t + jx_t}\right)^*\right), \tag{2.84}$$

where v_{ref} stands for the specified voltage magnitude of bus c, and x_{sl} as usual is the voltage droop.

Finally the active and reactive powers injected to the grid are

$$p_G = -p_{ki} \tag{2.85}$$

$$q_G = -q_{ki} \tag{2.86}$$

$$0 \leqslant p_G \leqslant p_G^{max} \tag{2.87}$$

$$q_G^{min} \leqslant q_G \leqslant q_G^{max}, \tag{2.88}$$

where

$$p_{ki} + jq_{ki} = \bar{v}_k \left(\frac{\bar{v}_k - \bar{v}_i}{r_t + jx_t}\right)^*. \tag{2.89}$$

2.2.6.6 Deloading and Load-Frequency Control

Implementing wind plant controls that provide something similar to governor response is possible [Ackermann, 2012; Loukarakis et al., 2009; Miller et al., 2013; Vittal and Ayyanar, 2012]. In order to allow for an increase of wind plant active power output in response to an underfrequency condition, some active power production must be kept in reserve (spilled). The maximum power production of the wind plant is, therefore, constrained to a value less than that available from the wind. The potential for wind generation to respond quickly makes this resource effective in arresting and correcting frequency deviations, much as fast a governor response does in thermal generation.

From a implementation point of view, DFIG and PSMG are deloaded to calculate the base case with

$$p_G = p_G^{max}\,(1-\eta)\ . \tag{2.90}$$

By adding Eq. (2.90) the pitch angle β will *move* to spill wind and deload wind generation. Thus, when the disturbance is applied, p_G will have to meet

$$p_G = p_{G,0} + \Delta p_G = p_G^{max}\,(1-\eta) + \frac{1}{R}\Delta f \tag{2.91}$$

$$0 \leqslant p_G \leqslant p_G^{max}\,, \tag{2.92}$$

where R is the machine's speed droop. With this equation, wind generation will respond to system frequency deviations, which will decrease the pitch angle, and consequently the wind generator will provide active power support.

2.3 Conclusions

This chapter has shown a step-by-step procedure on how obtain steady-state models of nonconventional electrical networks' devices. The modeling stage was performed trying to include every relevant part of each device as well as its operative limits.

The following chapters will include these steady-state models in a unified power flow solver.

Chapter 3

Power Flow Analysis of Electrical Networks with Wind Generation

3.1 Introduction

In this chapter models of load, a induction machine, FACTS controllers, synchronous and wind generators embedded in the power system are presented. The studies carried out in this chapter are deterministic.

Once every model has been mathematically defined, the resulting equations are included in the power flow problem formulation. Limits of these devices are considered in the unified formulation by using complementarity constraints.

Finally, by using the numerical Newton-Raphson (NR) method, a set of case studies incorporating different operation conditions are presented and analyzed.

3.2 Basic Formulation

The power flow problem consists of the calculation of power flows and voltages of a network for specified terminal bus conditions [Stagg and Abiad, 1968]. The mathematical formulation of this problem results in a set of algebraic nonlinear equations that describes the equilibrium point of the system,

$$\mathbf{0} = \mathbf{g}(\mathbf{y}) \,, \tag{3.1}$$

where $\mathbf{g} : \mathbb{R}^{n_y} \mapsto \mathbb{R}^{n_y}$ is the vector function that defines the power balance at all network buses, and can be written in several ways.

By using matrix operations, the vector of currents injected at each network's bus is

$$\bar{\mathbf{i}} = \bar{\mathbf{Y}}\bar{\mathbf{v}}\,. \tag{3.2}$$

On the other hand, the complex power injections at each bus can be written

$$\bar{\mathbf{s}} = [\bar{\mathbf{v}}]\,\bar{\mathbf{i}}^{*} = [\bar{\mathbf{v}}]\,\bar{\mathbf{Y}}^{*}\bar{\mathbf{v}}^{*}\,, \tag{3.3}$$

where $[\bar{\mathbf{v}}] = \mathrm{diag}\,(\bar{v}_1, \bar{v}_2, \ldots, \bar{v}_{n_b})$, and n_b is the number of network buses. In tensorial form, Eq. (3.3) becomes

$$\bar{s}_k = \bar{v}_k \bar{i}_k^{*} = p_k + jq_k, \qquad \forall k \in \mathcal{B} \tag{3.4a}$$

$$= \bar{v}_k \sum_{m\in\mathcal{B}} \bar{y}_{km}^{*}\bar{v}_m^{*}, \qquad \forall k \in \mathcal{B}\,, \tag{3.4b}$$

where $\mathcal{B} = \{1, 2, \ldots, n_b\}$, and $\bar{y}_{km}$ is the element (k, m) of the nodal admittance matrix $\bar{\mathbf{Y}}$. The power flow solution must satisfy Kirchhoff's laws, which implies that the algebraic sum of all flows at bus k must equal zero, $\forall k \in \mathcal{B}$. Hence, considering a generator and a load embedded at bus k, the power injection $\bar{s}_k$ is defined as the difference of powers injected to that bus by these components

$$\bar{s}_k = \left(p_{G,k} - p_{L,k}\right) + j\left(q_{G,k} - q_{L,k}\right)\,. \tag{3.5}$$

This power injection must be equal to the power injected to all transmission components embedded at bus k: Eq. (3.4b) = Eq. (3.5). By performing some algebra manipulations and separating in real and imaginary parts, the resulting equation is the existing power balance at bus k that can be written as

$$p_k = v_k \sum_{m\in\mathcal{B}} v_m \left(g_{km}\cos\left(\delta_{km}\right) + b_{km}\sin\left(\delta_{km}\right)\right) \qquad = p_{G,k} - p_{L,k} \tag{3.6}$$

$$q_k = v_k \sum_{m\in\mathcal{B}} v_m \left(g_{km}\sin\left(\delta_{km}\right) - b_{km}\cos\left(\delta_{km}\right)\right) \qquad = q_{G,k} - q_{L,k}\,, \tag{3.7}$$

where $\bar{y}_{km} = g_{km} + jb_{km}$ and $\delta_{km} = \delta_k - \delta_m$. By reordering terms, the latter equations are written as active and reactive power mismatches:

$$\Delta p_k = p_{G,k} - p_{L,k} - v_k \sum_{m \in \mathcal{B}} v_m \left(g_{km} \cos\left(\delta_{km}\right) + b_{km} \sin\left(\delta_{km}\right) \right) = 0 \tag{3.8}$$

$$\Delta q_k = q_{G,k} - q_{L,k} - v_k \sum_{m \in \mathcal{B}} v_m \left(g_{km} \sin\left(\delta_{km}\right) - b_{km} \cos\left(\delta_{km}\right) \right) = 0\,. \tag{3.9}$$

Finally, this basic power flow formulation can be written in a more generalized fashion as a set of nonlinear equations:

$$\mathbf{g}(\mathbf{y}) = \begin{bmatrix} \boldsymbol{\Delta p} \\ \boldsymbol{\Delta q} \end{bmatrix} = \mathbf{0}\,, \tag{3.10}$$

where $\mathbf{y}$ represents the set of state variables, for this case is a stacked vector of nodal voltage angles and magnitudes, $\boldsymbol{\theta}$ and $\boldsymbol{v}$, respectively, i.e.:

$$\mathbf{y} = \begin{bmatrix} \boldsymbol{\theta} \\ \boldsymbol{v} \end{bmatrix}\,. \tag{3.11}$$

This basic formulation is far from practical or even solvable. For instance, there is no way to refer the voltage angles to a fixed bus; thus, the set of power mismatch equations are unbounded (mathematically speaking). On the other hand, network losses are not considered; hence the power mismatch will not be zero. To avoid these issues, a more detailed representation of the power flow problem must be carried out. In this context, the inclusion of prior steady state models of synchronous generation, wind generation, load, FACTS, induction machine and transmission branches into this basic power flow problem is shown below.

3.3 Limits Handling

In order to have a better approximation of the real physical network equilibrium point, a set of operative limits must be taken into account. These are included inside the nonlinear equations using complementarity constraints. In this approach, checking violated limits at the end of each iteration of the solution process of Eq. (3.10) is not necessary because these limits are directly introduced in the unified framework solution.

Each device can have one or more complementarity constraints:

$$\mathrm{y}^{\min} \leqslant \mathrm{y} \leqslant \mathrm{y}^{\max} \quad \perp \quad \mathrm{g}(\mathbf{y}) = 0\,, \tag{3.12}$$

where this complementarity problem states an equilibrium between the control law of the device $\mathrm{g}(\mathbf{y})$ and the rating limits $\mathrm{y}^{\min}$ and $\mathrm{y}^{\max}$ of the variable y. This mixed complementarity problem (MCP) is transformed into a set of nonlinear equations without inequalities as described in Appendix A, resulting in

$$\mathrm{g}(\mathbf{y}) - \mathrm{z_a} + \mathrm{z_b} = 0 \tag{3.13}$$

$$\phi_{\min}(\mathbf{y}) = \sqrt{\mathrm{z_a^2} + (\mathrm{y} - \mathrm{y}_{\min})^2} - (\mathrm{z_a} + (\mathrm{y} - \mathrm{y}_{\min})) = 0 \tag{3.14}$$

$$\phi_{\max}(\mathbf{y}) = \sqrt{\mathrm{z_b^2} + (\mathrm{y}_{\max} - \mathrm{y})^2} - (\mathrm{z_b} + (\mathrm{y}_{\max} - \mathrm{y})) = 0\,, \tag{3.15}$$

where $\{\mathrm{z_a}, \mathrm{z_b}\} \in \mathbf{z} \subset \mathbf{y}$ is a new pair of complementarity variables that relax Eq. (3.13). This set of new complementarity variables and its associated complementarity constraints will be denoted by $\mathbf{z} \in \mathbb{R}^{\mathrm{n_z}}$ and $\mathbf{\Phi} : \mathbb{R}^{\mathrm{n_y}} \mapsto \mathbb{R}^{\mathrm{n_z}}$, respectively.

While this implementation was inspired by [Rosehart et al., 2005; Sundaresh and Nagendra Rao, 2014], those works only considerate the reactive power limits of *PV buses*. The presented work goes beyond that by including all the operative limits within a complementarity basis.

The author offers a special discussion about the advantages and disadvantages of this technique.

- The concept of complementarity is synonymous with the notion of system equilibrium [Ferris and Pang, 1997]; thereby, the usage of MCP is the more direct way to include operative limits in a constrained power flow study.
- There is no need to have a *special* part of the code to *check limits* while these ones are included in the global formulation; therefore, the problem formulation remains the same.
- The use of complementarity constraints avoids changing the structure of the Jacobian matrix, which has a major computational advantage: the Jacobian sparsity pattern remains the same along the iterative process Thus, no reordering is needed, and the backward or forward substitution steps are identical at each iteration.

- A major drawback is introduced: the number of nonlinear equations is expanded as much as the number of inequality constraints.

3.4 Generalized Power Flow Formulation

The explicit inclusion of previously reported steady state electric component models in the power flow problem is accomplished by expanding the set of state variables of the previous basic formulation (Eq. (3.11)):

$$\mathbf{y} = \begin{bmatrix} \boldsymbol{\theta} \\ \boldsymbol{v} \\ \boldsymbol{x} \\ \boldsymbol{z} \end{bmatrix} , \tag{3.16}$$

where $\boldsymbol{\theta}$ is the vector of bus voltage angles, and $\boldsymbol{v}$ is the vector of bus voltage magnitudes. Additional variables are considered in $\boldsymbol{x}$ which is a vector that can contain the system frequency (Δf) or internal device variable (e.g. induction motor's mechanical angular speed (ω_m) or a wind generator variable) Finally, $\boldsymbol{z}$ represents the set of complementarity variables.

In the same way, the set of nonlinear equations $\mathbf{g}(\mathbf{y})$ is expanded by grouping together active power mismatches first ($\boldsymbol{\Delta p}$), then reactive power ones ($\boldsymbol{\Delta q}$), then, additional functions $\mathbf{h}$ to be solved and, finally, the set of complementarity constraints $\boldsymbol{\Phi}$:

$$\mathbf{g}(\mathbf{y}) = \left[\begin{array}{c} \boldsymbol{\Delta p} \\ \hline \boldsymbol{\Delta q} \\ \hline \mathbf{h} \\ \hline \boldsymbol{\Phi} \end{array}\right] . \tag{3.17}$$

3.5 Solution of the Power Flow Problem

Having defined our mathematical problem, it is necessary to find a solution thereof. From a mathematical viewpoint, the solution of the power flow problem consists of finding the zero of a set of nonlinear equations starting from an adequate initial guess

$$\mathbf{0} = \mathbf{g}(\mathbf{y}) . \tag{3.18}$$

These kinds of equations need an iterative method to be solved. In this context of iterative nonlinear solvers, the Newton-Raphson (NR) method for solving the power flow problem is described in many books and papers (e.g. [Stagg and Abiad, 1968]). Because of its numerical and time performances is nowadays the most commonly used algorithm for solving the power flow problem [Tinney and Hart, 1967; Milano, 2010].

3.5.1 Newton-Raphson Method

The essence of the method consists of determining which vector of algebraic variables $\mathbf{y}$, that satisfies Eq. (3.18), by performing a Taylor series expansion of $\mathbf{g}(\mathbf{y})$ for an initial estimate $\mathbf{y}^{(0)}$

$$\mathbf{g}(\mathbf{y}) = \mathbf{g}(\mathbf{y}^{(0)}) + \mathbf{g}_{\mathbf{y}}(\mathbf{y}^{(0)}) \left(\mathbf{y} - \mathbf{y}^{(0)}\right) + \text{higher-order terms}\,, \tag{3.19}$$

where $\mathbf{g}_{\mathbf{y}}(\mathbf{y}) \in \mathbb{R}^{n_{\mathbf{y}} \times n_{\mathbf{y}}}$ is the Jacobian matrix of $\mathbf{g}(\mathbf{y})$.

This expansion lends itself to a suitable formulation for calculating the vector of algebraic variables $\mathbf{y}$ by assuming that $\mathbf{y}^{(1)}$ is the value computed by the algorithm at iteration 1 and is sufficiently close to the initial estimate $\mathbf{y}^{(0)}$. Based on this premise, all high-order terms in Eq. (3.19) may be neglected. Thus, by involving Eqs. (3.18) and (3.19) and solving for $\mathbf{y}^{i}$

$$\mathbf{y}^{(i)} = \mathbf{y}^{(i-1)} - \mathbf{g}_{\mathbf{y}}(\mathbf{y}^{(i-1)})^{-1}\mathbf{g}(\mathbf{y}^{(i-1)}), \quad \forall i \geqslant 1\,. \tag{3.20}$$

The iterative solution can be expressed as a function of the correction vector $\boldsymbol{\Delta}\mathbf{y}^{(i)} = \mathbf{y}^{(i)} - \mathbf{y}^{(i-1)}$:

$$\boldsymbol{\Delta}\mathbf{y}^{(i)} = -\mathbf{g}_{\mathbf{y}}(\mathbf{y}^{(i-1)})^{-1}\mathbf{g}(\mathbf{y}^{(i-1)}), \quad \forall i \geqslant 1\,. \tag{3.21}$$

In addition, the state variables are updated by using:

$$\mathbf{y}^{(i)} = \mathbf{y}^{(i-1)} + \boldsymbol{\Delta}\mathbf{y}^{(i)}, \quad \forall i \geqslant 1\,. \tag{3.22}$$

This iterative procedure is performed until the mismatches $\boldsymbol{\Delta}\mathbf{y}$ are within a prescribed tolerance (i.e. $1e-12$).

Power Flow Jacobian Matrix In order to apply the Newton-Raphson method to the power flow problem, the set of nonlinear equations must be linearized using the Jacobian matrix, which can be written as

$$\mathbf{g}_{\mathbf{y}}(\mathbf{y}) = \left[\begin{array}{cc|c|c} \boldsymbol{\Delta p}_{\boldsymbol{\theta}} & \boldsymbol{\Delta p}_{\boldsymbol{v}} & \boldsymbol{\Delta p}_{\boldsymbol{x}} & \boldsymbol{\Delta p}_{\boldsymbol{z}} \\ \boldsymbol{\Delta q}_{\boldsymbol{\theta}} & \boldsymbol{\Delta q}_{\boldsymbol{v}} & \boldsymbol{\Delta q}_{\boldsymbol{x}} & \boldsymbol{\Delta q}_{\boldsymbol{z}} \\ \hline \mathbf{h}_{\boldsymbol{\theta}} & \mathbf{h}_{\boldsymbol{v}} & \mathbf{h}_{\boldsymbol{x}} & \mathbf{h}_{\boldsymbol{z}} \\ \hline \boldsymbol{\Phi}_{\boldsymbol{\theta}} & \boldsymbol{\Phi}_{\boldsymbol{v}} & \boldsymbol{\Phi}_{\boldsymbol{x}} & \boldsymbol{\Phi}_{\boldsymbol{z}} \end{array}\right], \tag{3.23}$$

where $\boldsymbol{\Delta p}_{\boldsymbol{\theta}} = \nabla_{\boldsymbol{\theta}}^{\mathsf{T}} \boldsymbol{\Delta p}$, $\boldsymbol{\Delta p}_{\boldsymbol{v}} = \nabla_{\boldsymbol{v}}^{\mathsf{T}} \boldsymbol{\Delta p}$, $\boldsymbol{\Delta p}_{\boldsymbol{x}} = \nabla_{\boldsymbol{x}}^{\mathsf{T}} \boldsymbol{\Delta p}$, $\boldsymbol{\Delta p}_{\boldsymbol{z}} = \nabla_{\boldsymbol{z}}^{\mathsf{T}} \boldsymbol{\Delta p}$, $\boldsymbol{\Delta q}_{\boldsymbol{\theta}} = \nabla_{\boldsymbol{\theta}}^{\mathsf{T}} \boldsymbol{\Delta q}$, $\boldsymbol{\Delta q}_{\boldsymbol{v}} = \nabla_{\boldsymbol{v}}^{\mathsf{T}} \boldsymbol{\Delta q}$, $\boldsymbol{\Delta q}_{\boldsymbol{x}} = \nabla_{\boldsymbol{x}}^{\mathsf{T}} \boldsymbol{\Delta q}$, $\boldsymbol{\Delta q}_{\boldsymbol{z}} = \nabla_{\boldsymbol{z}}^{\mathsf{T}} \boldsymbol{\Delta q}$, $\mathbf{h}_{\boldsymbol{\theta}} = \nabla_{\boldsymbol{\theta}}^{\mathsf{T}} \mathbf{h}$, $\mathbf{h}_{\boldsymbol{v}} = \nabla_{\boldsymbol{v}}^{\mathsf{T}} \mathbf{h}$, $\mathbf{h}_{\boldsymbol{x}} = \nabla_{\boldsymbol{x}}^{\mathsf{T}} \mathbf{h}$, $\mathbf{h}_{\boldsymbol{z}} = \nabla_{\boldsymbol{z}}^{\mathsf{T}} \mathbf{h}$, $\boldsymbol{\Phi}_{\boldsymbol{\theta}} = \nabla_{\boldsymbol{\theta}}^{\mathsf{T}} \boldsymbol{\Phi}$, $\boldsymbol{\Phi}_{\boldsymbol{v}} = \nabla_{\boldsymbol{v}}^{\mathsf{T}} \boldsymbol{\Phi}$, $\boldsymbol{\Phi}_{\boldsymbol{x}} = \nabla_{\boldsymbol{x}}^{\mathsf{T}} \boldsymbol{\Phi}$ and $\boldsymbol{\Phi}_{\boldsymbol{z}} = \nabla_{\boldsymbol{z}}^{\mathsf{T}} \boldsymbol{\Phi}$.

Thus, Eq. (3.21) can be written in an expanded form as follows:

$$\left[\begin{array}{c} \boldsymbol{\Delta\theta} \\ \boldsymbol{\Delta v} \\ \hline \boldsymbol{\Delta x} \\ \hline \boldsymbol{\Delta z} \end{array}\right]^{(i)} = - \left[\begin{array}{cc|c|c} \boldsymbol{\Delta p}_{\boldsymbol{\theta}} & \boldsymbol{\Delta p}_{\boldsymbol{v}} & \boldsymbol{\Delta p}_{\boldsymbol{x}} & \boldsymbol{\Delta p}_{\boldsymbol{z}} \\ \boldsymbol{\Delta q}_{\boldsymbol{\theta}} & \boldsymbol{\Delta q}_{\boldsymbol{v}} & \boldsymbol{\Delta q}_{\boldsymbol{x}} & \boldsymbol{\Delta q}_{\boldsymbol{z}} \\ \hline \mathbf{h}_{\boldsymbol{\theta}} & \mathbf{h}_{\boldsymbol{v}} & \mathbf{h}_{\boldsymbol{x}} & \mathbf{h}_{\boldsymbol{z}} \\ \hline \boldsymbol{\Phi}_{\boldsymbol{\theta}} & \boldsymbol{\Phi}_{\boldsymbol{v}} & \boldsymbol{\Phi}_{\boldsymbol{x}} & \boldsymbol{\Phi}_{\boldsymbol{z}} \end{array}\right]^{(i-1)^{-1}} \left[\begin{array}{c} \boldsymbol{\Delta p} \\ \boldsymbol{\Delta q} \\ \hline \mathbf{h} \\ \hline \boldsymbol{\Phi} \end{array}\right]^{(i-1)}. \tag{3.24}$$

3.6 Power Flow Equations of Modeled Devices

The *power flow equations* of each device as well as their Jacobian structure are shown in this section.

For the sake of conciseness, each of the following presented models are embedded at bus k which can also have other embedded generation, load or transmission devices. The powers injected, drawn or transmitted by these other devices will be denoted by $(\mathsf{p}_{\mathsf{G},\mathsf{k}}, \mathsf{q}_{\mathsf{G},\mathsf{k}})$, $(\mathsf{p}_{\mathsf{L},\mathsf{k}}, \mathsf{q}_{\mathsf{L},\mathsf{k}})$ and $(\mathsf{p}_{\mathsf{k}}, \mathsf{q}_{\mathsf{k}})$, respectively.

3.6.1 Synchronous Generator

The synchronous generator steady state model is discussed in Section 2.2.1. This section presents the expanded model that includes its active and reactive power limits by using complementarity constraints, as well as the model's inclusion in the power flow equations.

By assuming a synchronous generator embedded at bus k, the equations that describe its steady state in a power flow problem are

$$\Delta p_k = p_G + p_{G,k} - p_{L,k} - p_k = 0 \tag{3.25}$$

$$\Delta q_k = q_G + q_{G,k} - q_{L,k} - q_k = 0 \tag{3.26}$$

$$h_{SG_1} = -p_G + p_{G,0} - \left(\frac{1}{R}\right)\Delta f + p_{G_a} - p_{G_b} = 0 \tag{3.27}$$

$$h_{SG_2} = -q_G + q_{G,0} + \frac{v_k\,(v_{ref} - v_k)}{x_{mq}} + q_{G_a} - q_{G_b} = 0 \tag{3.28}$$

$$\phi_{SG_1} = \sqrt{p_{G_a}^2 + \left(p_G - p_G^{min}\right)^2} - \left(p_{G_a} + \left(p_G - p_G^{min}\right)\right) = 0 \tag{3.29}$$

$$\phi_{SG_2} = \sqrt{p_{G_b}^2 + \left(p_G^{max} - p_G\right)^2} - \left(p_{G_b} + \left(p_G^{max} - p_G\right)\right) = 0 \tag{3.30}$$

$$\phi_{SG_3} = \sqrt{q_{G_a}^2 + \left(q_G - q_G^{min}\right)^2} - \left(q_{G_a} + \left(q_G - q_G^{min}\right)\right) = 0 \tag{3.31}$$

$$\phi_{SG_4} = \sqrt{q_{G_b}^2 + \left(q_G^{max} - q_G\right)^2} - \left(q_{G_b} + \left(q_G^{max} - q_G\right)\right) = 0 \tag{3.32}$$

$$\mathbf{g}(\mathbf{y})_{SG}^{(i)} = -\mathbf{g}_{\mathbf{y}}(\mathbf{y})_{SG}^{(i)} \Delta \mathbf{y}_{SG}^{(i)}, \tag{3.33}$$

with

$$\mathbf{g}(\mathbf{y})_{SG} = \begin{bmatrix} \Delta p_k & \Delta q_k & h_{SG_1} & h_{SG_2} & \phi_{SG_1} & \phi_{SG_2} & \phi_{SG_3} & \phi_{SG_4} \end{bmatrix}^T \tag{3.34}$$

$$\Delta \mathbf{y}_{SG} = \begin{bmatrix} \Delta\delta_k & \Delta v_k & \Delta p_G & \Delta q_G & \Delta p_{G_a} & \Delta p_{G_b} & \Delta q_{G_a} & \Delta q_{G_b} & \Delta\Delta f \end{bmatrix}^T \tag{3.35}$$

$$\mathbf{g}_{\mathbf{y}}(\mathbf{y})_{SG} = \begin{bmatrix} \frac{\partial \Delta p_k}{\partial \delta_k} & \frac{\partial \Delta p_k}{\partial v_k} & \frac{\partial \Delta p_k}{\partial p_G} & \frac{\partial \Delta p_k}{\partial q_G} & 0 & 0 & 0 & 0 & \frac{\partial \Delta p_k}{\partial \Delta f} \\ \frac{\partial \Delta q_k}{\partial \delta_k} & \frac{\partial \Delta q_k}{\partial v_k} & \frac{\partial \Delta q_k}{\partial p_G} & \frac{\partial \Delta q_k}{\partial q_G} & 0 & 0 & 0 & 0 & \frac{\partial \Delta q_k}{\partial \Delta f} \\ 0 & 0 & \frac{\partial h_{SG_1}}{\partial p_G} & 0 & \frac{\partial h_{SG_1}}{\partial p_{G_a}} & \frac{\partial h_{SG_1}}{\partial p_{G_b}} & 0 & 0 & \frac{\partial h_{SG_1}}{\partial \Delta f} \\ 0 & \frac{\partial h_{SG_2}}{\partial v_k} & 0 & \frac{\partial h_{SG_2}}{\partial q_G} & 0 & 0 & \frac{\partial h_{SG_2}}{\partial q_{G_a}} & \frac{\partial h_{SG_2}}{\partial q_{G_b}} & 0 \\ 0 & 0 & \frac{\partial \phi_{SG_1}}{\partial p_G} & 0 & \frac{\partial \phi_{SG_1}}{\partial p_{G_a}} & 0 & 0 & 0 & 0 \\ 0 & 0 & \frac{\partial \phi_{SG_2}}{\partial p_G} & 0 & 0 & \frac{\partial \phi_{SG_2}}{\partial p_{G_b}} & 0 & 0 & 0 \\ 0 & 0 & 0 & \frac{\partial \phi_{SG_3}}{\partial q_G} & 0 & 0 & \frac{\partial \phi_{SG_3}}{\partial q_{G_a}} & 0 & 0 \\ 0 & 0 & 0 & \frac{\partial \phi_{SG_4}}{\partial q_G} & 0 & 0 & 0 & \frac{\partial \phi_{SG_4}}{\partial q_{G_b}} & 0 \end{bmatrix}, \tag{3.36}$$

where the two state variables of the SG are $\mathbf{x}_{SG} = \begin{bmatrix} p_G & q_G \end{bmatrix}^T$ and its complementarity variables are $\mathbf{z}_{SG} = \begin{bmatrix} p_{G_a} & p_{G_b} & q_{G_a} & q_{G_b} \end{bmatrix}^T$.

If a user does not have the synchronous generator data, such as the direct and quadrature reactances, to obtain the x_{mq} reactance, Eq. (3.28) can be changed to

$$h_{SG_2} = v_c - v_{ref} + x_{sl} q_G - v_a + v_b = 0\,, \tag{3.37}$$

where v_c is the voltage magnitude of either the local or a remote bus, x_{sl} is a voltage droop with typical values of $2-4\%$, and finally, the complementarity variables q_{G_a} and q_{G_b} are renamed to v_a and v_b, respectively. These modifications must be applied to Eqs. (3.31) and (3.32):

$$\phi_{SG_3} = \sqrt{v_a^2 + \left(q_G - q_G^{min}\right)^2} - \left(v_a + \left(q_G - q_G^{min}\right)\right) \qquad = 0 \tag{3.38}$$

$$\phi_{SG_4} = \sqrt{v_b^2 + \left(q_G^{max} - q_G\right)^2} - \left(v_b + \left(q_G^{max} - q_G\right)\right) \qquad = 0\,. \tag{3.39}$$

Reference Generator In the case that the assumed generator is chosen to maintain the voltage reference angle, the following constraint is added to the previous set of linearized equations:

$$h_{SG_3} = \delta_k - \delta_{ref} = 0\,. \tag{3.40}$$

The addition of Eq. (3.40) includes a new variable to be computed in the NR solution. In this case, this variable is the system frequency deviation Δf.

Initialization

$$p_G^{(0)} = p_{G,0} \tag{3.41}$$

$$q_G^{(0)} = \begin{cases} q_G^{min}, & q_{G,0} \leqslant q_G^{min} \\ q_{G,0}, & q_G^{min} < q_G < q_G^{max} \\ q_G^{max}, & q_{G,0} \geqslant q_G^{max} \end{cases} \tag{3.42}$$

$$v_k^{(0)} = v_{ref} \tag{3.43}$$

$$p_{G_a}^{(0)} = p_{G_b}^{(0)} = 0 \tag{3.44}$$

$$q_{G_a}^{(0)} = \begin{cases} 0.05, & q_{G,0} \leqslant q_G^{min} \\ 0, & q_{G,0} > q_G^{min} \end{cases} \tag{3.45}$$

$$q_{G_b}^{(0)} = \begin{cases} 0.05, & q_{G,0} \geqslant q_G^{max} \\ 0, & q_{G,0} < q_G^{max} \end{cases}\,. \tag{3.46}$$

In case that the control law is in voltage terms (Eq. (3.37)), the initialization is as follows:

$$p_G^{(0)} = p_{G,0} \tag{3.47}$$

$$q_G^{(0)} = \begin{cases} q_G^{min}, & q_{G,0} \leqslant q_G^{min} \\ q_{G,0}, & q_G^{min} < q_G < q_G^{max} \\ q_G^{max}, & q_{G,0} \geqslant q_G^{max} \end{cases} \tag{3.48}$$

$$v_k^{(0)} = v_{ref} \tag{3.49}$$

$$p_{G_a}^{(0)} = p_{G_b}^{(0)} = 0 \tag{3.50}$$

$$v_a^{(0)} = \begin{cases} 0.05, & q_{G,0} \leqslant q_G^{min} \\ 0, & q_{G,0} > q_G^{min} \end{cases} \tag{3.51}$$

$$v_b^{(0)} = \begin{cases} 0.05, & q_{G,0} \geqslant q_G^{max} \\ 0, & q_{G,0} < q_G^{max} \end{cases} . \tag{3.52}$$

Some remarks must be made about this synchronous generator model.

- In this work, the classic algorithmic treatment for the different types of buses was not used. Instead all buses are treated as a *PQ bus* that can have embedded generation, transmission or load devices.
- The model considers a participation factor defined by $\frac{1}{R}$ which is affected by Δf, but we can also redefine this factor to solve a power flow problem considering inertial response, distribution of network losses or economic dispatch as proposed in [Lotfalian et al., 1985; Guoyu et al., 1985; Zobian and Ilic, 1997], respectively.
- The traditional single slack bus formulation is a particular case of this distributed slack bus model, which is $\frac{1}{R} = 0$ for all generators except for the slack bus that has $\frac{1}{R_{slack}} = 1$.
- As opposed to the traditional formulation, this model can have one or more synchronous generators embedded at the same bus, whereas reactive power contributions are computed automatically.

3.6.2 Transmission, Transformer and Phase-Shifter

The generalized transmission branch steady state model is described in Section 2.2.2. Note that Eqs. (2.13) and (2.14) represent only the powers injected at bus k through the l-th transmission element: $p_{k,l}$ and $q_{k,l}$. A practical system, however, will consist

of many buses and many transmission elements. This calls for Eqs. (2.13) and (2.14) to be expressed in more general terms, with the net power flow injected at bus k expressed as the summation of the powers flowing at each one of the transmission elements terminating at this bus. Therefore, the generic net active and reactive powers injected at bus k are included in the unified formulation as follows:

$$\Delta p_k = -p_k + p_{G,k} - p_{L,k} = 0 \tag{3.53}$$

$$\Delta q_k = -q_k + q_{G,k} - q_{L,k} = 0 \tag{3.54}$$

$$\begin{bmatrix} \Delta p_k \\ \Delta q_k \end{bmatrix}^{(i)} = - \begin{bmatrix} \frac{\partial \Delta p_k}{\partial \delta_k} & \frac{\partial \Delta p_k}{\partial v_k} \\ \frac{\partial \Delta q_k}{\partial \delta_k} & \frac{\partial \Delta q_k}{\partial v_k} \end{bmatrix}^{(i)} \begin{bmatrix} \Delta \delta_k \\ \Delta v_k \end{bmatrix}^{(i)} , \tag{3.55}$$

with

$$p_k = \sum_{l \in \mathcal{L}} p_{k,l} \tag{3.56}$$

$$q_k = \sum_{l \in \mathcal{L}} q_{k,l} , \tag{3.57}$$

where $\mathcal{L}$ is the set of branch devices in the network.

Computationally speaking, the sum expressed in Eqs. (3.56) and (3.57) is very expensive; therefore, these net power injections can be computed by using linear transformations by means of the well known $\mathbf{Y}_{\text{bus}}$ matrix [Stagg and Abiad, 1968]. Although this work does not try to introduce the reader to these power system concepts, there are a couple of works which show an efficient computation of these power injections as well as their derivatives: [Zimmerman, 2011; Milano, 2010].

3.6.3 Load

The nonlinear equations of the steady state model of load are presented in Section 2.2.3,and are solved iteratively with the NR method according to the next set of equations:

$$\Delta p_k = -p_L + p_{G,k} - p_{L,k} - p_k = 0 \tag{3.58}$$

$$\Delta q_k = -q_L + q_{G,k} - q_{L,k} - q_k = 0 \tag{3.59}$$

$$\begin{bmatrix} \Delta p_k \\ \Delta q_k \end{bmatrix}^{(i)} = - \begin{bmatrix} \frac{\partial \Delta p_k}{\partial \delta_k} & \frac{\partial \Delta p_k}{\partial v_k} & \frac{\partial \Delta p_k}{\partial \Delta f} \\ \frac{\partial \Delta q_k}{\partial \delta_k} & \frac{\partial \Delta q_k}{\partial v_k} & \frac{\partial \Delta q_k}{\partial \Delta f} \end{bmatrix}^{(i)} \begin{bmatrix} \Delta \delta_k \\ \Delta v_k \\ \Delta \Delta f \end{bmatrix}^{(i)} , \tag{3.60}$$

where

$$p_L = p_{L,0} \left(1 + k_{pf} \Delta f\right) \left[k_{pp} + k_{pc} \left(\frac{v_k}{v_{k_0}} \right) + k_{pz} \left(\frac{v_k}{v_{k_0}} \right)^2 \right] \tag{3.61}$$

$$q_L = q_{L,0} \left(1 + k_{qf} \Delta f\right) \left[k_{qp} + k_{qc} \left(\frac{v_k}{v_{k_0}} \right) + k_{qz} \left(\frac{v_k}{v_{k_0}} \right)^2 \right]. \tag{3.62}$$

This model does not expand the set of equations.

3.6.4 Induction Machine

The induction machine model is discussed in Section 2.2.4. By considering an induction machine connected at the terminal k of the system, the set of mismatch power flow equations is:

$$\Delta p_k = -p_L + p_{G,k} - p_{L,k} - p_k = 0 \tag{3.63}$$

$$\Delta q_k = -q_L + q_{G,k} - q_{L,k} - q_k = 0 \tag{3.64}$$

$$h_{IM_1} = p_c + p_m = 0 \tag{3.65}$$

$$\begin{bmatrix} \Delta p_k \\ \Delta q_k \\ h_{IM_1} \end{bmatrix}^{(i)} = - \begin{bmatrix} \frac{\partial \Delta p_k}{\partial \delta_k} & \frac{\partial \Delta p_k}{\partial v_k} & \frac{\partial \Delta p_k}{\partial \omega_m} & \frac{\partial \Delta p_k}{\partial \Delta f} \\ \frac{\partial \Delta q_k}{\partial \delta_k} & \frac{\partial \Delta q_k}{\partial v_k} & \frac{\partial \Delta q_k}{\partial \omega_m} & \frac{\partial \Delta q_k}{\partial \Delta f} \\ 0 & \frac{\partial h_{IM_1}}{\partial v_k} & \frac{\partial h_{IM_1}}{\partial \omega_m} & \frac{\partial h_{IM_1}}{\partial \Delta f} \end{bmatrix}^{(i)} \begin{bmatrix} \Delta \delta_k \\ \Delta v_k \\ \Delta \omega_m \\ \Delta \Delta f \end{bmatrix}^{(i)} , \tag{3.66}$$

where

$$p_L = v_k^2 g_{eq} \tag{3.67}$$

$$q_L = v_k^2 \left(-b_{eq}\right) \tag{3.68}$$

$$p_c = i_r^2 r_r \frac{1-s}{s} \tag{3.69}$$

$$p_m = p_{m,0}\left[a\left(\frac{\omega_m}{\omega_{m,0}}\right)^2 + b\frac{\omega_m}{\omega_{m,0}} + c\right]. \tag{3.70}$$

The induction machine state variable is $\mathbf{x}_{IM} = [\omega_m]$.

Initialization

$$\omega_m^{(0)} = \omega_{m,0}\,. \tag{3.71}$$

3.6.5 Static VAR Compensator

The steady state model of the SVC is described in Section 2.2.5.2. Typically, the SVC is connected to the transmission system bus through a step-down transformer which will be treated similarly to the other transformers in the system. A pair of complementarity constraints is added to properly model the firing angle limits. Hence, the following equations describe a SVC connected to bus k that controls the voltage magnitude of bus c:

$$\Delta p_k = p_{G,k} - p_{L,k} - p_k = 0 \tag{3.72}$$

$$\Delta q_k = q_G + q_{G,k} - q_{L,k} - q_k = 0 \tag{3.73}$$

$$h_{SVC_1} = v_c - v_{ref} + x_{sl} v_k b_e - v_a + v_b = 0 \tag{3.74}$$

$$h_{SVC_2} = \pi x_c x_l b_e + \sin(2\alpha) - 2\alpha + \pi\left(2 - \frac{x_l}{x_c}\right) = 0 \tag{3.75}$$

$$\phi_{SVC_1} = \sqrt{v_a^2 + \left(\alpha - \alpha^{min}\right)^2} - \left(v_a + \left(\alpha - \alpha^{min}\right)\right) = 0 \tag{3.76}$$

$$\phi_{SVC_2} = \sqrt{v_b^2 + \left(\alpha^{max} - \alpha\right)^2} - \left(v_b + \left(\alpha^{max} - \alpha\right)\right) = 0 \tag{3.77}$$

$$\begin{bmatrix} \Delta p_k \\ \Delta q_k \\ h_{SVC_1} \\ h_{SVC_2} \\ \phi_{SVC_1} \\ \phi_{SVC_2} \end{bmatrix}^{(i)} = - \begin{bmatrix} \frac{\partial \Delta p_k}{\partial \delta_k} & \frac{\partial \Delta p_k}{\partial v_k} & 0 & 0 & 0 & 0 & 0 \\ \frac{\partial \Delta q_k}{\partial \delta_k} & \frac{\partial \Delta q_k}{\partial v_k} & 0 & \frac{\partial \Delta q_k}{\partial b_e} & 0 & 0 & 0 \\ 0 & \frac{\partial h_{SVC_1}}{\partial v_k} & \frac{\partial h_{SVC_1}}{\partial v_c} & \frac{\partial h_{SVC_1}}{\partial b_e} & 0 & \frac{\partial h_{SVC_1}}{\partial v_a} & \frac{\partial h_{SVC_1}}{\partial v_b} \\ 0 & 0 & 0 & \frac{\partial h_{SVC_2}}{\partial b_e} & \frac{\partial h_{SVC_2}}{\partial \alpha} & 0 & 0 \\ 0 & 0 & 0 & 0 & \frac{\partial \phi_{SVC_1}}{\partial \alpha} & \frac{\partial \phi_{SVC_1}}{\partial v_a} & 0 \\ 0 & 0 & 0 & 0 & \frac{\partial \phi_{SVC_2}}{\partial \alpha} & 0 & \frac{\partial \phi_{SVC_2}}{\partial v_b} \end{bmatrix}^{(i)} \begin{bmatrix} \Delta \delta_k \\ \Delta v_k \\ \Delta v_c \\ \Delta b_e \\ \Delta \alpha \\ \Delta v_a \\ \Delta v_b \end{bmatrix}^{(i)}, \tag{3.78}$$

where

$$q_G = v_k^2 b_e \,. \tag{3.79}$$

Initialization An approximation to b_e can be obtained by considering $v_a^{(0)} = v_b^{(0)} = 0$ and solving it from Eq. (3.74):

$$b_e^{(0)} = -\frac{v_c^{(0)} - v_{ref}}{x_{sl} v_k^{(0)}} \,. \tag{3.80}$$

By having the value of b_e, α can be initialized by solving Eq. (3.75), but this equation is not solvable by algebraic means hence, a NR method is applied. Typically, this NR solution will only require one or two iterations to obtain a *good* initial value. Note that this NR is applied at the initialization process; it is not combined with the global NR.

3.6.6 Static Synchronous Compensator

The STATCOM power flow model can be readily obtained from the steady state equations stated in Section 2.2.5.3. By including the corresponding complementarity equations that constrain the operative limits and by assuming that the STATCOM is connected at bus k, its power flow equations are

$$\Delta p_k = p_G + p_{G,k} - p_{L,k} - p_k = 0 \quad (3.81)$$
$$\Delta q_k = q_G + q_{G,k} - q_{L,k} - q_k = 0 \quad (3.82)$$
$$h_{STC_1} = v_k - v_{ref} \pm (x_{sl} i + v_b) = 0 \quad (3.83)$$
$$h_{STC_2} = V_{DC} - V_{DC,ref} = 0 \quad (3.84)$$
$$h_{STC_3} = p_G + g_c V_{DC}^2 + r_t i^2 = 0 \quad (3.85)$$
$$h_{STC_4} = -p_G - v_k^2 g_t - k V_{DC} v_k g_t \cos(\delta_k - \alpha) + k V_{DC} v_k b_t \sin(\delta_k - \alpha) = 0 \quad (3.86)$$
$$h_{STC_5} = -q_G + v_k^2 b_t - k V_{DC} v_k b_t \cos(\delta_k - \alpha) + k V_{DC} v_k g_t \sin(\delta_k - \alpha) = 0 \quad (3.87)$$
$$\phi_{STC_1} = \sqrt{v_b^2 + (i^{max} - i)^2} - (v_b + (i^{max} - i)) = 0 \quad (3.88)$$

$$\mathbf{g}(\mathbf{y})_{STC}^{(i)} = -\mathbf{g}_{\mathbf{y}}(\mathbf{y})_{STC}^{(i)} \mathbf{\Delta y}_{STC}^{(i)}, \quad (3.89)$$

with

$$\mathbf{g}(\mathbf{y})_{STC} = \begin{bmatrix} \Delta p_k & \Delta q_k & h_{STC_1} & h_{STC_2} & h_{STC_3} & h_{STC_4} & h_{STC_5} & \phi_{STC_1} \end{bmatrix}^T \quad (3.90)$$
$$\mathbf{\Delta y}_{STC} = \begin{bmatrix} \Delta\delta_k & \Delta v_k & \Delta\alpha & \Delta V_{DC} & \Delta k & \Delta i & \Delta\theta & \Delta v_b \end{bmatrix}^T \quad (3.91)$$

$$\mathbf{g}_{\mathbf{y}}(\mathbf{y})_{STC} = \begin{bmatrix} \frac{\partial \Delta p_k}{\partial \delta_k} & \frac{\partial \Delta p_k}{\partial v_k} & 0 & 0 & 0 & \frac{\partial \Delta p_k}{\partial i} & \frac{\partial \Delta p_k}{\partial \theta} & 0 \\ \frac{\partial \Delta q_k}{\partial \delta_k} & \frac{\partial \Delta q_k}{\partial v_k} & 0 & 0 & 0 & \frac{\partial \Delta q_k}{\partial i} & \frac{\partial \Delta q_k}{\partial \theta} & 0 \\ 0 & \frac{\partial h_{STC_1}}{\partial v_k} & 0 & 0 & 0 & \frac{\partial h_{STC_1}}{\partial i} & 0 & \frac{\partial h_{STC_1}}{\partial v_b} \\ 0 & 0 & 0 & \frac{\partial h_{STC_2}}{\partial V_{DC}} & 0 & 0 & 0 & 0 \\ \frac{\partial h_{STC_3}}{\partial \delta_k} & \frac{\partial h_{STC_3}}{\partial v_k} & 0 & \frac{\partial h_{STC_3}}{\partial V_{DC}} & 0 & \frac{\partial h_{STC_3}}{\partial i} & \frac{\partial h_{STC_3}}{\partial \theta} & 0 \\ \frac{\partial h_{STC_4}}{\partial \delta_k} & \frac{\partial h_{STC_4}}{\partial v_k} & \frac{\partial h_{STC_4}}{\partial \alpha} & \frac{\partial h_{STC_4}}{\partial V_{DC}} & \frac{\partial h_{STC_4}}{\partial k} & \frac{\partial h_{STC_4}}{\partial i} & \frac{\partial h_{STC_4}}{\partial \theta} & 0 \\ \frac{\partial h_{STC_5}}{\partial \delta_k} & \frac{\partial h_{STC_5}}{\partial v_k} & \frac{\partial h_{STC_5}}{\partial \alpha} & \frac{\partial h_{STC_5}}{\partial V_{DC}} & \frac{\partial h_{STC_5}}{\partial k} & \frac{\partial h_{STC_5}}{\partial i} & \frac{\partial h_{STC_5}}{\partial \theta} & 0 \\ 0 & 0 & 0 & 0 & 0 & \frac{\partial \phi_{STC_1}}{\partial i} & 0 & \frac{\partial \phi_{STC_1}}{\partial v_b} \end{bmatrix}, \quad (3.92)$$

where

$$p_G = -v_k i \cos(\delta_k - \theta) \quad (3.93)$$
$$q_G = -v_k i \sin(\delta_k - \theta). \quad (3.94)$$

Initialization The process for initializing this device is based on the UWPFLOW source code [Canizares and Alvarado, 1999]:

$$i^{(0)} = \left| \frac{v_c^{(0)} - v_{ref}}{x_{sl}} \right| \tag{3.95}$$

$$\theta^{(0)} = \begin{cases} \delta_k^{(0)} + \frac{\pi}{2}, & \frac{v_c^{(0)} - v_{ref}}{x_{sl}} \leqslant 0 \\ \delta_k^{(0)} - \frac{\pi}{2}, & \frac{v_c^{(0)} - v_{ref}}{x_{sl}} > 0 \end{cases} \tag{3.96}$$

$$\alpha^{(0)} = \delta_k^{(0)} \tag{3.97}$$

$$V_{DC}^{(0)} = V_{DC,ref} \tag{3.98}$$

$$q_G^{(0)} = v_k^{(0)} i^{(0)} \sin\left(\delta_k^{(0)} - \theta^{(0)}\right) \tag{3.99}$$

$$p_G^{(0)} = g_c \left(V_{DC}^{(0)}\right)^2 + r_t \left(i^{(0)}\right)^2 \tag{3.100}$$

$$K^{(0)} = \frac{1}{V_{DC}^{(0)}} \left(\frac{q_G^{(0)}}{v_k^{(0)} b_t} + v_k^{(0)} \right) . \tag{3.101}$$

3.6.7 Fixed-Speed Wind Generator

The steady state model of the FSWG is very similar to the induction machine, in fact, this wind generator is an induction machine *powered* by a wind turbine. The steady state equations presented in Section 2.2.6.2 are included in the power flow study as

$$\Delta p_k = p_G + p_{G,k} - p_{L,k} - p_k = 0 \tag{3.102}$$

$$\Delta q_k = q_G + q_{G,k} - q_{L,k} - q_k = 0 \tag{3.103}$$

$$h_{FSWG_1} = p_c + p_W = 0 \tag{3.104}$$

$$\begin{bmatrix} \Delta p_k \\ \Delta q_k \\ h_{FSWG_1} \end{bmatrix}^{(i)} = - \begin{bmatrix} \frac{\partial \Delta p_k}{\partial \delta_k} & \frac{\partial \Delta p_k}{\partial v_k} & \frac{\partial \Delta p_k}{\partial \omega_m} & \frac{\partial \Delta p_k}{\partial \Delta f} \\ \frac{\partial \Delta q_k}{\partial \delta_k} & \frac{\partial \Delta q_k}{\partial v_k} & \frac{\partial \Delta q_k}{\partial \omega_m} & \frac{\partial \Delta q_k}{\partial \Delta f} \\ 0 & \frac{\partial h_{FSWG_1}}{\partial v_k} & \frac{\partial h_{FSWG_1}}{\partial \omega_m} & \frac{\partial h_{FSWG_1}}{\partial \Delta f} \end{bmatrix}^{(i)} \begin{bmatrix} \Delta \delta_k \\ \Delta v_k \\ \Delta \omega_m \\ \Delta \Delta f \end{bmatrix}^{(i)} , \tag{3.105}$$

where

$$p_g = -{v_k}^2 g_{eq} \tag{3.106}$$

$$q_g = -{v_k}^2 (-b_{eq}) \tag{3.107}$$

$$p_c = (v_k y_{eq} z_{mr})^2 r_r \frac{1-s}{s}\,. \tag{3.108}$$

p_W is computed by using Eq. (2.43).

Initialization As proposed in [Divya and Rao, 2006; Castro et al., 2011], the FSWG is initialized in the following way:

$$\omega_m^{(0)} = 1 - \frac{s_{nom}}{2}\,, \tag{3.109}$$

where s_{nom} is the slip corresponding to the rated speed of the generator. This parameter is given by the manufacturer.

3.6.8 DFIG-based Wind Generator

The mathematical modeling of a DFIG-based wind generator was addressed in Section 2.2.6.4. The equations to include in a power flow study are

$$\Delta p_k = p_G + p_{G,k} - p_{L,k} - p_k = 0 \tag{3.110}$$

$$\Delta q_k = q_G + q_{G,k} - q_{L,k} - q_k = 0 \tag{3.111}$$

$$h_{DF_1} = p_W + p_{mr}\,(1-s) = 0 \tag{3.112}$$

$$h_{DF_2} = v_c - v_{ref} + x_{sl} q_G - v_a + v_b = 0 \tag{3.113}$$

$$h_{DF_3} = q_{ck} = 0 \tag{3.114}$$

$$h_{DF_4} = p_{ck} + p_{rot} = 0 \tag{3.115}$$

$$h_{DF_5} = p_{mk} + p_{mr} = 0 \tag{3.116}$$

$$h_{DF_6} = q_{mk} + q_{mm} + q_{mr} = 0 \tag{3.117}$$

$$\phi_{DF_1} = \sqrt{v_a^2 + \left(q_G - q_G^{min}\right)^2} - \left(v_a + \left(q_G - q_G^{min}\right)\right) = 0 \tag{3.118}$$

$$\phi_{DF_2} = \sqrt{v_b^2 + \left(q_G^{max} - q_G\right)^2} - \left(v_b + \left(q_G^{max} - q_G\right)\right) = 0 \tag{3.119}$$

$$\phi_{DF_3} = \sqrt{\beta^2 + \left(p_{ref} - p_G\right)^2} - \left(\beta + \left(p_{ref} - p_G\right)\right) = 0 \tag{3.120}$$

$$\phi_{DF_4} = \sqrt{p_{G_b}^2 + \left(p_G^{max} - p_{ref}\right)^2} - \left(p_{G_b} + \left(p_G^{max} - p_{ref}\right)\right) = 0 \tag{3.121}$$

$$
\begin{bmatrix}
\Delta p_k \\ \Delta q_k \\ h_{DF_1} \\ h_{DF_2} \\ h_{DF_3} \\ h_{DF_4} \\ h_{DF_5} \\ h_{DF_6} \\ \phi_{DF_1} \\ \phi_{DF_2} \\ \phi_{DF_3} \\ \phi_{DF_4}
\end{bmatrix}^{(i)}
=
-
\begin{bmatrix}
\frac{\partial \Delta p_k}{\partial \delta_k} & \frac{\partial \Delta p_k}{\partial v_k} & 0 & \frac{\partial \Delta p_k}{\partial \delta_m} & \frac{\partial \Delta p_k}{\partial \delta_g} & 0 & \frac{\partial \Delta p_k}{\partial v_m} & \frac{\partial \Delta p_k}{\partial v_g} & 0 & 0 & 0 & 0 & \frac{\partial \Delta p_k}{\partial \Delta f} \\
\frac{\partial \Delta q_k}{\partial \delta_k} & \frac{\partial \Delta q_k}{\partial v_k} & 0 & \frac{\partial \Delta q_k}{\partial \delta_m} & \frac{\partial \Delta q_k}{\partial \delta_g} & 0 & \frac{\partial \Delta q_k}{\partial v_m} & \frac{\partial \Delta q_k}{\partial v_g} & 0 & 0 & 0 & 0 & \frac{\partial \Delta q_k}{\partial \Delta f} \\
0 & 0 & 0 & \frac{\partial h_{DF_1}}{\partial \delta_m} & 0 & \frac{\partial h_{DF_1}}{\partial \delta_r} & \frac{\partial h_{DF_1}}{\partial v_m} & 0 & \frac{\partial h_{DF_1}}{\partial v_r} & 0 & 0 & \frac{\partial h_{DF_1}}{\partial \beta} & \frac{\partial h_{DF_1}}{\partial \Delta f} \\
\frac{\partial h_{DF_2}}{\partial \delta_k} & \frac{\partial h_{DF_2}}{\partial v_k} & \frac{\partial h_{DF_2}}{\partial v_c} & \frac{\partial h_{DF_2}}{\partial \delta_m} & \frac{\partial h_{DF_2}}{\partial \delta_g} & 0 & \frac{\partial h_{DF_2}}{\partial v_m} & \frac{\partial h_{DF_2}}{\partial v_g} & 0 & \frac{\partial h_{DF_2}}{\partial v_a} & \frac{\partial h_{DF_2}}{\partial v_b} & 0 & 0 \\
\frac{\partial h_{DF_3}}{\partial \delta_k} & \frac{\partial h_{DF_3}}{\partial v_k} & 0 & 0 & \frac{\partial h_{DF_3}}{\partial \delta_g} & 0 & 0 & \frac{\partial h_{DF_3}}{\partial v_g} & 0 & 0 & 0 & 0 & 0 \\
\frac{\partial h_{DF_4}}{\partial \delta_k} & \frac{\partial h_{DF_4}}{\partial v_k} & 0 & \frac{\partial h_{DF_4}}{\partial \delta_m} & \frac{\partial h_{DF_4}}{\partial \delta_g} & \frac{\partial h_{DF_4}}{\partial \delta_r} & \frac{\partial h_{DF_4}}{\partial v_m} & \frac{\partial h_{DF_4}}{\partial v_g} & \frac{\partial h_{DF_4}}{\partial v_r} & 0 & 0 & 0 & 0 \\
\frac{\partial h_{DF_5}}{\partial \delta_k} & \frac{\partial h_{DF_5}}{\partial v_k} & 0 & \frac{\partial h_{DF_5}}{\partial \delta_m} & 0 & \frac{\partial h_{DF_5}}{\partial \delta_r} & \frac{\partial h_{DF_5}}{\partial v_m} & 0 & \frac{\partial h_{DF_5}}{\partial v_r} & 0 & 0 & 0 & 0 \\
\frac{\partial h_{DF_6}}{\partial \delta_k} & \frac{\partial h_{DF_6}}{\partial v_k} & 0 & \frac{\partial h_{DF_6}}{\partial \delta_m} & 0 & \frac{\partial h_{DF_6}}{\partial \delta_r} & \frac{\partial h_{DF_6}}{\partial v_m} & 0 & \frac{\partial h_{DF_6}}{\partial v_r} & 0 & 0 & 0 & 0 \\
\frac{\partial \phi_{DF_1}}{\partial \delta_k} & \frac{\partial \phi_{DF_1}}{\partial v_k} & 0 & \frac{\partial \phi_{DF_1}}{\partial \delta_m} & \frac{\partial \phi_{DF_1}}{\partial \delta_g} & 0 & \frac{\partial \phi_{DF_1}}{\partial v_m} & \frac{\partial \phi_{DF_1}}{\partial v_g} & 0 & \frac{\partial \phi_{DF_1}}{\partial v_a} & 0 & 0 & 0 \\
\frac{\partial \phi_{DF_2}}{\partial \delta_k} & \frac{\partial \phi_{DF_2}}{\partial v_k} & 0 & \frac{\partial \phi_{DF_2}}{\partial \delta_m} & \frac{\partial \phi_{DF_2}}{\partial \delta_g} & 0 & \frac{\partial \phi_{DF_2}}{\partial v_m} & \frac{\partial \phi_{DF_2}}{\partial v_g} & 0 & 0 & \frac{\partial \phi_{DF_2}}{\partial v_b} & 0 & 0 \\
\frac{\partial \phi_{DF_3}}{\partial \delta_k} & \frac{\partial \phi_{DF_3}}{\partial v_k} & 0 & \frac{\partial \phi_{DF_3}}{\partial \delta_m} & \frac{\partial \phi_{DF_3}}{\partial \delta_g} & 0 & \frac{\partial \phi_{DF_3}}{\partial v_m} & \frac{\partial \phi_{DF_3}}{\partial v_g} & 0 & 0 & 0 & \frac{\partial \phi_{DF_3}}{\partial \beta} & \frac{\partial \phi_{DF_3}}{\partial \Delta f} \\
0 & 0 & 0 & 0 & 0 & 0 & 0 & 0 & 0 & 0 & 0 & \frac{\partial \phi_{DF_4}}{\partial p_{G_a}} & \frac{\partial \phi_{DF_4}}{\partial \Delta f}
\end{bmatrix}^{(i)}
\begin{bmatrix}
\Delta \delta_k \\ \Delta v_k \\ \Delta v_c \\ \Delta \delta_m \\ \Delta \delta_g \\ \Delta \delta_r \\ \Delta v_m \\ \Delta v_g \\ \Delta v_r \\ \Delta v_a \\ \Delta v_b \\ \Delta \beta \\ \Delta p_{G_a} \\ \Delta \Delta f
\end{bmatrix}^{(i)}
\tag{3.122}
$$

where

$$p_G = -(p_{km} + p_{kc}) \tag{3.123}$$

$$q_G = -(q_{km} + q_{kc}) \tag{3.124}$$

$$p_{ref} = p_G^{max}(1-\eta) - \frac{1}{R}\Delta f - p_{G_b}\,. \tag{3.125}$$

A special discussion below is necessary for understanding these power flow equations.

- Eq. (3.113) is used to control the voltage magnitude of bus c. This remote bus could be the high-voltage side of the step-down transformer or the common coupling point bus. This control law is constrained by the complementarity functions stated in Eqs. (3.118) and (3.119).
- On the other hand, concerning active power, the proposed deloading control is able to spill η percentage of wind power in order to support future active power imbalances. In this case, Eqs. (3.120) and (3.121) work as follows:
  - When computing the base case without distributed slack (i.e. $\Delta f = 0$), if $p_G \leqslant p_{ref} = p_G^{max}(1-\eta)$, then the wind turbine cannot spill wind, which implies $\beta = 0$.

    In case $p_G > p_{ref}$, the wind generator is able to spill wind, $\beta > 0$ and $p_G = p_{ref} = p_G^{max}(1-\eta)$, which means that the wind generator is deloaded.
  - Now with the base case computed, wind generators that were deloaded will support active power imbalances by $p_G = p_G^{max}(1-\eta) - \frac{1}{R}\Delta f - p_{G_b}$, until wind generator reaches its active power rating: $p_G \leqslant p_G^{max}$, and thereby $p_{G_b} > 0$.

Initialization The proposed initialization is obtained by assuming the following steps.

1. Firstly, the optimal angular speed is found by using Eq. (2.48); this optimal speed must be within bounds:

$$\beta^{(0)} = 0 \tag{3.126}$$

$$\omega_m^{(0)} = \begin{cases} \omega_m^{max}, & \omega_{m,opt} \geqslant \omega_m^{max} \\ \omega_{m,opt}, & \omega_m^{min} < \omega_{m,opt} < \omega_m^{max} \\ \omega_m^{min}, & \omega_{m,opt} \leqslant \omega_m^{min} \end{cases} \tag{3.127}$$

$$s^{(0)} = 1 - \omega_m^{(0)}\,. \tag{3.128}$$

2. RSC, magnetization and GSC voltage magnitudes are supposed to be close to the stator voltage v_k:

$$\frac{v_r}{s}^{(0)} = v_m^{(0)} = v_g^{(0)} = v_k^{(0)} . \tag{3.129}$$

3. By neglecting resistive and core losses, the following power flows can be obtained [Vittal and Ayyanar, 2012]:

$$p_{mr} = -\frac{p_W}{\omega_m^{(0)}} \tag{3.130}$$

$$p_{mk} = -p_{mr} \tag{3.131}$$

$$p_{gk} = -s^{(0)} p_{mk} , \tag{3.132}$$

where p_W is computed by using Eq. (2.43).

4. By using the DC power flow approximation, the voltage angles are then computed as follows:

$$\delta_m^{(0)} = \delta_k^{(0)} + p_{mk} x_s \tag{3.133}$$

$$\delta_g^{(0)} = \delta_k^{(0)} + p_{gk} x_t \tag{3.134}$$

$$\delta_r^{(0)} = \delta_m^{(0)} - p_{mr} x_r . \tag{3.135}$$

5. The set of complementarity variables are initialized to zero:

$$v_a = v_b = p_{G_a} = 0 . \tag{3.136}$$

The presented model has the following differences with respect to [Li, 2013] as mentioned below.

- The proposed model examines three regions of operation: MPPT, wind spillage to maintain power generation in a secure region and deloading action to support future active power imbalances.
- A terminal voltage control is added to provide reactive support within reactive bounds, whereas [Li, 2013] proposed a fixed reactive generation.
- By using the initialization process described before, the NR method needs at least two iterations less than the method described in those references.
- Lastly, the model is solved in a unified way as opposed to the sequential solution described in such references.

3.6.9 PMSG-based Wind Generator

Lastly, this section presents the set of algebraic equations suitable for power flow analysis considering PMSG-based wind generators. The mathematical formulation of this model was discussed in Section 2.2.6.5. By considering a PMSG-based wind generator embedded at bus k, the power flow equations are

$$\Delta p_k = p_G + p_{G,k} - p_{L,k} - p_k = 0 \tag{3.137}$$

$$\Delta q_k = q_G + q_{G,k} - q_{L,k} - q_k = 0 \tag{3.138}$$

$$h_{PM_1} = p_W - p_{gr} = 0 \tag{3.139}$$

$$h_{PM_2} = q_{rg} - \alpha(p_{rg}) = 0 \tag{3.140}$$

$$h_{PM_3} = p_{rg} + p_{ik} = 0 \tag{3.141}$$

$$h_{PM_4} = v_c - v_{ref} + x_{sl} q_G - v_a + v_b = 0 \tag{3.142}$$

$$\phi_{PM_1} = \sqrt{v_a^2 + \left(q_G - q_G^{min}\right)^2} - \left(v_a + \left(q_G - q_G^{min}\right)\right) = 0 \tag{3.143}$$

$$\phi_{PM_2} = \sqrt{v_b^2 + \left(q_G^{max} - q_G\right)^2} - \left(v_b + \left(q_G^{max} - q_G\right)\right) = 0 \tag{3.144}$$

$$\phi_{PM_3} = \sqrt{\beta^2 + \left(p_{ref} - p_G\right)^2} - \left(\beta + \left(p_{ref} - p_G\right)\right) = 0 \tag{3.145}$$

$$\phi_{PM_4} = \sqrt{p_{G_b}^2 + \left(p_G^{max} - p_{ref}\right)^2} - \left(p_{G_b} + \left(p_G^{max} - p_{ref}\right)\right) = 0 \tag{3.146}$$

$$
\begin{bmatrix}
\Delta p_k \\
\Delta q_k \\
h_{PM_1} \\
h_{PM_2} \\
h_{PM_3} \\
h_{PM_4} \\
\phi_{PM_1} \\
\phi_{PM_2} \\
\phi_{PM_3} \\
\phi_{PM_4}
\end{bmatrix}^{(i)}
=
-
\begin{bmatrix}
\frac{\partial \Delta p_k}{\partial \delta_k} & \frac{\partial \Delta p_k}{\partial v_k} & 0 & 0 & \frac{\partial \Delta p_k}{\partial \delta_i} & 0 & \frac{\partial \Delta p_k}{\partial v_i} & 0 & 0 & 0 & \frac{\partial \Delta p_k}{\partial \Delta f} \\
\frac{\partial \Delta q_k}{\partial \delta_k} & \frac{\partial \Delta q_k}{\partial v_k} & 0 & 0 & \frac{\partial \Delta q_k}{\partial \delta_i} & 0 & \frac{\partial \Delta q_k}{\partial v_i} & 0 & 0 & 0 & \frac{\partial \Delta q_k}{\partial \Delta f} \\
0 & 0 & 0 & \frac{\partial h_{PM_1}}{\partial \delta_r} & 0 & \frac{\partial h_{PM_1}}{\partial v_r} & 0 & 0 & 0 & \frac{\partial h_{PM_1}}{\partial \beta} & 0 \\
0 & 0 & 0 & \frac{\partial h_{PM_2}}{\partial \delta_r} & 0 & \frac{\partial h_{PM_2}}{\partial v_r} & 0 & 0 & 0 & 0 & 0 \\
\frac{\partial h_{PM_3}}{\partial \delta_k} & \frac{\partial h_{PM_3}}{\partial v_k} & 0 & \frac{\partial h_{PM_3}}{\partial \delta_r} & \frac{\partial h_{PM_3}}{\partial \delta_i} & \frac{\partial h_{PM_3}}{\partial v_r} & \frac{\partial h_{PM_3}}{\partial v_i} & 0 & 0 & 0 & 0 \\
\frac{\partial h_{PM_4}}{\partial \delta_k} & \frac{\partial h_{PM_4}}{\partial v_k} & \frac{\partial h_{PM_4}}{\partial v_c} & 0 & \frac{\partial h_{PM_4}}{\partial \delta_i} & 0 & \frac{\partial h_{PM_4}}{\partial v_i} & \frac{\partial h_{PM_4}}{\partial v_a} & \frac{\partial h_{PM_4}}{\partial v_b} & 0 & 0 \\
\frac{\partial \phi_{PM_1}}{\partial \delta_k} & \frac{\partial \phi_{PM_1}}{\partial v_k} & 0 & 0 & \frac{\partial \phi_{PM_1}}{\partial \delta_i} & 0 & \frac{\partial \phi_{PM_1}}{\partial v_i} & \frac{\partial \phi_{PM_1}}{\partial v_a} & 0 & 0 & 0 \\
\frac{\partial \phi_{PM_2}}{\partial \delta_k} & \frac{\partial \phi_{PM_2}}{\partial v_k} & 0 & 0 & \frac{\partial \phi_{PM_2}}{\partial \delta_i} & 0 & \frac{\partial \phi_{PM_2}}{\partial v_i} & 0 & \frac{\partial \phi_{PM_2}}{\partial v_b} & 0 & 0 \\
\frac{\partial \phi_{PM_3}}{\partial \delta_k} & \frac{\partial \phi_{PM_3}}{\partial v_k} & 0 & 0 & \frac{\partial \phi_{PM_3}}{\partial \delta_i} & 0 & \frac{\partial \phi_{PM_3}}{\partial v_i} & 0 & 0 & \frac{\partial \phi_{PM_3}}{\partial \beta} & \frac{\partial \phi_{PM_3}}{\partial p_{G_a}} \\
0 & 0 & 0 & 0 & 0 & 0 & 0 & 0 & 0 & \frac{\partial \phi_{PM_4}}{\partial \beta} & \frac{\partial \phi_{PM_4}}{\partial p_{G_a}}
\end{bmatrix}^{(i)}
\begin{bmatrix}
\Delta \delta_k \\
\Delta v_k \\
\Delta v_c \\
\Delta \delta_r \\
\Delta \delta_i \\
\Delta v_r \\
\Delta v_i \\
\Delta v_a \\
\Delta v_b \\
\Delta \beta \\
\Delta p_{G_a} \\
\Delta \Delta f
\end{bmatrix}^{(i)}
, \tag{3.147}
$$

where

$$p_G = -p_{ki} \tag{3.148}$$

$$q_G = -q_{ki} \tag{3.149}$$

$$p_{ref} = p_G^{max}(1-\eta) - \frac{1}{R}\Delta f - p_{G_b}\,. \tag{3.150}$$

Note that the approach to control the voltage magnitude of bus c and the deloading action is the same as in the DFIG. Wind power p_W as usual is computed by using Eq. (2.43).

Initialization The procedure to initialize the PMSG's state variables is very similar to those of a DFIG.

Firstly, the optimal angular speed is found by using Eq. (2.48):

$$\beta^{(0)} = 0 \tag{3.151}$$

$$\omega_m^{(0)} = \begin{cases} \omega_m^{max}, & \omega_{m,opt} \geqslant \omega_m^{max} \\ \omega_{m,opt}, & \omega_m^{min} < \omega_{m,opt} < \omega_m^{max} \\ \omega_m^{min}, & \omega_{m,opt} \leqslant \omega_m^{min} \end{cases}. \tag{3.152}$$

The mechanical wind power is then computed by means of Eq. (2.43).

By using linear approximations the following voltage initializations can be obtained:

$$\delta_r^{(0)} = \delta_g^{(0)} - p_W \omega_m^{(0)} x_s \tag{3.153}$$

$$v_r^{(0)} = v_g^{(0)} \tag{3.154}$$

$$\delta_i^{(0)} = \delta_k^{(0)} + p_W x_t \tag{3.155}$$

$$v_i^{(0)} = v_k^{(0)}\,, \tag{3.156}$$

where $v_k^{(0)}$ and $\delta_k^{(0)}$ are the initial values of voltage magnitude and angle at bus k, respectively, which should be given as input data or initialized as $v_k = 1$ and $\delta_k = 0$ (i.e. flat start). δ_g is fixed to zero, and $v_g = \omega_m \psi_{pm}$; both are treated as parameters throughout the iterative solution process. The set of complementarity variables are initialized to zero: $v_a = v_b = p_{G_a} = 0$.

As far as the author is concerned, no similar work exists that models the full converter wind generator with such detail for steady state analysis purposes.

3.7 Modeling of Wind Farms

A wind farm is a group of wind generators located in the same geographic area which can be placed onshore or offshore and connected to either a transmission or distribution bus. The radial collector system may connect up to several hundred wind generators which transport their generated power to the point of common coupling (PCC) of the network. In this thesis, all wind generators making up the wind farm are simulated, as shown in Fig. 3
generato
For inst
be appe
in the fu
wind ge
solution

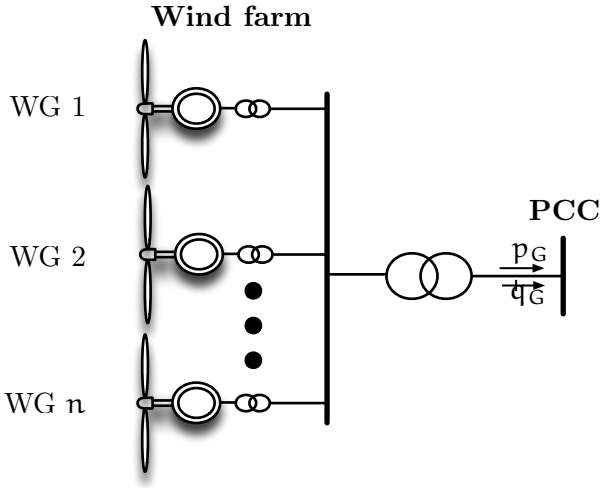

FIGURE 3.1: Schematic diagram of a wind farm equivalent.

3.8 Case Studies

The models shown in this chapter were implemented in a digital computer program. The main implementation is through Python programming language by using C language extensions for number crunching operations (e.g. Jacobian and complementarity constraints' computation). Even by including all the extra state variables that this unified framework considers, in some cases the solver has demonstrated a better computing performance than MATPOWER [Zimmerman et al., 2011] or PSAT [Milano, 2005]. The main reasons for this performance is the low-level programming (where it is needed) and the solution of sparse linear systems by using KLU, which is a state-of-the-art solver specialized in matrices that arise from electrical circuit analysis [Davis and Palamadai Natarajan, 2010].

3.9 Reactive Power Limits Using Complementarity Constraints

In order to evaluate and prove the robustness of the complementarity approach, a set of power flow runs are performed to compare the results of this approach against other limits-handling schemes. Eight test systems are considered: IEEE 14, 30, 57, 118 and 300 bus test systems, as well as one large real network from the Polish system [Zimmerman et al., 2011], and two test systems that represent the size and the complexity of the European Union power system [Fliscounakis et al., 2013]. The number of buses, generators, transmission devices and loads of each test system is shown in Table 3.1.

TABLE 3.1: General structure of the test systems.

Test system	# Buses	# Generators	# Branches	# Loads
IEEE 14	14	5	20	11
IEEE 30	30	6	41	21
IEEE 57	57	7	80	42
IEEE 118	118	54	186	99
IEEE 300	300	69	411	201
Polish 2383	2383	327	2896	1826
EU 2869	2869	510	4582	1491
EU 9241	9241	1445	16049	4895

The experiment design is

1. For each test system to run a power flow by considering two cases below.

Case A Power flow without considering reactive power limits:

$$-\infty \leqslant q_{G,i} \leqslant \infty, \quad \forall i \in \mathcal{G}\,. \tag{3.157}$$

Case B Power flow constraining reactive power limits:

$$q_{G,i}^{\min} \leqslant q_{G,i} \leqslant q_{G,i}^{\max}, \quad \forall i \in \mathcal{G}\,. \tag{3.158}$$

By excluding the reference generator, the rest of the generators in system are constrained to their reactive power limits.

2. In order to test the quality of the final solutions for bus voltage magnitudes, a parameter called voltage quality index (VQI) [Pirnia et al., 2013] is computed for each test system as follows:

$$\mathrm{VQI} = \frac{\sum\limits_{k \in \mathcal{B}_{PQ}} |v_k - v_0|}{|\mathcal{B}_{PQ}|}, \tag{3.159}$$

where $\mathcal{B}_{PQ}$ is the set of buses without embedded generation (load buses), v_0 is the desired bus voltage magnitude of 1.0 pu, and v_k is the converged bus voltage magnitude. Note that a better value of this index means less loss and reactive power flows in the system; thus it is an adequate means for judging the quality of the solution.

3. Every solver is timed since the Newton-Raphson loop starts until the convergence or maximum number of iterations is reached. The execution time is measured as CPU time.

4. Flat start, a newton tolerance of $|\mathbf{g}(\mathbf{y})| \leqslant 1e-9$ and a maximum of 20 iterations were the parameters used for all the solvers.

Four softwares packages are employed to be tested against the complementarity approach.

PSAT[**Milano, 2005**] The power flow solver in this Matlab toolbox is able to constrain reactive power limits by checking those at a prescribed iteration; the second iteration was considered in the simulations.

MATPOWER[**Zimmerman et al., 2011**] In this case, the limits handling on this Matlab software is rather different: the limits are checked by the end of the power flow solution. If a generator has reached one limit, it is changed to a *PQ bus* and the power flow problem is solved again. This process is performed until no generator has violated limits. It the author's opinion this is an expensive and inefficient algorithm, computationally speaking.

FACTS[**Fuerte-Esquivel and Acha, 1997**] This power system analysis program is coded under the C++ programming language. The low-level programming and the use of the object oriented programming paradigm make the program easy to modify conserving fast computing times. The software changes the type of bus k from *PV* to a *PQ bus* if $\Delta p_k \leqslant 1e-3$ and $q_{G,k} > q_{G,k}^{max}$ or $q_{G,k} < q_{G,k}^{min}$. Note that this algorithm is more robust for two reasons: the limits are checked *on the fly* which means that it is not necessary to obtain the final solution, and, conversely to PSAT, the directive to check limits is based on the convergence of the active power mismatch of the *PV buses*. To avoid oscillatory convergence, the number of type changes is limited to two for each *PV bus*.

PSS/E This commercial software is able to constrain reactive power limits. The default mode to apply reactive power limits was used. Under this default mode, the reactive power limits are ignored until the greatest reactive power mismatch has been reduced to a preset multiple of the mismatch convergence tolerance. The program operation manual does not indicate which is the multiple used or how to modify it.

For the sake of easy identification, the coded program that uses the complementarity approach and incorporates all the steady state models described before will be called SANPOWER hereinafter.

TABLE 3.2: Details of the software and hardware employed in the power flow runs.

Description	SANPOWER	MATPOWER	PSAT	FACTS	PSS/E
Programming language	Python/C	Matlab	Matlab	C++	-
Interpreter/compiler	2.7.10/LLVM 6.1.0	r2013A	r2013A	LLVM 6.1.0	-
RAM memory	4 Gb				
Cores/clock speed	4/1.7 GHz				
Operating system	OS X 10.10.4				Windows XP

Details about the programming languages, compilers and hardware resources used in the simulations are reported in Table 3.2.

TABLE 3.3: VQI indices for Case A.

Testy System	SANPOWER	MATPOWER	PSAT	FACTS	PSS/E
IEEE 14	0.0448	0.0448	0.0448	0.0448	0.0448
IEEE 30	0.0261	0.0261	0.0261	0.0261	0.0261
IEEE 57	0.0247	0.0247	0.0247	0.0247	0.0247
IEEE 118	0.0225	0.0225	0.0225	0.0225	0.0225
IEEE 300	0.0235	0.0235	0.0235	0.0235	0.0235
Polish 2383	0.0095	0.0095	0.0095	0.0095	NC
EU 2869	0.0333	0.0333	0.0334	0.0333	0.0333
EU 9241	0.0309	0.0309	0.0309	0.0309	0.0309

Note: "NC" means that solver failed to converge.

Table 3.3 depicts the VQI for all test systems ignoring reactive power limits; observe that VQI is very small in all cases. In fact the VQI index of each system is very similar for all the solvers. The PSS/E failed to converge for the Polish test system.

Table 3.4 shows the VQI indexes now constraining reactive power limits. In this case, the complementarity approach and the FACTS program were the only ones capable of finding the solution for all the test systems. The MATPOWER solver had an oscillatory convergence in the Polish test system, which means that the conversion PV *bus*$\rightleftarrows PQ$ *bus* never ended. Furthermore, MATPOWER is constraining reactive power limits of the slack generator; thus, the VQI index differs from the rest of the solvers. Concerning the PSAT software, the solver exhibited strange behavior solving the Polish test system where the solver never checked reactive power limits. While the purpose of this work

Table 3.4: VQI indices for Case B.

Testy System	SANPOWER	MATPOWER	PSAT	FACTS	PSS/E
IEEE 14	0.0448	0.0453	0.0448	0.0448	0.0448
IEEE 30	0.0258	0.0284	0.0261	0.0258	0.0258
IEEE 57	0.0247	0.0247	0.0247	0.0247	0.0247
IEEE 118	0.0222	0.0222	0.0225	0.0222	0.0222
IEEE 300	0.0235	0.0240	NC	0.0235	0.0235
Polish 2383	0.0233	NC	0.0095†	0.0238	NC
EU 2869	0.0328	0.0328	NC	0.0328	0.0328
EU 9241	0.0308	0.0308	NC	0.0308	NC

Note: "NC" means that solver failed to converge.
†: Wrong solution. The solver did not check reactive power limits.

is not to modify other software, the results are presented as they were obtained. The FACTS solver successfully converged for all the test systems, but the VQI index of the Polish system is different from the one obtained by SANPOWER. This has two consequences: the obtained equilibrium points are different, and the solution obtained by the FACTS program could be more inefficient, i.e. more loss and reactive power flows. Furthermore, the FACTS solver was limited to two changes of bus type; without this limitation, the program has an oscillatory convergence when solving the Polish and EU 9241 buses' test systems.

Finally, the PSS/E commercial software could not obtain the steady state equilibrium point of the Polish and EU 9241 bus test systems. In both cases, the solver reached the maximum number of iterations, and according to what could be observed, the convergence was oscillatory.

The following Figs. 3.2 to 3.9 show the reactive power generated by selected generators of the analyzed test systems. The figures only show results of converged solutions. For most of the figures, the MATPOWER solution is very different from the rest of the solvers' solutions, because MATPOWER considers reactive power limits of the *slack bus*.

In Fig. 3.3 the reactive power obtained by means of the PSAT solver differs from the rest of the solvers, because the checking limits' step was performed at the second iteration at which the NR method had a large value of error. Under such circumstances, the PSAT anomalously changed some *PV buses* to *PQ buses*.

In regards to Fig. 3.4, the solution is the same for all the solvers. On the other hand, as shown in Fig. 3.5, the PSAT solution is different from the rest. Again the iteration-based limit checking scheme of PSAT fixes some generators at their limits when in fact they have not yet been violated.

By excluding the MATPOWER solution, the solution obtained by means of the SANPOWER, FACTS and PSS/E programs is the same for the IEEE 300 bus test system, as shown in Fig. 3.6.

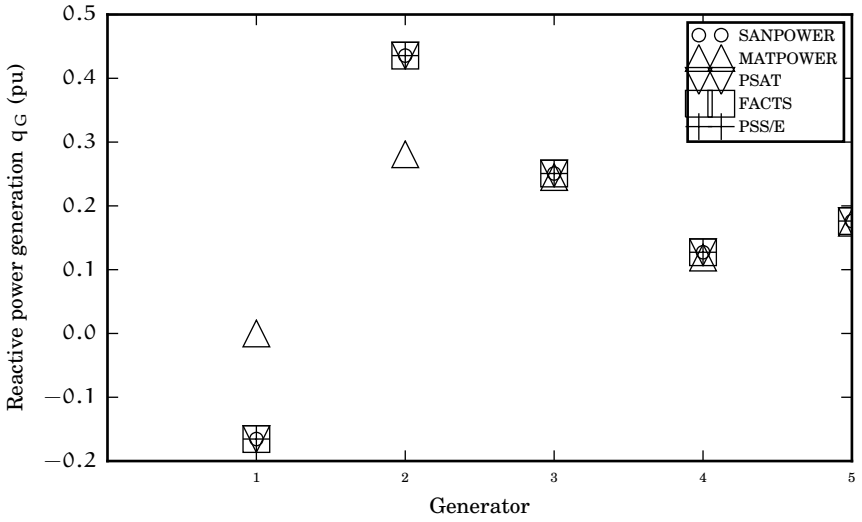

FIGURE 3.2: Reactive power generation of the IEEE 14 bus test system considering reactive power limits.

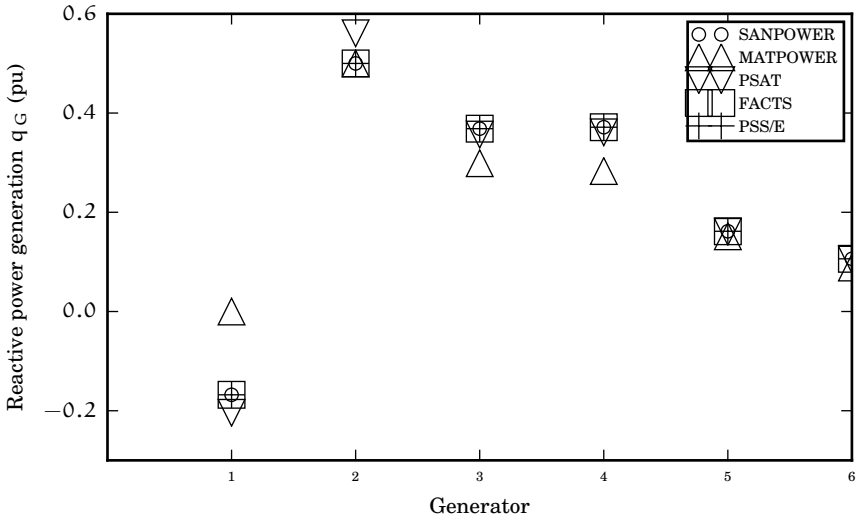

FIGURE 3.3: Reactive power generation of the IEEE 30 bus test system considering reactive power limits.

Fig. 3.7 shows the reactive power generation obtained by SANPOWER, PSAT and FACTS solvers for the Polish test system. For some unusual reason, PSAT did not check limits when solving this system; hence, the obtained solution is different from the rest.

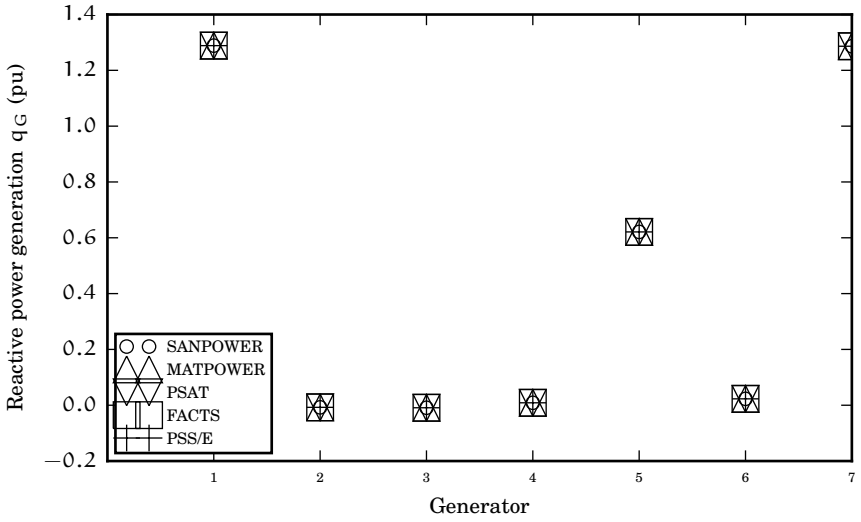

FIGURE 3.4: Reactive power generation of the IEEE 57 bus test system considering reactive power limits.

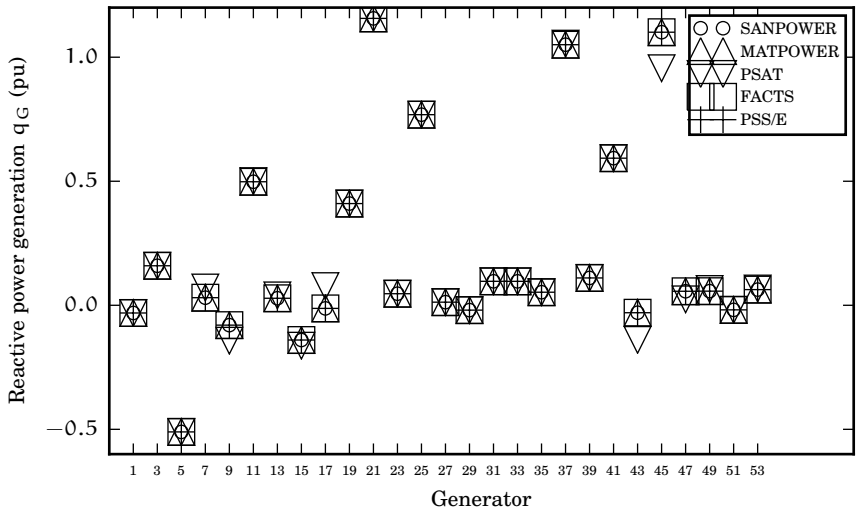

FIGURE 3.5: Reactive power generation of the IEEE 118 bus test system considering reactive power limits.

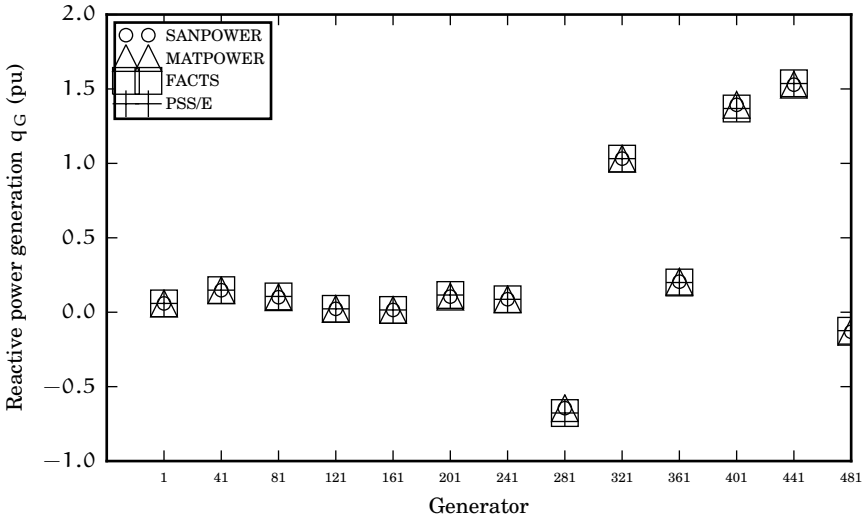

FIGURE 3.8: Reactive power generation of the EU 2869 test system considering reactive power limits.

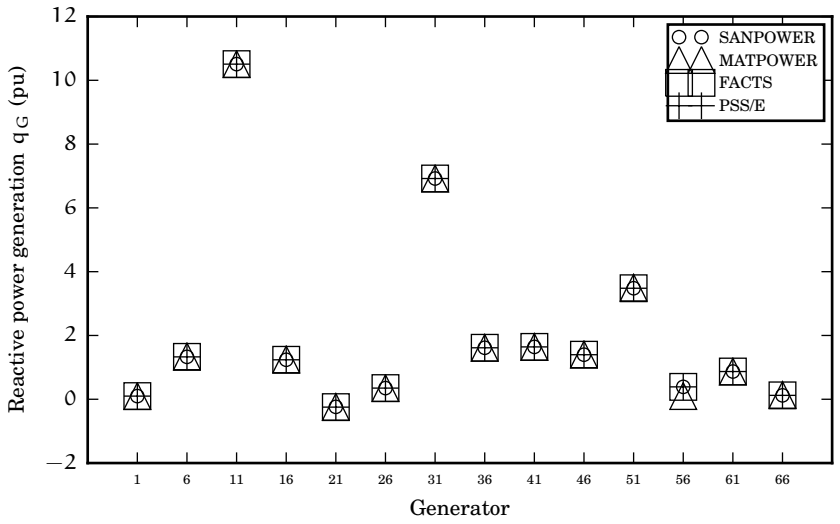

FIGURE 3.6: Reactive power generation of the IEEE 300 test system considering reactive power limits.

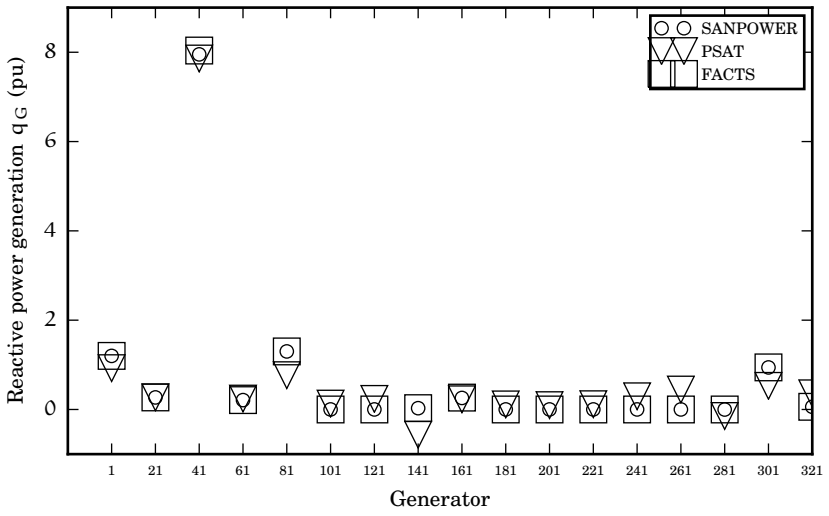

FIGURE 3.7: Reactive power generation of the Polish 2383 test system considering reactive power limits.

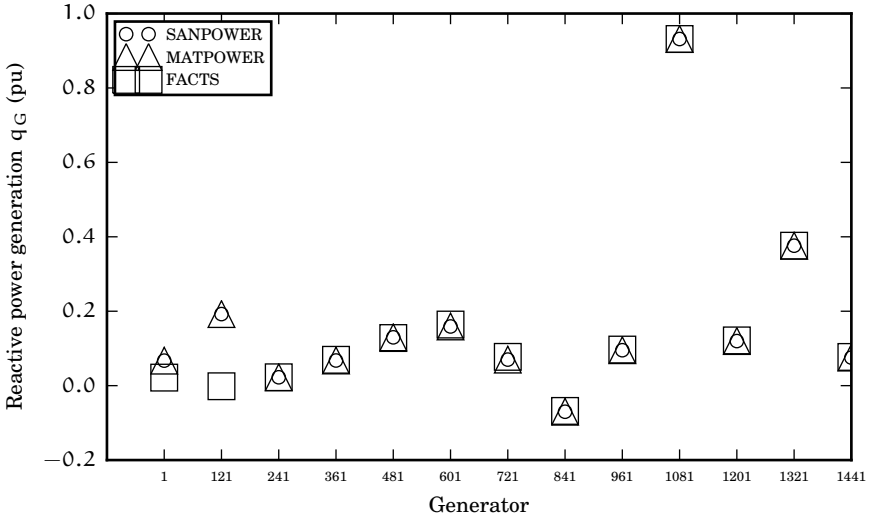

FIGURE 3.9: Reactive power generation of the EU 9241 test system considering reactive power limits.

Finally, Figs. 3.8 and 3.9 show the obtained reactive power solutions of the European Union test systems. With exception of the MATPOWER solutions, the rest of the solvers match very closely.

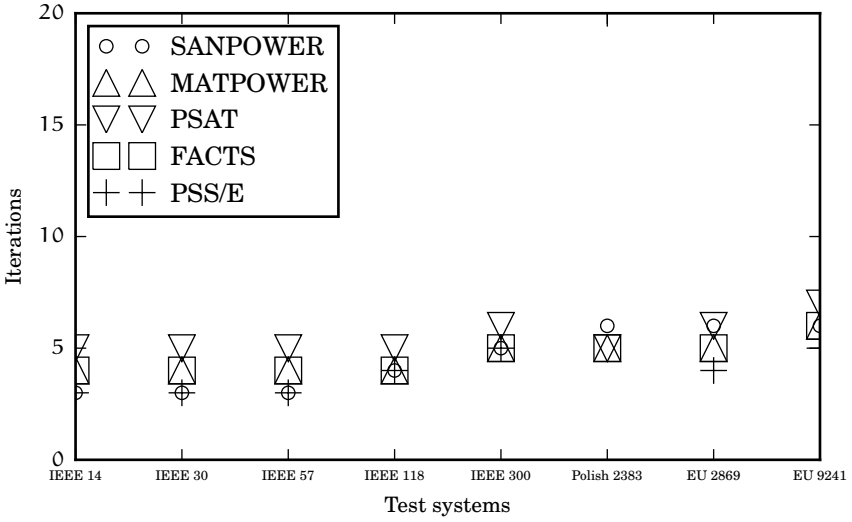

(a) Case A.

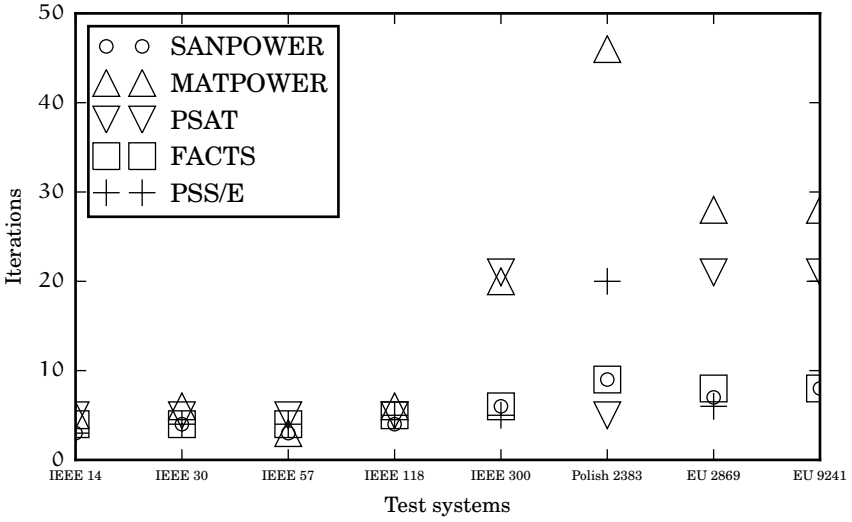

(b) Case B.

FIGURE 3.10: Number of iterations.

Fig. 3.10 depicts the number of iterations needed by the solvers in each test system for both Case A and Case B. Regarding Case A, when no reactive power is fixed, the solvers have almost the same number of iterations. Nevertheless, the PSS/E software reached the maximum number of iterations when *solving* the Polish test system. On the other hand, for Case B, the MATPOWER reached almost 70 iterations; this was because the MATPOWER runs several power flow studies in order to reach the adjusted power flow solution. While the complementarity approach tends to increase by two iterations when

solving the Polish test system, this scheme is more robust by reaching the convergence for all the test systems. Finally, both the FACTS program and the complementarity approach present a small number of iterations for all the test systems.

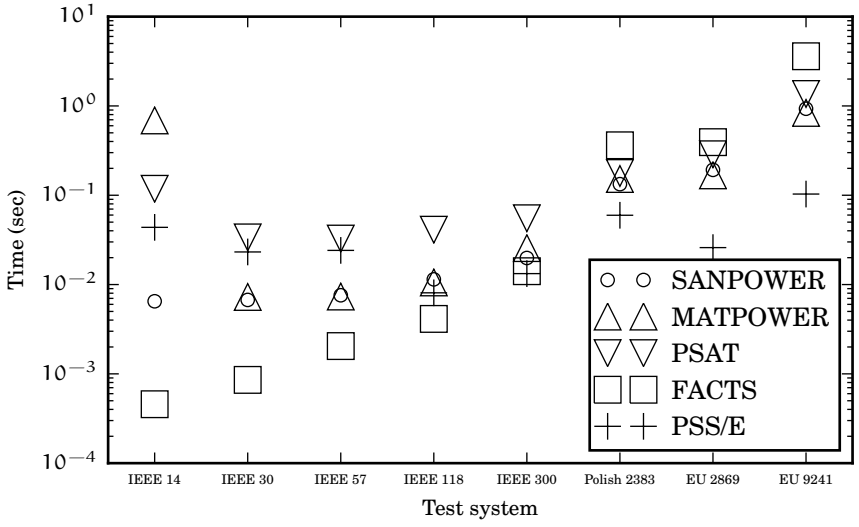

(a) Case A.

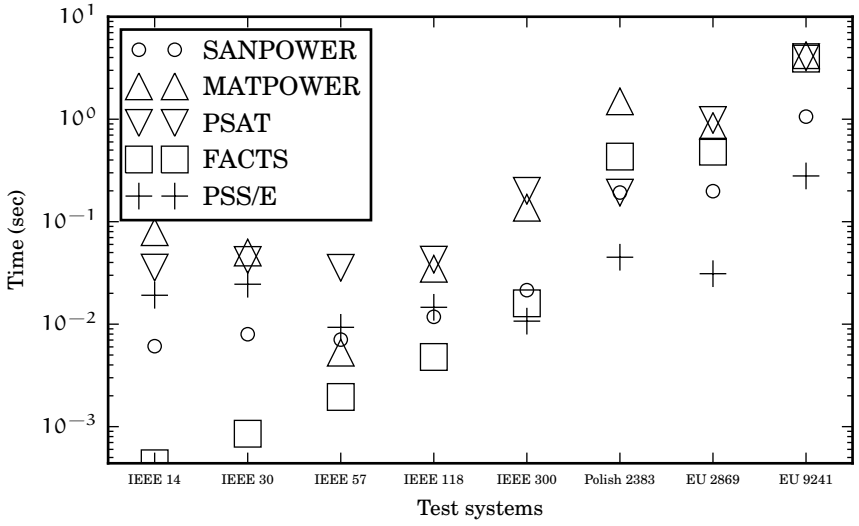

(b) Case B.

FIGURE 3.11: Computing times.

Now Fig. 3.11 shows both the computing time needed by each power flow solver. Even considering that the coded program is based on an interpreted language, the computing time is competitive with other softwares. The smallest computing times were obtained by the PSS/E commercial software which, according to what was observed on a CPU monitor, uses a parallel computing approach. The MATLAB-based programs have the highest computing times.

3.9.1 Effective Initialization of Complementarity Constraints

For the purpose of comparing the employed complementarity approach with the one proposed in [Sundaresh and Nagendra Rao, 2014], this section assesses the convergence characteristic of constrained power flows with and without a proper initialization.

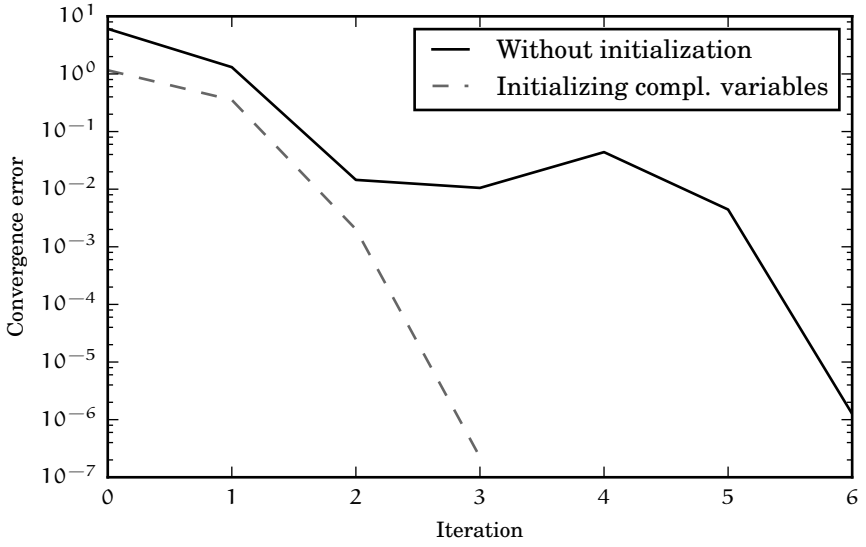

FIGURE 3.12: Convergence characteristics of the IEEE 14 bus test system.

Fig. 3.12 shows the convergence characteristics of the IEEE 118 bus test system both with and without initialization of the complementarity variables. In this case the number of iterations is reduced by two.

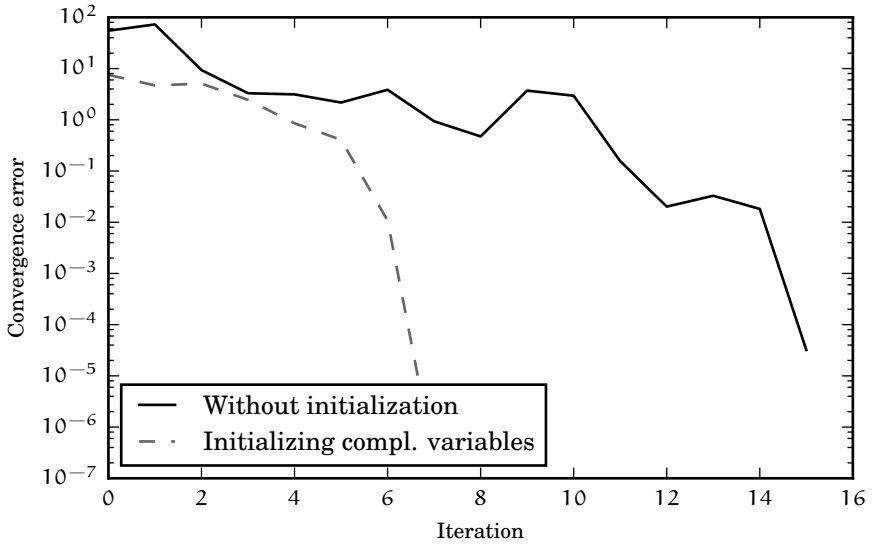

FIGURE 3.13: Convergence characteristics of the EU 9241 bus test system.

Fig. 3.13, now, shows the same curves but for the EU 9241 bus test system. Using a proper initialization, the systems converge in 11 iterations, counter to the 15 iterations needed without initialization. These two results show that an enhanced initialization of the complementarity variables reduces the number of iterations and thereby the computation burden.

Finally, the author considers it necessary to mention the principal differences between the proposed approach and the one reported in [Sundaresh and Nagendra Rao, 2014] below.

- The described scheme is able to handle several generators connected to the same bus, which are automatically dispatched or constrained to independent reactive power levels.
- The synchronous generators can control either a local or a remote bus voltage magnitude.
- A voltage droop χ_{sl} or the fictional reactance χ_{mq} can be considered to ensure the proper sharing of the reactive power produced by several generators connected to the same bus [Cutsem and Vournas, 2007].
- The employed approach includes a proper initialization step that enhances the convergence characteristic.

3.10 Wind Response

An assessment of wind production under different wind speeds is presented in this section. Three types of wind generators are considered: FSWG, DFIG and PMSG. The test system is a small 2-bus system (Fig. 3.14): one bus has an embedded reference generator, and the other bus serves to connect the different wind generators (one-by-one).

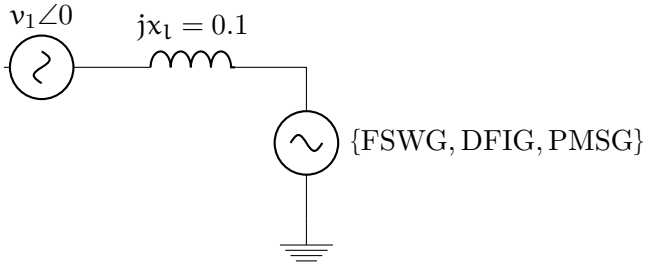

FIGURE 3.14: Two bus test system.

For each wind speed value, from 0 to 25 m/s with a resolution of 1 m/s, a power flow was solved by obtaining the operative states under such a wind condition. For each

wind speed value, the optimal mechanical angular speed $\omega_{m,opt}$ at which maximum wind power is extracted was computed for both DFIG and PMSG.

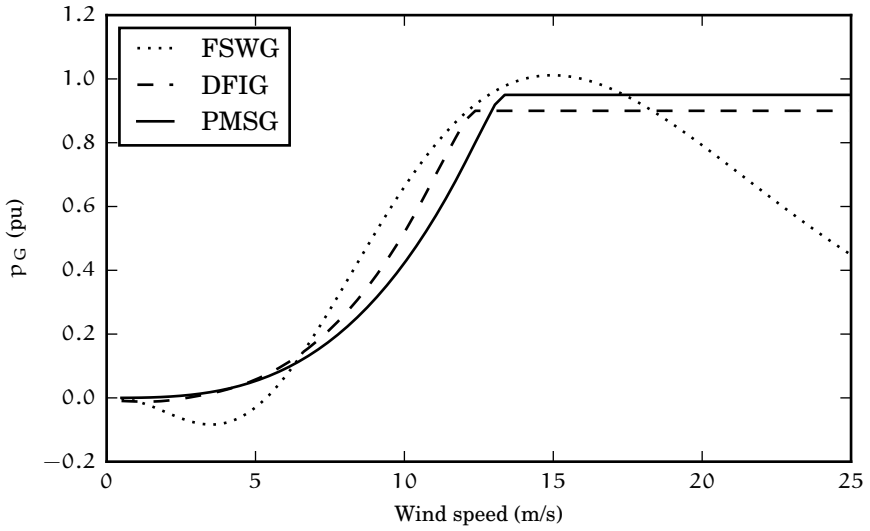

FIGURE 3.15: Active power output of wind generators.

Fig. 3.15 shows the active power output of each type of wind generation. Since the FSWG cannot have a MPPT control, it has the worst wind generation at low wind speeds. Furthermore, with high wind the passive stall control inherently reduces the active power generation. On the other hand, variable-speed wind generators (DFIG and PMSG) produce the maximum amount of wind power until their ratings are reached. The difference between DIFG and PMSG active power curves is because each one has different coefficients in the performance function (Eq. (2.44a)). Clearly, this behavior agrees with the aerodynamics stated in Section 2.2.6.1.

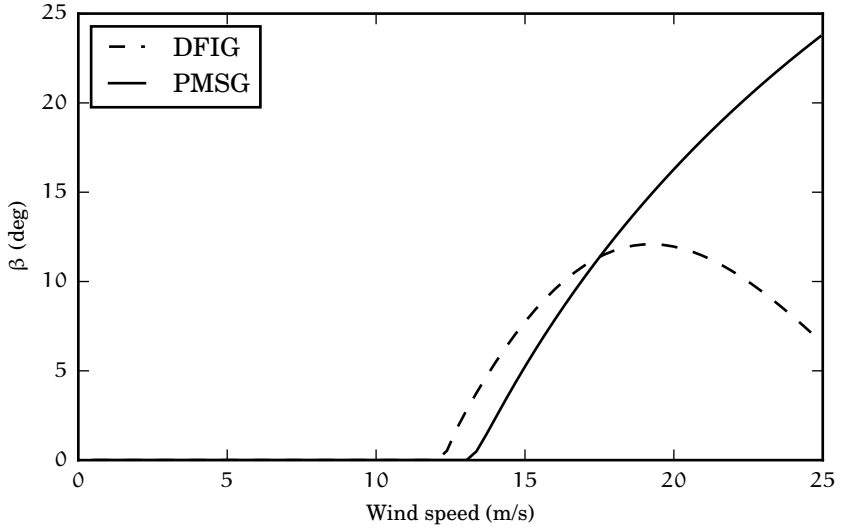

FIGURE 3.16: Pitch angle of variable speed wind generators.

Next Fig. 3.16 shows the pitch angle variation under different wind speed values. Note that the angle increases as soon as the active power generation reaches the rating, which means that wind turbines start to spill wind thus reducing the mechanical input power.

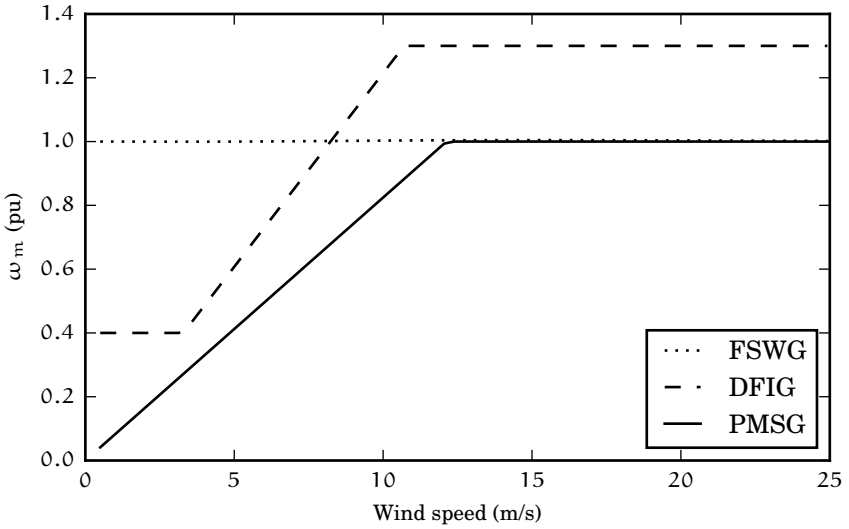

FIGURE 3.17: Mechanical angular speed.

Now the dynamics of the mechanical angular speed under different wind speeds are depicted in Fig. 3.17. In this case, DFIG and PMSG wind generators always extract the maximum wind power by modulating the mechanical angular speed while is inbounds, i.e. $\omega_m^{min} \leqslant \omega_{m,opt} \leqslant \omega_m^{max}$, or else this angular speed is fixed at its maximum or minimum value.

While these curves represent the wind power behavior and agree with the traditional curves reported in the literature [Vittal and Ayyanar, 2012; Lubosny, 2010; Pardalos et al., 2014], there is a lack that must be attended to: the inclusion of the representation of cut-in $v_{W,ci}$ and cut-out $v_{W,co}$ wind speeds. These speeds impose an interval constraint to only generate active power between the necessary wind speed to start moving the rotor shaft (cut-in speed) and the maximum secure wind speed (cut-out speed). Studies in this work only consider the following wind speed interval $v_W \in [v_{w,ci}, v_{w,co}]$; hence, cut-in and cut out constraints do not interfere in the steady-state analysis.

Finally, a particular study is presented to show the DFIG's powers response for different slip values.

Fig. 3.18 shows the plots of mechanical (wind) power p_W, output power p_G and RSC power p_{rot} for various values of slips ranging from -0.3 to 0.4 . For the RSC power, negative values mean the power flow is from the rotor to the grid. In the supersynchronous mode of operation, $-0.3 < s < 0$, the RSC power is negative; hence, power is absorbed from the rotor and fed into the grid through the RSC and GSC. For

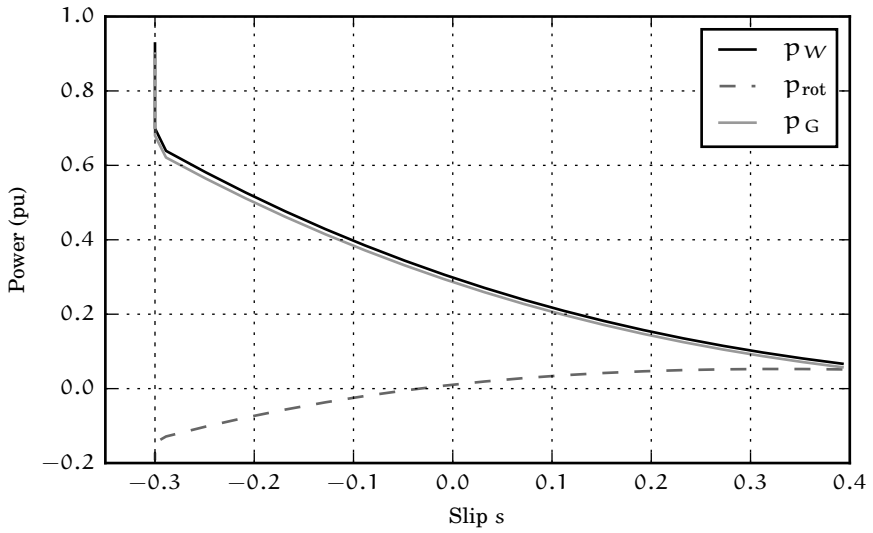

FIGURE 3.18: Mechanical, output and RSC power at different slips, corresponding to maximum power capture from wind.

the sub-synchronous mode of operation, $0 < s < 0.4$, the RSC power is positive; hence, power is absorbed from the grid through GSC and fed into the rotor. It may noted from Fig. 3.18 that because of the small loss in the rotor winding, the transition from negative to positive power in the RSC occurs at $s = -0.01$ instead of exactly at $s = 0$. On the other hand, the overall output power is equal to the mechanical power minus a small value of resistive losses. Lastly, the slip remains constant after $s = -0.3$; this is done to limit the rotational angular speed and operate the DFIG within a safe region.

3.11 Frequency Response of Wind Generators During System Disturbances

The IEEE 39 bus test system [Pai, 1989; Zimmerman et al., 2011] is used to examine the frequency response in the joint operation of wind and conventional generators. A base case and five different wind technology cases are considered as follows.

Case A Base case without wind generation. A 1.5 MW induction machine was connected to bus 16; parameters of this induction machine are reported in Appendix B. All conventional generators support the frequency disturbance with a speed droop of $R = 0.05$ based on each machine's rating.

Cases B, C and D Case A is slightly modified to analyze three cases with different technologies of wind generation : FSWG, DFIG, and PMSG, respectively. Data of individual wind generators are reported in Appendix B. In each case, approximately 12% (720 MW) of wind penetration is included by using four wind

farms with a 180 MW of active power rating with the structure shown in Table 3.5. Wind farms are connected to the system through step-up transformers at buses 25, 26, 28 and 29, as shown in Fig. 3.19.

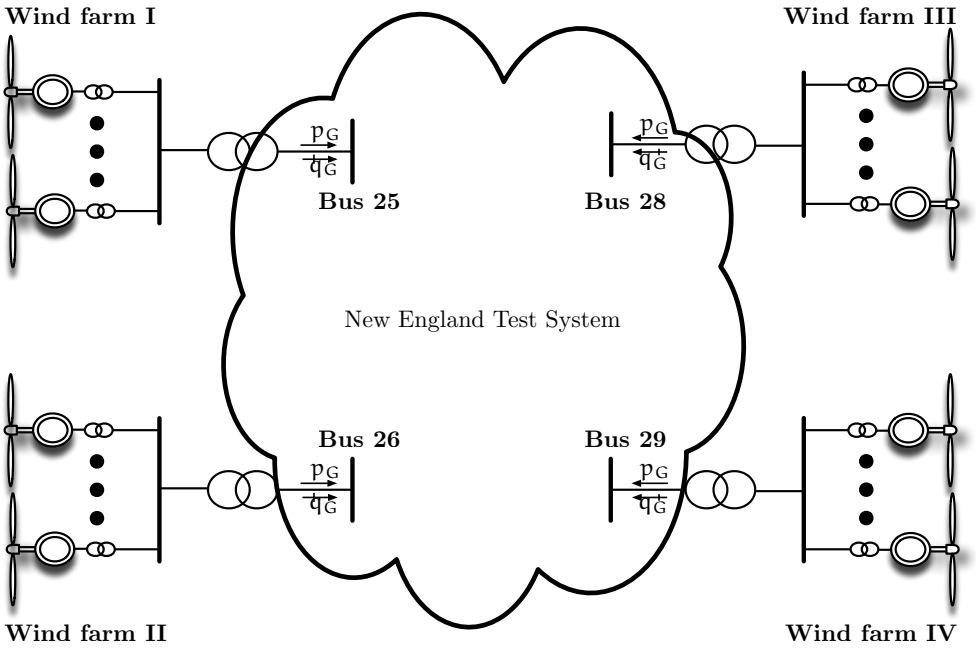

FIGURE 3.19: Modified New England test system.

TABLE 3.5: Wind farm data

	Case B	Case C	Case D
Type	FSWG	DFIG	PMSG
WG rating (MW)	0.9	2.0	5.0
Number of WG	200	90	36
Wind farm rating (MW)	180		
Transformer reactance	$\chi = 0.1$ pu		

The addition of wind, and the associated decommitment and redispatch of thermal generation, is implemented following the procedure shown in [Miller et al., 2011]. Based on this methodology, the addition of every 3 MW of wind generation is accomplished with a 2 MW of decommitment and 1 MW reduction in thermal generation. The newly added wind turbine generators were assumed to be operating at 66.66% rated capacity in order to capture the operational reality that all wind plants in a system are never operating simultaneously at rated power. Therefore, it is assumed that 480 MW (66.66% rated capacity) of wind power generation with a rating of 720 MW need to be accommodated, and there are two thermal units that can be displaced. One thermal unit (unit 8) is a 689 MVA plant with 540 MW of output which is connected to bus 25 through a step-up transformer, and the other (unit 9), which is connected to bus 29 through a step-up transformer, is a 990 MVA plant with 830 MW of output. The total output of the thermal units is 1370 MW, and the total rating is 1679 MVA.

For 480 MW of additional wind production, the $\frac{2}{3}$ decommitment objective is 320 MVA; in addition, the $\frac{1}{3}$ redispatch objective is 160 MW.

First, the 689 MVA thermal plant is replaced by four 180 MW (720 MW total) rated wind farms with approx 120 MW of output for each. This constitutes a thermal decommitment of 689 MVA. Second, the MVA in the second thermal unit is increased from 990 MVA to 1359 MVA. This represents a transfer of 369 MVA of thermal decommitment to this unit. As a result, the net thermal decommitment is 320 MVA: −689 MVA at the first plant and +369 MVA at the second plant. The original total thermal MVA was reduced from 1679 MVA to 1359 MVA.

Consider the above changes from the perspective of the thermal plant dispatch, rather than commitment. The total thermal plant output was originally 1370 MW. The decommitment of 320 MVA results in an equivalent reduction in actual output or an interim thermal output of 1050 MW. Thus, the 160 MW redispatch is implemented, giving a final total thermal output of 890 MW on the second unit.

The final network includes four 180 MW rated wind farms embedded at buses 25, 26, 28 and 29, a totally displaced thermal unit (unit 8), and a thermal plant (unit 9) with an output of 890 MW and a rating of 1359 MVA. Concerning reactive power margins, those were modified with the same ratio of the active power modification, but the proportion to its original rates was conserved; hence the maximum and minimum power factors remain the same.

Cases E and F For voltage analysis purposes, two additional cases were considered, both based in the network of Case B. Given the fact that FSWGs tend to aggravate the overall network voltage profile, Case E considers four 60 MVAr SVCs embedded at buses 25,26,28 and 29. Instead of SVCs, Case F considers four 60 MVAr STATCOMs. Data of both compensators is given in Appendix B.

To analyze the system frequency and voltage response, a tripping generation is applied. Wind speed applied to each wind farm is 12, 14, 12, and 14 m/s for wind farm I, II, III and IV, respectively. The applied convergence criterion is 10^{-9}.

Tripping generator 7 imposes a substantial frequency excursion by losing 560 MW (approx. 9% of total generation). The frequency response of the no wind case (Case A) is performed by the remaining units. In this case, one unit reaches their rated power limits with a primary frequency response of 49.7995 Hz, as shown in Table 3.6.

As shown in Table 3.7, by considering wind generation without frequency support, Case B, the unit that was redispatched to higher level continues contributing to the frequency modulations; however, there is a more range to increase the output power: more headroom. As a result, the rest of the units reach no limits, but with a thermal unit displaced the overall system speed droop is affected; thus, frequency is decreased to 49.7797 Hz (Case B).

TABLE 3.6: Power generation response of conventional an wind generator under the tripping of generator 7 (Case A)

Gen.	$p_{G,0}$ (pu)	p_G (pu)	$q_{G,0}$ (pu)	q_G (pu)
CG 1	10.000	10.880	0.784	0.850
CG 2	6.795	7.410	2.218	2.390
CG 3	6.500	7.080	2.070	2.230
CG 4	6.320	6.940	1.083	1.260
CG 5	5.080	5.590	1.667	1.670
CG 6	6.500	6.870	2.107	2.270
CG 7	5.600	0.000	1.002	0.000
CG 8	5.400	5.950	0.000	0.100
CG 9	8.300	9.090	0.215	0.550
CG 10	2.500	2.830	1.614	1.770

TABLE 3.7: Power generation response of conventional an wind generator under the tripping of generator 7 (Case B)

Gen.	$p_{G,0}$ (pu)	p_G (pu)	$q_{G,0}$ (pu)	q_G (pu)	$\omega_{m,0}$ (pu)	ω_m (pu)	β_0 (deg.)	β (deg.)
WF I	1.601	1.588	-0.458	-0.454	1.004	1.000	0.000	0.000
WF II	1.800	1.779	-0.633	-0.636	1.005	1.000	0.000	0.000
WF III	1.601	1.588	-0.486	-0.490	1.004	1.000	0.000	0.000
WF IV	1.800	1.779	-0.618	-0.613	1.005	1.000	0.000	0.000
CG 1	10.000	10.970	1.046	1.130	-	-	-	-
CG 2	4.077	4.760	2.113	2.150	-	-	-	-
CG 3	6.500	7.140	2.184	2.360	-	-	-	-
CG 4	6.320	7.000	1.325	1.620	-	-	-	-
CG 5	5.080	5.640	1.670	1.670	-	-	-	-
CG 6	6.500	6.870	2.303	2.610	-	-	-	-
CG 7	5.600	0.000	1.283	0.000	-	-	-	-
CG 8	0.000	0.000	0.000	0.000	-	-	-	-
CG 9	8.900	10.100	2.159	2.930	-	-	-	-
CG 10	2.500	2.870	2.193	2.540	-	-	-	-

Furthermore, when DFIG and PMSG wind farms are deloaded (Cases C and D), governor-like controls allow the plant to provide a frequency response similar to that of a conventional plant. Tables 3.8 and 3.9 show plants II and IV initially deloaded by 5% of the available wind power. In these cases, the governor controls lead to better frequency responses; 49.7987 and 49.7981 Hz, for Case C and D, respectively. In fact, both responses are very similar and are almost as *good* as the base case. Wind farms I and III remain with the same output because they were not deloaded.

Finally, when including static compensators such as in Cases E and F, the frequency response is improved to 49.7827 and 49.7824 Hz, respectively. The static operation of FSWG wind farms is very similar with and without static compensators as shown in Tables 3.10 and 3.11, for Case E and F, respectively.

The same frequency behavior has been reported by using dynamic analysis, as in [Miller et al., 2011, 2012].

TABLE 3.8: Power generation response of conventional an wind generator under the tripping of generator 7 (Case C)

Gen.	$p_{G,0}$ (pu)	p_G (pu)	$q_{G,0}$ (pu)	q_G (pu)	$\omega_{m,0}$ (pu)	ω_m (pu)	β_0 (deg.)	β (deg.)
WF I	1.566	1.560	0.005	0.267	1.300	1.300	0.000	0.000
WF II	1.620	1.765	0.318	0.280	1.300	1.300	5.517	3.928
WF III	1.563	1.558	0.138	0.342	1.300	1.300	0.000	0.000
WF IV	1.620	1.765	0.091	0.282	1.300	1.300	5.574	3.931
CG 1	10.000	10.890	0.746	0.770	-	-	-	-
CG 2	5.330	5.950	2.048	2.110	-	-	-	-
CG 3	6.500	7.080	2.029	2.160	-	-	-	-
CG 4	6.320	6.950	1.099	1.290	-	-	-	-
CG 5	5.080	5.590	1.670	1.670	-	-	-	-
CG 6	6.500	6.870	2.120	2.290	-	-	-	-
CG 7	5.600	0.000	1.021	0.000	-	-	-	-
CG 8	0.000	0.000	0.000	0.000	-	-	-	-
CG 9	8.900	9.990	0.425	0.760	-	-	-	-
CG 10	2.500	2.830	1.584	1.670	-	-	-	-

TABLE 3.9: Power generation response of conventional an wind generator under the tripping of generator 7 (Case D)

Gen.	$p_{G,0}$ (pu)	p_G (pu)	$q_{G,0}$ (pu)	q_G (pu)	$\omega_{m,0}$ (pu)	ω_m (pu)	β_0 (deg.)	β (deg.)
WF I	1.314	1.314	0.067	0.294	0.989	0.989	0.000	0.000
WF II	1.620	1.765	0.269	0.281	1.000	1.000	3.282	1.746
WF III	1.314	1.314	0.157	0.403	0.989	0.989	0.000	0.000
WF IV	1.620	1.765	0.068	0.283	1.000	1.000	3.282	1.746
CG 1	10.000	10.890	0.737	0.760	-	-	-	-
CG 2	5.818	6.440	2.095	2.180	-	-	-	-
CG 3	6.500	7.090	2.037	2.170	-	-	-	-
CG 4	6.320	6.950	1.094	1.270	-	-	-	-
CG 5	5.080	5.590	1.670	1.670	-	-	-	-
CG 6	6.500	6.870	2.116	2.280	-	-	-	-
CG 7	5.600	0.000	1.015	0.000	-	-	-	-
CG 8	0.000	0.000	0.000	0.000	-	-	-	-
CG 9	8.900	10.000	0.412	0.670	-	-	-	-
CG 10	2.500	2.840	1.548	1.610	-	-	-	-

Fig. 3.20 shows the network voltage profile of the six cases and the base case (no wind, no disturbance). As it can be noted, the worst voltage deviations occur when considering fixed-speed wind generators with fixed capacitors (Case B); this is because induction machines require reactive power to magnetize the stator and rotor windings, and the fixed capacitor is incapable of providing all of it.

In order to quantify the voltage deviation, the following voltage error is applied for all the cases:

$$v_{\text{error},k} = \frac{v_{0,k} - v_{c,k}}{v_{0,k}}, \quad \forall k \in \mathcal{B}\,, \tag{3.160}$$

where $v_{0,k}$ is the base-case voltage magnitude without disturbance nor wind generation, and $v_{c,k}$ is the voltage magnitude of each case after the disturbance was applied. These

TABLE 3.10: Power generation response of conventional an wind generator under the tripping of generator 7 (Case E)

Gen.	$p_{G,0}$ (pu)	p_G (pu)	$q_{G,0}$ (pu)	q_G (pu)	$\omega_{m,0}$ (pu)	ω_m (pu)	β_0 (deg.)	β (deg.)
WF I	1.601	1.589	-0.438	-0.434	1.004	0.999	0.000	0.000
WF II	1.800	1.779	-0.588	-0.587	1.004	1.000	0.000	0.000
WF III	1.601	1.589	-0.452	-0.450	1.004	1.000	0.000	0.000
WF IV	1.800	1.779	-0.584	-0.576	1.004	1.000	0.000	0.000
CG 1	10.000	10.960	0.839	0.880	-	-	-	-
CG 2	4.657	5.330	2.041	2.080	-	-	-	-
CG 3	6.500	7.130	2.071	2.220	-	-	-	-
CG 4	6.320	7.000	1.171	1.390	-	-	-	-
CG 5	5.080	5.630	1.670	1.670	-	-	-	-
CG 6	6.500	6.870	2.178	2.390	-	-	-	-
CG 7	5.600	0.000	1.104	0.000	-	-	-	-
CG 8	0.000	0.000	0.000	0.000	-	-	-	-
CG 9	8.900	10.080	0.955	1.420	-	-	-	-
CG 10	2.500	2.860	1.781	1.950	-	-	-	-

TABLE 3.11: Power generation response of conventional an wind generator under the tripping of generator 7 (Case F)

Gen.	$p_{G,0}$ (pu)	p_G (pu)	$q_{G,0}$ (pu)	q_G (pu)	$\omega_{m,0}$ (pu)	ω_m (pu)	β_0 (deg.)	β (deg.)
WF I	1.601	1.589	-0.438	-0.433	1.004	0.999	0.000	0.000
WF II	1.800	1.779	-0.588	-0.587	1.004	1.000	0.000	0.000
WF III	1.601	1.589	-0.452	-0.450	1.004	1.000	0.000	0.000
WF IV	1.800	1.779	-0.584	-0.575	1.004	1.000	0.000	0.000
CG 1	10.000	10.960	0.839	0.880	-	-	-	-
CG 2	4.662	5.330	2.041	2.080	-	-	-	-
CG 3	6.500	7.130	2.071	2.210	-	-	-	-
CG 4	6.320	7.000	1.171	1.390	-	-	-	-
CG 5	5.080	5.630	1.670	1.670	-	-	-	-
CG 6	6.500	6.870	2.178	2.390	-	-	-	-
CG 7	5.600	0.000	1.104	0.000	-	-	-	-
CG 8	0.000	0.000	0.000	0.000	-	-	-	-
CG 9	8.900	10.080	0.955	1.400	-	-	-	-
CG 10	2.500	2.860	1.781	1.950	-	-	-	-

voltage magnitude errors are depicted in Fig. 3.21. As shown, by adding either SVCs or STATCOMs to each wind farm facility, voltage errors are decreased (Case E and Case F). Moreover, when considering DFIG and PMSG wind farms, the voltage errors from the base case are almost conserved. Note that voltage control of DFIGs would not be possible by using fixed reactive power generation as suggested in [Li, 2013].

3.12 Conclusions

This section has shown a step-by-step procedure on how to model and incorporate steady state models of nonconventional electrical networks' devices in a power flow solver. The modeling stage was performed by trying to include every relevant part of each device as well as its operative limits. In this sense a set of complementarity constraints were

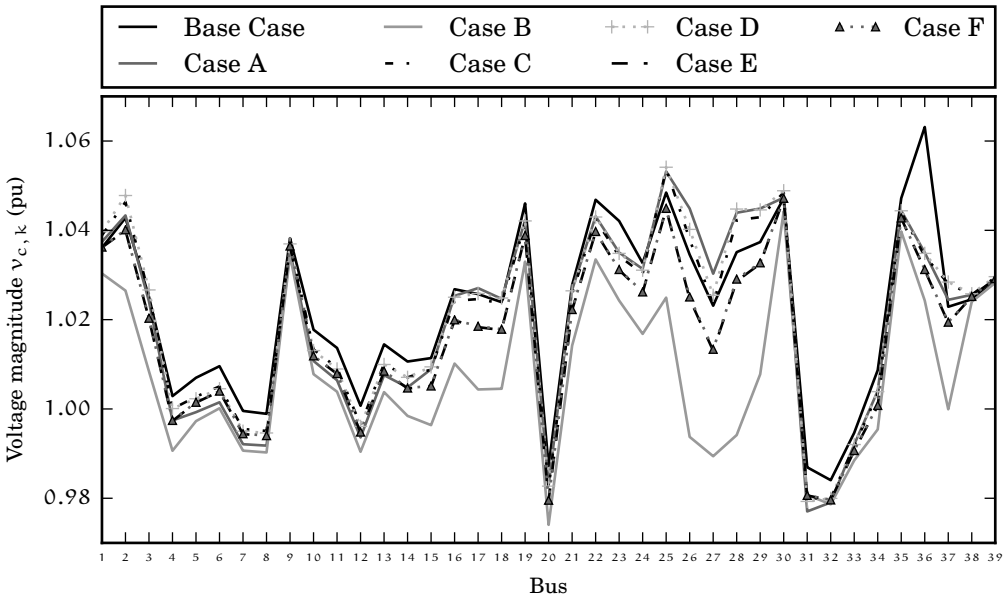

FIGURE 3.20: Voltage differences under generator outage.

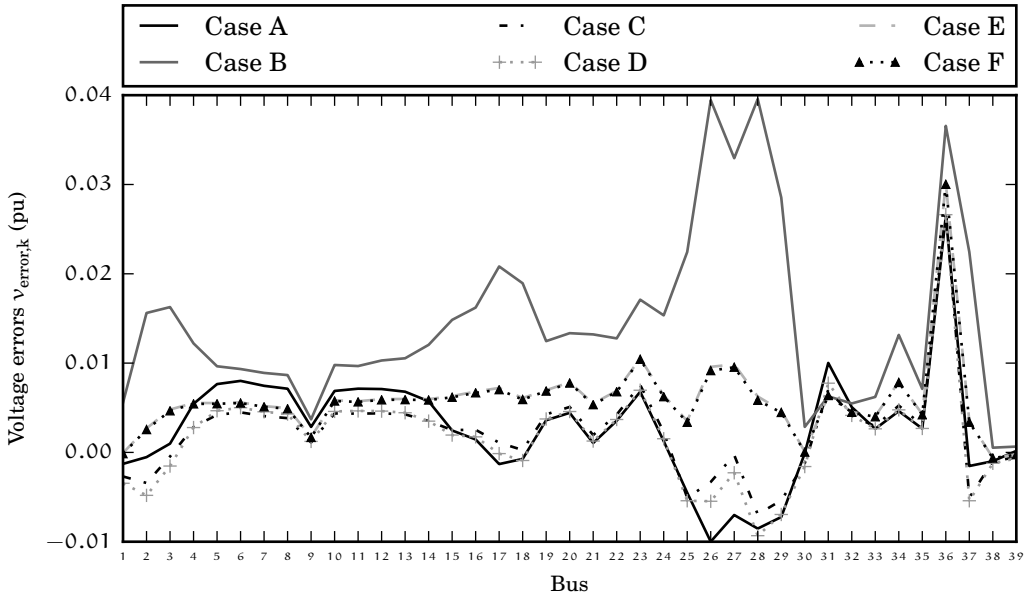

FIGURE 3.21: Voltage relative errors under generator outage.

included through the Fischer-Burmeister merit functions which were solved along with the traditional power flow equations in a unified way.

Both the models and the framework solution were tested with a set of benchmarks. First, the complementarity approach has been proven to deliver well when solving constrained power flows. Furthermore, the wind speed characteristics of the most popular wind generation technologies were reported as obtaining very similar results to those reported in the existing literature, which implies that the steady state models are correct. Finally, the interaction of conventional and wind generation in a primary

control-based power flow was assessed, where it was proved how the asynchronous generation without frequency support tends to aggravate the overall frequency response of the system. In contrast, the asynchronous wind generation, which is deloaded and considered for the primary frequency control, has deteriorated much less the frequency response of the system.

Chapter 4

Impact of Wind Generation on the Voltage Collapse Phenomena

4.1 Introduction

Two techniques for determining the point of voltage collapse (PVC) in a power system network with embedded wind generators are described in this chapter. A *new method* to compute the PVC through a conventional power flow approach, but by using a new type of bus [Ghiocel and Chow, 2014], is compared against the traditional continuation power flow (CPF) method [Ajjarapu and Christy, 1992]. A critical analysis is carried out to demonstrate that the former is a particular case of a homotopy method.

Finally, a comparison of both techniques with an emphasis on analyzing the different type of wind power technologies and its impact on the voltage stability phenomena is performed. All previous is performed in a deterministic context.

4.2 Voltage Stability and Theoretical Concepts

Power system stability may be defined as the property of a power system that enables it to remain in a normal state of operating equilibrium, as well as to regain an acceptable state of equilibrium after being subjected to a disturbance[Kundur et al., 1994].

Power systems are subjected to a large range of disturbances under different operating conditions, which can lead the system to its loss of stability. In this context, voltage stability is the ability of a power system to maintain acceptable values of voltages' magnitudes at all buses under normal operating conditions and after being subjected to a disturbance. On the other hand, voltage instability occurs in the system when a disturbance, an increase in load demand or a change in the system operating condition

causes a progressive and uncontrollable drop in voltage magnitudes. The main factor causing instability is the inability of the power system to meet the demand for reactive power[Kundur et al., 1994].

One way in which the voltage instability is manifested depends on the process by which the voltage magnitude at some buses falls to a low, unacceptable value as a result of a an avalanche of events; this is referred to as voltage collapse [Taylor, 1994]. Voltage collapse is classified as a static phenomenon mathematically related to a saddle node bifurcation (SNB) or a limit-induced bifurcation (LIB) induced by a violation of operational limits, during which the system equilibrium disappears as system parameters, mostly system loads, change slowly [Taylor, 1994; Cutsem and Vournas, 2007]. Hence, from a physical viewpoint, at voltage collapse the system loses the ability to supply enough reactive power to a heavily loaded network.

4.2.1 Two Bus Example

With the aim of clarifying the voltage collapse phenomena and its relation to the maximum power load that a network can supply, the two bus system shown in Fig. 4.1 is analyzed.

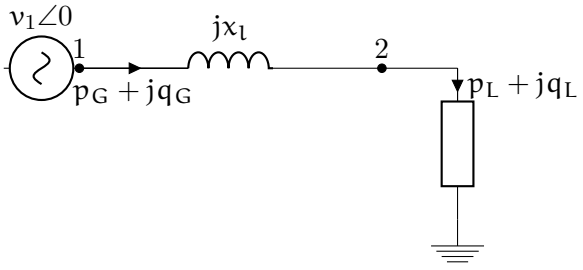

FIGURE 4.1: Two bus system.

From Fig. 4.1, the following power flow equations are obtained:

$$-p_L = \frac{v_2 v_1}{x_l} \sin \delta_2 \tag{4.1a}$$

$$-q_L = \frac{v_2^2}{x_l} - \frac{v_2 v_1}{x_l} \cos \delta_2 \,, \tag{4.1b}$$

where it is assumed that bus 1 is the reference generator.

After some simple manipulations the above equations can be rewritten as

$$p_L^2 = \frac{v_2^2 v_1^2}{x_l^2} \sin^2 \delta_2 \tag{4.2}$$

$$q_L^2 + \frac{v_2^4}{x_l^2} + 2q_L \frac{v_2^2}{x_l} = \frac{v_2^2 v_1^2}{x_l^2} \cos^2 \delta_2 \,. \tag{4.3}$$

In addition, by considering $\sin^2 \delta_2 + \cos^2 \delta_2 = 1$ the latter equations are combined as

$$p_L^2 + q_L^2 + \frac{v_2^4}{x_l^2} + 2q_L \frac{v_2^2}{x_l} - \frac{v_2^2 v_1^2}{x_l^2} = 0 \,. \tag{4.4}$$

Therefore, the load bus voltage magnitude v_2 can be written as a function of the load power p_L[Milano, 2010]:

$$v_2 = \sqrt{-a \pm \sqrt{a^2 - x_l^2 p_L^2 \left(1 + \tan^2 \phi\right)}} \,, \tag{4.5}$$

where

$$a = p_L \tan(\phi) x_l - \frac{v_1^2}{2} \,, \tag{4.6}$$

and ϕ is the angle of the load power factor, i.e. $q_L = p_L \tan \phi$.

Eq. (4.5) is depicted in Fig. 4.2 and is known as the *PV curve* or *nose curve*, because of its characteristic shape.

Some relevant remarks of Eq. (4.5) are found below.

1. The system is characterized by a maximum value of the load p_L^{max}, which is known as the maximum loading condition.
2. For $p_L > p_L^{max}$ the power flow equations (Eq. (4.1)) have no solution. For this reason, the power flow solution for $p_L = p_L^{max}$ is known as the point of collapse. In physical terms, this means that the system cannot supply a load with a power of $p_L > p_L^{max}$. Hence, p_L^{max} is the maximum power that can be transmitted by the network, and it can be considered a limit of the transmission system.
3. For $p_L < p_L^{max}$ there are two values of v_2 that satisfy Eq. (4.1). Only the upper solution is physically acceptable, however. The lower solution has only a mathematical interest.

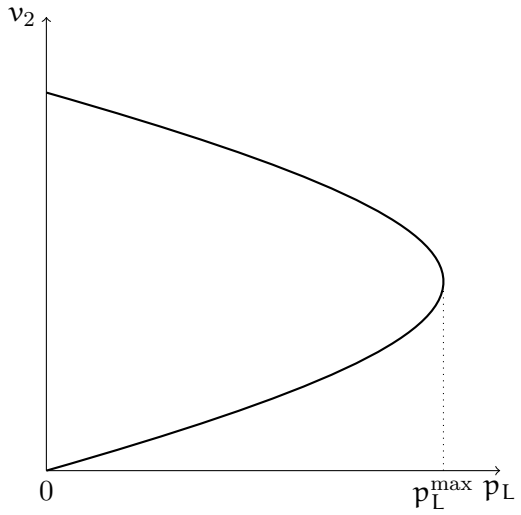

FIGURE 4.2: PV curve for the two bus system.

The PV curve depicted in Fig. 4.2 was obtained assuming that the reference generator at bus 1 can supply any amount of active and reactive power. If the hypothesis about the reactive power is removed, there can be a value of p_L for which the reactive power generated by the generator is the maximum, say $q_G = q_G^{max}$. Since the system has no other reactive power source, the load power cannot be increased any further. If the generator's reactive power limit is reached before the transmission system limit, the former yields the point of collapse or, which is the same, the p_L^{max} value.

4.2.2 System Modeling Considering Loading Factor

The above example is generalized to formulate a multi-nodal network model suitable for encountering the maximum loading condition. With this objective in mind, the set of power flow equations presented in Eq. (3.18) is expanded by considering the system loading factor λ:

$$\mathbf{0} = \mathbf{g}(\mathbf{y}, \lambda)\,, \tag{4.7}$$

where $\mathbf{y}$ is as usual the set of algebraic state variables, and $\lambda \in \mathbb{R}$ is the loading parameter which scales the generator and load powers.

Therefore, by including the loading factor λ, the load power computed by Eq. (2.20) is now *scaled* as follows:

$$p_L = p_{L,0}\,(1+\lambda k_L)\left(1+k_{pf}\Delta f\right)\left[k_{pp}+k_{pc}\left(\frac{v_k}{v_{k_0}}\right)+k_{pz}\left(\frac{v_k}{v_{k_0}}\right)^2\right] \tag{4.8a}$$

$$q_L = q_{L,0}\,(1+\lambda k_L)\left(1+k_{qf}\Delta f\right)\left[k_{qp}+k_{qc}\left(\frac{v_k}{v_{k_0}}\right)+k_{qz}\left(\frac{v_k}{v_{k_0}}\right)^2\right]. \tag{4.8b}$$

In the same way, the mechanical power (Eq. (2.27)) drawn by induction machines is modified to

$$p_m = p_{m,0}\,(1+\lambda k_M)\left[a\left(\frac{\omega_m}{\omega_{m,0}}\right)^2+b\frac{\omega_m}{\omega_{m,0}}+c\right]. \tag{4.9}$$

The same procedure is applied to the synchronous generator model (Eq. (2.1a)):

$$p_G = p_{G,0}\,(1+\lambda k_G)-\left(\frac{1}{R}\right)\Delta f\,, \tag{4.10}$$

where k_L, k_M and k_G are the load, induction machine and generator dispatch directions, respectively. These parameters define a custom path along which the system is loaded through the parameter λ.

Some highlights of this formulation are below.

- If $k_G = 0$ for all generators, then the generation will be increased with a distributed slack basis. This means that each generator will augment the active power output according to its capacity and speed droop parameter.
- In case $k_G \neq 0$, this parameter will define the dispatch direction of each generator. In this case, a distributed slack approach can also be used to compensate the active power losses or another active power imbalance of the system.

4.2.3 Saddle-Node Bifurcation

The saddle-node bifurcation (SNB) is the formal mathematical notation of the transmission system limit described in Section 4.2.1. Fig. 4.2 shows that the tangent to the curve $v_2(p_L)$ at the maximum loading point is vertical: $\frac{\partial v_2}{\partial p_L}\Big|_{p_L=p_L^{max}} \to \infty$.

In a multi-nodal network defined by the set of power flow equations $\mathbf{g}(\mathbf{y}, \lambda)$, the SNB is presented when the following conditions are met [Cutsem and Vournas, 2007]:

$$\mathbf{g}(\mathbf{y}, \lambda) = 0 \tag{4.11}$$

$$\mathbf{g}_{\mathbf{y}}(\mathbf{y}, \lambda)\boldsymbol{v} = 0 \tag{4.12}$$

$$\boldsymbol{w}^{\mathsf{T}}\mathbf{g}_{\lambda}(\mathbf{y}, \lambda) \neq 0 \tag{4.13}$$

$$\boldsymbol{w}^{\mathsf{T}}\mathbf{g}_{\lambda\lambda}(\mathbf{y}, \lambda)\boldsymbol{v}\boldsymbol{v} \neq 0\,, \tag{4.14}$$

where $\boldsymbol{v}$, $\boldsymbol{w}$ are the right and left eigenvectors of $\mathbf{g}_{\mathbf{y}}(\mathbf{y}, \lambda)$, respectively.

The first condition implies that the solution of the power flow equations must exist; the second implies that the Jacobian matrix at this point is singular. Finally, the third and fourth conditions ensure transversality so that the bifurcations are not degenerate cases.

4.2.4 Limit-Induced Bifurcation

In power systems, control and/or operational limits have been shown to yield bifurcations known as limit-induced bifurcations (LIB) . As the load increases, there exists a major demand for reactive power, and a voltage collapse scenario can be precipitated by the hitting of reactive power limits of generators or other voltage regulating controllers. For instance, once one of the limits of reactive power generation q_{G} is reached, the reactive power output can no longer be regulated; therefore, the generator terminal voltage cannot be maintained at the specified value. In this case, there exists the reduction on the voltage stability margin, which leads to two possible operating point scenarios. First, no local equilibria may exist for increasing loading conditions [Dobson and Lu, 1992], resulting in a voltage collapse, which is similar to what happens in the occurrence of a SNB. It is also possible that the system remains stable, since the equilibrium point may be in the stable part of the limit-induced model's bifurcation diagram. In other words, the equilibrium points continue to exist after the LIB is reached as the bifurcation parameter changes.

4.3 Continuation Method

Note that in order to trace the loading path depicted in Fig. 4.2, a set of equilibrium points must be obtained. This set of solutions can be obtained by incrementing the loading parameter and computing the power flow solution for the corresponding loading condition. This sequential approach, however, has some drawbacks.

- At SNB points, the Jacobian matrix is singular. Hence, Newton's method will diverge for cases close enough to the SNB points.
- The number of steps or even an adequate step size of the loading parameter, say $\Delta\lambda$, is not known *a priori*; thus, in some cases the power flow mismatch equations cannot be satisfied, because $\Delta\lambda$ is too large to ensure that the equilibrium point is inside the solution space.

An alternative scheme for avoiding these problems is to use a continuation method which consists of defining a homotopy map which generates a convergent series solution for the nonlinear set defined in Eq. (4.7) [Ajjarapu and Christy, 1992].

The continuation method adopted in this work is fully detailed and reported in [Ajjarapu and Christy, 1992; Ilić and Zaborszky, 2000], such that only the most relevant principles and procedures associated with this computation are discussed here.

The method consists of a three-step approach for tracing the equilibrium points as one system parameter changes: find the solution to the power flow equations $\mathbf{g}(\mathbf{y},\lambda) = \mathbf{0}$ for a given set of parameter values. Normally the loading factor λ is the varying parameter; as the system gets close to a bifurcation point, however, the classical power flow Jacobian becomes ill-conditioned[Canizares and Alvarado, 1993]. A parameterization (e.g., switching from λ to, for example, a bus voltage $v_k \in \mathbf{y}$) makes the power flow Jacobian nonsingular at the PVC and is used for avoiding this numerical problem. Mathematically, the continuation power flow is described as follows [Ajjarapu and Christy, 1992; Canizares and Alvarado, 1993].

Predictor Starting the method from a known solution $\mathbf{g}(\mathbf{y},\lambda)^{(i)} = \mathbf{0}$, where i denotes the i-th solution of the ongoing continuation process, the prediction is along the tangent direction of the continuum at the current operating point Furthermore, this tangent direction is found by solving:

$$\boldsymbol{\Delta\tau}^{(i)} = \begin{bmatrix} \boldsymbol{\Delta y} \\ \Delta\lambda \end{bmatrix}^{(i)} = - \begin{bmatrix} \mathbf{g}_{\mathbf{y}}(\mathbf{y},\lambda) & \mathbf{g}_{\lambda}(\mathbf{y},\lambda) \\ \boldsymbol{e}_{\mathbf{k}} & \end{bmatrix}^{(i)^{-1}} \begin{bmatrix} \mathbf{0} \\ 1 \end{bmatrix}, \tag{4.15}$$

where $\boldsymbol{\Delta\tau}^{(i)}$ is the tangent vector being sought, $\boldsymbol{\tau} = \begin{bmatrix} \mathbf{y}^{\mathsf{T}} & \lambda \end{bmatrix}^{\mathsf{T}}$, and $\boldsymbol{e}_{\mathbf{k}}$ is an appropriately dimensioned row vector with all elements at zero except the k-th, which equals one and corresponds to the continuation parameter. A step size control σ must be chosen for determining the final increment of $\boldsymbol{\Delta y}^{(i)}$ and $\Delta\lambda^{(i)}$, along with a normalization that avoids large steps when $\|\boldsymbol{\Delta\tau}^{(i)}\|_2$ increases:

$$\Delta\hat{\mathbf{y}}^{(i)} = \sigma\frac{\Delta\mathbf{y}^{(i)}}{\|\Delta\boldsymbol{\tau}^{(i)}\|_2} \tag{4.16}$$

$$\Delta\hat{\lambda}^{(i)} = \sigma\frac{\Delta\lambda^{(i)}}{\|\Delta\boldsymbol{\tau}^{(i)}\|_2}\,, \tag{4.17}$$

where σ is a scalar that defines the step size and direction of the tangent vector to the solution path. The selection of the sign of σ is based on the direction of the continuum. On the other hand, the absolute value of σ is user defined, $|\sigma| = 1$ yields good results. Finally, the prediction can be obtained as follows:

$$\hat{\mathbf{y}}^{(i+1)} = \mathbf{y}^{(i)} + \Delta\hat{\mathbf{y}}^{(i)} \tag{4.18}$$

$$\hat{\lambda}^{(i+1)} = \lambda^{(i)} + \Delta\hat{\lambda}^{(i)}\,. \tag{4.19}$$

Corrector After the predictor has produced an approximate solution for the next equilibrium point, the corrector stage finds the exact solution with the initial guess provided by Eqs. (4.18) and (4.19). This exact solution is obtained by means of a local parameterization, whereby the original set of equations $\mathbf{g}(\mathbf{y},\lambda)$ is augmented by one equation $\zeta(\mathbf{y},\lambda)$:

$$\begin{bmatrix}\mathbf{g}(\mathbf{y},\lambda)\\ \zeta(\mathbf{y},\lambda)\end{bmatrix} = \mathbf{0}\,, \tag{4.20}$$

where $\zeta : \mathbb{R}^{n_y+1} \mapsto \mathbb{R}^{n_y+1}$ is called a *continuation function* which forces either the parameter λ or a variable y_k to be an assigned value:

$$\zeta(\mathbf{y},\lambda) = \lambda - \hat{\lambda}^{(i+1)} \qquad = 0 \tag{4.21}$$

or

$$\tag{4.22}$$

$$\zeta(\mathbf{y},\lambda) = y_k - \hat{y}_k^{(i+1)} \qquad = 0\,. \tag{4.23}$$

Parameterization Once the *exact* equilibrium point is obtained, checking the relative change in all system variables is necessary; and trade k with the variable that presents the largest change. In other words,

$$k \leftarrow \max\left\{\frac{\Delta y_1}{y_1}, \frac{\Delta y_2}{y_2}, \ldots, \frac{\Delta y_{n_y}}{y_{n_y}}, \frac{\Delta\lambda}{\lambda}\right\}. \tag{4.24}$$

Note that if $k > n_y$, the continuation parameter is then the loading factor λ; otherwise it is a system state variable.

In general, the continuation parameter k changes from the loading parameter λ to either the voltage magnitude or the voltage angle parameter with the largest rate of decrease.

The three-step process described above is depicted in Fig. 4.3.

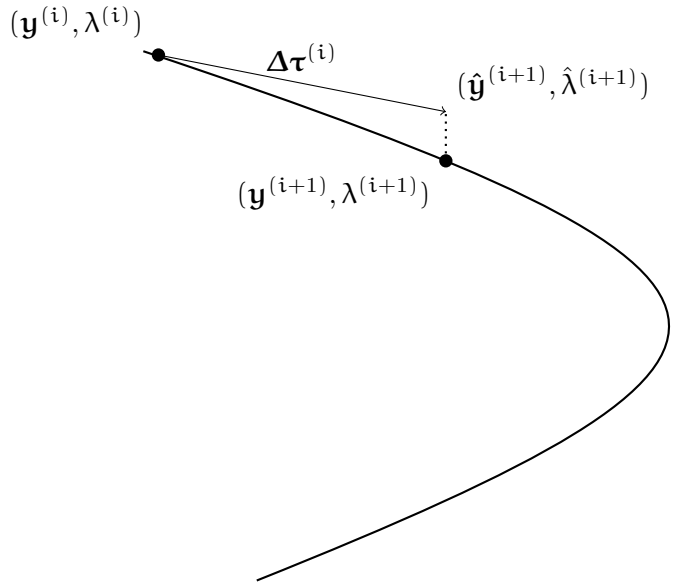

FIGURE 4.3: Continuation power flow steps.

4.4 *AQ-bus* Method

An alternative approach to the previous continuation power flow is presented here. This alternative is based on [Ghiocel and Chow, 2014].

By contemplating again the two bus system presented in Fig. 4.1, the following power flow equations are obtained:

$$p_{12} = \frac{v_1 v_2}{x_l} \sin(\delta_1 - \delta_2) \tag{4.25}$$

$$q_{12} = \frac{v_1}{x_l} (v_1 - v_2 \cos(\delta_1 - \delta_2)) \tag{4.26}$$

$$p_{21} = -\frac{v_1 v_2}{x_l} \sin(\delta_1 - \delta_2) \tag{4.27}$$

$$q_{21} = -\frac{v_2}{x_l} (v_1 \cos(\delta_1 - \delta_2) - v_2) \ . \tag{4.28}$$

Next, the set of mismatch power equations are formed:

$$\Delta p_1 = p_G - p_{12} \tag{4.29}$$

$$\Delta q_1 = q_G - q_{12} \tag{4.30}$$

$$\Delta p_2 = -p_{21} - (1 + \lambda k_L)\, p_{L,0} \tag{4.31}$$

$$\Delta q_2 = -q_{21} - (1 + \lambda k_L)\, q_{L,0} \tag{4.32}$$

where λ is the loading parameter.

By linearizing through the NR method,

$$\mathbf{g}(\mathbf{y}) = -\mathbf{g}_{\mathbf{y}}(\mathbf{y})\boldsymbol{\Delta}\mathbf{y} \tag{4.33}$$

$$\begin{bmatrix} \Delta p_1 \\ \Delta p_2 \\ \Delta q_1 \\ \Delta q_2 \end{bmatrix} = - \begin{bmatrix} \frac{\partial \Delta p_1}{\partial \delta_1} & \frac{\partial \Delta p_1}{\partial \delta_2} & \frac{\partial \Delta p_1}{\partial v_1} & \frac{\partial \Delta p_1}{\partial v_2} \\ \frac{\partial \Delta p_2}{\partial \delta_1} & \frac{\partial \Delta p_2}{\partial \delta_2} & \frac{\partial \Delta p_2}{\partial v_1} & \frac{\partial \Delta p_2}{\partial v_2} \\ \frac{\partial \Delta q_1}{\partial \delta_1} & \frac{\partial \Delta q_1}{\partial \delta_2} & \frac{\partial \Delta q_1}{\partial v_1} & \frac{\partial \Delta q_1}{\partial v_2} \\ \frac{\partial \Delta q_2}{\partial \delta_1} & \frac{\partial \Delta q_2}{\partial \delta_2} & \frac{\partial \Delta q_2}{\partial v_1} & \frac{\partial \Delta q_2}{\partial v_2} \end{bmatrix} \begin{bmatrix} \Delta \delta_1 \\ \Delta \delta_2 \\ \Delta v_1 \\ \Delta v_2 \end{bmatrix} . \tag{4.34}$$

For the sake of conciseness, the conventional definition of *slack bus* is used here; the use of additional equations as proposed in the previous chapter is avoided). Hence, by defining $\bar{v}_1 = 1\angle 0$,

$$\begin{bmatrix} 0 \\ \Delta p_2 \\ 0 \\ \Delta q_2 \end{bmatrix} = - \begin{bmatrix} 1 & 0 & 0 & 0 \\ 0 & \frac{\partial \Delta p_2}{\partial \delta_2} & 0 & \frac{\partial \Delta p_2}{\partial v_2} \\ 0 & 0 & 1 & 0 \\ 0 & \frac{\partial \Delta q_2}{\partial \delta_2} & 0 & \frac{\partial \Delta q_2}{\partial v_2} \end{bmatrix} \begin{bmatrix} \Delta \delta_1 \\ \Delta \delta_2 \\ \Delta v_1 \\ \Delta v_2 \end{bmatrix} \tag{4.35}$$

$$= - \begin{bmatrix} 1 & 0 & 0 & 0 \\ 0 & -\frac{v_2}{x_l} \cos(\delta_2) & 0 & -\frac{1}{x_l} \sin(\delta_2) \\ 0 & 0 & 1 & 0 \\ 0 & -\frac{v_2}{x_l} \sin(\delta_2) & 0 & \frac{1}{x_l}(-2v_2 + \cos(\delta_2)) \end{bmatrix} \begin{bmatrix} \Delta \delta_1 \\ \Delta \delta_2 \\ \Delta v_1 \\ \Delta v_2 \\ \Delta \lambda \end{bmatrix} . \tag{4.36}$$

This Jacobian matrix is singular when $\det(\mathbf{g}_{\mathbf{y}}(\mathbf{y})) = 0$:

$$\det(\mathbf{g}_{\mathbf{y}}(\mathbf{y})) = \frac{v_2}{x_l^2}(2v_2 \cos(\delta_2) - 1) , \tag{4.37}$$

which occurs at the PVC [Ghiocel and Chow, 2014]. Note that $\det\left(\mathbf{g}_{\mathbf{y}}(\mathbf{y})\right) = 0$ when $2v_2\cos\left(\delta_2\right) = 1$.

Now to avoid the singularity, let us fix the voltage angle at bus 2. This fixed angle can be modeled as an extra equation; thus, the previous power flow equations (Eq. (4.33)) are expanded:

$$\mathbf{g}(\mathbf{y}) = \begin{bmatrix} \Delta p_1 \\ \Delta q_1 \\ \Delta p_2 \\ \Delta q_2 \\ h_{AQ} = \delta_2 - \delta_{\text{ref}} \end{bmatrix}, \tag{4.38}$$

where δ_{ref} is a parameter that defines the fixed angle of the *AQ-bus*. This parameter is selected to change the equilibrium point of the whole system, as shown later.

Adding a new constraint implies that a new variable must be defined; in this case this new variable is the loading factor λ that was previously treated as a parameter. Therefore the new Jacobian is rewritten:

$$\begin{bmatrix} 0 \\ \Delta p_2 \\ 0 \\ \Delta q_2 \\ h_{AQ} \end{bmatrix} = -\begin{bmatrix} 1 & 0 & 0 & 0 & 0 \\ 0 & \frac{\partial \Delta p_2}{\partial \delta_2} & 0 & \frac{\partial \Delta p_2}{\partial v_2} & \frac{\partial \Delta p_2}{\partial \lambda} \\ 0 & 0 & 1 & 0 & 0 \\ 0 & \frac{\partial \Delta q_2}{\partial \delta_2} & 0 & \frac{\partial \Delta q_2}{\partial v_2} & \frac{\partial \Delta q_2}{\partial \lambda} \\ 0 & 1 & 0 & 0 & 0 \end{bmatrix} \begin{bmatrix} \Delta\delta_1 \\ \Delta\delta_2 \\ \Delta v_1 \\ \Delta v_2 \\ \Delta\lambda \end{bmatrix} \tag{4.39}$$

$$= -\begin{bmatrix} 1 & 0 & 0 & 0 & 0 \\ 0 & -\frac{v_2}{x_l}\cos\left(\delta_2\right) & 0 & -\frac{1}{x_l}\sin\left(\delta_2\right) & -k_L p_{L,0} \\ 0 & 0 & 1 & 0 & 0 \\ 0 & -\frac{v_2}{x_l}\sin\left(\delta_2\right) & 0 & \frac{1}{x_l}\left(-2v_2 + \cos\left(\delta_2\right)\right) & -k_L q_{L,0} \\ 0 & 1 & 0 & 0 & 0 \end{bmatrix} \begin{bmatrix} \Delta\delta_1 \\ \Delta\delta_2 \\ \Delta v_1 \\ \Delta v_2 \\ \Delta\lambda \end{bmatrix}. \tag{4.40}$$

The determinant of this modified Jacobian is

$$\det\left(\mathbf{g}_{\mathbf{y}}(\mathbf{y})\right) = \frac{k_L}{x_l}\left(-2p_{L,0}v_2 + p_{L,0}\cos\left(\delta_2\right) + q_{L,0}\sin\left(\delta_2\right)\right). \tag{4.41}$$

For the two bus system of Fig. 4.1, the numerical value of Eqs. (4.37) and (4.41) are computed by using $x_l = 0.1$pu, $p_{L,0} = q_{L,0} = k_L = 1$pu. Given the fact that Eqs. (4.37)

and (4.41) are not explicit functions of λ, a CPF study was carried out to obtain the values of v_2, and δ_2 under different loading conditions.

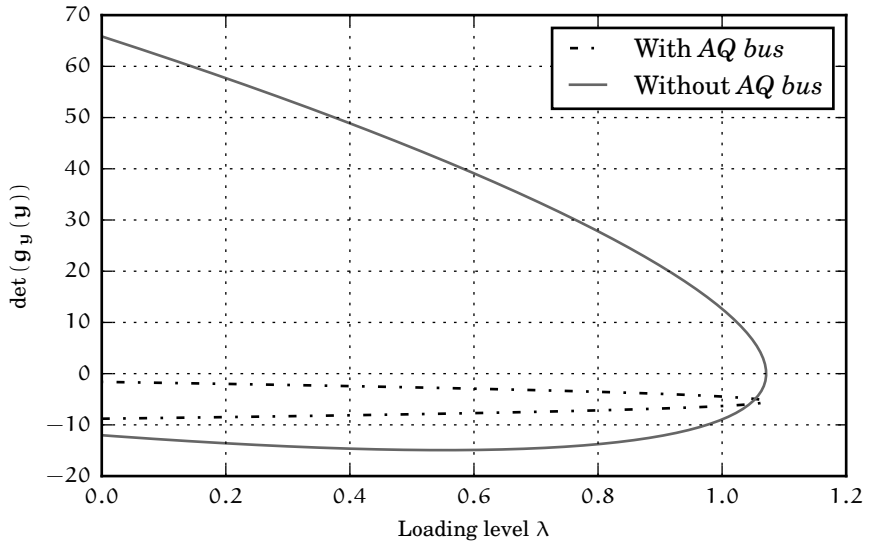

FIGURE 4.4: Determinant of $\mathbf{g_y}(\mathbf{y})$ with and without *AQ-bus*.

The definition of a fixed angle bus within the power flow equations avoids the singularity of the Jacobian matrix close to the PVC, as shown in Fig. 4.4. In other words, when no *AQ-bus* is defined the determinant is zero at the PVC; however, when including the *AQ-bus* the determinant is different from zero. Hence, the system is solvable.

The previous procedure is the essence of the *AQ-bus* method and is summarized as follows.

1. From a current operating point (base case), use a conventional power flow program with increasing loading factor λ until the NR method no longer converges.

2. Starting from the last converged solution of the previous step, apply the *AQ-bus* power flow by expanding the set of equations with $\mathbf{h_{AQ}}$. Continue the power flow solution by increasing the angle separation, in other words increase δ_{ref}. The initial value of δ_{ref} is equal to the voltage angle of the *AQ-bus* at the last converged solution. Moreover, δ_{ref} is increased in the same direction that was varying with the conventional power flow but with a step value $\Delta\delta_{\text{ref}}$ user-defined. Typically, the bus with the largest voltage magnitude decrease, the weakest bus, will be selected to be the *AQ-bus*. In these power flow solutions, λ is no longer a parameter and must be computed as a state variable inside the unified solution.

3. In some cases, the power flow with the *AQ-bus* stops converging because the Jacobian matrix is again singular. In such cases, remove the *AQ-bus* and continue decreasing the loading parameter λ. Typically this occurs after the PVC has been reached.

Note that this approach is very similar to the continuation method.

- The *AQ-bus* method does not need a predictor step; indeed the loading factor is incremented manually until the method diverges. In case the *AQ-bus* is defined, the loading factor is incremented indirectly by increasing the voltage angle at the *AQ-bus*.
- The additional equation $\mathtt{h}_{\mathtt{AQ}}$ is in fact the continuation function, i.e. $\mathtt{h}_{\mathtt{AQ}}(\mathbf{y}, \lambda) \sim \zeta(\mathbf{y}, \lambda)$. With this in mind, it must be noted that Eq. (4.38) is the same set of equations that is solved in the corrector step (Eq. (4.20)).
- The parameterization is performed by determining the bus with the largest voltage magnitude decrease, which is very similar when applying Eq. (4.24).

As far as the author is concerned, this *new* method is in fact a particular case of the continuation method presented before and does not present any additional advantages. On the other hand, this *AQ-bus* method presents some drawbacks.

- The increase of the loading factor must be done in a heuristic fashion.
- The user does not know *a priori* which increment is adequate; in some cases a small increment will slow the computing time by calculating more points than necessary.
- Other state variables, like wind generator or FACTS controller variables, are not considered to be the continuation parameter; hence the method is less robust.

4.5 Case Studies

A comparison between the *AQ-bus* and the continuation method is addressed by using the IEEE 14-bus test system. The complementarity approach is then tested in a CPF study with the purpose of proving its applicability in modeling devices' limits.

Finally, the same test system employed in the previous chapter (the New England test system) is used again to address its voltage stability considering different types of wind generators and FACTS controllers.

4.5.1 *AQ-bus* and Continuation Method

In order to have a reference to evaluate the performance of both methods coded in a homemade program, the PSAT software [Milano, 2005] was used to simulate the same case study.

The IEEE 14 bus test system is used in these simulations. Three cases are analyzed below.

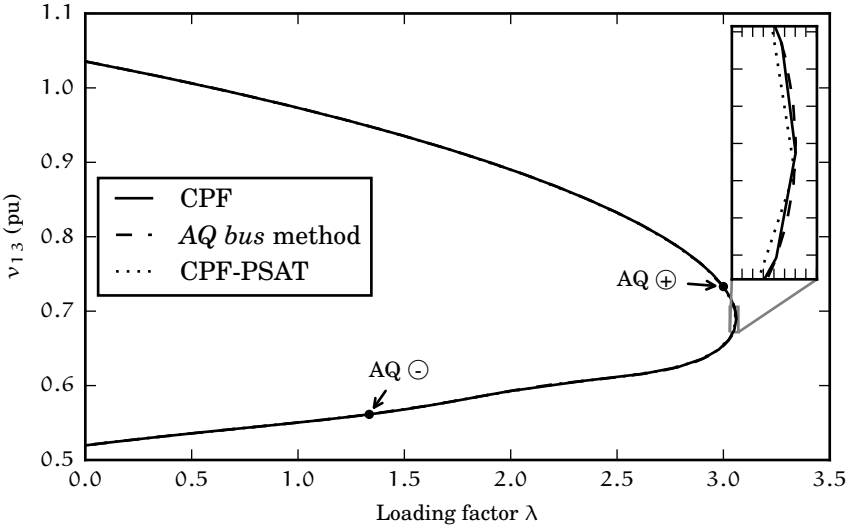

FIGURE 4.5: PV curve for the voltage magnitude at bus 13 without reactive power limits.

Case A Fig. 4.5 shows the PV curves at bus 13 obtained through the developed CPF, the *AQ-bus* method and the CPF-PSAT software. Concerning the *AQ-bus* method, the bus 9 was selected as the *AQ-bus* when the loading factor was exactly $\lambda = 3.0$; this point is depicted as AQ $\bigoplus$. From there, the reference angle $\delta_{\text{ref},9}$ was decreased by two degrees for every power flow run until the NR method diverged at $\lambda = 1.33$, point AQ $\ominus$.

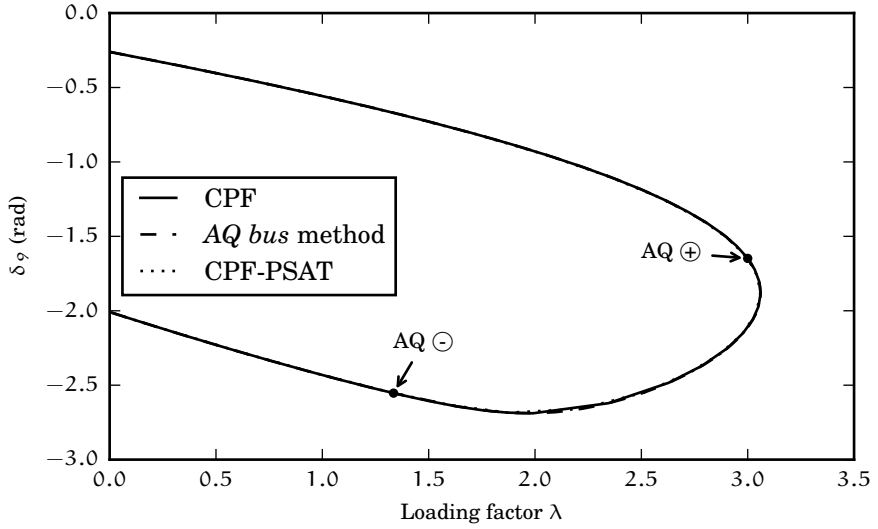

FIGURE 4.6: PV curve for the voltage magnitude at bus 13 without reactive power limits.

The voltage angle variation of bus 9 across the different values of λ is shown in Fig. 4.6. The solutions are overlapped, which means that even by defining the *AQ-bus* the same equilibrium points are obtained.

Furthermore, these PV curves are obtained by neglecting reactive power limits of synchronous generators. In this case, the maximum loading condition is due to a SNB. The maximum loading factor reached is 3.0598, 3.06 and 3.0587 for the developed CPF, *AQ-bus* method and the CPF-PSAT, respectively.

Case B Fig. 4.7 shows the same PV curves, but by enforcing synchronous generators reactive power limits; the limits of the slack generator are not considered. To simplify the discussion, note first that there are two bifurcations depicted in Fig. 4.7. These are labeled LIB ① and SNB ②. For simplicity, the author may also refer to these bifurcations through their numbers ① and ②, respectively. The acronyms indicate types of bifurcations: LIB refers to a limit-induced bifurcation, and SNB stands for a saddle-node bifurcation. For ease of reference, the value of a variable x at which the bifurcation occurs is denoted by $x^{(*)}$, where $*$ is the referred bifurcation.

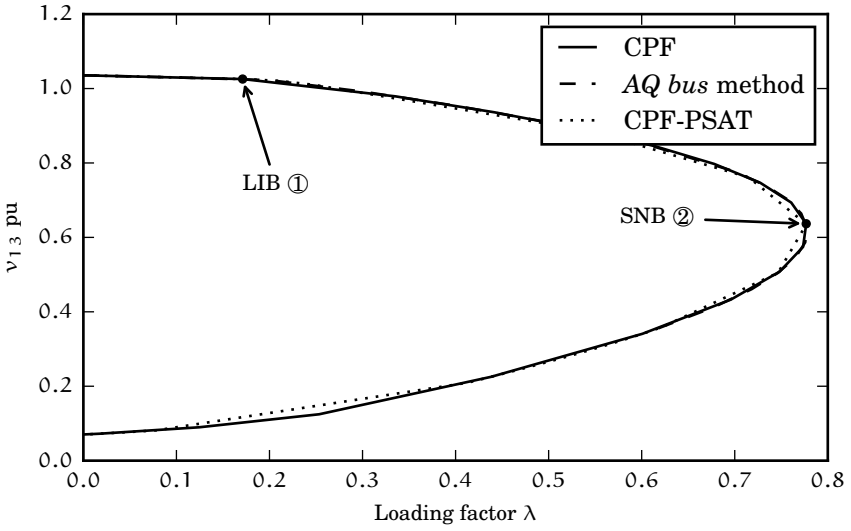

FIGURE 4.7: PV curve for the voltage magnitude at bus 13 considering reactive power limits.

For $\lambda < \lambda^{(1)}$, the set of equilibrium points exists with voltage magnitude in the neighborhood of 1.05. As λ is increased, a LIB is encountered at the point labeled LIB ① in Fig. 4.7. At this point all generators, except the reference one, reached their reactive power limits. Finally, the maximum loading condition is reached with a SNB (denoted by SNB ②), because the slack generator is assumed to have unlimited reactive power reserves and continues providing voltage control support.

The trace of the PV curve using the *AQ-bus* method is smoother because the increment of δ_{ref} was very small: $\Delta\delta_{\text{ref}} = 2\,^{\circ}$.

Case C Finally, Fig. 4.8 shows the PV curve of voltage magnitude at bus 13. Now the reactive power of the slack generator is constrained by $-1\text{pu} \leqslant q_G \leqslant 1\text{pu}$.

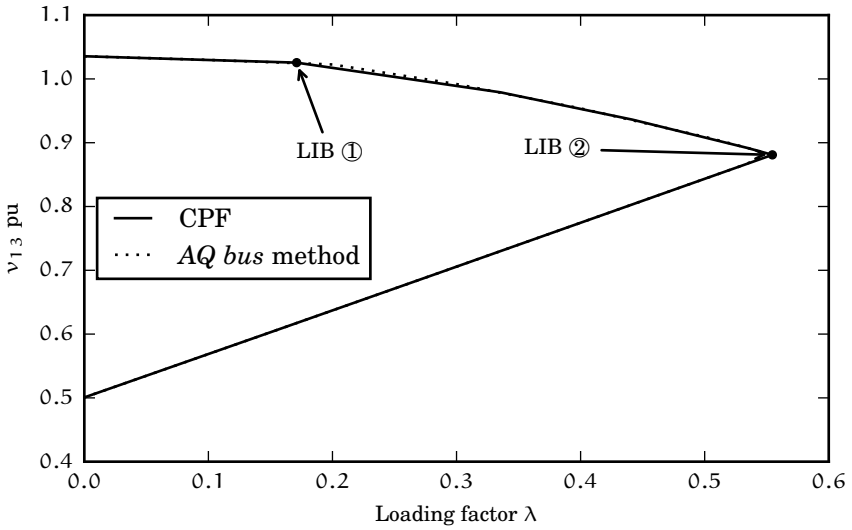

FIGURE 4.8: PV curve for the voltage magnitude at bus 13 forcing reactive power limits (including the slack limits).

Note that for $\lambda < \lambda^{②}$, the PV curve is very similar to the one obtained in the previous case. At the point LIB ②, the slack generator reached its maximum reactive power limit which implies that the voltage magnitude at the buses of the system cannot be controlled anymore. After this point, the voltage magnitude abruptly falls. This figure does not show the PV curve computed by PSAT, because this software was not able to enforce the reactive power limits of the slack generator and thus yields the same PV curve of the previous case.

Because of the similarity between the PSAT and the developed software results, the author concludes that either the continuation or the *AQ-bus* method is an adequate tool to assess the voltage collapse phenomena.

4.5.2 Complementarity Constraints in a CPF Study

An analysis of the suitability of the complementarity approach in a CPF is analyzed in this experiment.

Consider again the two bus test system of Fig. 4.1, whereas a SVC, a STATCOM and a shunt capacitor of 300 MVAr are added to bus 2. The shunt capacitor is fixed, and therefore, does not variate with the loading factor λ. Parameters of the FACTS controllers are shown in Appendix B. The CPF study is carried out with $\sigma = 0.1$, $k_L = 1$, $k_{pz} = k_{qz} = k_{pc} = k_{qc} = k_{pp} = k_{qp} = \frac{1}{3}$ and $k_G = 1$. Reactive power limits of the reference generator are considered as $-1 \leqslant q_{G,1} \leqslant 1$. The results to be shown were

obtained by means of the continuation method, however, the *AQ-bus* method produced the same results.

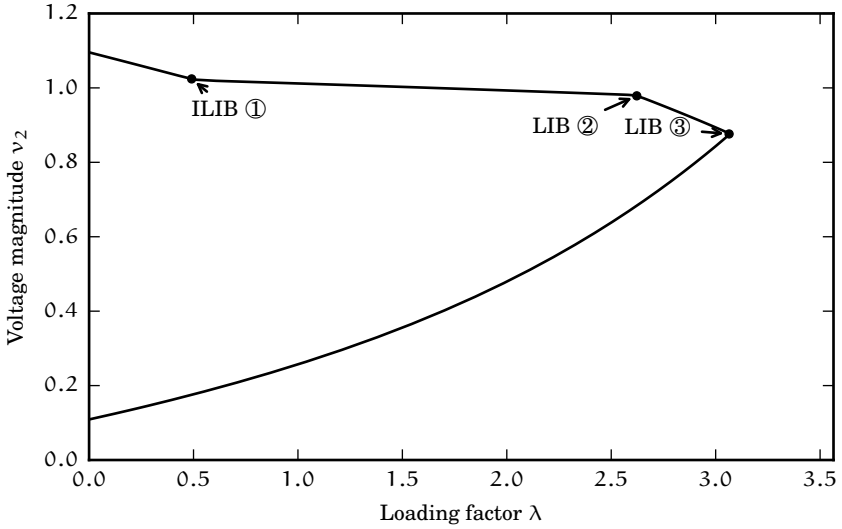

FIGURE 4.9: PV curve of the two bus example.

Fig. 4.9 shows the PV curve of the load bus. Three bifurcations are labeled in the figure as ILIB ①, LIB ② and LIB ③. In this experiment, ILIB means an inverse limit-induced bifurcation which occurs when a certain device's limit is unfixed.

The voltage magnitude of bus 2 is above its rated value (1 pu) for $\lambda < \lambda^{①}$. Within this range of loading factor values, the excessive reactive power of the fixed shunt capacitor is *consumed* by the static compensators.

Before $\lambda^{①}$ the static compensators were operating at their minimum limits, i.e. $i^{①}_{\text{STATCOM}} = i^{\min}_{\text{STATCOM}}$, and $\alpha^{①}_{\text{SVC}} = \alpha^{\min}_{\text{SVC}}$. After this point both compensators are *released* and regulate the voltage magnitude of bus 2. As λ increases, the LIB ② is encountered where the static compensators now reach their maximum limits. After this point, the voltage magnitude of bus 2 is not controlled anymore and starts to fall abruptly. Finally the maximum loading condition is reached at $\lambda = \lambda^{③} = 2.9897$. This LIB ③ is caused by the reference generator of bus 1 reaches its maximum reactive power limit.

Now the same points are depicted in Fig. 4.10, but now this figure shows the VI characteristics of both SVC and STATCOM controllers. These VI characteristics were obtained by collecting the values of voltage and current for each loading condition. These sets of values are then graphed in a (x, y) plot. As shown in the figure, before LIB ① the SVC behaves as a constant reactance and the STATCOM as a constant current source. In fact the STATCOM reached its minimum current limit before the SVC reached its minimum firing angle limit; hence the SVC yielded the LIB ①. For current values between $i^{①} \leqslant i \leqslant i^{②}$, both the SVC and the STATCOM control the

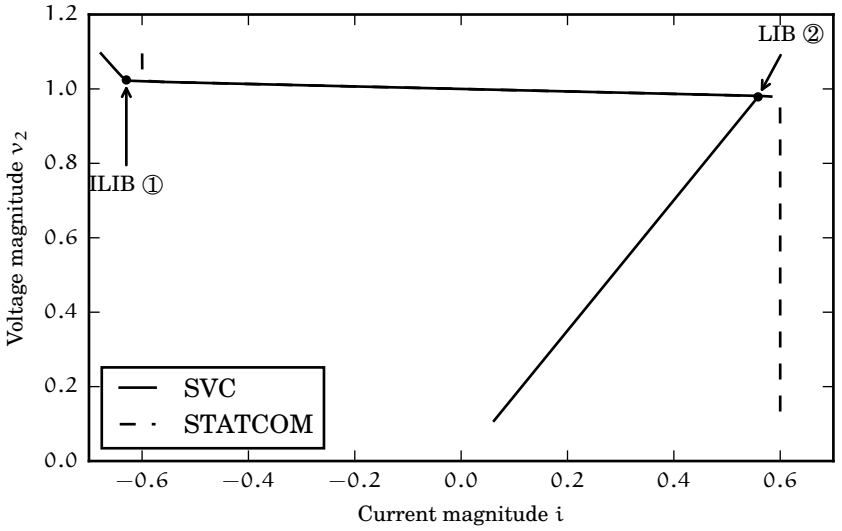

FIGURE 4.10: VI characteristics of SVC and STATCOM.

voltage magnitude of bus 2 with a small voltage droop defined by the parameter χ_{sl}. After LIB ② the SVC behaves as a constant capacitance and the STATCOM as a constant current source. Note that these curves are very similar to those presented in Section 2.2.5.

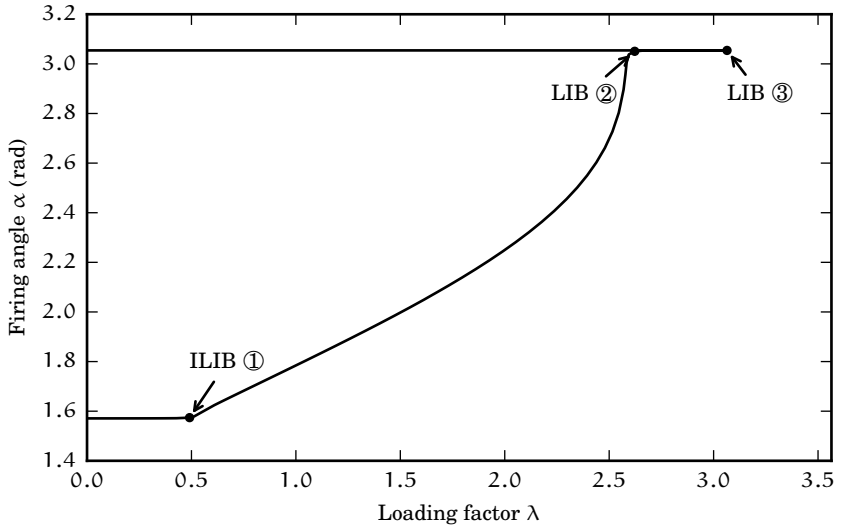

FIGURE 4.11: Firing angle of the SVC.

Next, Figs. 4.11 and 4.12 show both the firing angle and the complementarity variables of the SVC controller, respectively. The SVC data establishes that the firing angle must be constrained by $90\,^\circ \leqslant \alpha \leqslant 175\,^\circ$, which in radians is $\frac{\pi}{2}\text{rad} \leqslant \alpha \leqslant 3.05\text{rad}$. At the beginning, for $\lambda < \lambda^{①}$, the SVC's firing angle is fixed at its minimum value which is achieved by increasing the reference voltage magnitude using the complementarity variable ν_a. For $\lambda^{①} \leqslant \lambda < \lambda^{②}$ the firing angle then operates inbounds; hence both complementarity variables are zero. Finally, the second LIB is caused by the maximum

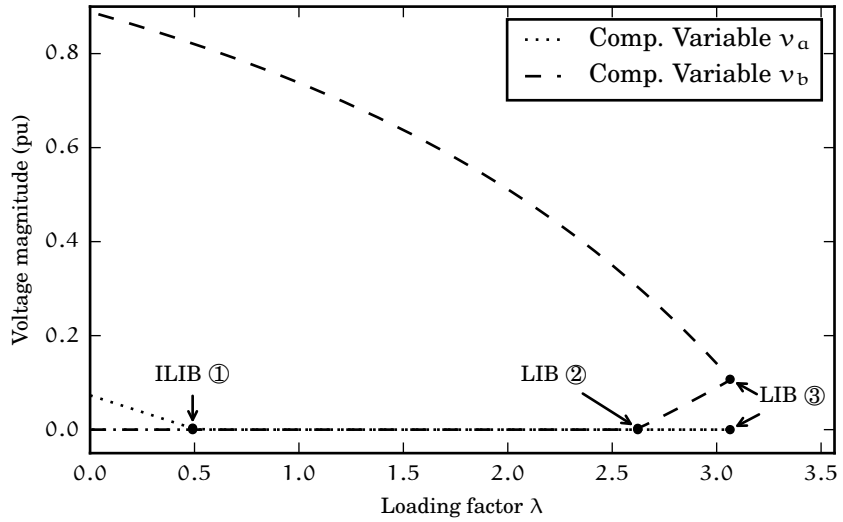

FIGURE 4.12: Complementarity variables of the SVC.

firing angle limit of the SVC; thus, for $\lambda^{②} \leqslant \lambda < \lambda^{③}$ and then for $\lambda < \lambda^{③}$ the complementarity variable ν_b increases by constraining the firing angle at its maximum.

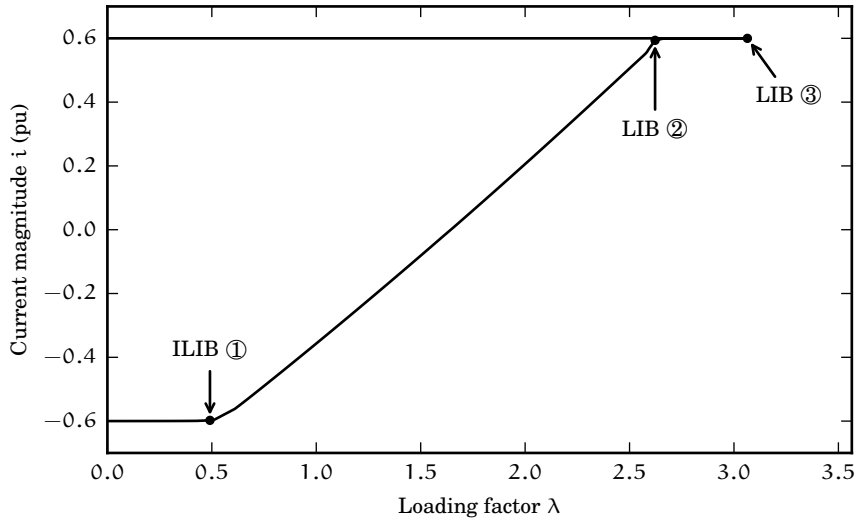

FIGURE 4.13: Current magnitude of the STATCOM.

In the same way, the behavior of both the current magnitude and the complementarity variable of the STATCOM are shown in Figs. 4.13 and 4.14. For $\lambda < \lambda^{①}$, the STATCOM's current magnitude is fixed at its minimum value. This constraint is achieved by relaxing the control law that controls the voltage magnitude of bus 2; increasing the complementarity variable ν_b. For $\lambda^{①} \leqslant \lambda < \lambda^{②}$, the STATCOM operates inbounds; hence the complementarity variable ν_b is zero. Finally, from $\lambda^{②}$, the STATCOM is fixed to its maximum current limit which is accomplished by increasing the complementarity variable ν_b.

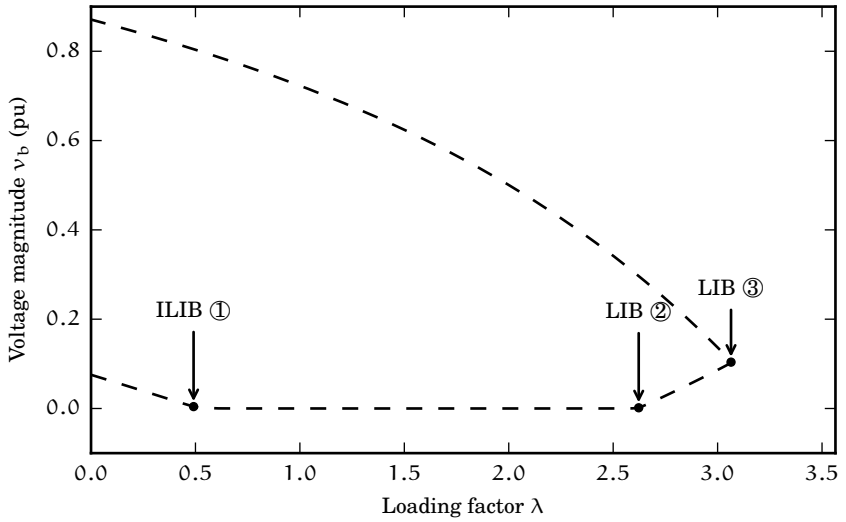

FIGURE 4.14: Complementarity variable of the STATCOM.

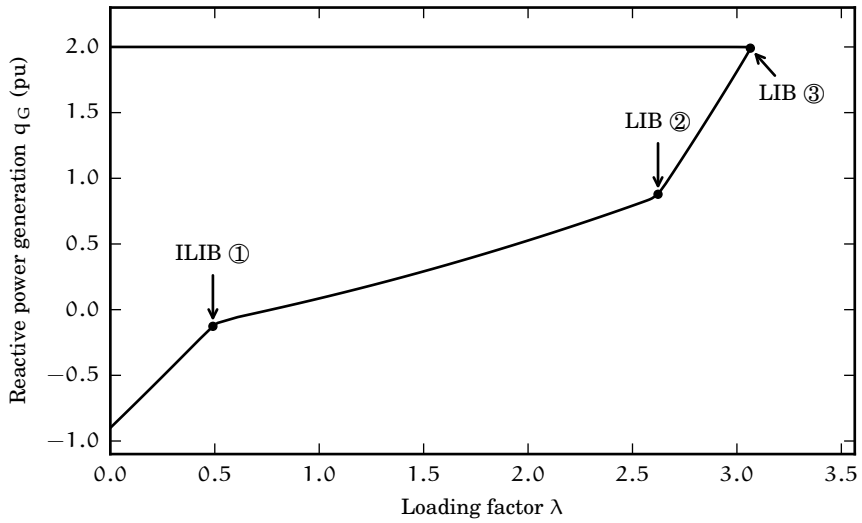

FIGURE 4.15: Reactive power of the synchronous generator.

Finally, the synchronous generator operates in the same way, but by controlling the voltage magnitude at bus 1. As shown in Fig. 4.15, the slope of the reactive power increases when the SVC and the STACOM are either at their minimum or maximum limits: $\lambda^{①} \leqslant \lambda < \lambda^{②}$. On the other hand, when this synchronous generator reaches its maximum reactive power limit at $\lambda^{③}$, the complementarity variable ν_b changes to positive values as depicted in Fig. 4.16. From Figs. 4.15 and 4.16, clearly the reactive power saturation of the synchronous generator leads the system to a LIB which occurs at $\lambda = \lambda^{③}$.

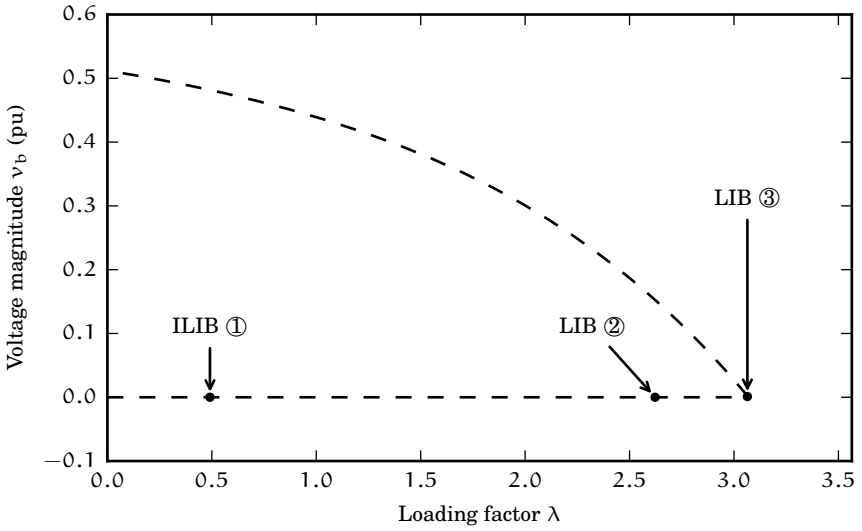

FIGURE 4.16: Complementarity variable of the synchronous generator.

4.5.3 New England Test System Including Wind Generation

In order to continue the steady-state analysis carried out in Section 3.11, this section assesses the voltage stability of those previously defined cases, which are newly reported below for completeness.

Case A The base case without wind generation. All conventional generators support the frequency disturbance with a speed droop $\mathsf{R} = 0.05$ based on each machine's rating.

Cases B, C and D Case A is slightly modified to analyze three cases with different technologies of wind generation : FSWG, DFIG, and PMSG, respectively. Data of individual wind generators are reported in Appendix B. In each case, an approximate of 12% (720 MW) of wind penetration is included by using four wind farms with a 180 MW of active power rating with the structure shown in Table 3.5. Wind farms are connected to the system through step-up transformers at buses 25, 26, 28 and 29, as shown in Fig. 3.19.

Cases E and F Given the fact that FSWGs tend to aggravate the overall network voltage profile, Case E considers four 60 MVAr SVCs embedded at buses 25,26,28 and 29. Instead of SVCs, Case F considers four 60 MVAr STATCOMs. Data of both compensators are given in Appendix B.

The results shown below were obtained by means of the continuation power flow method. The *AQ-bus* method fails to compute the PV curves when the continuation parameter needs to be a complementarity variable or a FACTS or wind generator's state variable.

Two scenarios for the power dispatch directive are considered below.

Increase by loading factor In this scenario, $k_G = 1$ for all generators; hence, each generator increases its active power as λ increases. In addition a distributed slack approach is used to provide active power support because of the system losses.

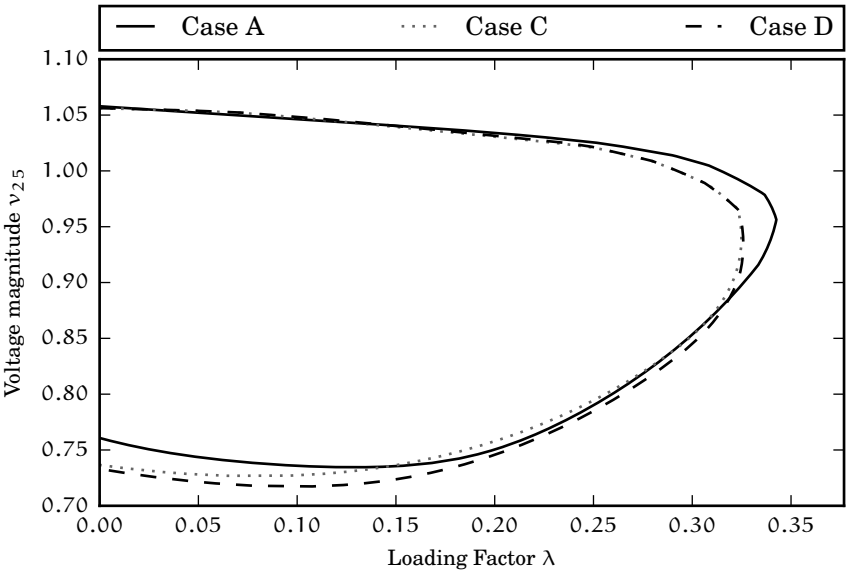

FIGURE 4.17: PV curves of bus 25 for Cases A, C, and D (loading factor as dispatch directive).

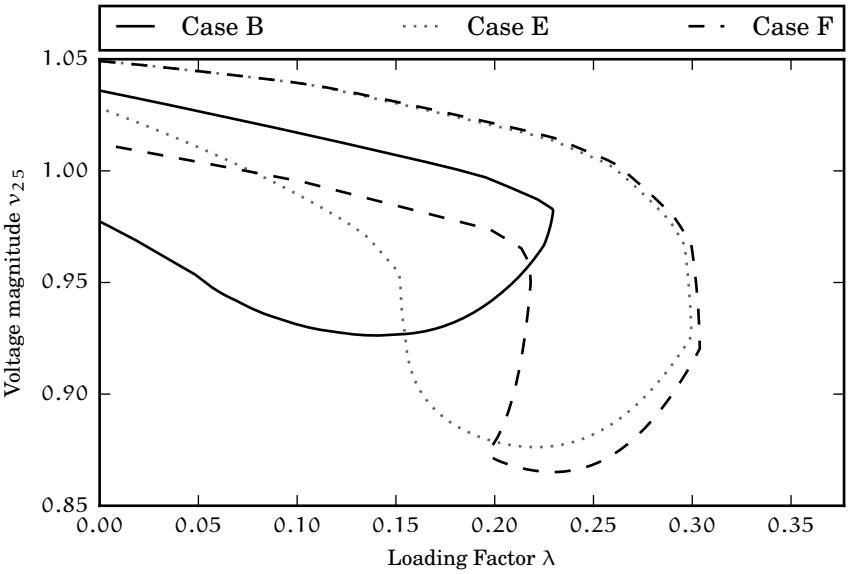

FIGURE 4.18: PV curves of bus 25 for Cases B, E, and F (loading factor as dispatch directive).

The PV curves of the voltage magnitude at bus 25 under different wind technology conditions are depicted in Figs. 4.17 and 4.18. The replaced synchronous generator was embedded at bus 37 which is directly connected to bus 25; hence, bus 25 has the most impact in the deterioration of voltage stability.

First, the most robust system is the one that does not consider wind generation, Case A; in such system the maximum loading factor was $\lambda = 0.3425$, which means that the power system can be loaded by 34.25% from its base loadability level. The voltage behavior is very similar for cases where variable-speed wind generators are embedded. For such cases, the maximum loading condition was $\lambda = 0.3248$ and $\lambda = 0.3258$ for Cases C and D, respectively.

In regards to Fig. 4.18, the smallest loading condition is when FSWGs are introduced into the system without any compensation devices, Case B, with $\lambda = 0.2295$. By adding SVCs and STATCOMs to the FSWG wind farms, the voltage stability is improved to $\lambda = 0.2995$ and $\lambda = 0.3038$ for Cases E and F, respectively.

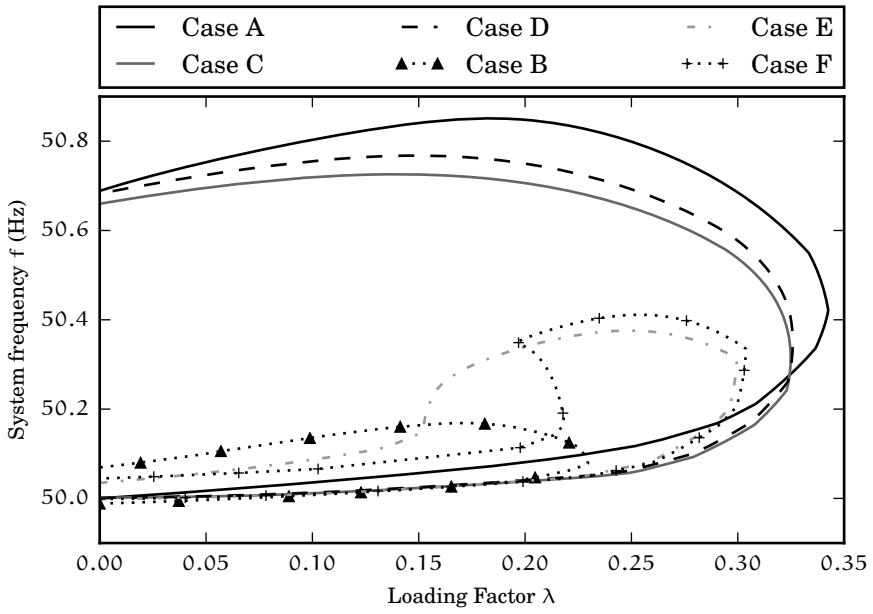

FIGURE 4.19: Frequency profile using loading factor as dispatch directive.

Next, Fig. 4.19 depicts the frequency behavior for all Cases under different loading conditions. Probably the reader expects to see that frequency decreases as much as the system's loading condition increases, but in this case, the frequency deviation is positive because of the load representation, as described below. The parameters used in Eq. (2.20) are the same for all the loads: $k_{pz} = k_{qz} = k_{pc} = k_{qc} = k_{pp} = k_{qp} = \frac{1}{3}$ and $k_{pf} = k_{qf} = 0.04$, which implies that the load is a balanced mixture of loads that behaves as constant impedance, constant current and constant power. This represents that the less voltage magnitude at the load buses. the lower the active and reactive power demands, because of both constant current and the constant impedance behaviors. With this in mind, and by considering that both the generation and the demand are equally increased by the loading factor λ, the demand is increased; however at the same time the power may also be decreased because of its voltage magnitude dependency.

Now consider that power system imbalance is only modulated by the reference generator, i.e. concentrated slack system. Remaining generators increase their active power only based on the loading factor. This is the conventional manner for performing a CPF study.

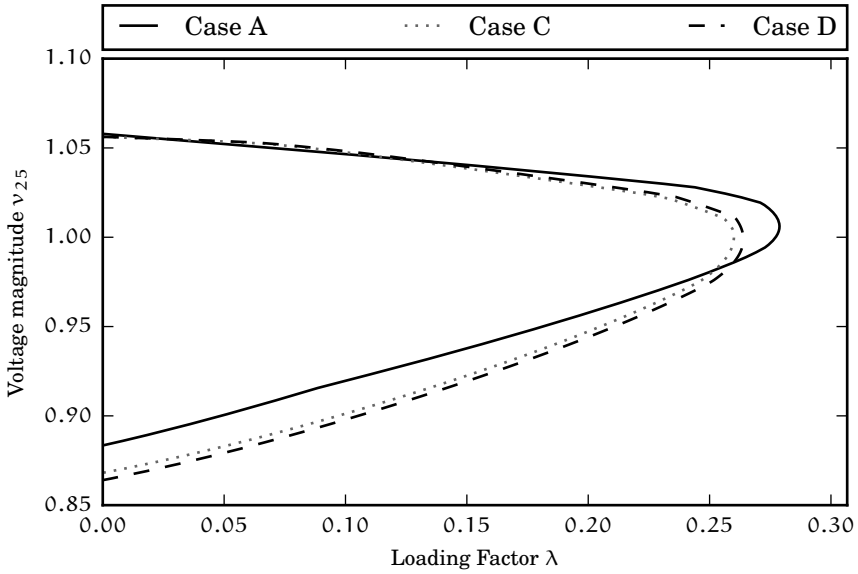

FIGURE 4.20: PV curves of bus 25 for Cases A, C, and D (loading factor as dispatch directive and concentrated slack).

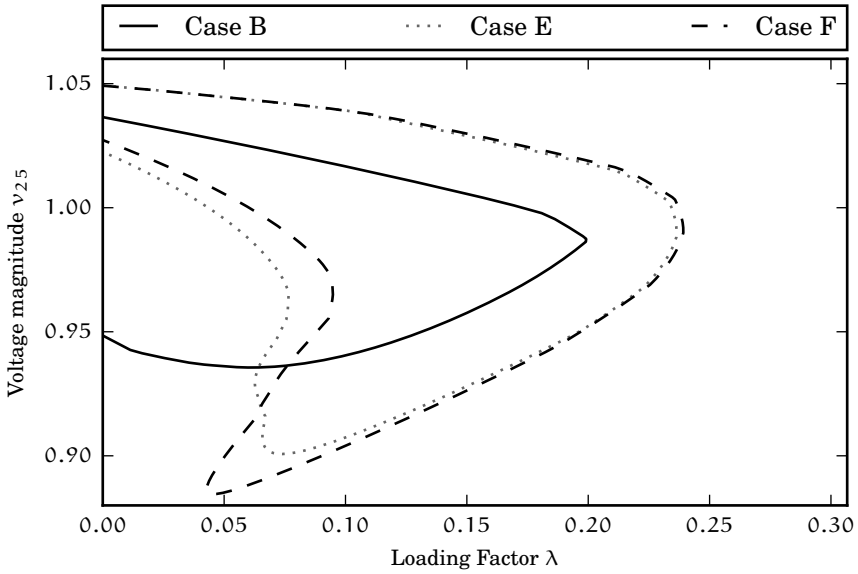

FIGURE 4.21: PV curves of bus 25 for Cases B, E, and F (loading factor as dispatch directive and concentrated slack).

Figs. 4.20 and 4.21 show the same PV curves of the voltage magnitude at bus 25, but by considering that the reference generator is the only one that modulates the active power imbalance. For Cases A, C, and D the loading factor λ was aggravated to 0.2788, 0.26, and 0.2639, respectively. The same deteriorated

behavior is presented in the FSWG-based Cases where the maximum loading factors are 0.1991, 0.2364, and 0.2392, for Cases B, E, and F, respectively. In this case, the system frequency behavior is not presented since it does not vary because of the concentrated slack basis.

Distributed slack Conversely, this scenario considers $k_G = 0$ for all generators; thus, the active power mismatch is balanced with a distributed slack basis: each generator supports the active power imbalance according to its speed droop and rated power.

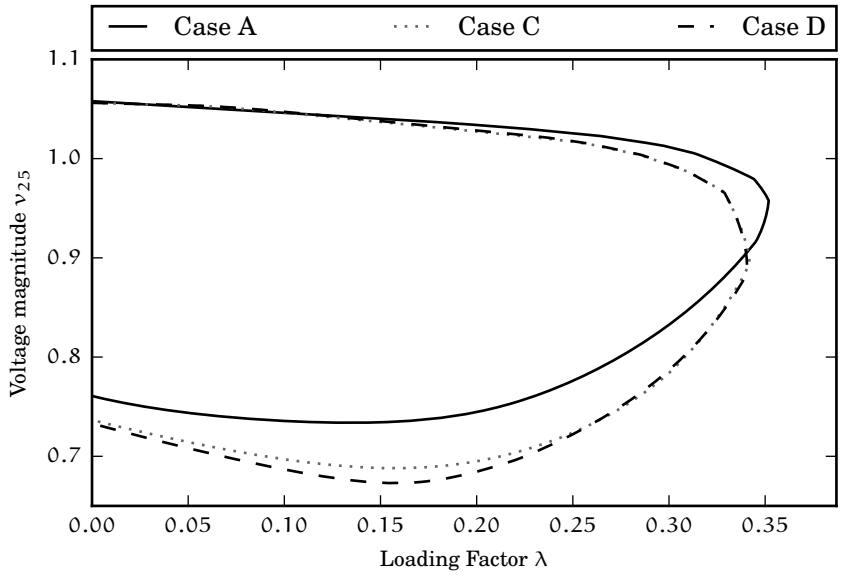

FIGURE 4.22: PV curves of bus 25 for Cases A, C, and D (distributed slack dispatch).

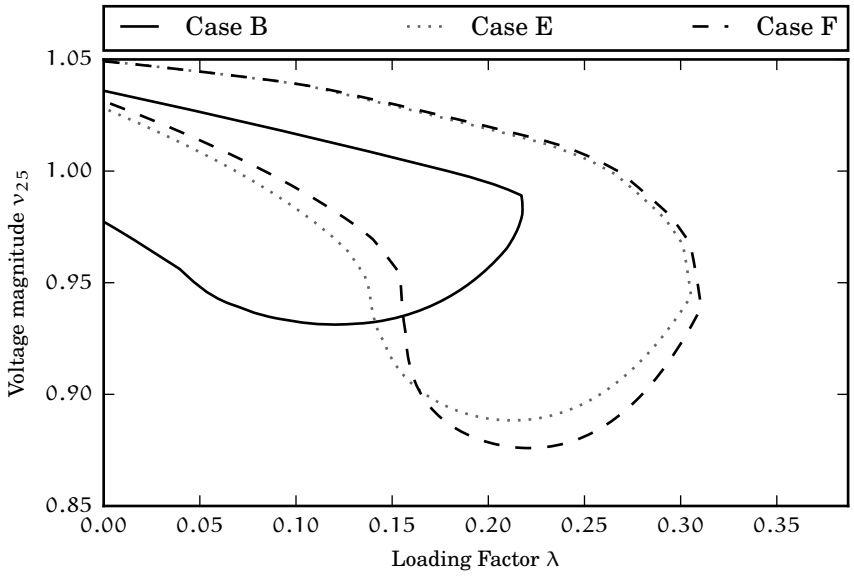

FIGURE 4.23: PV curves of bus 25 for Cases B, E, and F (distributed slack dispatch).

The PV curves of bus 25 are illustrated Figs. 4.22 and 4.23. By using a distributed slack model, the power system loadability is improved to $\lambda = 0.3518$ for Case A. By including variable-speed wind generation the loading factor is also increased to 0.3419 and 0.3405 for Cases C and D, respectively. Concerning Fig. 4.23, the voltage stability margin is established at 0.2178, 0.3054 and 0.3106 for Cases B, E and F, respectively. The shapes of the curves are very similar to those depicted in Figs. 4.17 and 4.18.

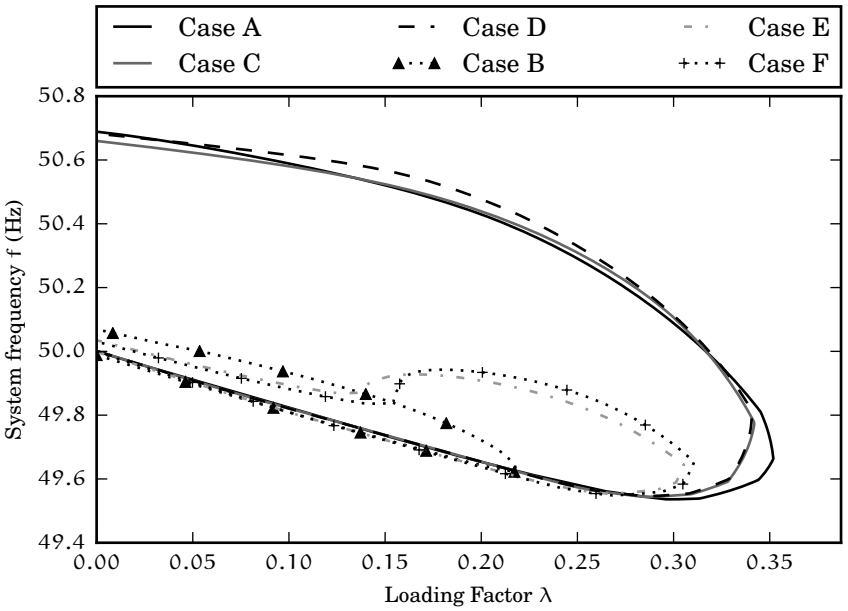

FIGURE 4.24: Frequency profile using a distributed slack as the dispatch directive.

Finally, Fig. 4.24 shows the frequency behavior for all the Cases under different loading conditions. Now the load is the only one that is increased by the loading factor λ. This consideration implies that the system's generators must modulate the active power imbalance by means of the frequency deviation Δf. As a result, from $\lambda = 0$ the system's frequency starts to decrease, which represents that the set of equilibrium points are computed from a condition where the power imbalance is negative: more demand than generation. As soon as the overall voltage profile of the system has deteriorated, the loads reduce their active and reactive power consumptions; hence, the system's frequency starts to increase.

4.6 Conclusions

In this chapter, the proposed wind generator models have been put through their paces in order to demonstrate their suitability when assessing the voltage stability phenomena. This assessment mainly relied on the continuation power flow method. Both the CPF and the *AQ-bus* method performed well when solving traditional networks (without

FACTS or wind generation). The latter, through, encountered some problems when introducing nonconventional devices and when the continuation parameter cannot be a voltage angle.

Concerning the complementarity approach, the CPF results proved that it is valid scheme for introducing the operative limits in a unified way. How the complementarity variables change their values in order to maintain the equilibrium between the control laws and the operative limits has also been shown.

The simulation results showed that the FSWG weakens the voltage stability in a power system. On the other hand, when considering static compensators like SVC or STATCOM, the loading factor is improved to almost the same level obtained in a purely conventional generation case. Finally DFIGs and PMSGs have essentially shown the same performance, which is slightly below the conventional generation case.

Chapter 5

Power Flow Analysis Considering Wind Uncertainties

5.1 Introduction

Wind turbine power sources vary in unique ways. Sometimes their output varies nearly continuously, but during light wind conditions they can produce no power for long periods of time.

This section will tackle the issues caused by the random nature of wind power by means of characterizing and analyzing this stochastic behavior with a point estimation method. The methodology presented below has been proposed in [Outcalt, 2009], and this work gives a detailed derivation of this proposal, as well as some applications by using a *probabilistic power flow* approach.

5.2 Five-Point Estimation Method

The direct approach for analyzing power flows under uncertainties is to use the well-known Monte Carlo methods. These methods have a large drawback: the the better desired accuracy, the more power flow runs. In this context, it is necessary to have a tool that approaches the *exact* solution with less computational burden. [Outcalt, 2009] proposed the five-point estimation method (5PEM), which discretizes the continuous probability distribution function associated with wind power into five distinct points, each point with its own probability. This five-point distribution is calculated to have the same mean and standard deviation of the true power distribution generated by wind data.

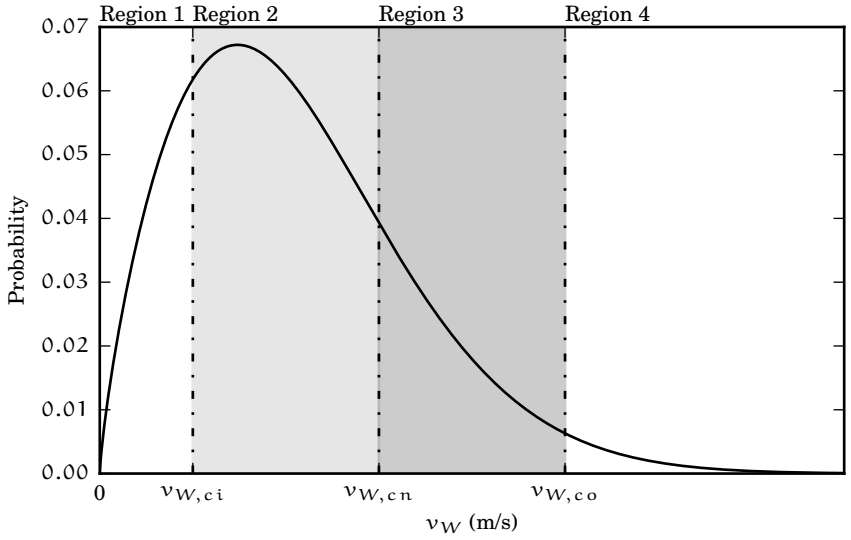

FIGURE 5.1: Weibull continuous PDF of wind speed.

Fig. 5.1 displays a Weibull probability distribution function (PDF) which describes the probabilistic behavior of wind speed for a particular location-time. For analysis purposes, this curve is divided into four regions. Regions 1 and 4 represent times when wind speed is either to low to generate electricity or too high, which causes a safety shutdown of the wind generator. Hence, power in these regions is zero. In region 3, the wind is sufficient to produce full power; therefore, a pitch control, as described in Section 2.2.6.1, is used to regulate this power. Finally, region 2 represents the region where the wind generation truly varies.

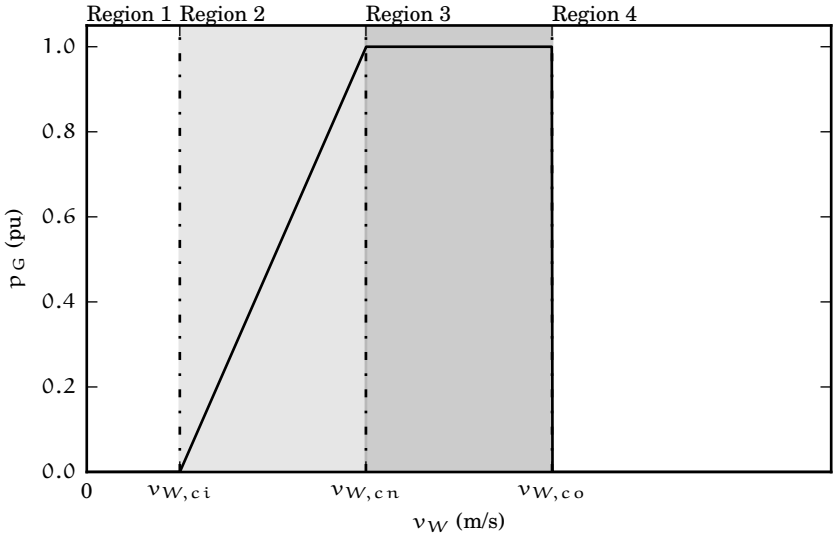

FIGURE 5.2: Output power at different wind speeds.

These four regions can be translated into a typical wind power curve, as shown in Fig. 5.2. Note that this figure is very similar to the output power curves obtained in Section 3.10.

This curve clearly represents the behavior described in the previous paragraph: zero power in regions 1 and 4 and rated power in region 3. Furthermore region 2 shows that the power increases as wind increases. The method assumes that in region 2 wind power linearly varies with the wind speed, which is a valid approximation [Fu et al., 2011].

The core of the 5PEM is the approximation of the mixture of a discrete and continuous probability distribution by a discrete distribution with all probability mass concentrated at five-points, as follows. The first point is determined from the tail areas under the Weibull distribution: regions 1 plus 4 producing zero power. Another point represents the full power region: region 3. Finally, the remaining three points represent the discretized version of region 2. The following sections show how the Weibull PDF is translated to a wind power, PDF and, the latter is then discretized into five-points.

5.2.1 Algorithm

The analytical function that describes the Weibull PDF is [Weibull, 1951]

$$f_{v_W}(v_W|\lambda,k) = \frac{k}{\lambda}\left(\frac{v_W}{\lambda}\right)^{k-1} e^{-\left(\frac{v_W}{\lambda}\right)^k}, \tag{5.1}$$

where λ is the scale parameter, and k is the shape parameter. These constants may be determined from meteorological data at a specific site, over a specified period of time. This work considers that these constants are known. For the reader's interest, there are a number of mathematical methods which perform the Weibull curve fitting: [Seguro and Lambert, 2000; Jaramillo and Borja, 2004]. The Weibull cumulative distribution function (CDF) is the area under the Weibull PDF and is expressed as [Weibull, 1951]

$$F_{v_W}(v_W|\lambda,k) = \int_{-\infty}^{v_W} f_{v_W}(v_W|\lambda,k)\,dv_W \tag{5.2a}$$

$$= 1 - e^{\left(\frac{v_W}{\lambda}\right)^k}. \tag{5.2b}$$

Regarding wind power, the curve shown in Fig. 5.2 is mathematically expressed by a piecewise-defined function:

$$p_W = \begin{cases} 0 & v_W \leqslant v_{W,ci} \\ \alpha + \beta v_W & v_{W,ci} \leqslant v_W \leqslant v_{W,n} \\ p_W^{max} & v_{W,n} \leqslant v_W \leqslant v_{W,co} \\ 0 & v_{W,co} \leqslant v_W \end{cases}, \tag{5.3}$$

where v_W is the wind speed, $v_{W,ci}$ is the cut-in wind speed below which no power is generated, $v_{W,co}$ is the cut-out wind speed above which no power is generated and $v_{W,n}$ stands for the full power wind speed. Constants α, and β are chosen to correspond with $v_{W,ci}$ and v_n such that $\alpha + \beta v_{W,ci} = 0$ and $\alpha + \beta v_n = p_W^{max}$.

The formulation to discretize this function into 5 points $\phi_i = (P_i, C_i)\, \forall i \in \{1 \dots 5\}$, each point with power P_i and its own probability C_i, is shown below.

5.2.1.1 Point ϕ_1

Point ϕ_1 is associated with the probability that power is equal to zero. This only happens either when wind speed is very light, and the wind turbine cannot sustain any generation, or when wind speed is very high, and wind turbine is safety turned off. Therefore, it is calculated from the Weibull CDF as

$$P_1 = 0 \tag{5.4}$$

$$C_1 = \Pr(p_W = 0) = \Pr(v_W \leqslant v_{W,ci}) + \Pr(v_W \geqslant v_{W,co}) \tag{5.5}$$

$$= F_{v_W}(v_{W,ci}|\lambda, k) + \left(1 - F_{v_W}(v_{W,co}|\lambda, k)\right) , \tag{5.6}$$

where F_{v_W} is computed by using Eq. (5.2). The first term represents the area under the Weibull PDF between $v_W \in \left[0, v_{W,ci}\right]$, whereas the second term is the area of the Weibull PDF in $v_W \in \left[v_{W,co}, \infty\right]$.

5.2.1.2 Point ϕ_5

This fifth point represents the rated power operation and is similarly determined by using the Weibull CDF:

$$P_5 = p_W^{max} \tag{5.7}$$

$$C_5 = \Pr(p_W = p_W^{max}) = \Pr(v_{W,n} \leqslant v_W \leqslant v_{W,co}) \tag{5.8}$$

$$= \left(1 - F_{v_W}(v_{W,n}|\lambda, k)\right) - \left(1 - F_{v_W}(v_{W,co}|\lambda, k)\right) . \tag{5.9}$$

5.2.1.3 Points ϕ_2, ϕ_3 and ϕ_4

There are two points, ϕ_1 and ϕ_5, already determined and 3 more points to be determined from the continuous function of region 2.

Change of Variables If a variable y is a function of another variable x, that is, $y = g(x)$, then a change of variables is needed to obtain the PDF of variable y, by taking into account that x has a known PDF. According to [Villanueva et al., 2011], when g is monotonic and $f_x(x)$ is the PDF of x, then the following equation can be applied to change the variables of the PDF:

$$f_y(y) = \left|g_y^{-1}(y)\right| f_x(g^{-1}(y)), \tag{5.10}$$

where $f_y(y)$ is the new PDF in terms of the variable y, $g_y(y)$ stands for the derivative of the original function $g(y)$, and $g^{-1}(y)$ is the inverse function of $g(y)$.

Thus, by considering that $g(v_W) = p_W = \alpha + \beta v_W$ is function of v_W and is monotonic, the following is defined:

$$g(v_W) = \alpha + \beta v_W \tag{5.11}$$

$$g^{-1}(p_W) = \frac{p_W - \alpha}{\beta} \tag{5.12}$$

$$g_{p_W}^{-1}(p_W) = \frac{1}{\beta}. \tag{5.13}$$

Therefore, by substituting Eqs. (5.12) and (5.13) in Eq. (5.10),

$$f_{p_W|\lambda,k} = \left|g_{p_W}^{-1}(p_W)\right| f_{v_W}(g^{-1}(y)|\lambda, k) \tag{5.14}$$

$$= \frac{1}{\beta} f_{v_W}\left(\frac{p_W - \alpha}{\beta}|\lambda, k\right). \tag{5.15}$$

Note that Eq. (5.15) does not have an *area of one* under the curve [Outcalt, 2009]; this area is instead:

$$P_{R2} = \Pr(0 < p_W < p_W^{max}) = \int_0^{p_W^{max}} f_{p_W}(p_W|\lambda, k)\, dp_W \tag{5.16}$$

$$= \int_{v_{W,ci}}^{v_{W,n}} f_{v_W}(v_W|\lambda, k)\, dv_W = 1 - C_1 - C_5. \tag{5.17}$$

Since PDFs must have an integrated area of one under the curve, this fact will be used in the discretization of the continuous component of p_W to obtain ϕ_2, ϕ_3 and ϕ_4. Therefore, Eq. (5.15) is redefined to be a valid PDF:

$$\bar{f}_{p_W}(p_W|\lambda,k) = \frac{f_{p_W}(p_W|\lambda,k)}{P_{R2}}\,. \tag{5.18}$$

Hence,

$$\int_0^{p_W^{max}} \bar{f}_{p_W}(p_W|\lambda,k)\,dp_W = 1\,. \tag{5.19}$$

Finally, Eq. (5.18) is translated into the original Weibull PDF:

$$\bar{f}_{p_W}(p_W|\lambda,k) = \frac{f_{p_W}(p_W|\lambda,k)}{P_{R2}} \tag{5.20}$$

$$= \frac{f_{v_W}(\frac{p_W-\alpha}{\beta}|\lambda,k)}{(1-C_1-C_5)\,\beta} \tag{5.21}$$

By using the expression obtained in Eq. (5.21), the curve in region 2 can be discretized into three points, resulting in an overall five-point distribution. The following equations show the mathematical procedure to obtain these final three points ($\phi 2$, $\phi 3$ and $\phi 4$).

Define the following statistical moments [DeGroot and Schervish, 2012]:

$$\bar{\mu} = \int_0^{p_W^{max}} p_W \bar{f}_{pw}(p_W|\lambda,k)\,dp_W \tag{5.22}$$

$$\bar{\sigma}^2 = \int_0^{p_W^{max}} (p_W-\bar{\mu})^2\,\bar{f}_{p_W}(p_W|\lambda,k)\,dp_W \tag{5.23}$$

$$\lambda_j = \int_0^{p_W^{max}} \left(\frac{p_W-\bar{\mu}}{\bar{\sigma}}\right)^j \bar{f}_{p_W}(p_W|\lambda,k)\,dp_W \tag{5.24}$$

$$z = \frac{p_W-\bar{\mu}}{\bar{\sigma}}\,, \tag{5.25}$$

where $\bar{\mu}$ stands for the mean value of $\bar{f}_{p_W}$, which is the expected value or central tendency of p_W, $\bar{\sigma}^2$ is the variance of $\bar{f}_{p_W}$ that measures the spread out of p_W, λ_j is the standard central moment of the random variable, and z denotes the standardized value of p_W and relates the distance of p_W from the mean.

TABLE 5.1: Three-point discrete distribution

Discretized z	z_2	z_3	z_4
Discrete probability	p_2	p_3	p_4

The continuous distribution in region 2 is discretized into three points, as shown in Table 5.1. This discrete distribution must meet:

$$p_2 + p_3 + p_4 = 1\,. \tag{5.26}$$

The discrete probabilities, p_2, p_4, and the standardized values, z_2, z_4, are obtained by equating the moments of this discrete distribution with the λ_j moments of the continuous one [Hong, 1998]:

$$\sum_{i=2}^{4} p_i z_i^j = \lambda_j \quad \forall j \in \{1,2,3,4\}\,. \tag{5.27}$$

By expanding Eq. (5.27),

$$\lambda_1 = p_2 z_2 + p_3 z_3 + p_4 z_4 \tag{5.28}$$
$$\lambda_2 = p_2 z_2^2 + p_3 z_3^2 + p_4 z_4^2 \tag{5.29}$$
$$\lambda_3 = p_2 z_2^3 + p_3 z_3^3 + p_4 z_4^3 \tag{5.30}$$
$$\lambda_4 = p_2 z_2^4 + p_3 z_3^4 + p_4 z_4^4\,. \tag{5.31}$$

By definition $\lambda_1 = 0$ and $\lambda_2 = 1$, and by considering $z_3 = 0$, the set of equations is transformed:

$$0 = p_2 z_2 + p_4 z_4 \tag{5.32}$$
$$1 = p_2 z_2^2 + p_4 z_4^2 \tag{5.33}$$
$$\lambda_3 = p_2 z_2^3 + p_4 z_4^3 \tag{5.34}$$
$$\lambda_4 = p_2 z_2^4 + p_4 z_4^4\,. \tag{5.35}$$

By using Eqs. (5.32) and (5.33), p_2 and p_4 are calculated:

$$p_2 = -\frac{1}{z_2\,(z_4 - z_2)} \tag{5.36}$$
$$p_4 = \frac{1}{z_4\,(z_4 - z_2)}\,. \tag{5.37}$$

By substituting Eqs. (5.36) and (5.37) in Eqs. (5.34) and (5.35), z_2 and z_4 are solved:

$$z_2 = \frac{\lambda_3}{2} + \sqrt{\lambda_4 - \frac{3\lambda_3^2}{4}} \tag{5.38}$$

$$z_4 = \frac{\lambda_3}{2} - \sqrt{\lambda_4 - \frac{3\lambda_3^2}{4}}\,. \tag{5.39}$$

Finally, $z_3 = 0$ and $p_3 = 1 - p_2 - p_4$.

Once z_i and p_i are obtained, the corresponding points ϕ_i can be revealed as

$$P_2 = \bar{\mu} + \bar{\sigma} z_2 \qquad C_2 = p_2\,(1 - C_1 - C_5) \tag{5.40}$$

$$P_3 = \bar{\mu} + \bar{\sigma} z_3 \qquad C_3 = p_3\,(1 - C_1 - C_5) \tag{5.41}$$

$$P_4 = \bar{\mu} + \bar{\sigma} z_4 \qquad C_4 = p_4\,(1 - C_1 - C_5)\,, \tag{5.42}$$

where $\bar{\mu}$, $\bar{\sigma}$, as well as previously used λ_3 and λ_4, are computed by numerically integrating Eqs. (5.22) to (5.24), respectively.

Lastly, the power distribution of a wind generator is discretized by the following five ϕ points:

TABLE 5.2: Five-point discrete distribution

Point	ϕ_1	ϕ_2	ϕ_3	ϕ_4	ϕ_5
Wind farm power	0	P_2	P_3	P_4	$p_W^{\max}$
Discretized probability	C_1	C_2	C_3	C_4	C_5

5.3 Case Studies

The accuracy and efficiency of the 5PEM is tested by comparing its results with those obtained from the Monte Carlo simulation considering 10,000 samples. This number of simulations is high enough to guarantee the convergence of the Monte Carlo method [Morales and Perez-Ruiz, 2007]. Because of the high number of power flow runs when using the MC method, the High Performance Computing Cluster (HPCC) of the *Facultad de Ingeniería Eléctrica* was used for the simulations. Again the probabilistic power flow was coded in the Python and C programming languages, with a multithreading approach in order to parallelize several power flow runs.

With the stated purpose, the New England 39 bus system is analyzed when it contains different numbers of wind farms, each one with a 180 MW output rated power. The effect of wind generation was incorporated by using simple synchronous generation dispatched at the active power obtained by either the 5PEM or the MC method. Each

wind generator has voltage magnitude control capability; hence these *wind generators* are treated as *PV buses.*With aim of examining the overall system behavior (active and reactive power generation and transmission losses), these simulations were performed by using a concentrated slack generator.

The 5PEM approach is carried out by means of the following steps.

1. Estimate five discrete points for each wind farm by using the 5PEM algorithm.
2. Perform a cartesian product with each five-point set; hence, the total combinations yield $n = 5^{n_w}$ set of powers and the associated probabilities, where n_w is the total number of wind farms.
3. Run n load flows by considering each power combination.

The Monte Carlo simulations are performed as follows.

1. Generate 10,000 random wind speed values based on the Weibull distribution function of each wind farm. The random number generation is computed with a Mersenne Twister algorithm by using the built-in C language function. This number of MC simulations has demonstrated good results in other probabilistic power flows [Morales and Perez-Ruiz, 2007].
2. Evaluate this set of random wind speeds using Eq. (5.3); hence, a total of 10,000 wind powers are obtained.
3. Run n load flows considering each power of the previous step.

In order to provide a general overview of the overall performance of the 5PEM, the following error indices are defined for each output random variable x:

$$\epsilon_{\mu}^{x} = \left| \frac{\mu_{MC}^{x} - \mu_{5PEM}^{x}}{\mu_{MC}^{x}} \right| \times 100\,[\%] \tag{5.43}$$

$$\epsilon_{\sigma}^{x} = \left| \frac{\sigma_{MC}^{x} - \sigma_{5PEM}^{x}}{\sigma_{MC}^{x}} \right| \times 100\,[\%]\ , \tag{5.44}$$

where μ_{MC}^{x} and σ_{MC}^{x} are the mean and standard deviation associated with the results obtained by the Monte Carlo simulation, which are taken as reference values. Similarly, μ_{5PEM}^{x} and σ_{5PEM}^{x} are the mean and standard deviation associated with the 5PEM's results. Finally, x is a variable that may refer to bus voltage magnitude/angle (v_k, δ_k), active/reactive power injections (p_k,q_k) or active/reactive power line flows (p_{km}, q_{km}).

Table 5.3: Wind farm data.

Wind farm	Bus	k	λ (m/s)	$v_{W,ci}$ (m/s)	$v_{W,n}$ (m/s)	$v_{W,co}$ (m/s)	p_W^{max} (pu)	v_{ref} (pu)
I	25	1.768	11.861	3.57	13.4	25	1.8	1.0
II	26	2.5034	10.0434	3.57	13.4	25	1.8	1.0
III	28	1.768	11.861	3.57	13.4	25	1.8	1.0
IV	29	2.5034	10.0434	3.57	13.4	25	1.8	1.0

Three cases are analyzed: case A incorporates one wind farm (WF I) connected at bus 25, case B includes two wind farms (WFs I and II) connected at buses 25 and 26 and finally case C considers four wind farms, WFs I, II, III and IV, embedded to buses 25, 26, 28 and 29. Wind farm data is shown in Table 5.3 which was obtained from [Jaramillo and Borja, 2004].

Table 5.4: Calculated five-points for each wind farm.

Wind farm	ϕ_1	ϕ_2	ϕ_3	ϕ_4	ϕ_5
I	$(0, 0.137)$	$(1.578, 0.155)$	$(0.877, 0.280)$	$(0.206, 0.163)$	$(1.8, 0.265)$
II	$(0, 0.072)$	$(1.565, 0.198)$	$(0.890, 0.400)$	$(0.231, 0.202)$	$(1.8, 0.128)$
III	$(0, 0.137)$	$(1.578, 0.155)$	$(0.877, 0.280)$	$(0.206, 0.163)$	$(1.8, 0.265)$
IV	$(0, 0.072)$	$(1.565, 0.198)$	$(0.890, 0.400)$	$(0.231, 0.202)$	$(1.8, 0.128)$

By applying the 5PEM, the wind power PDF of each wind farm is discretized into the five-points shown in Table 5.4. Data are presented as $\phi_i = (P_i, C_i) \forall i \in \{1 \dots 5\}$, where P_i is the power of point ϕ_i in per unit values, and C_i is its associated probability. Note that $\sum_{i \in \{1 \dots 5\}} C_i = 1$.

Case A In this case, only one wind farm is connected at bus 25, $n_W = 1$, then five run flows are performed, each one considering a point of the discretized distribution. Table 5.5 shows the mean and standard deviation results for a selected set of output random variables, which have been representative of the general results obtained from both probabilistic approaches. As can be observed, the 5PEM provides good results compared with the Monte Carlo values, both for mean and standard deviation. By comparing the slack output power, the 5PEM represents the overall stochastic active power flow in the system well.

Table 5.5: Mean and standard deviation for Case A (selected Values).

Case A		$p_{WF\ I}$	$q_{WF\ I}$	p_{slack}	q_{slack}	v_{16}	δ_{16}
Monte Carlo	μ	0.9957	−0.4722	5.5697	1.9857	1.0317	−0.1225
	σ	0.6840	0.0568	0.5824	0.0987	0.0002	0.0254
5PEM	μ	1.0018	−0.4723	5.5366	1.9801	1.0317	−0.1208
	σ	0.6820	0.0569	0.5716	0.0963	0.0002	0.0249
Error (%)	ϵ_μ	0.6160	0.0020	0.5941	0.2798	0.0019	1.3319
	ϵ_σ	0.2952	0.1636	1.8408	2.4738	3.1684	2.0189

Figs. 5.3 and 5.4 show the PDF and CDF of the active and reactive powers at the wind farm bus. It must be noted that the PDF for the 5PEM is concentrated at five-points which are those obtained by the described scheme. On the other hand, the 5PEM CDF is similar to the CDF obtained by means of the MC simulations.

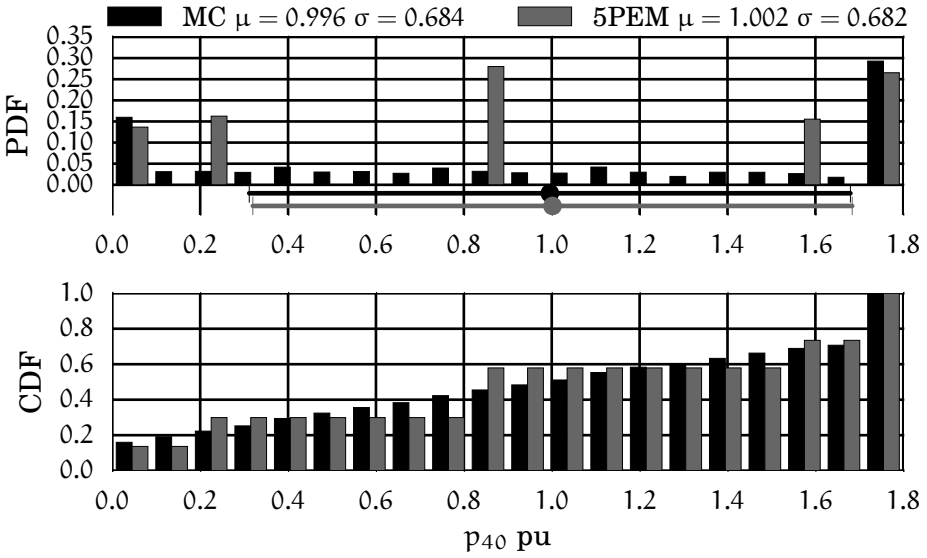

FIGURE 5.3: PDF and CDF of the wind farm active power (Case A).

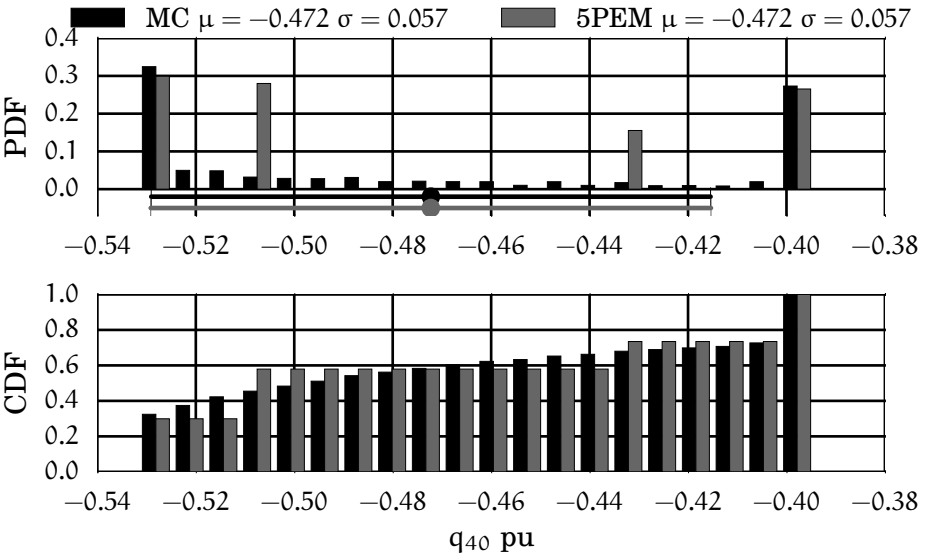

FIGURE 5.4: PDF and CDF of wind farm reactive power (Case A).

Finally, Figs. 5.5 and 5.6 show distribution functions of the slack active and reactive powers, respectively. The PDF and CDF agree in both approaches.

Case B It follows that this case considers two wind farms connected at buses 25 and 26. For this case the number of load flows computed by the 5PEM is $5^2 = 25$. Table 5.6 shows the obtained results of both methodologies. In this case, the

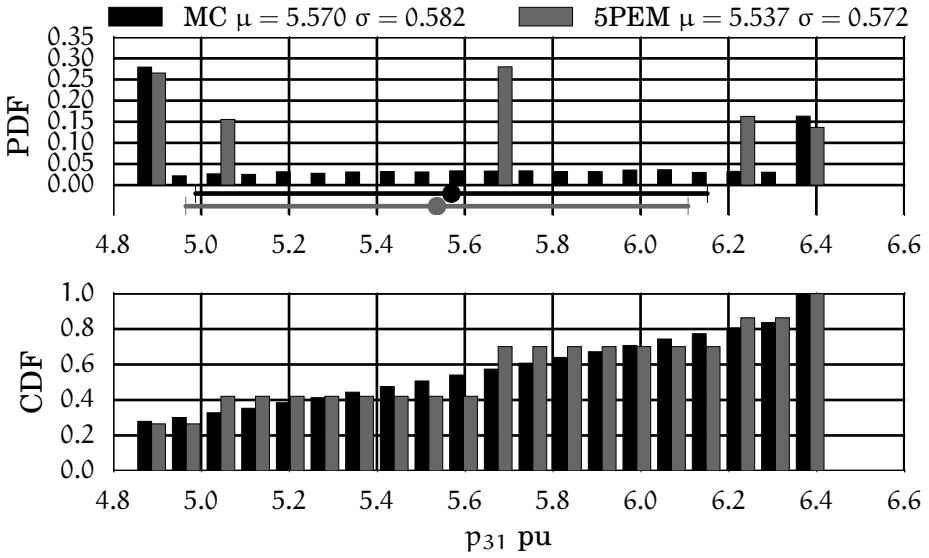

FIGURE 5.5: PDF and CDF of slack active power (Case A).

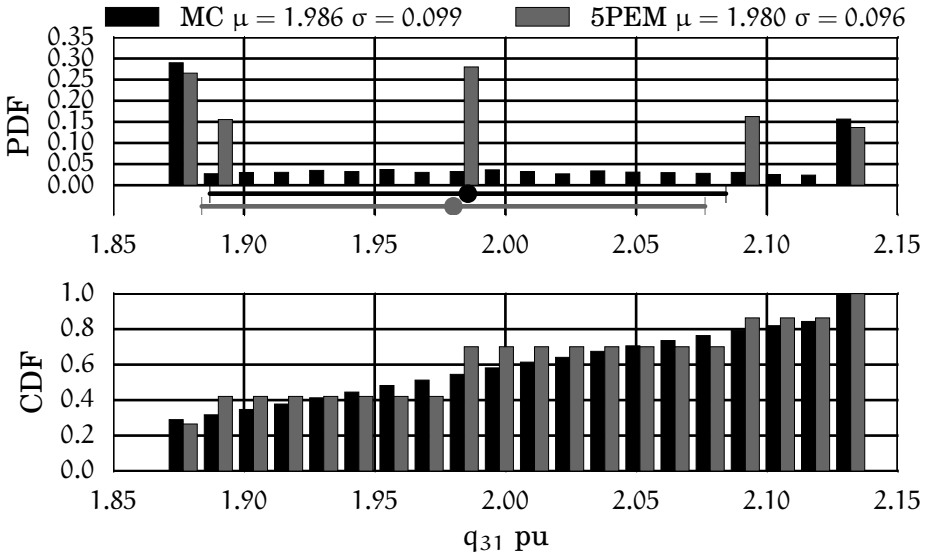

FIGURE 5.6: PDF and CDF of slack reactive power (Case A).

TABLE 5.6: Mean and standard deviation for Case B (selected Values).

Case B		$p_{WF\ I}$	$q_{WF\ I}$	p_{slack}	q_{slack}	v_{16}	δ_{16}
Monte Carlo	μ	1.0074	−0.4585	4.7495	1.8880	1.0299	−0.0838
	σ	0.6805	0.0575	0.7774	0.1033	0.0005	0.0350
5PEM	μ	1.0018	−0.4598	4.5951	1.8682	1.0299	−0.0765
	σ	0.6820	0.0577	0.8279	0.1053	0.0006	0.0375
Error (%)	ϵ_μ	0.5582	0.2878	3.2512	1.0508	0.0003	8.7754
	ϵ_σ	0.2193	0.3393	6.4895	1.9018	13.5836	7.0815

5PEM scheme exhibits a higher error especially in the active and reactive power standard deviations of the slack generator, both with error values of 6.4895% and

1.9018%, respectively. In addition, the voltage at bus 16 presents high error values of standard deviation, but in fact the real difference between both schemes is very small.

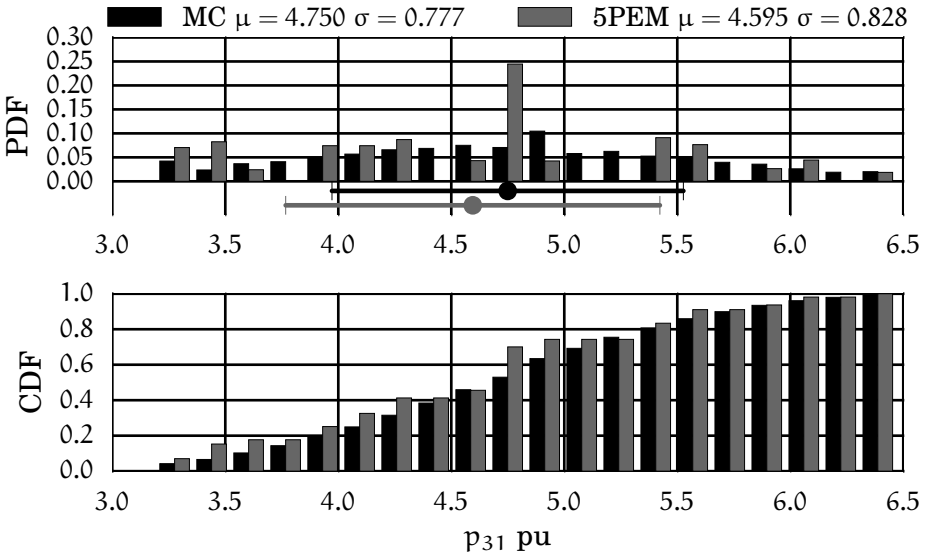

FIGURE 5.7: PDF and CDF of slack generator active power (Case B).

Figs. 5.7 and 5.8 show the distribution functions of both active and reactive powers of the slack generator. In this case, how the 5PEM concentrates a set of continuous values in a finite number of discrete points is clearer.

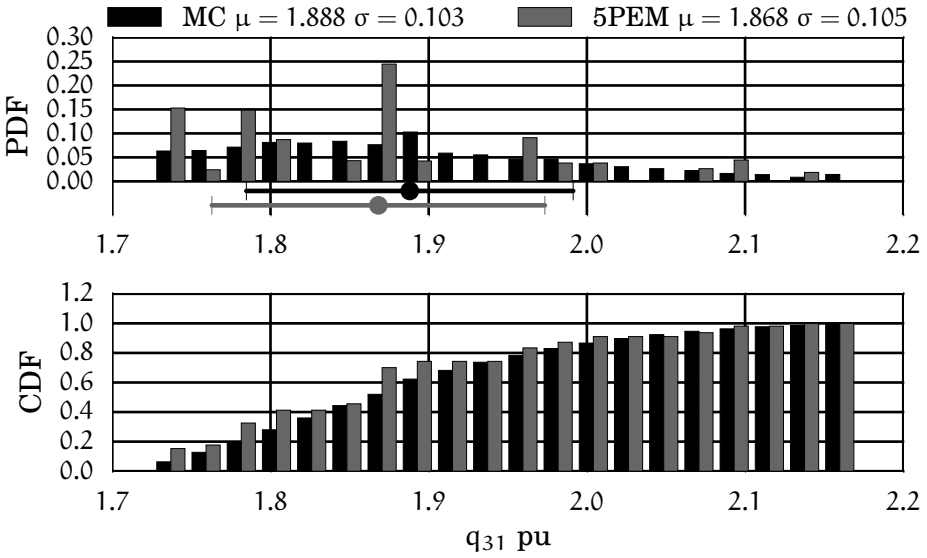

FIGURE 5.8: PDF and CDF of slack generator reactive power (Case B).

Case C Now consider four wind farms connected to buses 25, 26, 28 and 29. In this case the 5PEM required $5^4 = 625$ power flow runs to take into account all the possible combinations of the discretized wind power distribution functions.

TABLE 5.7: Mean and standard deviation for Case C (selected Values).

Case C		$p_{WF\ I}$	$q_{WF\ I}$	p_{slack}	q_{slack}	v_{16}	δ_{16}
Monte Carlo	μ	0.9948	−0.4405	3.1505	1.7821	1.0266	−0.0084
	σ	0.6886	0.0592	1.1198	0.0712	0.0016	0.0516
5PEM	μ	1.0018	−0.4393	3.0208	1.7789	1.0263	−0.0023
	σ	0.6820	0.0592	1.1782	0.0691	0.0018	0.0545
Error (%)	ϵ_μ	0.7029	0.2683	4.1155	0.1782	0.0224	72.7875
	ϵ_σ	0.9546	0.0166	5.2113	2.9357	13.5751	5.7121

Table 5.7 shows the obtained results by using both the MC and 5PEM schemes. Again the standard deviation errors are greater than the mean ones in almost all the cases. In general, the mean values of the selected values present reasonable errors, except the mean value of the voltage angle at bus 16 δ_{16}. Note that these angles are almost zero for practical purposes.

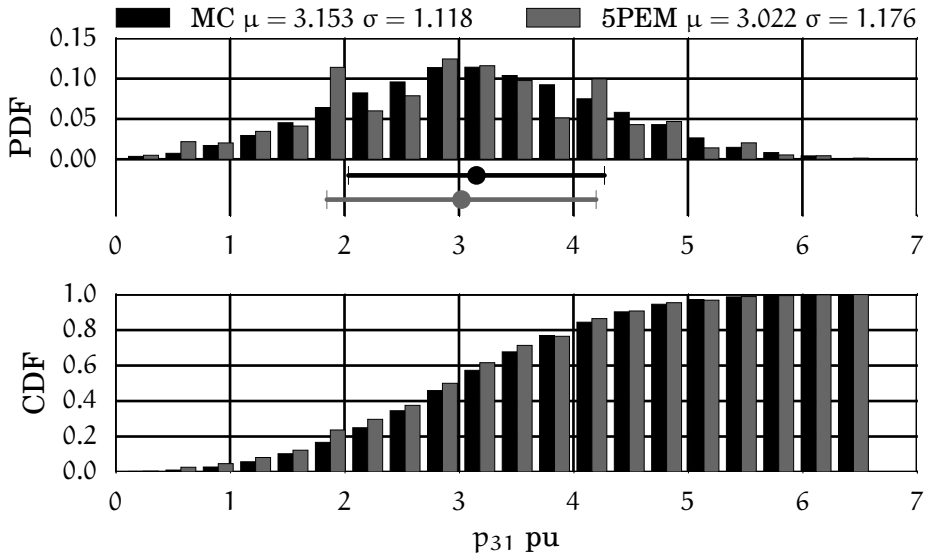

FIGURE 5.9: PDF and CDF of slack generator active power (Case C).

Finally, Figs. 5.9 and 5.10 show the PDF and CDF of both active and reactive powers of the slack generator. The CDF agrees better with both active and reactive power cases.

Table 5.8 shows the average error indices corresponding to the estimation of the 5PEM method. Note that the standard deviation's average errors are greater than the mean ones in almost all the cases. This makes evident that the accuracy of the point estimation methods worsens as the order of the estimated statistical becomes higher. On the other hand, bus voltage magnitudes and angles seem to be very sensitive to the estimation methods where the active and reactive output powers have acceptable average error values. Nevertheless, the PDF and CDF of voltage magnitude and the angle at bus 16 seem to agree well with the MC method, as shown in Figs. 5.11 and 5.12

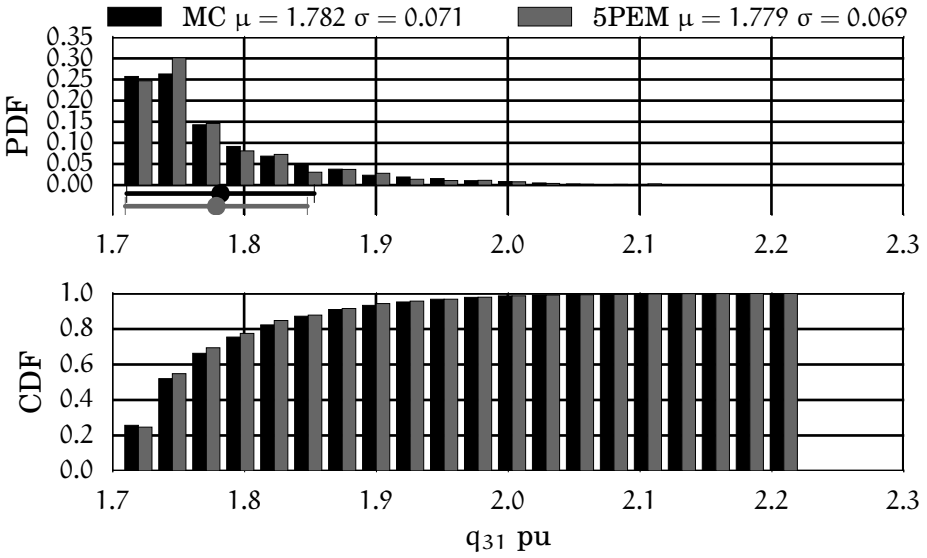

FIGURE 5.10: PDF and CDF of slack generator reactive power (Case C).

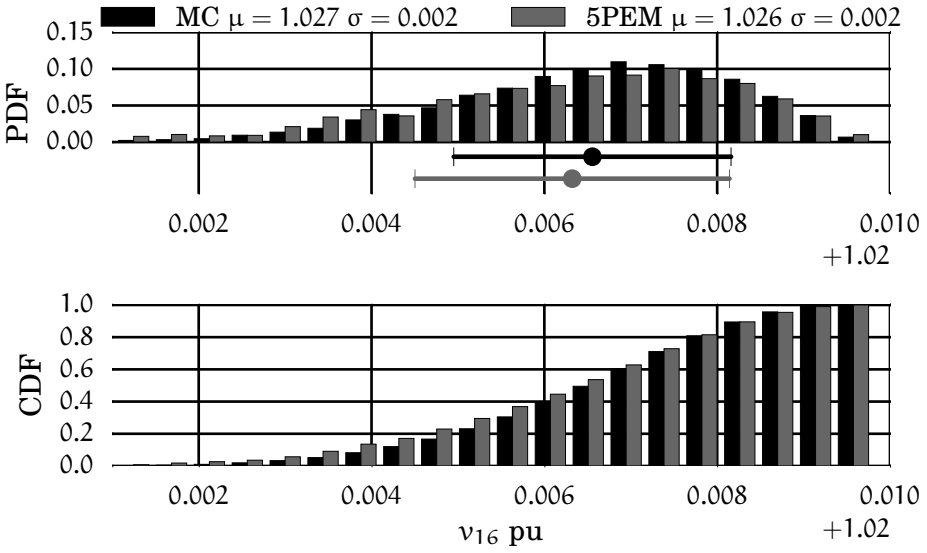

FIGURE 5.11: PDF and CDF of voltage magnitude at bus 16 (Case C).

Lastly, it is important to state that the 5PEM is much faster than the conventional MC scheme. For instance 10,000 power flow runs took 7.856 seconds, in contrast to 0.3255, 0.3533 and 0.9792 seconds for Cases A, B and C, respectively. From a practical viewpoint, this property of the 5PEM is very attractive when analyzing actual large-scale networks.

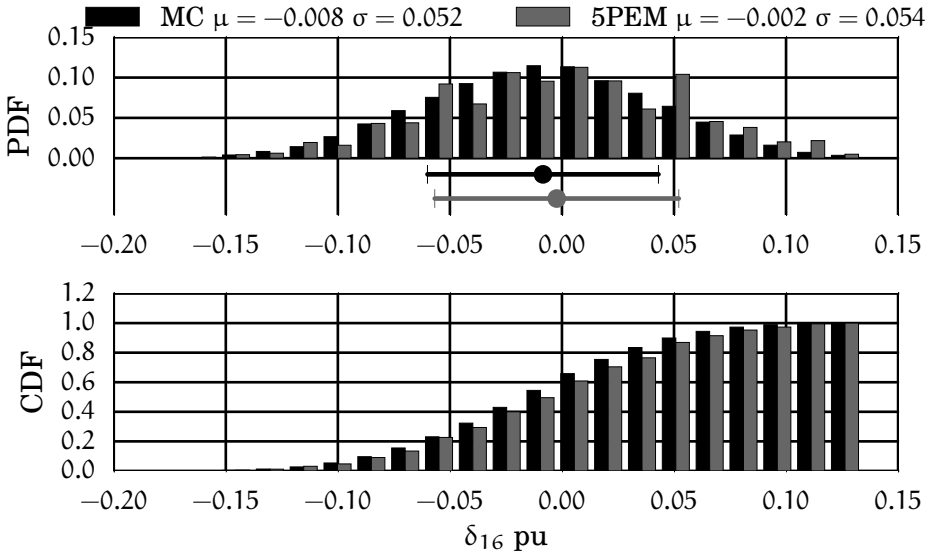

FIGURE 5.12: PDF and CDF of voltage angle at bus 16 (Case C).

TABLE 5.8: Average error indices for the three cases.

Case		v	δ	p_G	q_G
Case A	$\bar{\epsilon}^*_\mu$	0.0011	4.9603	0.0382	0.0647
	$\bar{\epsilon}^*_\sigma$	3.7710	2.3400	0.0792	1.0386
Case B	$\bar{\epsilon}^*_\mu$	0.0025	18.4428	0.3059	0.2108
	$\bar{\epsilon}^*_\sigma$	9.2759	7.7131	0.6195	3.2069
Case B	$\bar{\epsilon}^*_\mu$	0.0150	14.1353	0.4767	0.4981
	$\bar{\epsilon}^*_\sigma$	9.8030	6.3499	0.9707	3.5713

5.4 Conclusions

This chapter has described an alternative to the traditional Monte Carlo probabilistic power flows. In this sense, the 5PEM has been mathematically detailed in order to understand how a combination of discrete and continuous probability distribution functions can be concentrated in five-points.

The employed estimate method is an appropriate tool to for handling stochastic power system problems, because good results can be achieved by using the same routines as in the associated deterministic problem, while keeping the computational burden low. Including the 5PEM provides an appropriate solution for the trade-off between the accuracy of the results and the efficiency of the computational procedure for large-scale power system problems.

Although this chapter focuses on solving the probabilistic power flow under with uncertainties, the presented procedure can be applied to other power system problems affected by uncertainty, including optimization algorithms such as the probabilistic optimal power flow.

Chapter 6

Security-Constrained Optimal Power Flow Under Wind Uncertainties

6.1 Introduction

Power systems operate today in conditions that are more *stressed* and were not foreseen at the planning stage. In particular, load increments have not been supported by an adequate upgrade of generation and transmission systems. Furthermore, the creation of electricity markets has led to the trading of significant amounts of electrical energy over long distances. In addition, operating conditions are also more uncertain, because of the development of distributed generation based on renewable sources and the introduction of intra day electricity markets. In order to tackle these trends, an increasing number of complex control devices (e.g. HVDC links, and FACTS devices) are being installed. As a result of all these changes, it can be argued that the level of security systems has been weakened to the point where in some systems the *N-1* security criterion cannot be met without resorting to corrective actions.

Within this context, it is important to have appropriate tools that perform an economically and operationally secure active power dispatch. The objective of this dispatch would be to determine a generation schedule that minimizes the system operating cost, but that operation point must be able to a defined set of contingencies. These contingencies will lead the system to new equilibrium points that must also satisfy system operating constraints (i.e. line flows, bus voltage levels, machines rates, etc.).

This chapter shows the formulation of an improved version of the conventional security-constrained optimal power flow (SC-OPF)[Alsac and Stott, 1974; Monticelli et al., 1987]

that takes into account post-contingency corrective actions and wind uncertainties. The main idea of this work was proposed but not implemented in [Capitanescu et al., 2011].

6.2 Problem Formulation

6.2.1 Conventional Optimal Power Flow

The standard optimal power flow is formulated as an optimization problem that minimizes the total generation cost and as a consequence maximizes the social welfare. A relatively general OPF-based problem can be formulated by using the following nonlinear programming problem (NLP):

$$\underset{\mathbf{y}}{\text{minimize}}\, \mathbf{f}(\mathbf{p_G}) = \underset{\mathbf{y}}{\text{minimize}} \sum_{i \in \mathcal{G}} \left(a_i + b_i p_{G,i} + c_i p_{G,i}^2\right) \tag{6.1}$$

$$\begin{aligned}
\mathbf{g}(\mathbf{y}) = 0 \quad & \rightarrow \text{ Power flow equations} && (6.2)\\
p_{G,i}^{min} \leqslant p_{G,i} \leqslant p_{G,i}^{max}, \quad \forall i \in \mathcal{G} \quad & \rightarrow \text{ Active power limits} && (6.3)\\
q_{G,i}^{min} \leqslant q_{G,i} \leqslant q_{G,i}^{max}, \quad \forall i \in \mathcal{G} \quad & \rightarrow \text{ Reactive power limits} && (6.4)\\
v_k^{min} \leqslant v_k \leqslant v_k^{max}, \quad \forall k \in \mathcal{B} \quad & \rightarrow \text{ Voltage limits} && (6.5)\\
|\bar{s_l}| \leqslant s_l^{max}, \quad \forall l \in \mathcal{L} \quad & \rightarrow \text{ Line flow limits}, && (6.6)
\end{aligned}$$

where $\mathbf{y} = \left[\boldsymbol{\theta}^T \boldsymbol{v}^T \mathbf{p_G}^T\right]^T$ is the vector of state variables considered in the optimization problem.

6.2.2 Security-Constrained Optimal Power Flow

The SC-OPF is an extension to the standard OPF which takes into account line and/or generator outages that have an effect on the line flows and generation limits; hence, they change the system equilibrium point obtained with the standard OPF. This optimization should determine a generation dispatch with the lowest costs, while ensuring the system remains N-1 secure in the occurrence of these outages. The conventional SC-OPF is

formulated as follows [Monticelli et al., 1987]:

$$\underset{\mathbf{y}_{c_0}}{\text{minimize}} \quad \mathbf{f}_{c_0}\left(\mathbf{p}_{\mathbf{G}\,c_0}\right) \tag{6.7a}$$

$$\text{s.t.} \qquad \mathbf{g}_c(\mathbf{y}_c) = 0, \qquad \forall c \in \mathcal{C} \tag{6.7b}$$

$$p_{G,i}^{\min} \leqslant p_{G,i,c} \leqslant p_{G,i}^{\max}, \qquad \forall c \in \mathcal{C}, i \in \mathcal{G} \tag{6.7c}$$

$$q_{G,i}^{\min} \leqslant q_{G,i,c} \leqslant q_{G,i}^{\max}, \qquad \forall c \in \mathcal{C}, i \in \mathcal{G} \tag{6.7d}$$

$$v_k^{\min} \leqslant v_{k,c} \leqslant v_k^{\max}, \qquad \forall c \in \mathcal{C}, k \in \mathcal{B} \tag{6.7e}$$

$$\left|\bar{s_{l,c}}\right| \leqslant s_l^{\max}, \qquad \forall c \in \mathcal{C}, l \in \mathcal{L} \tag{6.7f}$$

$$-\text{ramp}_i^{\text{down}} \leqslant p_{G,i,c} - p_{G,i,c_0} \leqslant \text{ramp}_i^{\text{up}}, \qquad \forall c \in \mathcal{C} \setminus \{c_0\}, i \in \mathcal{G}, \tag{6.7g}$$

where f_{c_0} is the production cost under normal operation, and $\mathcal{C} = \{c_0, c_1, c_2, \ldots, c_f\}$ stands for the set of possible system configurations. In other words, c_0 corresponds to the pre-contingency configuration, whereas c_i corresponds to the i-th post-contingency configuration.

Constraints of Eqs. (6.7b) to (6.7f) enforce the feasibility of every configuration system, and Eq. (6.7g) represents the possible range of rescheduling actions to eliminate the constraint violations. These possible ranges depend on time constraints and generator limits. Note that this constraint serves as a *bridge* between the base case (c_0) and the rest of system configurations.

The preventive SC-OPF [Alsac and Stott, 1974] (PSC-OPF) is a particular formulation of the SC-OPF that does not consider the possibility of corrective actions in post-contingency states, other than those that occur automatically: active power of generators participating in frequency control, automatic tap-changers, capacitor and reactor bank switching. Therefore in the PSC-OPF, the values of the non-automatic control variables are thus the same in all system states, i.e. $\text{ramp}_i^{\text{up}} = \text{ramp}_i^{\text{down}} = 0$.

In some cases the SC-OPF converges to infeasible solutions because of system configurations. For instance, consider a 100 MVA load fed by two lines of 50 MVA; if we consider a system configuration c without one of those lines, the NLP problem will be infeasible. For that reason, the original objective function (Eq. (6.7a)) is modified in order to penalize the load shedding which achieves the NLP problem feasibility:

$$\underset{\mathbf{y}_c, \xi_{k,c}}{\text{minimize}}\, \mathbf{f}_{c_0}\left(\mathbf{p}_{\mathbf{G}\,c_0}\right) + \Lambda \sum_{k \in \mathcal{B}, c \in \mathcal{C}} \xi_{k,c} \left|\bar{s}_{L,k,c_0}\right|, \tag{6.8}$$

where Λ is the value of lost load (VoLL) which in this work is considered $\Lambda = 30000\$/\text{MVA}$, $\xi_{k,c}$ is a shedding factor such that $\bar{s}_{L,k,c} = \bar{s}_{L,k,c_0}\left(1 - \xi_{k,c}\right)$, and $\bar{s}_{L,k,c} = p_{L,k,c} + jq_{L,k,c}$ is the load at bus k for the configuration c.

6.2.3 Robust Security-Constrained Optimal Power Flow

While SC-OPF brings a secure and economical dispatch, this approach does not consider stochastic variables that could change the generation behavior, such of wind speed or solar irradiation. The smaller the time-frame the bigger stochasticity; in other words, wind can be considered deterministic for a 10-year time-frame, because its behavior seems like a Weibull or other distribution function that are well-defined. In day-ahead operations, however, wind speed behavior is more complicated. In this context, the use of forecasters has reduced the uncertainty grade and can provide, if considered, valuable information to the system operator in order to have a secure operation in the electrical system.

One way to include forecast information is to perform a scenario-based SC-OPF. For each wind scenario, we have a certain amount of wind(active power) and its associated probability. As the number of scenarios in the SC-OPF increases, so does the computation burden. This burden can be reduced by implementing a scenario reduction technique that lumps together similar scenarios. This approximation, however, reduces the accuracy of the uncertainty model and increases the operation cost [Dvorkin et al., 2014].

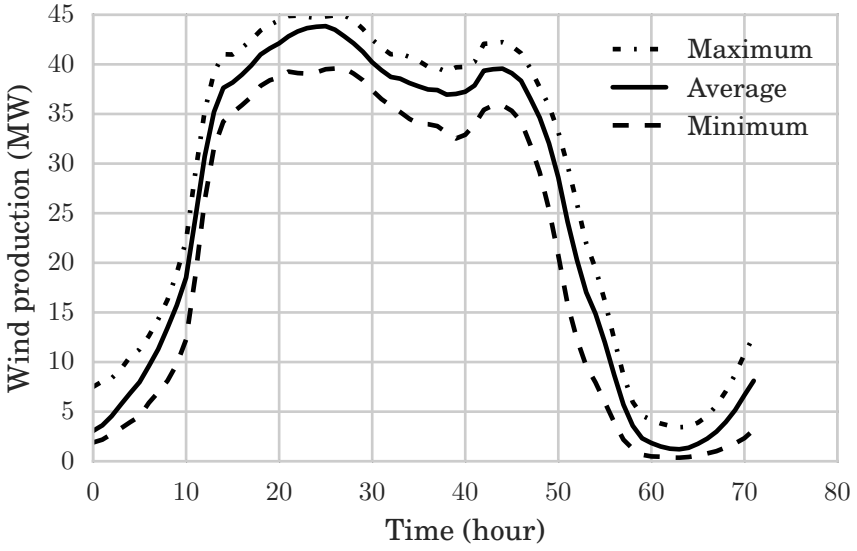

FIGURE 6.1: Wind forecast.

Fig. 6.1 shows 72 hours of wind forecast obtained from [Administration, 2015], where the predicted wind power is the solid line, and the enveloping curves represent the probable maximum and minimum bounds. By understanding that system operators have this type of forecast information and by aiming to limit the computation burden to preserve accuracy, this work considers an interval OPF formulation [Wang et al., 2011]. This formulation simplifies the representation of uncertainty by considering only three wind scenarios: a central forecast and the upper and lower bounds of wind generation.

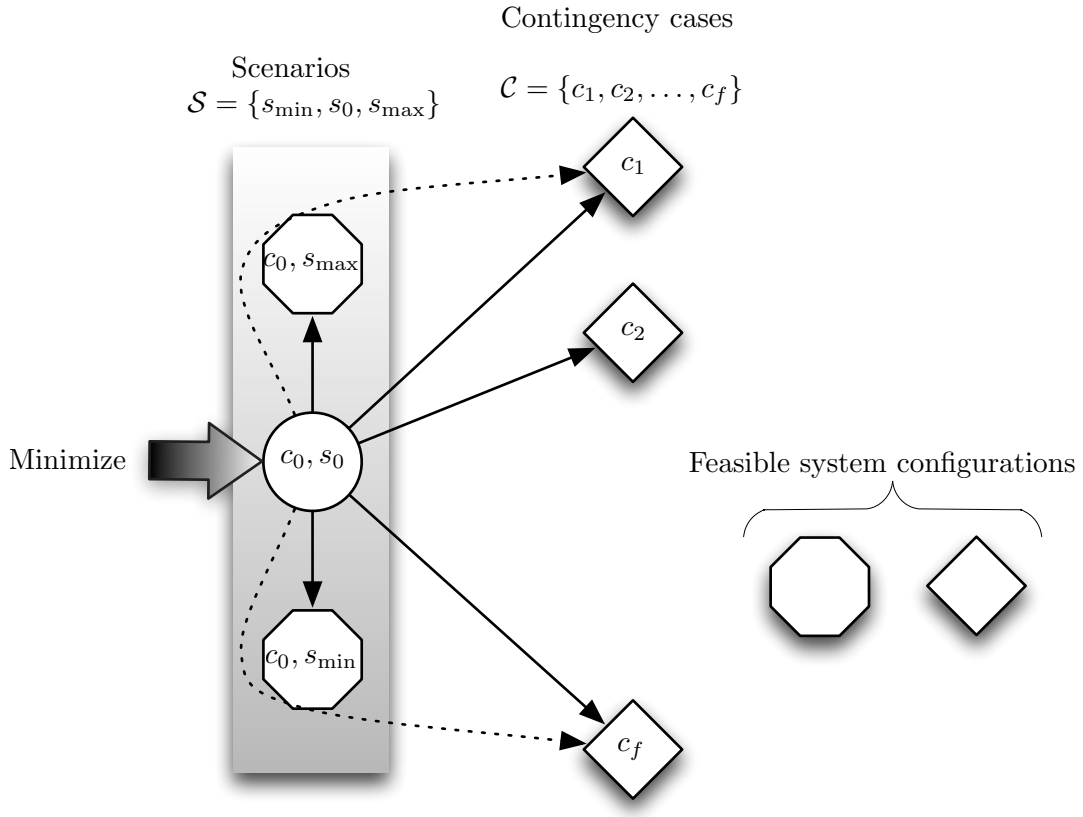

FIGURE 6.2: Schematic representation of the relation between wind scenarios and contingency cases.

As depicted in Fig. 6.2, the objective function of this robust SC-OPF(RSC-OPF) is to minimize the operating cost of the central forecast and to add constraints which enforce the feasibility of all system configurations (disturbances). The concept of *robust* in this work is related to the ability of the system to meet a N-1 contingency, even in the worst-case scenario of wind.

With these assumptions, the previous SC-OPF formulation (Eq. (6.7)) is extended to include three possible wind scenarios $\mathcal{S} = \{\mathrm{s}_{\min}, \mathrm{s}_0, \mathrm{s}_{\max}\}$:

$$\begin{aligned} \underset{\mathbf{y}, \xi_{\mathrm{k,c,s}}}{\text{minimize}} \quad & \mathbf{f}_{\mathrm{c}_0,\mathrm{s}_0}\left(\mathbf{p}_{\mathbf{G}\,\mathrm{c}_0,\mathrm{s}_0}\right) \\ & + \Lambda \sum_{\mathrm{k}\in\mathcal{B},\mathrm{c}\in\mathcal{C},\mathrm{s}\in\mathcal{S}} \xi_{\mathrm{k,c,s}} \left|\bar{\mathrm{s}}_{\mathrm{L,k}}\right| \end{aligned} \tag{6.9a}$$

$$\text{s.t.} \quad \mathbf{g}_{c,s}(\mathbf{y}_{c,s}) = 0, \qquad \forall c \in \mathcal{C}, s \in \mathcal{S} \tag{6.9b}$$

$$p^{\min}_{G,i} \leqslant p_{G,i,c,s} \leqslant p^{\max}_{G,i}, \qquad \forall c \in \mathcal{C}, s \in \mathcal{S}, i \in \mathcal{G} \tag{6.9c}$$

$$q^{\min}_{G,i} \leqslant q_{G,i,c,s} \leqslant q^{\max}_{G,i}, \qquad \forall c \in \mathcal{C}, s \in \mathcal{S}, i \in \mathcal{G} \tag{6.9d}$$

$$v^{\min}_{k} \leqslant v_{k,c,s} \leqslant v^{\max}_{k}, \qquad \forall c \in \mathcal{C}, s \in \mathcal{S}, k \in \mathcal{B} \tag{6.9e}$$

$$\left|s^{-}_{l,c,s}\right| \leqslant s^{\max}_{l}, \qquad \forall c \in \mathcal{C}, s \in \mathcal{S}, l \in \mathcal{L} \tag{6.9f}$$

$$-\text{ramp}^{\text{down}}_{i} \leqslant p_{G,i,c,s} - p_{G,i,c_0,s_0} \leqslant \text{ramp}^{\text{up}}_{i}, \qquad \forall c \in \mathcal{C}, s \in \mathcal{S}, i \in \mathcal{G} \tag{6.9g}$$

$$p_{\mathcal{W},j,c,s} = \Phi_{j,s} - \text{ws}_{j,c,s}, \qquad \forall c \in \mathcal{C}, s \in \mathcal{S}, j \in \mathcal{W} \tag{6.9h}$$

$$\xi_{k,c_0,s_0} = 0, \qquad \forall k \in \mathcal{B} \tag{6.9i}$$

$$0 \leqslant \xi_{k,c,s} \leqslant 1, \qquad \forall c \in \mathcal{C}, s \in \mathcal{S}, k \in \mathcal{B} \tag{6.9j}$$

$$0 \leqslant \text{ws}_{j,c,s} \leqslant \Phi_{j,s}, \qquad \forall c \in \mathcal{C}, s \in \mathcal{S}, j \in \mathcal{W}, \tag{6.9k}$$

where ws_j stands for the wind spillage of each generator $j \in \mathcal{W}$, $\Phi_{j,s}$ is a parameter which contains forecast information (minimum, central and maximum wind) of each wind farm. Eq. (6.9h) determines the amount of dispatched energy for every wind generator, considering that for all cases and scenarios wind spillage is available. Under normal operating circumstances wind spillage is discouraged, because conventional generation would need to feed the demand that otherwise would be served by wind power generation. Since this increases the system operating cost, wind spillage is indirectly penalized in the objective function. Eqs. (6.9i) and (6.9j) fix the shedding factor $\xi_{k,c,s}$ to zero in the base case and make it positive for all cases (no negative loads). Moreover, Eq. (6.9g) is a set of *coupling* constraints that serve as a bridge between the optimized base case and all possible contingencies and/or wind scenarios. Finally, the power flow equations $\mathbf{g}_{c,s}$ are conformed by

$$\mathbf{g}_{c,s}(\mathbf{y}_{c,s}) = \begin{bmatrix} \boldsymbol{\Delta}\mathbf{p}(\mathbf{y}_{c,s}) \\ \boldsymbol{\Delta}\mathbf{q}(\mathbf{y}_{c,s}) \end{bmatrix} \tag{6.10}$$

$$= \begin{bmatrix} \sum_{i \subset k} p_{G,i,c,s} + \sum_{j \subset k} p_{\mathcal{W},j,c,s} - p_{L,k,c,s} - p_{k,c,s} \\ \sum_{i \subset k} q_{G,i,c,s} + \sum_{j \subset k} q_{\mathcal{W},j,c,s} - q_{L,k,c,s} - q_{k,c,s} \end{bmatrix}, \quad \forall k \in \mathcal{B}, \tag{6.11}$$

where $p_{k,c,s}$ and $q_{k,c,s}$ stand for the net active and reactive power injections at bus k, as stated in Eqs. (2.13) and (2.14).

6.2.3.1 Linear Approximation

Solving Eqs. (6.9a) to (6.9k) is computationally difficult not only because they implicitly involve the solution of the power flow equations, but also because they are nonlinear. Instead of using a full and accurate AC model, we could instead alternatively carry out this optimization on the basis of a linearized model by using the DC power flow equations. These equations are derived from the equations of the AC power flow by making the following assumptions [Kirschen and Strbac, 2004].

- The resistance of each branch is negligible compared to the reactance.
- The magnitude of the voltage at every bus is equal to its nominal value (1 pu).
- The differences in voltage angles across each branch are sufficiently small to allow the following approximations:

$$\cos\left(\delta_k - \delta_m\right) \approx 1$$
$$\sin\left(\delta_k - \delta_m\right) \approx \delta_k - \delta_m\,.$$

Under these assumptions, the flow of reactive power in the system is negligible, and the net active power injections are related to the bus voltage angles through the following equation:

$$p_{k,c,s} = \sum_{m \in \mathcal{B}} \frac{\delta_{k,c,s} - \delta_{m,c,s}}{x_{l,k,m}}, \quad \forall c \in \mathcal{C}, s \in \mathcal{S}, k \in \mathcal{B}\,, \tag{6.12}$$

where $x_{l,k,m}$ represents the reactance of the branch l between buses k and m.

This linear approximation of the RSC-OPF leads the previous NLP problem into a quadratic programming (QP)[1] problem which can be solved faster when analyzing large networks.

6.3 Case Studies

This section demonstrates the useful information that brings a RSC-OPF to system operators. Two test systems are considered: a modified version of a three bus network [Kirschen and Strbac, 2004] and the IEEE 24 bus RTS [Wong et al., 1999].

Optimization problems were solved by using the AMPL language, as well as the Gurobi and KNITRO solvers for LP/QP and NLP problems, respectively.

[1] QP can be easily solved using linear approaches such as simplex or interior point methods [Wolfe, 1959; Lobo et al., 1998].

6.3.1 Three Bus Example

To exemplify and observe the advantages and disadvantages of the RSC-OPF, this section uses a modified version of a three bus system [Kirschen and Strbac, 2004]. Actual parameters are shown in Tables 6.1 and 6.2. Possible system configurations are the base case and outage of each transmission line ($\mathcal{C} = \{c_0, l_1, l_2, l_3\}$). Regarding wind scenarios, a forecast of 180 MW with ±10 MW of error (the three wind scenarios) is considered. Therefore the total system configurations for the RSC-OPF approach will be $|\mathcal{S}|\,(|\mathcal{C}|) = 3\,(4) = 12$. For the sake of conciseness, a linear version of power flow equations is used in this example (DC formulation); this avoids the use of excessive decimal quantities and reactive power flows, and the example better demonstrates each approach's main idea (i.e. active power dispatch).

Gen $i \in \mathcal{G}$	Bus	$p_{G,i}^{max}$ (MW)	$ramp_i^{down} = ramp_i^{up}$ (MW)	Cost curve coefficients (a, b, c)
A	1	140	10	$(0, 7.5, 0)$
B	1	285	30	$(0, 6.0, 0)$
C	2	90	10	$(0, 14, 0)$
W	3	200	60	$(0, 2.0, 0)$

TABLE 6.1: Generator data, three bus system.

Line $l \in \mathcal{L}$	Bus 1	Bus 2	x_l (pu)	s_l^{max} (MVA)
1	1	2	0.2	126
2	1	3	0.2	250
3	2	3	0.1	130

TABLE 6.2: Line data, three bus system.

Fig. 6.3 shows the solutions obtained by means of each approach: OPF, SC-OPF, and RSC-OPF. The conventional OPF (Fig. 6.3(a)) presents the lowest cost. Under this dispatch, however, when the worst-case operation is presented (the outage of line 2), the ramp down of generator B is accomplished with a ramp up generation in the remaining generators. This coordination is infeasible because of the ramp constraints; hence, the system is insecure for a N-1 contingency.

Moreover, if we consider three additional contingencies (the three line outages) and solve again with a SC-OPF, the system will be secure under any line outage and will be able to redispatch active power generation in order to feed the specified load (Fig. 6.3(b)). At this point, the SC-OPF problem does not consider wind variability. By having a pure SC-OPF, a minimum wind scenario (−10MW at bus 3), and the worst of the three cases, the system will have to shed load. To eliminate this shedding, a new dispatch is performed under the RSC-OPF basis (Fig. 6.3(c)). This solution raises the cost but a secure system operation is guaranteed under any line outage or wind variation. For

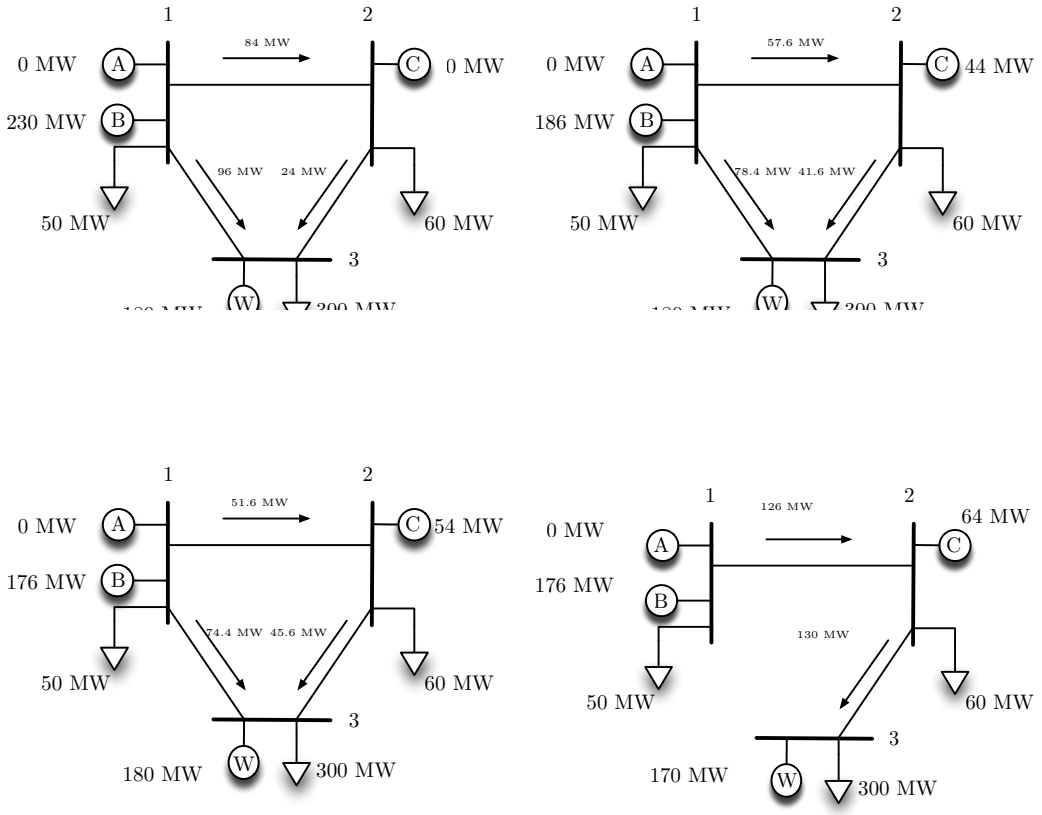

cost = 2172 $/h

(c) RSC-OPF

cost = 2295.91 $/h

(d) Outage of line l_2(1-3) and minimum wind scenario, under RSC-OPF dispatch

FIGURE 6.3: Three bus economic dispatch using different approaches.

instance, Fig. 6.3(d) reveals the necessary system redispatch starting from the RSC-OPF operating point when line l_2 is out: flow between buses 1 and 2 is constrained to 126 MVA and to 130 MVA between 2 and 3; hence, generation at bus 2 must satisfy local demand (60 MW) and generate an additional 4 MW or a total of 64 MW. Therefore, the greatest economical dispatch for this generator is $p_{G,C,c_0,s_0} = 64 - \text{ramp}_C = 54\text{MW}$.

This brief and simple example shows that robustness and security can be achieved by dispatching generation in an optimal way. This active power dispatch is more expensive under normal operations, but probably the cost of load shedding or the value of energy not served would be greater as shown in the next example.

6.3.2 IEEE 24 Bus Example

Proposed RSC-OPF is tested against another less hypothetic system. The IEEE 24 bus system [Wong et al., 1999] is used to include four wind farms at buses 13,23,16 and 17. Each wind farm with a rated power of 2 MW is modeled without voltage or reactive support (unity power factor).

Table 6.3: Wind power forecast.

W.G. ($j \in \mathcal{W}$)	Bus	$\Phi_{j,s_{min}}$	Φ_{j,s_0}	$\Phi_{j,s_{max}}$
1	13	95.111	142.210	173.793
2	23	94.381	137.281	180
3	16	47.647	87.991	116.105
4	17	22.271	46.551	85.436

Table 6.4: Summary of different formulations.

	OPF	SC-OPF	RSC-OPF	RSC-OPF (DC)
Production cost ($/h)	49973.094	50737.601	55970.851	54157.890
Conventional generation (MW)	2511.817	2500.723	2514.873	2479.588
Wind generation (MW)	414.037	414.037	382.890	370.412
Wind spillage (MW)	0.000	0.000	31.147	43.625
Solution time (sec.)	0.095	3.567	24.293	2.145

The economic dispatch was performed with each of the following approaches.

OPF Traditional economic dispatch.

SC-OPF Security-constrained economic dispatch.

RSC-OPF Same as the SC-OPF, but by taking into account three possible wind scenarios.

RSC-DCOPF Same as the previous, but by using DC power flow equations (a QP problem).

Regarding SC-OPF-based formulations, the set of considered cases is composed of: the base case, the outage of each line and the outage of each conventional generator (N-1): $\mathcal{C} = \{c_0\} \cup \{c_x | x \in \mathcal{L}\} \cup \{c_x | x \in \mathcal{G}\}$. RSC-OPF (either the AC or DC version) considers three wind scenarios ($\mathcal{S} = \{s_{min}, s_0, s_{max}\}$) as shown in Table 6.3; this forecast information was obtained from [Administration, 2015].

Table 6.4 shows the economic dispatch obtained by each formulation. As expected, a cheaper operation cost is given by the traditional OPF. As soon as we increase the security grade by imposing new equilibrium points to be met, the production cost increases which makes the system robuster. Moreover, obtained solutions which employ RSC-OPF (either the AC or DC version) tend to spill wind, hence, to find the origin of this unexpected behavior a new economic dispatch was performed. This new dispatch is under the same RSC-OPF approach but constrains wind spillage to zero: $ws_{j,s} = 0$.

As shown in Tables 6.5 and 6.6, not only with wind spillage but also without it, all units are almost full capacity dispatched, with only the ramp rates as spinning reserves. Therefore, in order to meet the worst wind scenario, unit group U350 is dispatched down,

TABLE 6.5: Cost curves of conventional units.

Unit group	$\mathfrak{a}\left(\frac{\$}{\text{hr}}\right)$	$\mathfrak{b}\left(\frac{\$}{\text{MW hr}}\right)$	$\mathfrak{c}\left(\frac{\$}{\text{MW}^2\text{ hr}}\right)$
U12	86.385	56.564	0.328
U20	400.685	130	0.0
U50	0.001	0.001	0.0
U76	212.308	16.081	0.014
U100	781.521	43.661	0.053
U155	382.239	12.388	0.008
U197	832.758	48.580	0.007
U350	665.109	11.85	0.005
U400	395.375	4.423	0.0

TABLE 6.6: Conventional units ramp rates and power dispatch with and without wind spillage.

Unit group	Group type(bus)	Unit group rating (MW)	Ramp rate (MW)	Unit group generation RSC-OPF	Unit group generation RSC-OPF $ws_{j,s} = 0$
U12	Oil/Steam (15)	60	25	12	45
U20	Oil/CT (1,2)	80	30	64	64
U50	Hydro (22)	300	0	300	300
U76	Coal/Steam (1,2)	304	40	264	264
U100	Oil/Steam (7)	300	105	190	195
U155	Coal/Steam (15,16,23)	620	60	560	560
U197	Oil/Steam (13)	591	45	207	207
U350	Coal/Steam (23)	350	20	330	195
U400	Nuclear (18,21)	800	200	600	615

and its original power is now generated by unit group U12 and the wind generators (now without spillage). The production cost without spillage is more expensive: 60596\$/h, hence the *unexpected behavior* is now expected, and this is demonstrated to be a cheaper solution: with wind spillage the optimization problem does not need to increase the overall system ramp rate. On the other hand, without wind spillage, U350 is dispatched down, to increase this ramp rate, and more expensive generators (U12) replace this missing generation.

Finally, it has been found that the AC nonlinear formulation (RSC-OPF) could not provide important information that merits its implementations in real networks' assessments. In addition, the computing time of the linear version is more competitive.

Whereas these tables do not give important information concerning the system security with each dispatch, a new experiment is performed to assess the robustness of each implementation. The experiment design is as follows:

1 Perform an economic dispatch by using each formulation (OPF, SC-OPF, RSC-OPF, RSC-DCOPF).

2 Formulate a second optimization problem that minimizes load shedding given a fixed economic dispatch (the one obtained in the previous step), which as usual, must satisfy the power balance equations as well as the ramping constraints.

3 For each wind scenario $s_i \in \mathcal{S}$ and each contingency case $c_j \in \mathcal{C}$, solve the above optimization problem, and quantify the total load shedding (i.e. $ts_{c_j,s_i} = \sum_{k\in\mathcal{B}} \left(\xi_{k,c_j,s_i} \left|\bar{s}_{L,k,c_0,c_0}\right|\right)$).

4 Obtain the mean required load shedding for each wind scenario:

$$\bar{ts}_{s_i} = \frac{\sum_{c\in\mathcal{C}} ts_{c,s_i}}{|\mathcal{C}|}\,.$$

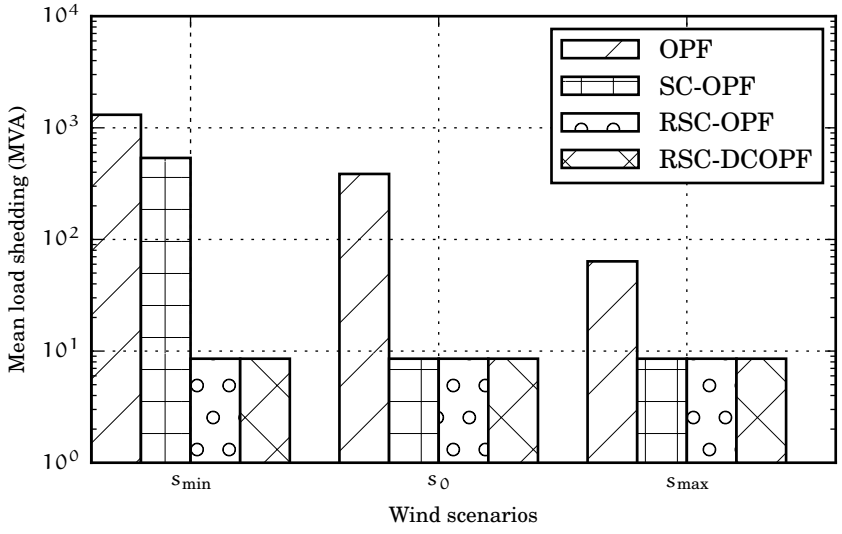

FIGURE 6.4: Mean load shedding for all cases under different wind scenarios (y axis in logarithmic scale).

Fig. 6.4 shows the mean curtailed power that each formulation requires under different wind scenarios. In addition, the y axis of the figure is log scaled in order to *see* small mean values. The main advantage of the proposed implementation is shown in this figure: while OPF gives the cheapest dispatch, it needs to approximately curtail 1309

MVA of load on each contingency (by considering the minimum wind scenario). On the other hand, SC-OPF dispatch is *secure* with favorable wind power productions, but the system operator will need to curtail 537 MVA during low wind production. Finally, both AC and DC SC-OPF versions present the most secure solution with only 8 MVA to curtail at any wind scenario.

6.4 Conclusions

An enhanced security-constrained OPF has been developed and analyzed in this chapter. The proposed RSC-OPF was tested against other more conservative economic dispatch schemes and yielded good results in terms of security.

The RSC-OPF power dispatch is an appropriate approach for the trade-off between the security of the power system and the production cost. This active power dispatch is robust from a security viewpoint: even in the worst-case wind scenario the system continues operating without several load sheddings.

The proposed RSC-OPF can be extended to a multi-period OPF, which is known as unit commitment, in order to asses the day-ahead active power generation dispatch including uncertainties; not only those imposed by wind but also the load uncertainty can be taken into account.

Chapter 7

General Conclusions and Suggestions for Future Research

7.1 General Conclusions

As wind generation continues to grow, it can prove to be a valuable and reliable resource in modern power systems. With low operational costs, zero emission generation sources will help power systems across the world meet their goals of CO_2 reduction, as well as reduce the reliance on other carbon fuels. In this context, this research, as well as other technical literature, describes and implements a set of useful techniques for simulating and analyzing the steady-state operation of highly wind penetrated power systems. These tools aim to solve the intrinsic problems that today's engineers are faced with when integrating large blocks of wind energy into hydrothermal power networks.

To this end, a detailed steady-state modeling of wind generators and its associated controller devices have been reported. Within this modeling stage, an enhanced DFIG wind generator considering both active and reactive power limits is proposed. On the other hand, a practical but at the same detailed model of the PMSG wind generator is introduced. Both the DFIG and the PMSG were modeled with the understanding that both provide ancillary services particularly voltage and primary frequency regulation.

By incorporating the developed models of variable-speed wind generators with the existent fixed-speed model in a steady-state analysis program, a set of power flows and continuation power flows were simulated. The simulations and the subsequent assessments were conducted in two ways. First, we focused on analyzing how the steady-state frequency value of a power system can be deviated from its nominal value when hydrothermal generation is replaced with wind energy-based generation. Second, we explained to perform an analysis to measure the maximum loading condition of a power system with high wind energy penetration. In both cases the behavior of the

system is improved or at least is not decreased when considering variable-speed wind generation. On the other hand, both the frequency and the voltage responses deteriorate when including large amounts of fixed-speed wind generation without appropriate reactive power control devices, such as SVCs or STATCOMs. This set of simulations were performed by considering devices' operative limits as complementarity constraints, which are mathematically represented by using the Fischer-Burmeister-based method. The reported results have proved that the complementarity formulation approach is an appropriate technique to model the devices' operative limits.

While these deterministic studies are valid and recommended for a single instant of time, evaluating how the wind power uncertainties affect the power system's operation becomes important. It is in this direction where this work describes and tests a point estimation technique which has recently appeared in the technical literature. This estimation method defines a finite number of points suitable for representing uncertainties associated with wind speed forecasts and for analyzing the probabilistic behavior of wind generation. This method has provided an appropriate solution for the trade-off between the accuracy of the results and the efficiency of the computational procedure for large-scale power system problems.

Lastly, an enhanced security-constrained OPF has been developed. The approach employed in this work considers that variation of wind speeds is within an interval which can be obtained by means of modern forecasters. Within this wind speed interval the solution of the SC-OPF ensures that the system is secure under a N-1 contingency. This approach is rather attractive because a system operator can dispatch the active power in the system in a secure way; not only the contingencies that change the system's topology are considered but also how wind generation varies in a closed interval.

The overall goal of this work has been to demonstrate the changing of the electric generation paradigm and how high levels of wind penetration require novel methods and models to analyze and maintain high levels of both stability and security in modern power systems. We realize that the problem at hand is one of a very complicated nature, and it was not expected that a single work, such as the present one, could provide a complete answer to it. Nevertheless, the author encourage the reader to use the present work as possible reference for future research projects.

7.2 Suggestions for Future Research

Interesting research could be performed with the proposals presented in this document as a basis. In this context, the following research items are suggested as future research.

- Improving the models of variable-speed wind generators is recommended. Specifically by appropriate operative limits based on the maximum current magnitude of the back-to-back converters.

- To modify the distributed slack formulation in order to obtain the inertial response of the system. By employing inertial response models, the power flow study will be able to obtain the power system's frequency nadir value.

- In order to have a more exhaustive analysis of the impact of renewable technologies in a power system, models of photovoltaic energy conversion systems can be included in the current steady-state analysis program.

- In order to quantify the effect of offshore wind farms that are generally connected through HVDC link systems, it is recommended to model AC-DC terminals as well as DC networks within a single AC/DC power flow program.

- The number of complementarity constraints n_z employed in this work can be reduced by including all of them in a single sum: $\psi(\mathbf{y}) = \frac{1}{2}\sum_{i=1}^{n_z} \phi_i(\mathbf{y})^2$.

- The current continuation power flow tool can be improved by including a secant-based predictor and by correcting this prediction using an enhanced perpendicular intersection method.

- The power flow program developed in this thesis can be extended to become a Newton-based optimal power flow. This task can be rapidly developed given the fact that the current program is coded under the object-oriented programming paradigm; hence, each device's *class* can be extended to include those derivatives that arise from the Lagrangian function. This OPF will directly handle operative limits by employing the already coded complementarity approach.

- After the previous point is completed, an interesting research area would be to develop a multi-period OPF with embedded integer variables. This mixed integer nonlinear problem will have the means to model a scenario-based unit commitment with the approach described in Chapter 6. The mixed integer nonlinear problem can be solved by using a nonlinear branch and bound method.

- For prototyping purposes, the previous point can be achieved by modifying the current SC-OPF which is coded by using a mathematical programming language. This implementation is attractive, because it expands the existing SC-OPF into a multi-period SC-OPF in a straightforward manner; however, caution has to be exercised because it could lead to tractability problems. Decomposition techniques such as Benders cuts can be considered to tackle these issues.

Appendix A

Including Complementarity Constraints in a Power Flow Study

A.1 Background

Equilibrium constraints in the form of complementarity conditions often appear in optimization problems, giving rise to mathematical programs with complementarity constraints (MPCCs). Problems of this type arise in many engineering and economic applications [Ferris and Pang, 1997].

The complementarity condition states that the product of two variables, $\mathfrak{a}$ and $\mathfrak{b}$, must be zero:

$$\mathfrak{a}\mathfrak{b} = 0\,, \tag{A.1}$$

which is only satisfied in three situations, as stated below.

1. $\mathfrak{a} = 0$ and $\mathfrak{b} \neq 0$,
2. $\mathfrak{a} \neq 0$ and $\mathfrak{b} = 0$, and
3. $\mathfrak{a} = 0$ and $\mathfrak{b} = 0$.

The first two solutions are said to satisfy *strict complementarity* conditions. The third solution, in which both values are zero, exhibits *nonstrict complementarity behavior* [Rosehart et al., 2005].

Equations involving *strict complementarity* are often written using $\perp$. For instance

$$a \perp b \iff ab = 0\,. \tag{A.2}$$

Furthermore, the complementarity operator $\perp$ is often used along with inequality constraints as

$$0 \leqslant a \perp b \geqslant 0\,, \tag{A.3}$$

which represents that in addition to the stated inequalities, $0 \leqslant a$ and $b \geqslant 0$, the equation $ab = 0$ also holds.

A.1.1 Solution Approach

The solution of Eq. (A.3) can be achieved by means of the Fischer-Burmeister (FB) merit function [Fischer, 1992]:

$$\phi_{FB}(a, b) = \sqrt{a^2 + b^2} - (a + b) \tag{A.4}$$

The most interesting property of this function is that, as it is easily verified,

$$\phi_{FB}(a, b) = 0 \Leftrightarrow \quad a \geqslant 0, \quad b \geqslant 0, \quad ab = 0\,; \tag{A.5}$$

note also that ϕ_{FB} is continuously differentiable everywhere but in the origin $(a, b) = (0, 0)$. This merit function can be improved with [Facchinei et al., 1999]

$$\phi_{\mu}(a, b) = \sqrt{(a - b)^2 + 4\mu^2} - (a + b)\ . \tag{A.6}$$

which satisfies that

$$\phi_{\mu}(a, b) = 0 \Leftrightarrow \quad a \geqslant 0, \quad b \geqslant 0, \quad ab = \mu^2\,. \tag{A.7}$$

This function is smooth (continuously differentiable) for every $\mu \neq 0$.

Both ϕ_{FB} and ϕ_{μ} can be easily incorporated in a power flow program, but the latter has shown better convergence behavior and does not present numerical problems when the solution is in the neighborhood of $(a, b) = (0, 0)$. These problems are presented when both a and b are very close to be $a > 0$ and $b > 0$, which in the context of this work this situation arises when studying a Continuation Power Flow or a device is near to reach its operative limit, as shown below.

For the sake of clearness the ϕ_{FB} is used for the explanations hereinafter, but the results shown in the previous chapters were obtained by means of the enhanced ϕ_{μ}.

A.1.2 Reactive Power Limits of a *PV Bus* Using Complementarity Constraints

A *PV bus* must adjust its reactive power in order to keep its bus voltage fixed at a given set point: $v_k = v_{ref}$. When its reactive power reaches one of the limits, the voltage magnitude at the bus regulated by that generator may move away from its set point. When it occurs, the bus essentially behaves as one without voltage regulation, but with a fixed reactive power generation. This behavior can be captured by the following complementarity problem:

$$0 \leqslant \left(q_G - q_G^{min}\right) \perp v_k - v_{ref} \geqslant 0 \tag{A.8}$$

$$0 \leqslant \left(q_G^{max} - q_G\right) \perp v_{ref} - v_k \geqslant 0\,. \tag{A.9}$$

These constraints restrict the bus voltage magnitude to be at its set point unless the generator's reactive power reaches one of its limits, as described below.

- While $q_G^{min} \leqslant q_G \leqslant q_G^{max}$ the voltage is fixed at its set point: $v_k - v_{ref} = v_{ref} - v_k = 0$.
- Now, if $q_G < q_G^{min}$, Eq. (A.8) fixes the reactive power at its minimum limit and the voltage magnitude of bus k increases: $q_G - q_G^{min} = 0 \Rightarrow v_k - v_{ref} > 0$.
- The same occurs when $q_G > q_G^{max}$. In this case Eq. (A.9) constraints the reactive power output to its maximum which is accompanied with a decreasing of the voltage magnitude: $q_G^{max} - q_G = 0 \Rightarrow v_{ref} - v_k > 0$.

Now, Eqs. (A.8) and (A.9) can be easily transformed into a set of nonlinear equations through Eq. (A.4):

$$\sqrt{\left(q_G - q_G^{\min}\right)^2 + \left(v_k - v_{ref}\right)^2} - \left[\left(q_G - q_G^{\min}\right) + \left(v_k - v_{ref}\right)\right] = 0 \tag{A.10}$$

$$\sqrt{\left(q_G^{\max} - q_G\right)^2 + \left(v_{ref} - v_k\right)^2} - \left[\left(q_G^{\max} - q_G\right) + \left(v_{ref} - v_k\right)\right] = 0\,. \tag{A.11}$$

These pair of functions can be readily incorporated into the set of power flow equations $g(y)$, but the resultant set of nonlinear equations will be oversized. To avoid this issue two complementarity variables v_a and v_b must be defined such that

$$v_k - v_{ref} - v_a + v_b = 0 \tag{A.12}$$

$$0 \leqslant \left(q_G - q_G^{\min}\right) \perp v_a \geqslant 0 \tag{A.13}$$

$$0 \leqslant \left(q_G^{\max} - q_G\right) \perp v_b \geqslant 0\,, \tag{A.14}$$

which are then transformed into

$$h_{PV_1} = v_k - v_{ref} - v_a + v_b \qquad = 0 \tag{A.15a}$$

$$\phi_{PV_1} = \sqrt{\left(q_G - q_G^{\min}\right)^2 + \left(v_a\right)^2} - \left[\left(q_G - q_G^{\min}\right) + \left(v_a\right)\right] \qquad = 0 \tag{A.15b}$$

$$\phi_{PV_2} = \sqrt{\left(q_G^{\max} - q_G\right)^2 + \left(v_b\right)^2} - \left[\left(q_G^{\max} - q_G\right) + \left(v_b\right)\right] \qquad = 0\,. \tag{A.15c}$$

Within this approach these three equations are included in the power flow problem coming with q_g, v_a and v_b; which are the state variables of the *PV bus* for the reactive power modeling.

A.1.2.1 Linearization of ϕ_{FB}

It is important to indicate the properties of the gradients of the Fischer-Burmeister function (Eq. (A.4)) for $(a, b) \neq (0, 0)$:

$$\nabla\phi_{FB}(a, b) = \begin{bmatrix} 1 - \frac{a}{\sqrt{a^2+b^2}} \\ 1 - \frac{b}{\sqrt{a^2+b^2}} \end{bmatrix}\,. \tag{A.16}$$

In addition if $a > 0$ and $b > 0$, it can be shown that

$$\boldsymbol{\nabla}\phi_{\mathrm{FB}}(a,0)=\begin{bmatrix}0\\1\end{bmatrix}\quad\text{and}\quad\boldsymbol{\nabla}\phi_{\mathrm{FB}}(0,b)=\begin{bmatrix}1\\0\end{bmatrix}. \tag{A.17}$$

It is interesting to observe how the complementarity constraints fixes the corresponding state variable to a maximum or minimum value. For instance, consider that set of equations stated in Eq. (A.15) are solved by means of the NR method, and the i-th is the iteration when the method has converged; hence $h_{\mathrm{PV}_1}=\phi_{\mathrm{PV}_1}=\phi_{\mathrm{PV}_2}\sim 0$.

The set of equations is linearized by means of the NR method as

$$-\begin{bmatrix}0 & -1 & 1\\ 1-\frac{q_G-q_G^{\min}}{\sqrt{(q_G-q_G^{\min})^2+\nu_a^2}} & 1-\frac{\nu_a}{\sqrt{(q_G-q_G^{\min})^2+\nu_a^2}} & 0\\ \frac{q_G^{\max}-q_G}{\sqrt{(q_G^{\max}-q_G)^2+\nu_b^2}}-1 & 0 & 1-\frac{\nu_b}{\sqrt{(q_G^{\max}-q_G)^2+\nu_b^2}}\end{bmatrix}^{(i-1)}\begin{bmatrix}\Delta q_G\\ \Delta\nu_a\\ \Delta\nu_b\end{bmatrix}^{(i)}=\begin{bmatrix}h_{\mathrm{PV}_1}\\ \phi_{\mathrm{PV}_1}\\ \phi_{\mathrm{PV}_2}\end{bmatrix}^{(i-1)}. \tag{A.18}$$

For the case that $q_G^{\min}\leqslant q_G\leqslant q_G^{\max}\rightarrow\nu_a=\nu_b=0$, it follows that

$$-\begin{bmatrix}0 & -1 & 1\\ 0 & 1 & 0\\ 0 & 0 & 1\end{bmatrix}\begin{bmatrix}\Delta q_G\\ \Delta\nu_a\\ \Delta\nu_b\end{bmatrix}^{(i)}=\begin{bmatrix}0\\0\\0\end{bmatrix}, \tag{A.19}$$

which means that both $\Delta\nu_a$ and $\Delta\nu_b$ are going to be zero, and q_G will be adjusted to satisfy $h_{\mathrm{PV}_1}=\nu_k-\nu_{\mathrm{ref}}=0$.

Similarly, for $q_G=q_G^{\min}\rightarrow\nu_a>0,\nu_b=0$, it can be shown that

$$-\begin{bmatrix}0 & -1 & 1\\ 1 & 0 & 0\\ 0 & 0 & 1\end{bmatrix}\begin{bmatrix}\Delta q_G\\ \Delta\nu_a\\ \Delta\nu_b\end{bmatrix}^{(i)}=\begin{bmatrix}0\\0\\0\end{bmatrix}, \tag{A.20}$$

which conveys that $\Delta q_G=0$ and the state variable q_G is no longer numerically updated. On the other hand $\Delta\nu_b=0$ and $\Delta\nu_a$ will update ν_a in order to meet $\nu_a=\nu_k-\nu_{\mathrm{ref}}$.

Finally, the linearized set of equations when $q_G=q_G^{\max}\rightarrow\nu_b>0,\nu_a=0$ is conformed as

$$-\begin{bmatrix} 0 & -1 & 1 \\ 0 & 1 & 0 \\ -1 & 0 & 0 \end{bmatrix} \begin{bmatrix} \Delta q_G \\ \Delta v_a \\ \Delta v_b \end{bmatrix}^{(i)} = \begin{bmatrix} 0 \\ 0 \\ 0 \end{bmatrix} . \tag{A.21}$$

In this case $\Delta q_G = 0$, and v_b will be updated to meet $v_b = v_{ref} - v_k$.

This numerical behavior is rather attractive because the switching heuristics used for the conversion of *PV bus⇄PQ bus* are automatically and numerically defined within the power flow problem formulation.

A.2 Generalized Complementarity Approach to Model Devices' Operative Limits

With the explanation stated above the reader can be easily introduced in a more general and abstract way to include the operative limits of each power system device.

Let $g : \mathbb{R}^n \to \mathbb{R}^n$ be a smooth function and $y \in \mathbb{R}^n$ the vector of state variables; the Non-Linear Complementarity Programming (NCP) consists of finding y such that [Ferris and Pang, 1997]:

$$0 \leqslant g(y) \perp y \geqslant 0 , \tag{A.22}$$

where, the operator $\perp$ means that in addition to the stated inequalities, $0 \leqslant g(y)$ and $y \geqslant 0$,the equation $y^T g(y) = 0$ also holds. Note that since $y^T g(y) = \sum_{i=1}^{n} y_i g_i(y)$, Eq. (A.22) can be equivalently stated as

$$y_i \geqslant 0, \qquad g_i(y) \geqslant 0, \qquad y_i g_i(y) = 0, \qquad i = 1, 2, \ldots n_y , \tag{A.23}$$

A.2.1 Mixed Complementarity Problem

The Mixed Complementarity Problem (MCP) results when only a portion of the vector $g(y)$ must obey the complementarity condition. In other words a MCP has nonlinear

algebraic equations, but also nonlinear complementarity constraints:

$$\mathbf{g}_1(\mathbf{y}_1, \mathbf{y}_2) = 0 \tag{A.24a}$$

$$0 \leqslant \mathbf{y}_2 \perp \mathbf{y}_2(\mathbf{y}_1, \mathbf{y}_2) \geqslant 0 \tag{A.24b}$$

In many MCPs, the objective is to find a vector $\mathbf{y}$, with lower and upper limits, $\mathbf{y}^{\min}$ and $\mathbf{y}^{\max}$, that complements a function $\mathbf{g}(\mathbf{y})$ in the following sense [Rosehart et al., 2005]:

$$\text{if} \quad y_i = y_i^{\min} \quad \rightarrow \quad g_i(\mathbf{y}) < 0 \tag{A.25a}$$

$$\text{if} \quad y_i^{\min} \leqslant y_i \leqslant y_i^{\max} \quad \rightarrow \quad g_i(\mathbf{y}) = 0 \tag{A.25b}$$

$$\text{if} \quad y_i = y_i^{\max} \quad \rightarrow \quad g_i(\mathbf{y}) > 0\,. \tag{A.25c}$$

The general notation of this problem is:

$$\mathbf{y}^{\min} \leqslant \mathbf{y} \leqslant \mathbf{y}^{\max} \quad \perp \quad \mathbf{g}(\mathbf{y}) \tag{A.26}$$

Moreover, we can separate and rearrange the inequality constraint and add two new set of positive variables, $\{\mathbf{y_a}, \mathbf{y_b}\} \subset \mathbf{y}$ such that:

$$0 \leqslant \mathbf{y} - \mathbf{y}^{\min} \quad \perp \quad \mathbf{y_a} \geqslant 0 \tag{A.27a}$$

$$0 \leqslant \mathbf{y}^{\max} - \mathbf{y} \quad \perp \quad \mathbf{y_b} \geqslant 0 \tag{A.27b}$$

where these new variables must meet:

$$\mathbf{g}(\mathbf{y}) - \mathbf{y_a} + \mathbf{y_b} = 0 \tag{A.28}$$

It is important to note the equivalence between the results in Eq. (A.25) and those in Eqs. (A.27) and (A.28): if $\mathbf{y} = \mathbf{y}^{\min}$ then $\mathbf{y_a} > 0$, thus, $\mathbf{g}(\mathbf{y}) < 0$ which means that $\mathbf{y}$ has been fixed at its lower bound and cannot meet $\mathbf{g}(\mathbf{y}) = 0$; On the other hand, if $\mathbf{y} = \mathbf{y}^{\max}$ then $\mathbf{y_b} > 0$ and $\mathbf{g}(\mathbf{y}) > 0$, which means the opposite, $\mathbf{y}$ has been fixed

at its upper bound and cannot meet $\mathbf{g}(\mathbf{y}) = 0$. Finally, the MCP problem stated in Eq. (A.24), can be restated using Eqs. (A.27) and (A.28):

$$\mathbf{g}(\mathbf{y}) - \mathbf{y}_{\mathfrak{a}} + \mathbf{y}_{\mathfrak{b}} = 0 \tag{A.29a}$$

$$\mathbf{0} \leqslant \begin{bmatrix} \mathbf{y} - \mathbf{y}^{\min} \\ \mathbf{y}^{\max} - \mathbf{y} \end{bmatrix} \quad \perp \quad \begin{bmatrix} \mathbf{y}_{\mathfrak{a}} \\ \mathbf{y}_{\mathfrak{b}} \end{bmatrix} \geqslant \mathbf{0} \tag{A.29b}$$

Finally, by employing the Fischer-Burmeister function defined in Eq. (A.5), the set of complementarity constraints stated in Eq. (A.29) are transformed into a set of nonlinear equations:

$$\mathbf{g}(\mathbf{y}) - \mathbf{y}_{\mathfrak{a}} + \mathbf{y}_{\mathfrak{b}} = \mathbf{0} \tag{A.30}$$

$$\boldsymbol{\Phi}_{\min}(\mathbf{y}, \mathbf{g}(\mathbf{y})) = \sqrt{\mathbf{y}_{\mathfrak{a}}{}^2 + (\mathbf{y} - \mathbf{y}_{\min})^2} - (\mathbf{y}_{\mathfrak{a}} + (\mathbf{y} - \mathbf{y}_{\min})) = \mathbf{0} \tag{A.31}$$

$$\boldsymbol{\Phi}_{\max}(\mathbf{y}, \mathbf{g}(\mathbf{y})) = \sqrt{\mathbf{y}_{\mathfrak{b}}{}^2 + (\mathbf{y}_{\max} - \mathbf{y})^2} - (\mathbf{y}_{\mathfrak{b}} + (\mathbf{y}_{\max} - \mathbf{y})) = \mathbf{0} \tag{A.32}$$

This set of nonlinear equations are included along with the power flow equations to be solved in a unified way.

Appendix B

Test Systems and Wind Generator Data

B.1 New England Test System

The presented below was obtained from [Pai, 1989; Zimmerman et al., 2011].

Bus	ν	δ
1	1.0395	-0.2364
2	1.0487	-0.1709
3	1.0308	-0.2144
4	1.0045	-0.2205
5	1.0061	-0.1954
6	1.0083	-0.1817
7	0.9984	-0.2227
8	0.9979	-0.2328
9	1.0384	-0.2476
10	1.0179	-0.1427
11	1.0134	-0.1561
12	1.0009	-0.1572
13	1.0150	-0.1560
14	1.0124	-0.1871
15	1.0162	-0.1982
16	1.0326	-0.1753
17	1.0343	-0.1942
18	1.0317	-0.2094
19	1.0501	-0.0946
20	0.9910	-0.1192
21	1.0324	-0.1333

22	1.0502	-0.0557
23	1.0452	-0.0592
24	1.0381	-0.1732
25	1.0579	-0.1463
26	1.0527	-0.1649
27	1.0385	-0.1985
28	1.0504	-0.1037
29	1.0502	-0.0555
30	1.0500	-0.1288
31	0.9820	0.0000
32	0.9841	-0.0034
33	0.9972	-0.0035
34	1.0123	-0.0286
35	1.0494	0.0308
36	1.0636	0.0778
37	1.0280	-0.0279
38	1.0265	0.0677
39	1.0300	-0.2538

Load	Bus	p_L	q_L	k_{pp}	k_{pc}	k_{pz}	k_{pf}	k_{qp}	k_{qc}	k_{qz}	k_{qf}
1	1	0.9761	0.4420	0.3300	0.3300	0.3400	0.0400	0.3300	0.3300	0.3400	0.0400
2	3	3.2204	0.0240	0.3300	0.3300	0.3400	0.0400	0.3300	0.3300	0.3400	0.0400
3	4	5.0001	1.8401	0.3300	0.3300	0.3400	0.0400	0.3300	0.3300	0.3400	0.0400
4	7	2.3381	0.8400	0.3300	0.3300	0.3400	0.0400	0.3300	0.3300	0.3400	0.0400
5	8	5.2201	1.7660	0.3300	0.3300	0.3400	0.0400	0.3300	0.3300	0.3400	0.0400
6	9	0.0650	-0.6660	0.3300	0.3300	0.3400	0.0400	0.3300	0.3300	0.3400	0.0400
7	12	0.0853	0.8801	0.3300	0.3300	0.3400	0.0400	0.3300	0.3300	0.3400	0.0400
8	15	3.2001	1.5301	0.3300	0.3300	0.3400	0.0400	0.3300	0.3300	0.3400	0.0400
9	16	3.2903	0.3230	0.3300	0.3300	0.3400	0.0400	0.3300	0.3300	0.3400	0.0400
10	18	1.5801	0.3000	0.3300	0.3300	0.3400	0.0400	0.3300	0.3300	0.3400	0.0400
11	20	6.8002	1.0300	0.3300	0.3300	0.3400	0.0400	0.3300	0.3300	0.3400	0.0400
12	21	2.7402	1.1501	0.3300	0.3300	0.3400	0.0400	0.3300	0.3300	0.3400	0.0400
13	23	2.4752	0.8461	0.3300	0.3300	0.3400	0.0400	0.3300	0.3300	0.3400	0.0400
14	24	3.0862	-0.9221	0.3300	0.3300	0.3400	0.0400	0.3300	0.3300	0.3400	0.0400
15	25	2.2405	0.4721	0.3300	0.3300	0.3400	0.0400	0.3300	0.3300	0.3400	0.0400
16	26	1.3901	0.1700	0.3300	0.3300	0.3400	0.0400	0.3300	0.3300	0.3400	0.0400
17	27	2.8104	0.7551	0.3300	0.3300	0.3400	0.0400	0.3300	0.3300	0.3400	0.0400
18	28	2.0601	0.2760	0.3300	0.3300	0.3400	0.0400	0.3300	0.3300	0.3400	0.0400
19	29	2.8352	0.2690	0.3300	0.3300	0.3400	0.0400	0.3300	0.3300	0.3400	0.0400
20	31	0.0920	0.0460	0.3300	0.3300	0.3400	0.0400	0.3300	0.3300	0.3400	0.0400
21	39	11.0404	2.5001	0.3300	0.3300	0.3400	0.0400	0.3300	0.3300	0.3400	0.0400

Gen	Bus	p_G	q_G	p_G^{min}	p_G^{max}	q_G^{min}	q_G^{max}	R	ν_{ref}	k_A	x_d	x_q	Slack
Gen 1	39	10.0000	0.7826	-0.0010	11.0000	-1.0000	3.0000	0.0500	1.0300	0.0000	0.0200	0.0190	0.0000
Gen 2	31	6.7823	2.2152	-0.0010	7.7100	-1.0000	3.0000	0.0500	0.9820	6.2000	0.2950	0.2820	1.0000
Gen 3	32	6.5000	2.0688	-0.0010	7.2500	1.5000	3.0000	0.0500	0.9841	5.0000	0.2495	0.2370	0.0000
Gen 4	33	6.3200	1.0822	-0.0010	7.7700	-0.0010	2.5000	0.0500	0.9972	5.0000	0.2620	0.2580	0.0000
Gen 5	34	5.0800	1.6661	-0.0010	6.3300	-0.0010	1.6700	0.0500	1.0123	40.0000	0.6700	0.6200	0.0000
Gen 6	35	6.5000	2.1059	-0.0010	6.8700	-1.0000	3.0000	0.0500	1.0494	5.0000	0.2540	0.2410	0.0000
Gen 7	36	5.6000	1.0006	-0.0010	5.8000	-0.0010	2.4000	0.0500	1.0636	40.0000	0.2950	0.2920	0.0000
Gen 8	37	5.4000	-0.0010	-0.0010	6.8900	-0.0010	2.5000	0.0500	1.0275	5.0000	0.2900	0.2800	0.0000
Gen 9	38	8.3000	0.2146	-0.0010	9.9000	-1.5000	3.0000	0.0500	1.0265	40.0000	0.2106	0.2050	0.0000
Gen 10	30	2.5000	1.6129	-0.0010	4.1500	1.4000	4.0000	0.0500	1.0499	5.0000	0.1000	0.0690	0.0000

Line	k	m	r	x	b^{sh}	τ	θ
1	1	2	0.0035	0.0411	0.6987	1.0000	0.0000
2	1	39	0.0010	0.0250	0.7500	1.0000	0.0000
3	2	3	0.0013	0.0151	0.2572	1.0000	0.0000
4	2	25	0.0070	0.0086	0.1460	1.0000	0.0000
5	2	30	0.0000	0.0181	0.0000	1.0250	0.0000
6	3	4	0.0013	0.0213	0.2214	1.0000	0.0000
7	3	18	0.0011	0.0133	0.2138	1.0000	0.0000
8	4	5	0.0008	0.0128	0.1342	1.0000	0.0000
9	4	14	0.0008	0.0129	0.1382	1.0000	0.0000
10	5	6	0.0002	0.0026	0.0434	1.0000	0.0000
11	5	8	0.0008	0.0112	0.1476	1.0000	0.0000
12	6	7	0.0006	0.0092	0.1130	1.0000	0.0000
13	6	11	0.0007	0.0082	0.1389	1.0000	0.0000
14	6	31	0.0000	0.0250	0.0000	1.0700	0.0000
15	7	8	0.0004	0.0046	0.0780	1.0000	0.0000
16	8	9	0.0023	0.0363	0.3804	1.0000	0.0000
17	9	39	0.0010	0.0250	1.2000	1.0000	0.0000
18	10	11	0.0004	0.0043	0.0729	1.0000	0.0000
19	10	13	0.0004	0.0043	0.0729	1.0000	0.0000
20	10	32	0.0000	0.0200	0.0000	1.0700	0.0000
21	12	11	0.0016	0.0435	0.0000	1.0060	0.0000
22	12	13	0.0016	0.0435	0.0000	1.0060	0.0000
23	13	14	0.0009	0.0101	0.1723	1.0000	0.0000
24	14	15	0.0018	0.0217	0.3660	1.0000	0.0000
25	15	16	0.0009	0.0094	0.1710	1.0000	0.0000
26	16	17	0.0007	0.0089	0.1342	1.0000	0.0000
27	16	19	0.0016	0.0195	0.3040	1.0000	0.0000
28	16	21	0.0008	0.0135	0.2548	1.0000	0.0000
29	16	24	0.0003	0.0059	0.0680	1.0000	0.0000
30	17	18	0.0007	0.0082	0.1319	1.0000	0.0000
31	17	27	0.0013	0.0173	0.3216	1.0000	0.0000
32	19	20	0.0007	0.0138	0.0000	1.0600	0.0000
33	19	33	0.0007	0.0142	0.0000	1.0700	0.0000
34	20	34	0.0009	0.0180	0.0000	1.0090	0.0000
35	21	22	0.0008	0.0140	0.2565	1.0000	0.0000
36	22	23	0.0006	0.0096	0.1846	1.0000	0.0000
37	22	35	0.0000	0.0143	0.0000	1.0250	0.0000
38	23	24	0.0022	0.0350	0.3610	1.0000	0.0000
39	23	36	0.0005	0.0272	0.0000	1.0000	0.0000
40	25	26	0.0032	0.0323	0.5310	1.0000	0.0000

41	25	37	0.0006	0.0232	0.0000	1.0250	0.0000
42	26	27	0.0014	0.0147	0.2396	1.0000	0.0000
43	26	28	0.0043	0.0474	0.7802	1.0000	0.0000
44	26	29	0.0057	0.0625	1.0290	1.0000	0.0000
45	28	29	0.0014	0.0151	0.2490	1.0000	0.0000
46	29	38	0.0008	0.0156	0.0000	1.0250	0.0000

B.2 Two bus system

Bus	v	δ
1	1.0000	0.0000
2	0.8799	-0.1139

Load	Bus	p_L	q_L
1	2	1.0000	1.0000

Gen	Bus	p_G	q_G	p_G^{min}	p_G^{max}	q_G^{min}	q_G^{max}	v_{ref}	Slack
PV 1	1	1.0000	1.2583	-0.0010	10.0000	-10.0000	10.0000	1.0000	1

Line	k	m	r	x	b^{sh}	τ	θ
1	1	2	0.0000	0.1000	0.0000	1.0000	0.0000

B.3 FSWG data

The following parameters were obtained from [Hwang et al., 2008] with respect to v_{base} = 0.690KV and s_{base} = 1MVA:

$r_s = 0.0027$, $r_r = 0.0022$, $x_s = 0.025$, $x_r = 0.046$, $x_m = 1.38$, $f = 50$, Vn =1/0.69, Sn = 1, p_G^{max} =0.009, $b^{comp} = 0.00345$, $x_t = 0.02$, r= 28.5, $n_{gb} = 65.27$, $\rho = 1.225$, n_{pp}=2., $c_1 = 0.5$, $c_2 = 116$, $c_3 = 0.4$, $c_4 = 0$, $c_5 = 0$, $c_6 = 5.$, $c_7 = 21.$, $c_8 = 0.08$, and c_9 = 0.035.

B.4 DFIG data

The following parameters were obtained from [Li, 2013] with respect to v_{base} = 1.0KV and s_{base} = 2MVA:

r_s = 0.0078, r_r = 0.025, x_s = 0.0794, x_r = 0.4, x_m = 4.1039, s_{nom} = -0.005, f = 50, n_{pp} = 2, r= 35.5, n_{gb} = 94, ρ = 1.225, x_t = 0.05, r_t = 0.03, c_1 = 0.73, c_2 = 151, c_3 = 0.58, c_4 = 0.002, c_5 = 2.14, c_6 = 13.2, c_7 = 18.4, c_8 = -0.02, c_9 = -0.003, p_G^{max} = 1.0, η = 0.10, R = 0.05, ω_m^{min} = 0.4, ω_m^{max} = 1.3, q_G^{max} = 0.32, q_G^{min} = -0.48, and x_{sl} = 0.02.

B.5 PMSG data

The presented below PMSG's data are from [Muyeen et al., 2007] with respect to v_{base} = 1.0KV and s_{base} = 5MVA:

x_s = 0.5, r_s=0.01, f = 20, n_{pp} = 75, r= 50, n_{gb} = 1, ρ = 1.225, r_t = 0.0, x_t = 0.03, c_1 = 0.73, c_2 = 151, c_3 = 0.58, c_4 = 0.002, c_5 = 2.14, c_6 = 13.2, c_7 = 18.4, c_8 = 0.02, c_9 = 0.003, pf= 0.98, ψ = 1.4, p_G^{max} = 1, η = 0.10, R = 0.05, x_{sl} = 0.02, q_G^{min} = -0.48, and q_G^{max} = 0.32.

B.6 SVC data

The SVC data is from [Canizares and Alvarado, 1999] with respect to v_{base} = 13.8KV and s_{base} = 60MVA:

x_c = 1.1708, x_l = 0.4925, α^{min} = 90 °, α^{max} = 175 °, x_{sl} = 0.02, and x_t = 0.2.

B.7 STATCOM data

The STATCOM is obtained from [Canizares and Alvarado, 1999] with respect to v_{base} = 13.8KV and s_{base} = 60MVA:

r_t = 0, x_t = 0.145, r_c = 588.23, x_{sl} = 0.02, $V_{DC,ref}$ = 1, and i^{max} = 1.

Bibliography

Acha, E., Fuerte-Esquivel, C. R., Ambriz-Pérez, H., and Angeles-Camacho, C. (2004). *FACTS: Modelling and Simulation in Power Networks*. John Wiley & Sons.

Ackermann, T., editor (2012). *Wind power in power systems*. Wiley, Chichester, West Sussex ; Hoboken, N.J, 2nd edition.

Administration, B. P. (2015). Wind Power Forecasting Data. Available from: `http://www.bpa.gov/Projects/Initiatives/Wind/pages/Wind-Power-Forecasting-Data.aspx`.

Ajjarapu, V. and Christy, C. (1992). The continuation power flow: a tool for steady state voltage stability analysis. *IEEE Transactions on Power Systems*, 7(1):416–423.

Alsac, O. and Stott, B. (1974). Optimal Load Flow with Steady-State Security. *IEEE Transactions on Power Apparatus and Systems*, PAS-93(3):745–751.

Anaya-Lara, O., Jenkins, N., Ekanayake, J., Cartwright, P., and Hughes, M. (2011). *Wind Energy Generation: Modelling and Control*. John Wiley & Sons.

Anderson, P. M. and Fouad, A. A. (2003). *Power system control and stability*. IEEE Press power engineering series. IEEE Press ; Wiley-Interscience, Piscataway, N.J, 2nd edition.

Aree, P. and Acha, E. (2011). Power flow initialisation of dynamic studies with induction motor loads. *IET Generation, Transmission Distribution*, 5(4):417–424.

Borkowska, B. (1974). Probabilistic Load Flow. *IEEE Transactions on Power Apparatus and Systems*, PAS-93(3):752–759.

Bouffard, F., Galiana, F. D., and Arroyo, J. M. (2005). Umbrella contingencies in security-constrained optimal power flow. In *15th Power Systems Computation Conference, PSCC*, volume 5.

Calvaer, A. and Van Geert, E. (1984). Quasi Steady State Synchronous Machine Linearization Around an Operating Point and Applications. *IEEE Transactions on Power Apparatus and Systems*, PAS-103(6):1466–1472.

Canizares, C. and Alvarado, F. (1993). Point of collapse and continuation methods for large AC/DC systems. *IEEE Transactions on Power Systems*, 8(1):1–8.

Canizares, C. and Alvarado, F. (1999). UWPFLOW: continuation and direct methods to locate fold bifurcations in AC/DC/FACTS power systems.

Canizares, C. and Faur, Z. (1999). Analysis of SVC and TCSC controllers in voltage collapse. *IEEE Transactions on Power Systems*, 14(1):158–165.

Capitanescu, F., Martinez Ramos, J. L., Panciatici, P., Kirschen, D., Marano Marcolini, A., Platbrood, L., and Wehenkel, L. (2011). State-of-the-art, challenges, and future trends in security constrained optimal power flow. *Electric Power Systems Research*, 81(8):1731–1741.

Cartwright, P., Holdsworth, L., Ekanayake, J., and Jenkins, N. (2004). Co-ordinated voltage control strategy for a doubly-fed induction generator (DFIG)-based wind farm. *Generation, Transmission and Distribution, IEE Proceedings-*, 151(4):495–502.

Castro, L., Fuerte-Esquivel, C., and Tovar-Hernandez, J. (2012). Solution of Power Flow With Automatic Load-Frequency Control Devices Including Wind Farms. *IEEE Transactions on Power Systems*, 27(4):2186–2195.

Castro, L. M., Fuerte-Esquivel, C. R., and Tovar-Hernández, J. H. (2011). A unified approach for the solution of power flows in electric power systems including wind farms. *Electric Power Systems Research*, 81(10):1859–1865.

Cañizares, C. A., Pozzi, M., Corsi, S., and Uzunovic, E. (2003). STATCOM modeling for voltage and angle stability studies. *International Journal of Electrical Power & Energy Systems*, 25(6):431–441.

Chang, S.-K. and Brandwajn, V. (1988). Adjusted solutions in fast decoupled load flow. *IEEE Transactions on Power Systems*, 3(2):726–733.

Cutsem, T. v. and Vournas, C. (2007). *Voltage Stability of Electric Power Systems*. Springer Science & Business Media.

Davis, T. A. and Palamadai Natarajan, E. (2010). Algorithm 907: KLU, A Direct Sparse Solver for Circuit Simulation Problems. *ACM Trans. Math. Softw.*, 37(3):36:1–36:17.

DeGroot, M. H. and Schervish, M. J. (2012). *Probability and Statistics*. Addison-Wesley.

Divya, K. C. and Rao, P. S. N. (2006). Models for wind turbine generating systems and their application in load flow studies. *Electric Power Systems Research*, 76(9–10):844–856.

Dobson, I. and Lu, L. (1992). Voltage collapse precipitated by the immediate change in stability when generator reactive power limits are encountered. *IEEE Transactions on Circuits and Systems I: Fundamental Theory and Applications*, 39(9):762–766.

Dvorkin, Y., Wang, Y., Pandzic, H., and Kirschen, D. (2014). Comparison of scenario reduction techniques for the stochastic unit commitment. In *2014 IEEE PES General Meeting | Conference Exposition*, pages 1–5.

Díaz, G. and Gonzalez-Moran, C. (2012). Fischer-Burmeister-Based Method for Calculating Equilibrium Points of Droop-Regulated Microgrids. *IEEE Transactions on Power Systems*, 27(2):959–967.

Díaz, G., González-Morán, C., and Viescas, C. (2012). Operating point of islanded microgrids consisting of conventional doubly fed induction generators and distributed supporting units. *IET Renewable Power Generation*, 6(5):303–314.

EIA (2015). *Annual Energy Outlook*. U.S. Energy Information Administration.

Facchinei, F., Jiang, H., and Qi, L. (1999). A smoothing method for mathematical programs with equilibrium constraints. *Mathematical Programming*, 85(1):107–134.

Feijoo, A. (2009). On PQ Models for Asynchronous Wind Turbines. *IEEE Transactions on Power Systems*, 24(4):1890–1891.

Feijoo, A. and Cidras, J. (2000). Modeling of wind farms in the load flow analysis. *IEEE Transactions on Power Systems*, 15(1):110–115.

Ferris, M. and Pang, J. (1997). Engineering and Economic Applications of Complementarity Problems. *SIAM Review*, 39(4):669–713.

Fischer, A. (1992). A special newton-type optimization method. *Optimization*, 24(3-4):269–284.

Fliscounakis, S., Panciatici, P., Capitanescu, F., and Wehenkel, L. (2013). Contingency Ranking With Respect to Overloads in Very Large Power Systems Taking Into Account Uncertainty, Preventive, and Corrective Actions. *IEEE Transactions on Power Systems*, 28(4):4909–4917.

Fox, B. (2007). *Wind Power Integration: Connection and System Operational Aspects*. IET.

Fu, Q., Yu, D., and Ghorai, J. (2011). Probabilistic load flow analysis for power systems with multi-correlated wind sources. In *2011 IEEE Power and Energy Society General Meeting*, pages 1–6.

Fuerte-Esquivel, C. and Acha, E. (1997). A Newton-type algorithm for the control of power flow in electrical power networks. *IEEE Transactions on Power Systems*, 12(4):1474–1480.

Fuerte-Esquivel, C., Acha, E., and Ambriz-Perez, I. (2000). Integrated SVC and step-down transformer model for Newton-Raphson load flow studies. *IEEE Power Engineering Review*, 20(2):45–46.

Fuerte-Esquivel, C., Tovar-Hernandez, J., Gutierrez-Alcaraz, G., and Cisneros-Torres, F. (2001). Closure to discussion of "modeling of wind farms in the load flow analysis". *IEEE Transactions on Power Systems*, 16(4):951–952.

Ghiocel, S. and Chow, J. (2014). A Power Flow Method Using a New Bus Type for Computing Steady-State Voltage Stability Margins. *IEEE Transactions on Power Systems*, 29(2):958–965.

Ghiocel, S., Chow, J., Quint, R., Kosterev, D., and Sobajic, D. (2014). Computing measurement-based voltage stability margins for a wind power hub using the AQ-bus method. In *Power and Energy Conference at Illinois (PECI), 2014*, pages 1–6.

Guoyu, X., Galiana, F., and Low, S. (1985). Decoupled Economic Dispatch Using the Participation Factors Load Flow. *IEEE Transactions on Power Apparatus and Systems*, PAS-104(6):1377–1384.

GWEC (2014). GLOBAL WIND REPORT 2014 - GWEC. Available from: `http://www.gwec.net/publications/global-wind-report-2/global-wind-report-2014-annual-market-update/`.

Hedayati, H., Nabaviniaki, S., and Akbarimajd, A. (2008). A Method for Placement of DG Units in Distribution Networks. *IEEE Transactions on Power Delivery*, 23(3):1620–1628.

Hingorani, N. G. and Gyugyi, L. (2000). *Understanding FACTS: Concepts and Technology of Flexible AC Transmission Systems*. Wiley.

Hong, H. P. (1998). An efficient point estimate method for probabilistic analysis. *Reliability Engineering & System Safety*, 59(3):261–267.

Hwang, P., Ahn, S., and Moon, S. (2008). Modeling of the fixed speed wind turbine generator system for DTS. In *2008 IEEE Power and Energy Society General Meeting - Conversion and Delivery of Electrical Energy in the 21st Century*, pages 1–7.

Ilić, M. and Zaborszky, J. (2000). *Dynamics and Control of Large Electric Power Systems*. Wiley.

Jaramillo, O. A. and Borja, M. A. (2004). Wind speed analysis in La Ventosa, Mexico: a bimodal probability distribution case. *Renewable Energy*, 29(10):1613–1630.

Kayikci, M. and Milanovic, J. (2007). Reactive Power Control Strategies for DFIG-Based Plants. *IEEE Transactions on Energy Conversion*, 22(2):389–396.

Kirschen, D. S. and Strbac, G. (2004). *Fundamentals of Power System Economics*. John Wiley & Sons.

Konopinski, R., Vijayan, P., and Ajjarapu, V. (2009). Extended Reactive Capability of DFIG Wind Parks for Enhanced System Performance. *IEEE Transactions on Power Systems*, 24(3):1346–1355.

Kundur, P., Balu, N. J., and Lauby, M. G. (1994). *Power system stability and control*. The EPRI power system engineering series. McGraw-Hill, New York.

Li, S. (2013). Power Flow Modeling to Doubly-Fed Induction Generators (DFIGs) Under Power Regulation. *IEEE Transactions on Power Systems*, 28(3):3292–3301.

Lobo, M. S., Vandenberghe, L., Boyd, S., and Lebret, H. (1998). Applications of second-order cone programming. *Linear Algebra and its Applications*, 284(1–3):193–228.

Lotfalian, M., Schlueter, R., Idizior, D., Rusche, P., Tedeschi, S., Shu, L., and Yazdankhah, A. (1985). Inertial, Governor, And Agc/Economic Dispatch Load Flow Simulations Of Loss Of Generation Contingencies. *IEEE Transactions on Power Apparatus and Systems*, PAS-104(11):3020–3028.

Loukarakis, E., Margaris, I., and Moutis, P. (2009). Frequency control support and participation methods provided by wind generation. In *2009 IEEE Electrical Power Energy Conference (EPEC)*, pages 1–6.

Lubosny, Z. (2010). *Wind Turbine Operation in Electric Power Systems: Advanced Modeling*. Springer Berlin Heidelberg.

Machowski, J., Bialek, J., and Bumby, D. J. (2011). *Power System Dynamics: Stability and Control*. John Wiley & Sons.

Mamandur, K. and Berg, G. (1982). Automatic Adjustment of Generator Voltages in Newton-Raphson Mehtod of Power Flow Solutions. *IEEE Transactions on Power Apparatus and Systems*, PAS-101(6):1400–1409.

Meliopoulos, A., Cokkinides, G., and Chao, X. (1990). A new probabilistic power flow analysis method. *IEEE Transactions on Power Systems*, 5(1):182–190.

Milano, F. (2005). An Open Source Power System Analysis Toolbox. *IEEE Transactions on Power Systems*, 20(3):1199–1206.

Milano, F. (2008). Assessing adequate voltage stability analysis tools for networks with high wind power penetration. In *Third International Conference on Electric Utility Deregulation and Restructuring and Power Technologies, 2008. DRPT 2008*, pages 2492–2497.

Milano, F. (2010). *Power System Modelling and Scripting*. Springer Science & Business Media.

Miller, N., Clark, K., and Shao, M. (2011). Frequency responsive wind plant controls: Impacts on grid performance. In *2011 IEEE Power and Energy Society General Meeting*, pages 1–8.

Miller, N., Loutan, C., Shao, M., and Clark, K. (2013). Emergency Response: U.S. System Frequency with High Wind Penetration. *IEEE Power and Energy Magazine*, 11(6):63–71.

Miller, N., Shao, M., Venkataraman, S., Loutan, C., and Rothleder, M. (2012). Frequency response of California and WECC under high wind and solar conditions. In *2012 IEEE Power and Energy Society General Meeting*, pages 1–8.

Monticelli, A., Pereira, M., and Granville, S. (1987). Security-Constrained Optimal Power Flow with Post-Contingency Corrective Rescheduling. *IEEE Transactions on Power Systems*, 2(1):175–180.

Morales, J. and Perez-Ruiz, J. (2007). Point Estimate Schemes to Solve the Probabilistic Power Flow. *IEEE Transactions on Power Systems*, 22(4):1594–1601.

Muyeen, S., Takahashi, R., Murata, T., Tamura, J., and Ali, M. (2007). Transient stability analysis of permanent magnet variable speed synchronous wind generator. In *International Conference on Electrical Machines and Systems, 2007. ICEMS*, pages 288–293.

Okamura, M., O-ura, Y., Hayashi, S., Uemura, K., and Ishiguro, F. (1975). A new power flow model and solution method-Including load and generator characteristics and effects of system control devices. *IEEE Transactions on Power Apparatus and Systems*, 94(3):1042–1050.

Ortega, J. M. and Rheinboldt, W. C. (1970). *Iterative Solution of Nonlinear Equations in Several Variables*. SIAM.

Outcalt, D. M. (2009). *Probabilistic load flow for high wind penetrated power systems based on a five point estimation method*. PhD thesis, The University of Wisconsin - Milwaukee.

Padron, J. and Lorenzo, A. (2010). Calculating Steady-State Operating Conditions for Doubly-Fed Induction Generator Wind Turbines. *IEEE Transactions on Power Systems*, 25(2):922–928.

Pai, M. A. (1989). *Energy Function Analysis for Power System Stability*. Springer Science & Business Media.

Pardalos, P., Rebennack, S., Pereira, M. V. F., Iliadis, N. A., and Pappu, V. (2014). *Handbook of Wind Power Systems*. Springer Science & Business Media.

Pirnia, M., Cañizares, C., and Bhattacharya, K. (2013). Revisiting the power flow problem based on a mixed complementarity formulation approach. *IET Generation, Transmission Distribution*, 7(11):1194–1201.

Restrepo Hernandez, J. F. (2011). *Impact of wind energy on the operation of power systems*. PhD thesis, McGill University.

Rico-Melgoza, J. J., Suarez, J. P., Barrera-Cardiel, E., and Martinez, M. M. (2012). Modeling and Analysis of Three-phase Diode Bridge Rectifiers as Linear Complementarity Systems. *Electric Power Components and Systems*, 40(15):1639–1655.

Roman, C. and Rosehart, W. (2006). Complementarity model for load tap changing transformers in stability based OPF problem. *Electric Power Systems Research*, 76(6–7):592–599.

Rosehart, W., Roman, C., and Schellenberg, A. (2005). Optimal power flow with complementarity constraints. *IEEE Transactions on Power Systems*, 20(2):813–822.

Ruiz-Vega, D., Asiain Olivares, T., and Salinas, D. (2002). An approach to the initialization of dynamic induction motor models. *IEEE Transactions on Power Systems*, 17(3):747–751.

Sauer, P. W. (1998). *Power System Dynamics and Stability*. Prentice Hall.

Schellenberg, A., Rosehart, W., and Aguado, J. (2005). Cumulant-based probabilistic optimal power flow (P-OPF) with Gaussian and gamma distributions. *IEEE Transactions on Power Systems*, 20(2):773–781.

Seguro, J. V. and Lambert, T. W. (2000). Modern estimation of the parameters of the Weibull wind speed distribution for wind energy analysis. *Journal of Wind Engineering and Industrial Aerodynamics*, 85(1):75–84.

Slootweg, J., Polinder, H., and Kling, W. (2001). Initialization of wind turbine models in power system dynamics simulations. In *Power Tech Proceedings, 2001 IEEE Porto*, volume 4, pages 6 pp. vol.4–.

Smed, T., Andersson, G., Sheble, G., and Grigsby, L. (1991). A new approach to AC/DC power flow. *IEEE Transactions on Power Systems*, 6(3):1238–1244.

Stagg, G. W. and Abiad, H. H. E. (1968). *Computer Methods in Power Systems Analysis*. Mac Graw Hill.

Stott, B. (1974). Review of load-flow calculation methods. *Proceedings of the IEEE*, 62(7):916–929.

Su, C.-L. (2005). Probabilistic load-flow computation using point estimate method. *IEEE Transactions on Power Systems*, 20(4):1843–1851.

Sundaresh, L. and Nagendra Rao, P. S. (2014). A modified Newton–Raphson load flow scheme for directly including generator reactive power limits using complementarity framework. *Electric Power Systems Research*, 109:45–53.

Taylor, C. W. (1994). *Power system voltage stability*. McGraw-Hill Ryerson, Limited.

Taylor, C. W., Scott, G., and Hammad, A. a. o. (1994). Static Var Compensator Models for Power Flow and Dynamic Performance Simulation. *IEEE Transactions on Power Systems*, 9:1.

Tinney, W. F. and Hart, C. (1967). Power Flow Solution by Newton's Method. *IEEE Transactions on Power Apparatus and Systems*, PAS-86(11):1449–1460.

Tinoco De Rubira, T. A. (2015). *Numerical optimization and modeling techniques for power system operations and planning*.

Ullah, N. and Thiringer, T. (2007). Variable Speed Wind Turbines for Power System Stability Enhancement. *IEEE Transactions on Energy Conversion*, 22(1):52–60.

Vaccaro, A., Cañizares, C., and Bhattacharya, K. (2013). A Range Arithmetic-Based Optimization Model for Power Flow Analysis Under Interval Uncertainty. *IEEE Transactions on Power Systems*, 28(2):1179–1186.

Van Cutsem, T. (1991). A method to compute reactive power margins with respect to voltage collapse. *IEEE Transactions on Power Systems*, 6(1):145–156.

Villanueva, D., Pazos, J., and Feijoo, A. (2011). Probabilistic Load Flow Including Wind Power Generation. *IEEE Transactions on Power Systems*, 26(3):1659–1667.

Vittal, E., O'Malley, M., and Keane, A. (2010). A Steady-State Voltage Stability Analysis of Power Systems With High Penetrations of Wind. *IEEE Transactions on Power Systems*, 25(1):433–442.

Vittal, V. and Ayyanar, R. (2012). *Grid Integration and Dynamic Impact of Wind Energy*. Springer Science & Business Media.

Wang, Y., Xia, Q., and Kang, C. (2011). Unit Commitment With Volatile Node Injections by Using Interval Optimization. *IEEE Transactions on Power Systems*, 26(3):1705–1713.

Weibull, W. (1951). A statistical distribution function of wide applicability. *Journal of applied mechanics*, 18(3):293–297. 05652.

Wolfe, P. (1959). The Simplex Method for Quadratic Programming. *Econometrica*, 27(3):382.

Wong, P., Albrecht, P., Allan, R., Billinton, R., Chen, Q., Fong, C., Haddad, S., Li, W., Mukerji, R., Patton, D., Schneider, A., Shahidehpour, M., and Singh, C. (1999). The IEEE Reliability Test System-1996. A report prepared by the Reliability Test System Task Force of the Application of Probability Methods Subcommittee. *IEEE Transactions on Power Systems*, 14(3):1010–1020.

Zimmerman, R., Murillo-Sánchez, C., and Thomas, R. (2011). MATPOWER: Steady-State Operations, Planning, and Analysis Tools for Power Systems Research and Education. *IEEE Transactions on Power Systems*, 26(1):12–19.

Zimmerman, R. D. (2011). AC power flows, generalized OPF costs and their derivatives using complex matrix notation. Technical report. Available from: `http://www.pserc.cornell.edu//matpower/#docs`.

Zobian, A. and Ilic, M. (1997). Unbundling of transmission and ancillary services. I. Technical issues. *IEEE Transactions on Power Systems*, 12(2):539–548.